DNA origami directed self-assembled hybrid nanoantennas for single molecule spectroscopic applications

SWATI TANWAR

A thesis submitted for the partial fulfillment of
the degree of Doctor of Philosophy

Institute of Nano Science and Technology
Habitat Centre, Sector-64, Phase-10, Mohali, Punjab 160062, India
Indian Institute of Science Education and Research Mohali
Knowledge city, Sector 81, SAS Nagar, Manauli PO, Mohali 140306, Punjab, India.

January 2020

Dedicated to my beloved family and respected teachers

Declaration

The work presented in this thesis has been carried out by me under the guidance of Dr.Tapasi Sen at the Institute of Nano Science and Technology Mohali. This work has not been submitted in part or in full for a degree, a diploma, or a fellowship to any other university or institute. Whenever contributions of others are involved, every effort is made to indicate this clearly, with due acknowledgement of collaborative research and discussions. This thesis is a bonafide record of original work done by me and all sources listed within have been detailed in the bibliography.

SWATI TANWAR

In my capacity as the supervisor of the candidate's thesis work, I certify that the above statements by the candidate are true to the best of my knowledge.

Dr. TAPASI SEN

Acknowledgements

Being a Ph.D. student at the Institute of Nano Science and Technology was a rich experience, academically as well as humanly. Many people contributed to the success of the work presented in this thesis and I will always be in their debt.

First and foremost, I would like to express my deep sense of gratitude to my Ph.D. supervisor Dr. Tapasi Sen, for believing in my research abilities and giving me a wonderful opportunity to pursue research in this amazing field of DNA nanotechnology. She gave me complete freedom of scientific research and always helped me in troubleshooting when I got stuck in my work. Her scientific suggestions have always helped me in accelerating the experimental procedures. Apart from scientific suggestions her constant guidance, support, and motivation have been immensely helpful in the completion of this journey. I am really honored to be her first Ph.D. student. I take this opportunity to thank her from the bottom of my heart for being my Ph.D. supervisor. I have enjoyed my research project and have learned much over the past 5 years.

I would like to thank the Institute of Nano Science and Technology for providing a wonderful research environment, facilities, and resources to accomplish my research work. I also want to thank IISER Mohali for the infrastructure facility.

My sincere and heartfelt thanks to Professor Ashok Kumar Ganguli, founding Director, INST Mohali for his support and guidance. His enthusiasm and dedication have always inspired me to work hard. I wish to express my gratitude to Professor Amitava Patra, Director, INST for his support and encouragement in the research. My special words of thanks go to late Shri P.K. Datta, former Dean Academics INST Mohali, for always being so kind, helpful, and motivating. I would like to thank Dr. Debabrata Patra for his kind support. I also thank my doctoral committee members Dr.Sangita Roy and Dr. Kamalakannan Kailasam for giving me valuable suggestions to improve my research work and supporting me. I want to thank Dr. Sonalika Vaidya for helping me learn TEM and the constant support she provided throughout my stay at INST Mohali. I am grateful to all faculty members and staff of INST Mohali for their direct and indirect support. My special words of thanks go to Dr. Krishna Kanta Haldar and Dr. Chayan Kanti Nandi our collaborators for always being so kind, helpful, and motivating.

I would like to acknowledge all the teachers I learned from since my childhood, I would not have been here without their guidance, blessing, and support. I want to thank Dr. Anant Narayan Bhatt, INMAS, DRDO for instigating in me the desire to pursue research. I extend my

sincere word of thanks to Dr. Raksha Sharma, who has always been there, more as a friend than a teacher. My special thanks to Dr. Pradip Nahar, Institute of Genomics and Integrative Biology, Delhi for being another role model for me.

I want to thank Vaibhav Bajpai (TEM operator) for his timely technical support.

I take this opportunity to extend my sincere thanks to my labmates Vishaldeep, Gagandeep, and Charanleen for their selfless co-operation and help in making my work successful. In addition to these individuals, Dr. Bhagwati Sharma deserves special thanks for being both my senior and a friend. He was always there to help whenever I needed him. My heartfelt thanks to my seniors Dr. Rajesh Ahirwar, Dr. Vinod Kumar, Dr. Sachin Rondiya for their guidance and moral support.

I personally want to extend my thanks to my batch mates and friends Dimple, Anup, Ritu, Naimat, Ashmeet, Munish, Ankur, Soumen, Renu, Pulkit, Harman, Arnob, and Sudhanshu, who were always there and never let me down during these Ph.D. days. My very special thanks go to Rajinder and Rashmi for being my close friends, without them I could have not enjoyed my time to the fullest. I am also obliged to my juniors Ankush, Pushpendra, Anirban, Rohit, Nadeem, Harsimran, Vijay, Pooja, Krishna, and Sushil for their help.

I want to thank my landlords Mr. Raj Kumar Sharma and Mrs. Promila Sharma for making me feel at home and hosting my every Sunday's breakfast.

Most importantly none of this would have been possible without the support of my family. I deeply express my love and gratitude to my lovable father Mr. Naresh Pal Tanwar and mother Mrs. Kanta Tanwar for their blessings, unconditional love, and support. I want to thank my paternal uncle Mr. Yashpal Singh for his care and love. My heartfelt regards go to my father-in-law Mr. Randhir Tanwar and mother-in-law Mrs. Kamlesh Devi for their love and moral support. I would like to take this opportunity to express my love to my lovable sisters Jyoti, Sonam, and brother Vaibhav for their care and affection. I am very grateful to my loving husband, Ashutosh Tanwar, for being a constant source of support and encouragement. He always understood me and stood beside me.

There are many more who have directly or indirectly contributed to making this journey successful, I thank them all.

I want to thank God, the almighty for providing me this opportunity and granting me the capability to complete it successfully.

SWATI TANWAR

TABLE OF CONTENTS

Chapter 2: Methodology

Chapter 3: Design of Au nanostar dimers for single molecule surface enhanced Raman scattering

Chapter 5: Synthesis and immobilization of single Si QD on DNA origami for sensing and imaging applications

LIST OF FIGURES

Chapter 1: Introduction

Chapter 2: Methodology

Chapter 3: Design of Au nanostar dimers for single molecule surface enhanced Raman scattering

Chapter 4: Au@Ag bimetallic nanostar dimer nanoantennas for single molecule SERS and fluorescence enhancement

Chapter 5: Synthesis and immobilization of single Si QD on DNA origami for sensing and imaging applications

Chapter 6: Plasmonic nanoantennas for label free sensing of single protein molecule

LIST OF SCHEMES

Chapter 1: Introduction

Chapter 2: Methodology

Chapter 3: Design of Au nanostar dimers for single molecule surface enhanced Raman scattering

Chapter 4: Au@Ag bimetallic nanostar dimer nanoantennas for single molecule SERS and fluorescence enhancement

Chapter 5: Synthesis and immobilization of single Si QD on DNA origami for sensing and imaging applications

Chapter 6: Plasmonic nanoantennas for label free sensing of single protein molecule

LIST OF TABLES

Chapter 1: Introduction

Chapter 3: Design of Au nanostar dimers for single molecule surface enhanced Raman scattering

Chapter 4: Au@Ag bimetallic nanostar dimer nanoantennas for single molecule SERS and fluorescence enhancement

Chapter 5: Synthesis and immobilization of single Si QD on DNA origami for sensing and imaging applications

Chapter 6: Plasmonic nanoantennas for label free sensing of single protein molecule

ACRONYMS

NPs	Nanoparticles
pH	The negative logarithm of hydronium-ion concentration ($-\log_{10} [H_3O^+]$)
UV-Vis	UV-Visible Spectroscopy
FTIR	Fourier Transform Infrared
XRD	X-ray diffraction
TEM	Transmission Electron Microscope
HRTEM	High Resolution Transmission Electron Microscope
XPS	X-ray Photoelectron Spectroscopy
EDX	Energy Dispersive X-ray spectroscopy
DNA	Deoxyribonucleic acid
AFM	Atomic Force Microscopy
SERS	Surface enhanced Raman spectroscopy
Cys	Cysteine
nt	nucleotide
EF	Enhancement factor
SM	Single molecule
SPR	Surface Plasmon Resonance
LSPR	Localized Surface Plasmon Resonance
LOD	Limit of detection

NOMENCLATURE

λ	Wavelength
ε	Extinction coefficient
α	Alpha
σ	Sigma
ϕ	Fluorescence quantum yield
π	Pi
Å	Angstrom
ºC	Degree Centigrade
nm	Nanometer
µm	Micrometer
cm	Centimeter
mL	Millilitre
µL	Microlitre
pM	Picomolar
µM	Micromolar
mM	Millimolar
Θ	Theta
mW	Milliwatt

Abstract

This thesis entitled “DNA origami directed self-assembled hybrid nanoantennas for single molecule spectroscopic applications” focuses on the fabrication of novel plasmonic nanoantenna materials and their applications in single molecule surface enhanced optical spectroscopy. Single molecule spectroscopy techniques enable the investigation of the individual nanoscale behavior of molecules which further helps in understanding the normally hidden heterogeneities of complex biological and chemical systems. It yields important information like distribution of behavior instead of a single population average and measurement of uncorrelated stochastic multistep processes. Due to weak interactions between an optical field and a single molecule, optimal signal to noise ratio is lost, limiting the utility of single molecule techniques for commercial applications. Plasmonic nanoantennas concentrate light into small volumes, which greatly enhances the local electromagnetic (EM) field near the metal nanostructures leading to a strong enhancement of usually weak single molecule signals. Anisotropic nanostructures because of high intensity electromagnetic field generated around their sharp edges result in enhancement factors (EFs) high enough for single molecule detection. For the fabrication of a highly efficient plasmonic nanoantenna, the two nanoparticles have to be placed close to each other with an interparticle gap of few nanometers. And the fluorophore/quantum dot has to be precisely placed in the conjunction region between the nanoparticles such that it experiences the highest electromagnetic field. This precision can be very easily achieved using DNA origami. DNA origami is a simple solution based technique that allows assembling of different types of particles in complex geometries with precise control over the interparticle gap, orientation, and stoichiometry. The design of Au nanostar (Au NS) dimer structures with tunable interparticle gap and stoichiometry on dimerized rectangular DNA origami has been described. Single Texas red (TR) dye molecule which acts as a Raman reporter molecule was precisely positioned in the junction of the dimerized DNA origami by modifying one of the branching staples of the DNA origami template with the dye molecule. The effect of the interparticle gap, stoichiometry, and negative curvature site of Au NSs on the Raman enhancement of single TR dye molecule has been investigated. The SERS enhancement factors (EFs) of single TR dye molecules located in the conjunction region of dimer structures having interparticle gaps of 7 and 13 nm were found to be in the range of 10^9-10^{10}, which are high enough for single analyte detection.

Bimetallic metal nanostructures are known to show better optical response as compared to their monometallic counterparts, due to the emergence of new optical and electronic properties

because of the combination of both the metals. Among all the bimetallic NPs Au@Ag NPs have gained immense attention because they combine the enhanced plasmonic properties (high extinction coefficient) of Ag and chemical stability of Au in one structure. Effect of Au@Ag bimetallic nanostars on the SERS signals of single FAM, Cy3, and Texas red (TR) dyes corresponding to different regions of the visible spectrum has been investigated. EFs for single Cy3 dye molecules were found to be higher than TR and FAM dyes due to close resonance between the surface plasmon resonance (SPR) of Au@AgNSs and the absorption maximum of Cy3 and higher Raman cross-section of Cy3 dye. The effect of different interparticle gaps and stoichiometry on the SERS EFs has also been demonstrated. The EFs were higher for dimer nanoantennas with 7 nm of interparticle gap than the 13 nm gap. And the EFs were higher for dimer nanoantennas than monomer nanoantennas. The EFs for all the three dyes were in the order of 10^9-10^{10} for Au@Ag NS dimer and monomer nanoantennas, sufficient for single molecule detection. Designed Au@Ag NS dimer nanoantennas with interparticle gap size of 5 nm were found to be showing 10-fold enhancement in fluorescence signals of single Cy3 molecule localized in the plasmonic hotspot. Further, the applicability of designed Au@Ag NS dimer nanoantenna for SERS based label-free detection of bacterial biomarker pyocyanin has been demonstrated. The Au@Ag NS dimer plasmonic nanoantenna was able to detect pyocyanin with a limit of detection (LOD) of 500 pM. The obtained results suggest that the designed nanoantennas have the potential to be transformed into a label-free SERS based plasmonic sensor.

The statistical accuracy of single molecule methods relying on fluorescent dyes gets limited due to irreversible loss of fluorescence signals because of photobleaching of dye molecules. Quantum dots (QDs) offer a better alternative label to fluorescent dyes because of its photostability to overcome photobleaching problem associated with fluorophores. The applicability of heavy metal chalcogenide based QDs such as CdSe and CdTe is limited for biological applications due to toxicity associated with Cd^{+2} ions. So there remains a pressing need for the synthesis of non-toxic and highly stable QDs. A one-pot, green, cost-effective and energy efficient strategy for the synthesis of blue emitting Si QDs has been proposed. The Si QDs were synthesized at room temperature using 3-aminopropyltriethoxysilane (APTES) as the silicon source and a commonly available sugar, glucose, as a reducing and stabilizing agent. These Si QDs showed a reversible thermo-responsive emission in the temperature range of 20-80 ^{0}C and high ionic stability required for bioconjugation. The as synthesized hydrophilic Si QDs have been exploited as a reducing agent for the reduction of Au^{3+} ions to Au NPs leading

to the formation of Au NP-Si QD nanocomposites. The nanocomposites were found to be possessing catalytic activity for the reduction of nitroarenes. The as synthesized Si QDs were further used for the generation of white light emitting mixture (WLEM) by controlled mixing with orange red emitting Au nanoclusters (Au NCs). The chromaticity color co-ordinate of the WLEM was found to be (0.33, 0.32), which was very close to that of perfect white light emitting source. The generated WLEM was found to be showing fast, sensitive, and selective reversible sensing of Hg^{+2} ions and thiol containing amino acid Cysteine with a LOD of 10 nM.

Owing to the interesting optical properties of QD, QD-metal hybrid nanostructures will open the window to a new class of photostable probes for single-molecule spectroscopic applications. Despite several advanced capabilities to produce the nanoantennas and the QDs separately, merging a single QD with a single plasmonic nanoantenna is an ongoing challenge. A simple strategy to immobilize single Si QD on the DNA origami template at a predefined position is demonstrated. Future works will focus on immobilization of single Si QD in the plasmonic hotspot of Au@Ag NS dimer structures for single molecule sensing and imaging applications.

Highly sensitive single-molecule label-free sensing methods have applications in both the fundamental research and healthcare diagnostics. Proteins are the structural elements and machinery of every single cell of the body. They are responsible for proper functioning and maintaining biological architecture and homeostasis of cells. In case of onset of disease such as cancer, the concentration level of several proteins in the body gets misregulated. Such proteins have the potential to inform regarding the early onset of disease which will further allow early diagnostic confirmation and effective treatment. Development of novel label free single protein detection methods is important for getting molecular information critical for fundamental biochemical research and for clinical laboratory diagnosis. We have demonstrated the applicability of designed Au@Ag NS dimer nanoantennas for label free SERS based sensing of single thrombin protein molecule. Thrombin protein plays a critical role in hemolysis and hemostasis in our body. For research and clinical diagnosis applications, it is important to develop a label free detection system for its sensing. Specific binding of single thrombin protein in the conjunction region between the Au@Ag NSs was achieved by incorporating thrombin binding aptamers on the DNA origami template. After binding of thrombin protein molecule in the plasmonic hotspot we were able to record Raman vibrational bands at 1140, 1540, and 1635 cm^{-1} characteristic of the protein. The designed plasmonic nanoantenna has the potential to be used as label free sensor for detection of proteins.

The work embodied in the present thesis represents a concerted effort to continue the development of novel plasmonic nanoantennas for single molecule spectroscopic and sensing applications. The study also discusses the scopes of future research work in extension of this investigation.

Chapter 1

Introduction

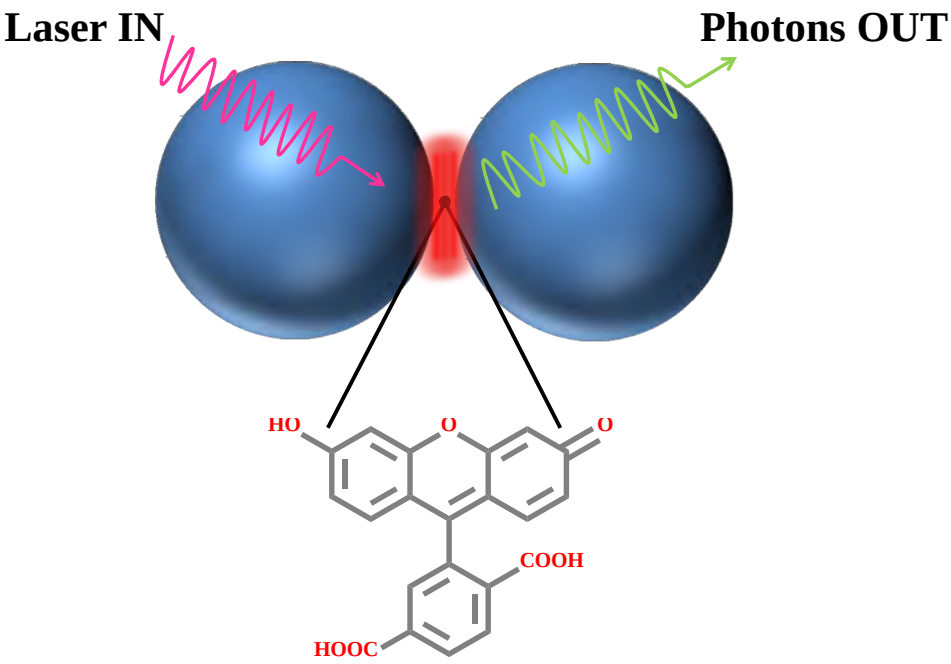

"When you look at single molecules, you see a distribution of behaviors"

Professor David Walt

1.1. Optical spectroscopy

Spectroscopy is a branch of science that deals with the study of interaction of matter with electromagnetic radiation. Electromagnetic radiation (light) is a form of energy which is known to have both particle and wave like nature. Depending on frequency and wavelength, electromagnetic radiation is divided into different regions collectively called as electromagnetic spectrum (shown in Figure 1.1). It includes microwaves, radiowaves, infrared, visible light, ultraviolet, X-rays, and gamma rays. Optical spectroscopy is the interaction of ultraviolet, visible, and infrared radiation with optically active molecules or materials. When light interacts with a matter it is either absorbed, emitted or scattered. Depending on the type of interaction they are further classified as absorption spectroscopy, emission spectroscopy, Raman spectroscopy, infrared (IR) spectroscopy, and nuclear magnetic resonance spectroscopy (NMR).

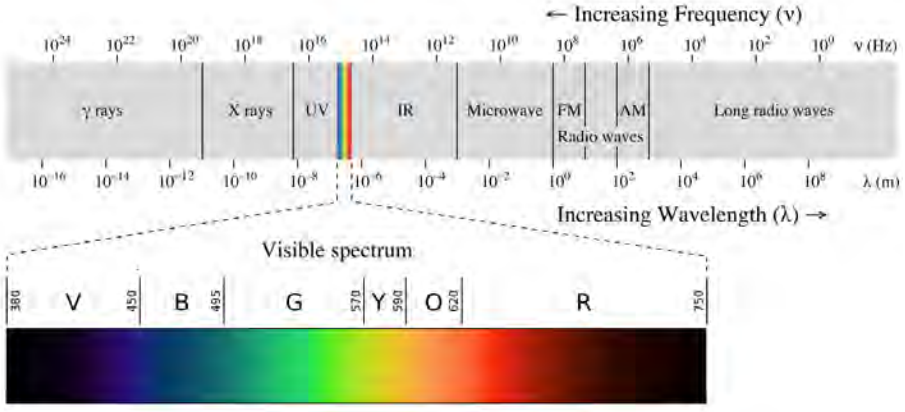

Figure 1.1. A diagram of the electromagnetic spectrum. (Taken from Wikipedia)

1.1.1. Ensemble spectroscopy

The interaction between light and matter is generally weak owing to the large mismatch between the wavelength of light and the size of the molecules, atoms, and electrons whose excitation and motion contain information about their molecular properties. Therefore, most of the spectroscopic investigations such as UV-visible spectroscopy, infrared spectroscopy, Raman spectroscopy, and NMR rely on the generation of a strong signal by a large number of molecules. Although this approach is beneficial because it results in a very high signal to noise ratio, it is also unsatisfactory because it yields only ensemble-averaged information. With ensemble measurements, only average properties are revealed, and it becomes difficult to study individual behavior of molecules which is highly desirable for studying dynamics and kinetics

of bio-molecules, observing intermediate states, studying stochastic procedures, and detection of static and dynamic heterogeneity in a population.[1-3]

1.1.2. Single molecule spectroscopy

Single molecule spectroscopy as the name suggests is the investigation of the interaction of optical radiation with exactly a single molecule. In single molecule spectroscopic methods, at a time, exactly one molecule is allowed to be observed by the optical radiation. This one by one scanning of molecules provide averaging-free insights of a system that is unattainable with ensemble methods. The first report on optical detection of a single molecule came around 30 years ago in 1989 by Moerner and Kador.[4] They recorded absorption spectrum of single pentacene molecule in p-terphenyl using a combination of frequency modulation spectroscopy and Stark modulation. Later in 1990, Orrit et al. recorded single molecule fluorescence spectrum of pentacene molecule and demonstrated that fluorescence is a better mode for single molecule detection than absorption as it yields superior signal to noise ratio.[5] In these two initial reports, the single molecule measurements were carried out at liquid helium temperature. Later, demonstration of single molecule detection at room temperature by Betzig et al.[6, 7] followed by aqueous medium detection by Funatsu et al.[8] led to the exponential growth of single molecule based applications in a variety of fields including material science, molecular biophysics, heterogeneous catalysis, molecular biology and many more. [9-13] In the last few years single molecules have provided necessary insights into some of the difficult problems which were difficult to achieve using ensemble methods. Single molecule enzymatic dynamics studies done by Lu et al.[3, 14] helped them in differentiating static and dynamic disorders associated with enzymes. Single molecule fluorescence resonance energy transfer (FRET) technique helped in shedding light on the protein folding dynamics,[15] chemomechanical mechanism of kinesin motor protein,[16] and real time monitoring of intermolecular interactions.[17] Roeffaers et al. used diffraction limited wide field microscopy for locating catalytic sites on single [Li^{+}-Al^{3+}] layered double hydroxide (LDH) heterogeneous catalysts.[18] Very recently Moerner et al. used advanced single molecule-based microscopy techniques for revealing initial steps of Hedgehog signaling pathways essential for normal embryonic development.[19] The 2014 Nobel Prize in Chemistry was jointly awarded to Eric Betzig, Stefan W. Hell and William E. Moerner for the development of super-resolution fluorescence microscopy.[20, 21]

So far most of the developed single molecule detection techniques such as DNA sequencing,[13] confocal fluorescence correlation spectroscopy (FCS),[10] single enzymes based immunoassays,[9]

and single-molecule counting,[22] are based on fluorescence spectroscopy. The ability of fluorescence based approaches to provide high sensitivity, high spatial and temporal resolution, and superior signal-to-noise ratio have laid the foundation for the dominance of fluorescence microscopy over all other optical techniques at the single-molecule level from past 25 years. Although widely employed, single molecule fluorescence based spectroscopic techniques are fundamentally restricted to fluorophores having high quantum yield (typically >0.1) [23] and fail to provide any molecule specific information. Raman spectroscopy is another spectroscopic technique that provides exquisite chemical specificity about molecular structure because Raman fingerprint is characteristic feature of a molecule.[24] Although powerful, it is highly insensitive because of very low Raman cross-section of molecules. The appeal of achieving single molecule detection using surface enhanced Raman spectroscopy in 1997[25, 26] triggered enormous interest in the scientific community for using SERS as an alternative to fluorescence based single molecule detection. Since then different types of SERS active substrates have been prepared and used for single molecule measurements.[27-29]

Although widely employed in different fields of science, single molecule measurements have not dramatically impacted commercial applications due to some associated key limitations.

1.1.2.1. Limitations of single molecule measurements

Diffraction limited resolution. Ernst Abbe in 1873 proposed that when light of certain wavelength (λ) travels through a medium with n refractive index making a half angle Θ on the objective angular aperture then the minimum resolution that it can provide is given by equation 1.1.

$$d = \frac{\lambda}{2nsin\theta} \qquad \text{Equation 1.1}$$

Where 2nsinΘ is termed as the numerical aperture (NA) of the objective. If green light of wavelength 500 nm is used for illuminating a sample through an objective of NA 1, the Abbe's limit comes out to be 250 nm. This means if the distance between two molecules is equal to or less than 250 nm than the microscope will not able to resolve it. To avoid this limitation, optical single molecule measurements are performed at ultra-low concentrations in the range of 1 pM to 1 nM to guarantee that only a single molecule resides in the observing volume. Working with such low concentration results in poor signal to noise ratio origin of which can be explained as:

The absorption cross-section (σ) of an organic fluorophore is on the order of 5×10^{-16} cm^2 and the area of light focused by high numerical aperture microscope objective (A) is 5×10^{-10} cm^2. As

a result, $\sigma/A = 1\times10^{-6}$, which can be translated as, out of 10^6 incident photons only one gets absorbed by the molecule of interest. With such poor absorption single molecule signals are usually hampered with background signals which lower the probability of detection and make the analysis difficult. Background signals may accrue for a variety of reasons, such as impurities within the sample, noise from the instrument, Raman scattering due to solvent molecules, scattering of light and dark counts from the detector.

Intrinsic Raman scattering. Raman scattering is a very strong source of background signals. Figure 1.2 shows the emission spectra of Rhodamine 6G dye along with the Raman spectrum of ethylene glycol. The absorption cross-section of a single molecule of Rhodamine 6G and

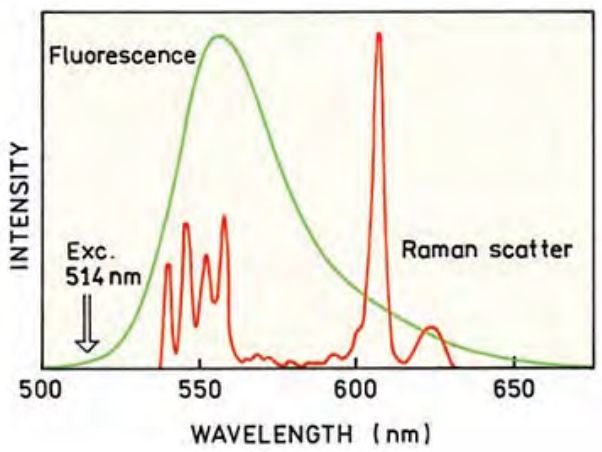

Figure 1.2. Emission spectrum of Rhodamine 6G and Raman spectrum of ethylene glycol. (Reprinted with permission from ref.[30], 2006 Springer Science Business Media, LLC)

Raman cross-section of ethylene glycol are 4×10^{-16} cm^2 and 3×10^{-28} cm^2 respectively. [30] So, the intensity of fluorescence emission from one Rhodamine 6G molecule will be equal to Raman scattering intensity of 1.3×10^{12} molecules of ethylene glycol (volume 120 µm^3). The emission spectrum of Rhodamine 6G and the Raman signals of ethylene glycol occupies almost similar wavelength range so despite using emission filters the Raman scattering cannot be completely eliminated. Therefore, in order to suppress the background signals arising from Raman scattering from billions of solvent molecules, the observing volume surrounding a single fluorophore should be 1 fL.

Concentration barrier. Figure 1.3 shows the different required working concentration range for carrying out single molecule sensing experiments and studying single molecule bio-interactions. A majority of biomolecular interactions such as protein-protein, protein-enzyme,

and protein-ligand takes place at higher concentrations often in micro to millimolar range. So to overcome the concentration limit it becomes imperative to reduce the observation volume to zepto (10^{-21}) or atto (10^{-18}) liter range, three times less than that of confocal microscopes (~10^{-15}).[31, 32] Further, investigating biomolecular interactions at single molecule level requires maintaining concentration in nano to millimolar range. This huge difference in the required working concentration for biological systems and single molecule detection has gravely obstructed the utility of single molecule techniques for commercial applications.

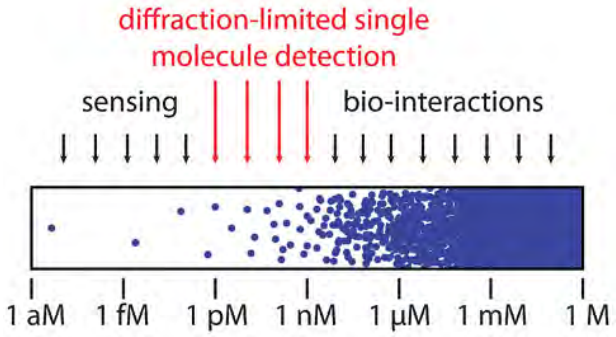

Figure 1.3. Dynamic concentration range required for optical single-molecule detection. (Reprinted with permission from ref.[33] 2014 Royal Society of Chemistry)

1.1.2.2. Single molecule detection techniques

Commonly, two different methods confocal [34] and total internal reflection (TIR) [35] are used for reducing the observing volume to 1 fL for carrying out single molecule measurements.

Confocal detection optics. In a confocal microscope (schematic shown in Figure 1.4), the incident laser beam is allowed to pass through an objective having high NA and focused to a diffraction-limited volume. In confocal optics, illumination and emission from the sample are collected through the same objective and is called an epifluorescence configuration. The emitted light is then passed through a dichroic mirror which allows only emitted light to reach the detectors and transmits the excitation light reflected from the sample. To exclude background signals from impurities and Raman scattering from solvent molecules a small microsized pinhole is inserted in the path of confocal optics. A pinhole blocks the light coming from below and above of the focal plane allowing only focused light from the sample to reach the detector. This leads to significant improvement in the signal to noise ratio. The size of the pinhole determines the quality of the image therefore, selecting a proper pinhole is very important for getting a superior axial resolution. In confocal microscopy, a sample is illuminated with a

smallest possible spot size so, an image is created by raster scanning the sample stage in x,y-direction. There are numerous reports where confocal microscopy alone or in combination with some other technique has been used for single molecule detection.[36, 37]

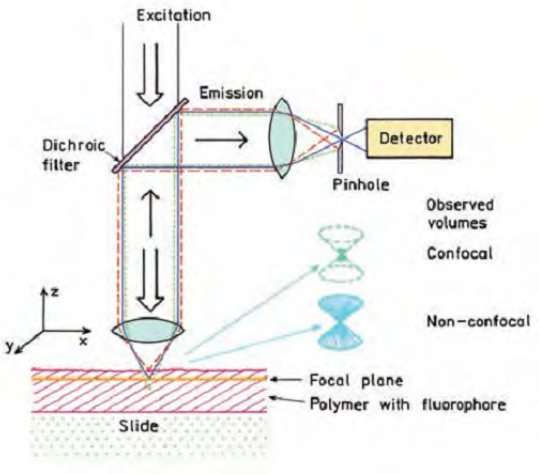

Figure 1.4. Schematic of optics of a confocal microscope. (Reprinted with permission from ref.[30], 2006 Springer Science Business Media, LLC)

Total internal reflection optics. This method utilizes the phenomenon of total internal reflection (TIR) for inducing an evanescent wave or field in a nanometer regime of the sample near to the interface. An incoming light gets totally reflected from an interface when it enters a medium having less refractive index at an incident angle greater than the critical angle. In TIR based microscopy, molecules present close to the glass-slide/sample interface are excited, minimizing the background signal generated through the bulk of the sample. Another advantage

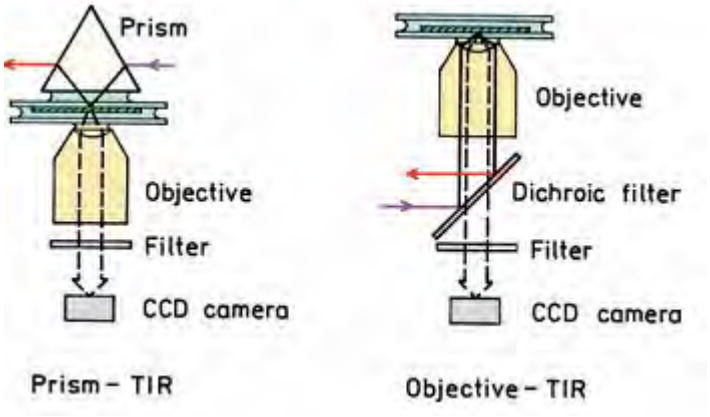

Figure 1.5. Schematic of a TIR based microscope optics. (Reprinted with permission from ref.[30], 2006 Springer Science Business Media, LLC)

of TIR microscopy is at a given time many individual fluorophores are observed whose motion can be monitored using video imaging. This helps in studying the translation of molecules/biomolecules in real-time. A TIR microscope can be used in two different configurations prism-TIR and objective–TIR (as shown in Figure 1.5). In a prism based TIR microscope, the incident laser beam is coupled with a prism for achieving TIR. A sample thickness of around 200 nm above the interface is illuminated by the generated evanescent field. It is important to focus the incident laser beam at the focal point of the objective with this approach. In objective-based TIR microscope, the incident laser beam is made to pass through the extreme edge of an objective with high NA. The generated evanescent field excites a thin plane of the sample near the glass/sample interface. TIR based microscopes have been widely used for single molecule studies.[8, 38]

1.2. Optical plasmonic nanoantennas

The limitations associated with single molecule measurements have sparked the efforts to develop a new class of techniques collectively called "Plasmon enhanced spectroscopy" that can provide single molecule sensitivity for the detection of both fluorescent and non-fluorescent molecules.[39] These techniques exploit the unique optical properties of metallic nanostructures to route and manipulate light at nanometer length scales. Dislocation of electrons on the surface of metal nanoparticle during the irradiation leads to creation of the electric dipole, as a result, a highly intense electromagnetic field is generated in the near proximity of the metal surface.[40, 41] The enhanced local electric field can remarkably enhance the interaction between photons and materials, leading to significant enhancements in the molecular absorption, scattering, and emission processes.

1.2.1. Metal nanoparticles

Metallic nanoparticles are, as the name suggests, nanosized metals with at least one of the dimensions within 1 to 100 nm. Metallic nanoparticles display fascinating properties that are quite different from those of individual atoms, surfaces or bulk materials. Due to their specific properties, they are the subject of intense research effort in the field of biology, chemistry, biotechnology, electronics, catalysis, biomedical application, diagnostics, molecular imaging and many more. [42-45] In 1857, Michael Faraday described the first scientific method for the synthesis of colloidal gold nanoparticles by the aqueous reduction of a gold salt by white phosphorous and stabilization with carbon disulfide.[46] He pointed out that intense color produced after the reduction of gold metal salts is due to the formation of small metallic

Figure 1.6. The Lycurgus cup in the British museum.[47]

nanoparticles. Although associated with modern science, the usage of nanoparticle dates back to the fourth century in the famous Lycurgus cup, known for changing color depending upon the light in which it is viewed (Figure 1.6).[47] The dichroic glass used for making the Lycurgus cup was made with small proportions of gold and silver colloidal particles (~ 70 nm) in an approximate molar ratio of 1:14 which resulted in the colored surface of the cup. Andreas Cassius a German physician and alchemist, in 1666 prepared a purple pigment called Purple of Cassius which was popular in the 17th century for staining glasses. The pigment was colloidal solution of gold nanoparticles formed by the reaction of gold salts with tin (II) chloride. Johann Kunckel a German chemist later modified the technique for making ruby-colored stained glass. He predicted the existence of gold nanoparticles well before Michael Faraday by writing in his book published in 1676 that "gold must be present in such a degree of communition that it is not visible to the human eye".[48] The first observation and size measurement of nanoparticles was done by Richard Adolf Zsigmondy using an ultramicroscope built by him. He was awarded the 1925 Nobel Prize in chemistry for studying the properties of gold sols and the methods used by him. Different types of metallic nanoparticles have different optical and electronic properties that enable their candidature for applications in different types of fields. For example, the propensity of palladium to adsorb hydrogen has also led to palladium nanoparticles being utilized in hydrogen storage and catalytic applications.[49, 50] Magnetic properties of iron oxide nanoparticles have been used in magnetic and biomedical applications as a contrast agent, drug delivery vehicle, and for magnetic resonance imaging.[51, 52] Due to a wide range of accessible oxidation states (Cu^0, Cu^I, Cu^{II}, and Cu^{III}), Cu-based nanocatalysts have been used in different types of catalytic reactions like organic transformations, electrocatalysis, and photocatalysis.[53] Among all types of metal-based nanoparticles (NPs), the stability and fascinating optical-electronic properties of Au NPs have led them to be used in diverse and interdisciplinary

applications such as sensory probes, electronic conductors, therapeutic agents, organic photovoltaics, drug delivery vehicle in biological and medical applications, and catalysis.[54-57]

1.2.2. Optical properties of metal nanoparticles

Bulk Au and Ag metal are yellow and silver in color. Whereas, Au NPs and Ag NPs solution can be of any color of the rainbow from red through green to violet.[58] The solution of 50 nm and 20 nm Au NPs look blue and brilliant red in color, respectively, and it steadily changes to brownish orange, through several tones of purple and red, as the particle size is reduced down to ~3 nm (Figure 1.7).[58] In 1908, Mie explained the origin of the red color of gold nanoparticles (Au NPs) solution by solving Maxwell's equations for the absorption and scattering of electromagnetic radiation by spherical metallic particles.[59] Later, Gans extended this theory to ellipsoidal geometries.[60] Since Mie's work, extensive investigation has been done to study the optical properties of metal nanoparticles whose metallic dielectric function is known and which

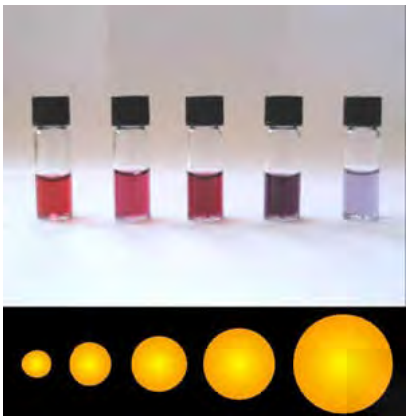

Figure 1.7. Colors of different sized Au nanoparticles. (Taken from Wikipedia)

are embedded in an environment of known dielectric constant.[61] The effect of the size and shape of the nanoparticles on their color is due to changes in the so-called surface plasmon resonance band.[62] Surface plasmon resonance (SPR) is the resonant collective oscillation of the conduction electrons near nanoparticle's surface when metallic nanoparticle is irradiated by light. In 1957, R.H. Ritchie was the first to predict the existence of the surface plasmon.[63]

1.2.3. Origin of surface plasmon resonance

The surface plasmon resonance is not excited in a smooth surface but in subwavelength surface structures and nanoparticles.[64] In noble metals, when the size of the particles becomes smaller than the wavelength of the incident light, λ ($d \ll \lambda$), the continuous band of electronic structure

is changed to a discrete electronic level and a large amount of the atoms appear on the surface. When a small metal nanoparticle is irradiated by light, the oscillating electric field causes the negatively charged conduction electrons to oscillate coherently (as shown in Figure 1.8). The electron cloud is displaced relative to the positively charged nuclei, a restoring force arises from coulomb attraction between electrons and nuclei that result in oscillation of the electron cloud relative to the nuclear framework. The frequency at which conduction electrons oscillate in

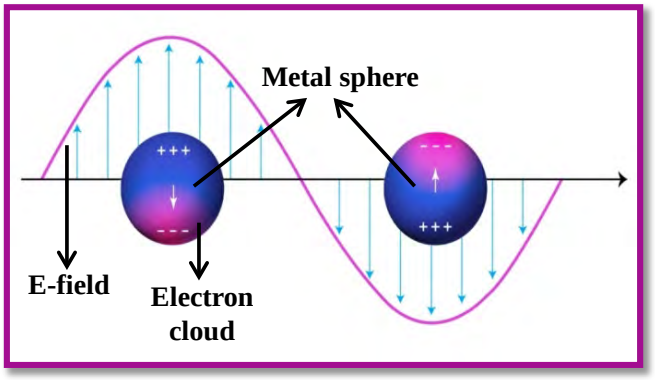

Figure 1.8. Schematic depiction of a localized surface plasmon of a spherical metal nanoparticle showing the displacement of the electron charge cloud relative to the nuclei. (Adapted from ref.[65] 2003 American Chemical Society)

response to the alternating electric field of incident electromagnetic radiation is called (localized) SPR, which gives rise to intense absorption in the visible-near-UV region.[62, 65, 66] Materials that possess a negative real and small positive imaginary dielectric constants in a given wavelength range, such as quasi-free electron metals, Ag, Au, Cu, and Al, are capable of supporting an SPR.[58, 67] The SPR is determined from absorption and scattering spectroscopy, and depends on several factors such as the density of electrons, shape, size, and dielectric properties of the metal from which the nanoparticle is created, and the dielectric permittivity of the environment.[67, 68]

The total extinction coefficient of small spherical metallic particles is given in Mie's theory as the summation of overall electric and magnetic multipole oscillations contributing to the absorption and scattering of the interacting electromagnetic field. For small spherical nanoparticles coefficient κ (sum of absorption and scattering) is given by the following equation 1.2.[69, 70]

$$k = \frac{18\pi NV\varepsilon_m^{3/2}}{\lambda}\frac{\varepsilon''}{(\varepsilon' + \chi\varepsilon_m)^2 + \varepsilon''^2} \qquad \text{Equation 1.2}$$

Where, λ is the wavelength of the incident radiation, N is the density of nanoparticles, V is the volume of a metallic sphere, ε' and ε'' are the real and imaginary parts of the metal dielectric function [$\varepsilon(\omega) = \varepsilon'(\omega) + i\varepsilon''(\omega)$, where ω is the angular frequency of the light], ε_m is the dielectric function of the medium, and χ is a parameter called form factor that depends on the shape of the spheroid, increasing from 2 for a sphere to 17 for a spheroid with an aspect ratio of 5:1.[71]

For a spherical metal nanoparticle, this formula predicts a resonant peak when $\varepsilon' \approx -2\varepsilon_m$, which for Ag and Au occurs in the visible region of the electromagnetic spectrum.[71]

1.2.4. Size and shape dependence of optical properties

The SPR is highly sensitive to changes in the shape or size of the nanoparticle. The induced surface geometry changes cause a shift in the electric field density on the surface, generating different cross-sections for the optical properties including absorption and scattering. According to equation 1.2, the SPR position is independent of changes in the size of metal nanoparticle. However, it has been experimentally proved that a change in the size affects the SPR band position as well as the bandwidth. The bandwidth is inversely proportional to the radius *r* of the particle for sizes smaller than about 20 nm. For larger nanoparticles (>25 nm for Au NPs) the extinction coefficient explicitly depends on the nanoparticle size as the wavelength of the incident light

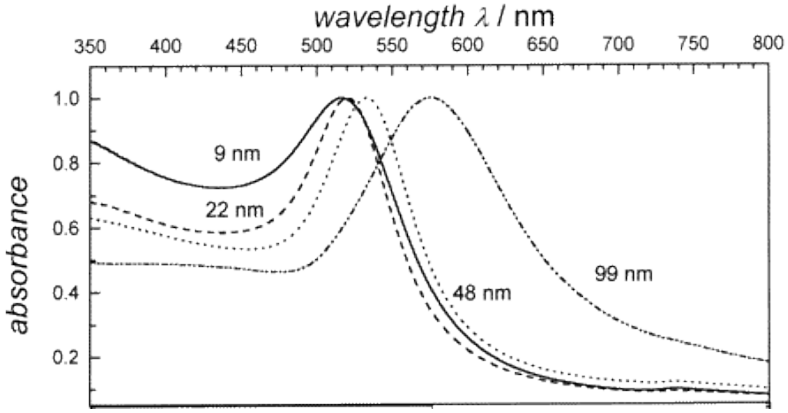

Figure 1.9. Effect of size on the surface plasmon absorption of spherical Au NPs. (Reprinted with permission from ref.[72], 1999 American Chemical Society)

becomes comparable to the dimension of the nanoparticle. The plasmon bandwidth increases with the increasing size of nanoparticles.[72] Figure 1.9 shows the effect of size on the SPR bandwidth and position of the spherical Au NPs. The SPR band of metal nanoparticles drastically changes with the change in the shape of metal nanoparticles. In case of anisotropic shaped nanoparticles such as nanorods, the plasmon absorption band splits into two distinct

bands corresponding to free oscillation of electrons in different directions (Figure 1.10).[58, 72] In case of Au nanorods, the transverse SPR band comes at around 520 nm, which is coincident with the plasmon band of spherical particles. Whereas longitudinal oscillations of electrons result in a red-shifted SPR absorption band whose position is very sensitive to the aspect ratio of Au nanorods. [73] The aspect ratio is defined as the length of the rod divided by the width of the rod. By changing the aspect ratio of nanorods the LSPR band position can be tuned from 550

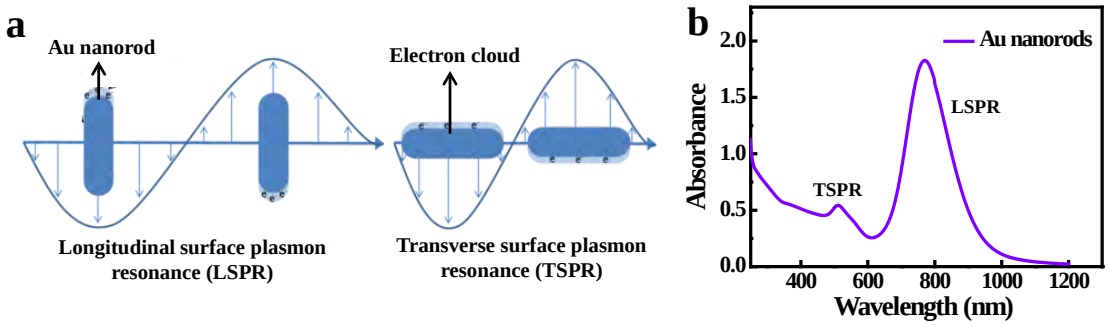

Figure 1.10. (a) Schematic depiction of LSPR excitation (Adapted from ref.[74] 2014 Elsevier B.V.), and (b) UV-Vis-NIR spectrum of Au nanorods.

nm to over 2000 nm, while the transverse SPR band remains relatively constant at 510-520 nm. El-Sayed and coworkers,[75] derived an empirical relationship between the aspect ratio and the LSPR of Au nanorods (Equation 1.3) using Gans theory[60] together with the known dielectric function for Au.

$$\lambda_{max} = 33.34\varepsilon_m R - 46.31\varepsilon_m + 472.31 \qquad \text{Equation 1.3}$$

Where λ_{max} is the LSPR band position, ε_m is dielectric constant of medium and R is the aspect ratio of Au nanorods.

The plasmonic responses of complex metal nanostructures such as nanoshells and nanostars can be understood as the interaction or "hybridization" of plasmons supported by metallic nanostructures. For example, in case of Au nanostars, the two distinct plasmon resonances are the result of hybridization of plasmons associated with the core and the individual tips of the particle (Figure 1.11).[76, 77] This plasmonic hybridization results in the splitting of the plasmon resonance into "bonding" and "antibonding" plasmons. The bonding plasmons are symmetric and are primarily composed of tip plasmons but with a finite contribution of the core plasmons. The mixing in of the core plasmon mode results in significantly enhanced excitation cross-

section of the bonding plasmons which leads to highly intensified local electric field enhancements around the tips, edges, corners, and gaps. The plasmonic resonances of the Au nanostars are highly tunable and can be red shifted with increasing tip length.[78]

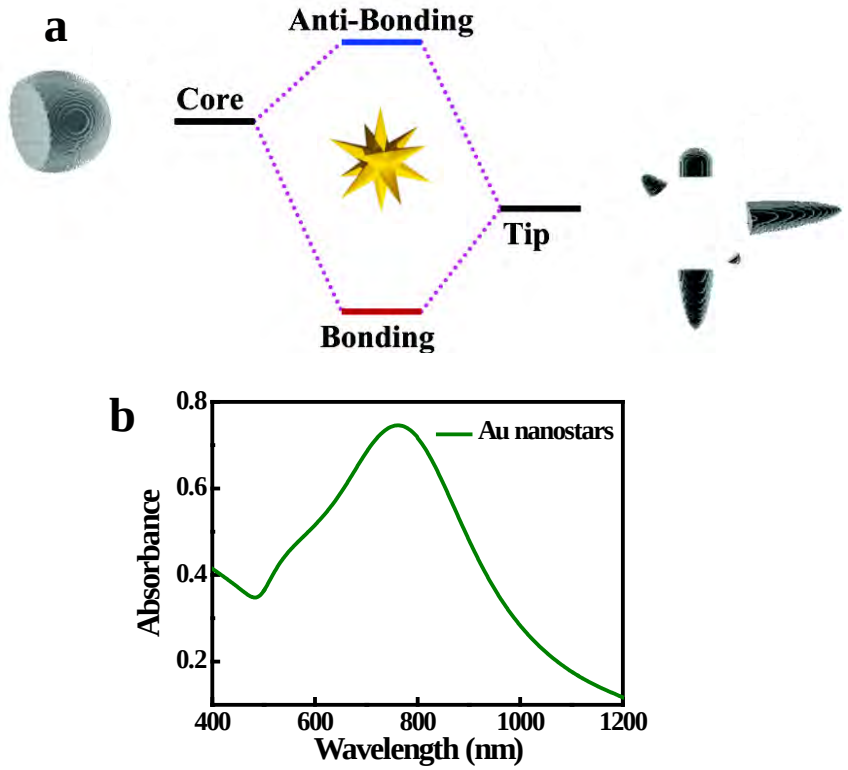

Figure 1.11. (a) Schematic illustration of the concept of plasmon hybridization in the nanostar, (Reprinted with permission from ref.[60]2007, American Chemical Society) and (b) UV-Vis absorption spectrum of Au nanostars.

1.2.5. Optical properties of core-shell nanostructures

Apart from the shape and size, optical properties of metal nanostructures are highly sensitive to their dielectric environment.[79] By coating a metal nanoparticle with different material its surrounding medium is modified and as a result, new optical properties emerge due to hybridization of the plasmons of core and shell. Core-shell metal nanostructures can have a range of combinations such as dielectric core and a metallic shell or metallic core and metallic shell. The choice of shell material of the core/shell nanoparticle is strongly dependent on the end application and use. In core-shell structures, the electromagnetically excited plasmons of the sphere and the cavity interact with each other and a surface charge is induced at the inner and outer surface of the metallic shell (Figure 1.12).

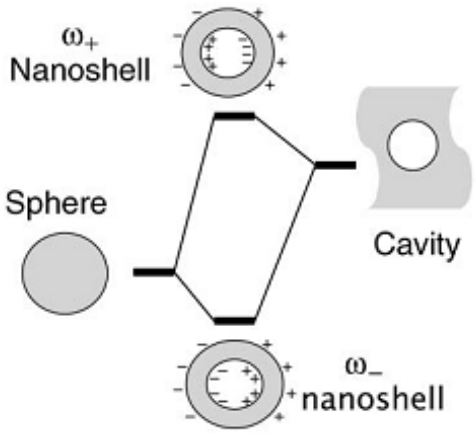

Figure 1.12. Schematic illustration of the hybridization of plasmons in core-shell metal nanostructures. (Reprinted with permission from ref. [79], 2005 Materials Research Society)

This interaction results in the splitting of the plasmon resonances into two new resonances: the lower energy symmetric or "bonding" plasmon and the higher energy antisymmetric or "antibonding" plasmon. The strength of the interaction between the sphere and cavity plasmons can be tuned by changing the ratio of core-shell thickness. In case of pure metal nanostructures the SPR band can be tuned to a limited extent by changing the size but in case of core-shell structures the SPR band can be very easily tuned to desired wavelength range by changing the core to shell ratio (as demonstrated in Figure 1.13).

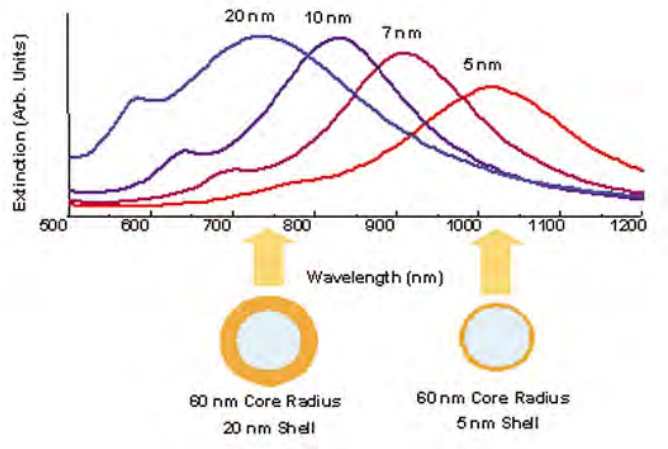

Figure 1.13. Plasmonic tunability demonstrated for Au nanoshells with core (silica) and Au shell thickness. (Reprinted with permission from ref.[80], 2004 SAGE publishing)

Bimetallic metal nanostructures are a type of core-shell structures that potentially outperform their pure metal counterparts because of improved optical properties arising due to integration

of properties of both the metals.[81, 82] Among all, Au/Ag bimetallic systems have been widely explored for a diversified range of applications because of high stability of Au and superior plasmonic properties of Ag.[83, 84] After Ag coating the SPR band can be very easily tuned to the desired region, which is useful for plasmon enhanced spectroscopy.[85, 86]

1.3. Plasmonic nanoparticles for surface enhanced optical spectroscopy

Plasmon-enhanced spectroscopy comprises a large family of techniques including plasmon-enhanced infrared spectroscopy,[87] surface enhanced Raman spectroscopy,[88, 89] and plasmon-enhanced fluorescence spectroscopy.[90] These techniques exploit the unique optical properties of metallic nanostructures to route and manipulate light at nanometer length scales. This nanoscale confinement of light generates a highly intense electromagnetic field in the near proximity of the metal surface (Scheme 1.1).[40, 91, 92] Benefited from the greatly enhanced local electric field, surface plasmons can dramatically enhance the processes that involve light matter interactions such as fluorescence, Raman scattering, heat generation, photoacoustic effects, photocatalysis, nonlinear optical conversion, solar energy conversion and so on.[93, 94] The distribution of the generated electromagnetic field is uniform for a spherical nanoparticle whereas for anisotropic shaped metal nanoparticles the intensity of the electromagnetic field at some places may be significantly larger than the intensity of the incident radiation. The strongest field enhancement is usually observed at the sharp edges and corners.[95] In the case of dimers and other agglomerates very large enhancement is observed when nanoparticles are very close to each other. Places with high intensity of electromagnetic fields are called "hot-spots".

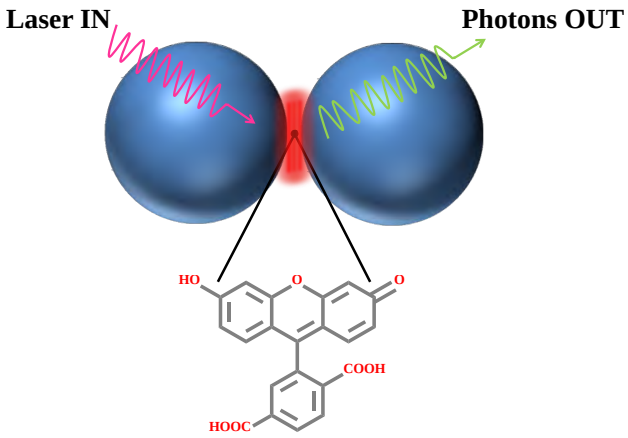

Scheme 1.1. Plasmonically coupled metal nanostructures showing high-intensity electromagnetic field generated in the ultrasmall nanogaps.

1.3.1. Surface enhanced Raman scattering

Raman spectroscopy named after Indian physicist C.V. Raman is a spectroscopic technique based on inelastic scattering of monochromatic light usually from a laser source. The phenomenon of inelastic scattering of light was first observed experimentally in 1928 by Raman and Krishnan.[96] C.V. Raman won the Nobel prize in physics in 1930 for this discovery. It is a non-invasive spectroscopic technique that provides molecule-specific spectroscopic characteristics enabling quick identification of analytes.[96] However, due to poor Raman scattering cross-section of molecules, the intensity of Raman signals of most molecules is inherently weak.[97] Surface enhanced Raman scattering (SERS) phenomenon, first observed by Fleischmann and co-workers[98] amplifies Raman signals of analytes by several orders of magnitude, enough for identification and quantification of analytes down to ultra-trace levels.[99] In comparison to normal Raman spectroscopy, SERS requires placing of the analytes in close proximity of metal nanostructures, whereby a huge enhancement in Raman signals is observed owing to plasmon assisted scattering of molecules.[97] The ability of SERS to identify a particular analyte within complex mixtures with high sensitivity has gained immense attention and has been applied in a myriad of fields including biology, medicine, forensic science, material science, electrochemistry and many more.[100-102]

1.3.1.1. Mechanism of SERS

Since its inception, a number of theories have been proposed to explain the mechanism contributing to the SERS phenomenon. Nowadays it is generally believed that the amplification of Raman signals is due to primary contribution coming from electromagnetic enhancement[89] and a minor enhancement due to charge transfer interactions between the metal nanoparticle and the adsorbate.[103]

Electromagnetic field enhancement in SERS. When plasmonic metal nanoparticles are irradiated with electromagnetic radiation, the LSPs get excited resulting in concentration of far-field incident light to nanoscale regime at sharp edges, tips or curvatures, thereby enhancing local electromagnetic field intensity. The enhancement of the electromagnetic field takes place in two steps (Figure 1.14).[104] At first step, the plasmonic nanoparticle serves as an optical nanoantenna and transforms the far-field incident light (frequency: ω_0) to near field which creates high-intensity electromagnetic field around the nanoparticle. Second, the enhancement arises due to mutual excitation of induced dipole of analyte and the dipole of nanoparticle. In second step the plasmonic nanoparticle act as transmitting optical antennae, which transfers the

near field to the far-field at the Raman scattered frequency (ω_R). The total enhancement factor (EF) is governed by both EF of first $G_1(\omega_0)$ and second step $G_2(\omega_R)$ and is given by equation 1.4.

$$G = G_1(\omega_0)\, G_2(\omega_R) = \frac{|E_{loc}(\omega_0)|^2\, |E_{loc}(\omega_R)|^2}{|E_0(\omega_0)|^2 |E_0(\omega_R)|^2} \approx \frac{|E_{loc}(\omega_R)|^4}{|E_0(\omega_0)|^4} \qquad \text{Equation 1.4}$$

Where E_{loc} and E_0 are the local electric fields generated in the presence and absence of plasmonic nanoparticles respectively. From equation 1.4 it is evident that the SERS enhancement factor (EF) is proportional to the fourth power of the enhancement of the local electric field.[105, 106] So, higher the intensity of the generated electric field better will the SERS EF. The magnitude of the electromagnetic field intensity depends on several factors like the interparticle gap, distance between the analyte and the metal nanoparticle, shape and size of metal nanoparticle, and orientation of the analyte with respect to the plasmonic surface. The local electromagnetic field is extremely intense between the dimer structures having

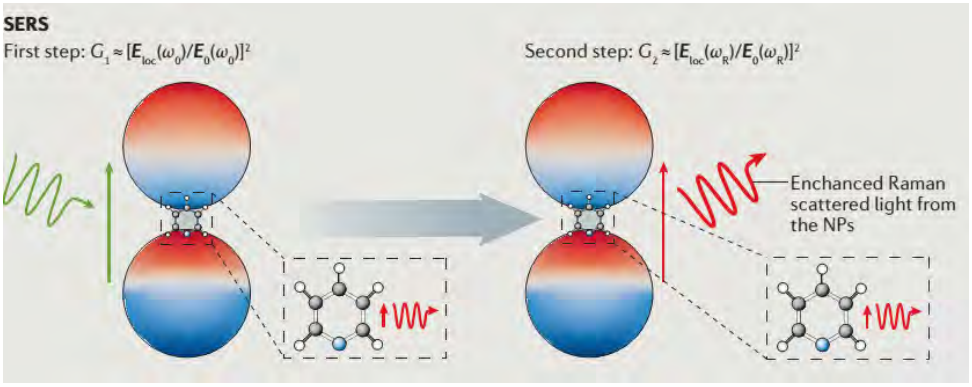

Figure 1.14. Mechanism of electromagnetic field enhancement in SERS. (Reprinted with permission from ref.[107], 2016 Springer Nature)

interparticle gaps of few nanometers due to strong electromagnetic coupling.[105] The small region where the intensity of the electromagnetic field is highest is generally termed as "plasmonic hotspots". It has been demonstrated that upon reducing the interparticle gap of Au nanosphere dimers from 10 to 2 nm the SERS EF increases from to 10^5 from 10^9.[105] But for subnanometre gaps ($d \leq 0.3-0.4$ nm), the plasmon modes of the dimers progressively diminish and the charge transfer plasmon modes gradually emerge. At this point, the two particles get conductively connected through electron tunneling which leads to quenching of the electric near field enhancement.[108, 109] The shape of metal nanoparticles has a strong influence on the SERS EF. Anisotropic nanostructures such as cubes, rods, triangles, and stars can sustain high

intensity electromagnetic fields around their sharp edges which results in higher SERS EFs as compared to their spherical counterparts.[95] Plasmonic mapping of Ag triangular plates[110] and Au nanostars[111] using energy loss spectroscopy (EELS) has shown high localization of localized SPR at the sharp-edged regions (Figure 1.15), thereby resulting in higher SERS EFs. Among all the different anisotropic shapes, Au nanostars have gathered immense research interest due to its intriguing structure–optical property relationship. An Au nanostar consists of a central core with several protruding tips. The LSPR of the nanostars can be very easily tuned to the desired visible or near-infrared region by changing the size, sharpness, and number of tips.[112] The intensity of electromagnetic field generated at the sharp tips of Au nanostars is very high and is reported to yield EFs to the order of 10^{10}.[111] Due to these key properties, Au nanostars have been used in a variety of SERS and non-SERS based applications.[113, 114]

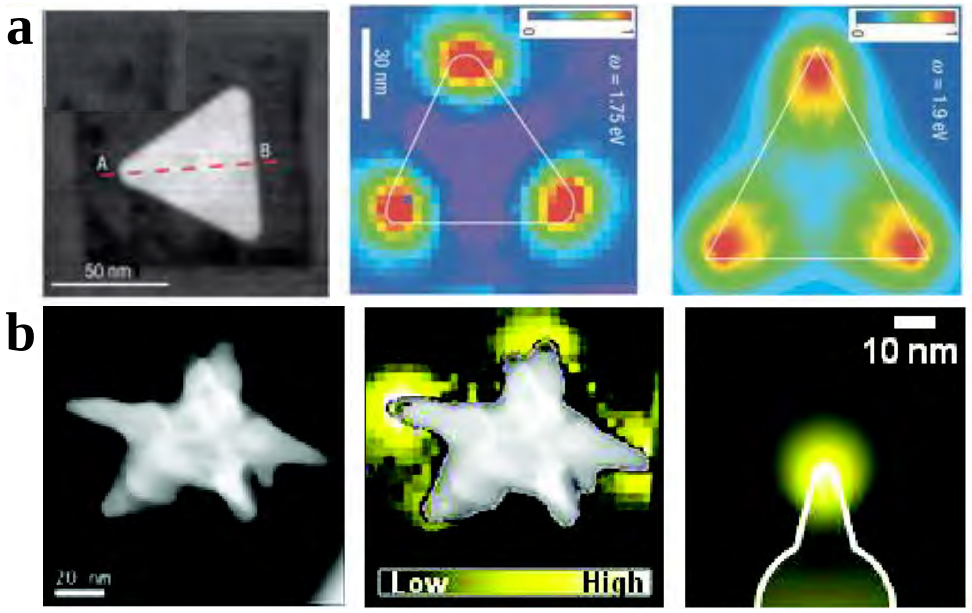

Figure 1.15. Dark field STEM image and EELS intensity mapping map of a single (a) Ag triangular plate and (b) Au nanostars. (Reprinted with permission from ref. [110], 2007 Springer Nature and ref. [111], 2009 American Chemical Society)

Chemical enhancement in SERS. A difference of around 200 in the SERS EF of N_2 and CO molecules on same substrate and under similar experimental conditions instigated the thought that apart from electromagnetic mechanisms there is a second mechanism that contributes to SERS EF.[115] This second effect is commonly addressed as the chemical effect. The most widely accepted mechanism for explaining this effect is the charge transfer mechanism.[105, 116]

The charge transfer can occur from the highest occupied molecular orbital (HOMO) of adsorbed molecules to the lowest unoccupied molecular orbital (LUMO) level of the metal clusters[117] or

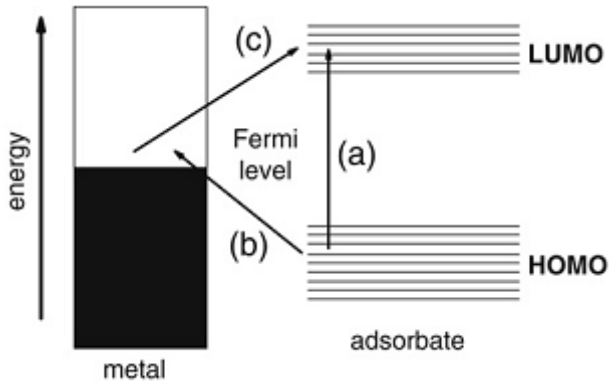

Figure 1.16. Schematic depiction of a charge-transfer mechanism in the SERS. (Reprinted with permission from ref.[105], 2009 Elsevier B.V)

from the metal state near the Fermi level to the LUMO of the adsorbed molecules resulting in the formation of metal-molecule charge-transfer complex.[118] The incident laser frequency can be in close resonance with the electronic transition of newly formed metal-molecule charge transfer complex (case (a) in Figure 1.16) or can profit from an indirect coupling through the metal (case (b+c) shown in Figure 1.16).[105] There are several examples in literature that demonstrated the existence of chemical enhancement mechanism. For example, Creighton in 1986 observed that the SERS spectrum of pyridine absorbed on the surface of copper and silver substrates exhibits four intense peaks at 1590, 1210, 1005, and 629 cm^{-1} unlike normal Raman spectrum of pyridine having very weak peaks at 1590, 1210, and 629 cm^{-1} and a strong peak at 1005 cm^{-1}. The enhancement in the four a_1 modes of pyridine (1590, 1210, 1005, and 629 cm^{-1}) was attributed to charge transfer from metal to lowest unoccupied π^* orbital of pyridine.[119]

Campion et al. observed 1000 fold enhancement in the SERS spectrum of Pyromellitic dianhydride adsorbed on the surface of Cu substrate when excited at 647 nm with respect to 725 nm excitation. On analyzing the electron energy loss spectrum of pyromellitic dianhydride-Cu complex they observed presence of additional peak at 1.9 eV. Upon adsorption on the surface of Cu, new low-energy states were created that showed enhanced Raman scattering at 647 nm excitation due to close resonance with the energy of the newly formed state.[115] It is generally believed that the contribution of the chemical enhancement effect to total EF is very less ($\sim 10^0$-10^2) than electromagnetic enhancement.[103] Park et al. carried out a systematic study to

investigate the contribution of charge transfer mechanism in total SERS EF of individual Au nanoparticle-4-aminobenzenethiol-Au film junctions. They found that only a small fraction of molecules contribute to charge transfer EF of 10^1-10^3.[120] The chemical enhancement mechanisms takes place due to transitions in the formed charge transfer complexes, so the primary requisite for chemical enhancement to occur is the analyte molecule should be directly or indirectly adsorbed on the surface of the metal nanoparticle.[105]

1.3.1.2. Surface enhanced resonance Raman scattering

Surface enhanced resonance Raman scattering (SERRS) arises when the wavelength of the exciting laser is simultaneously in close resonance with the SPR of the metal nanoparticle and electronic transition frequency of the analyte.[121, 122] Figure 1.17 illustrates the SERRS condition, where SERRS happens when SPR of Ag NPs is coincident with molecular absorption of dye which is dye 1 in this case and the excitation frequency.

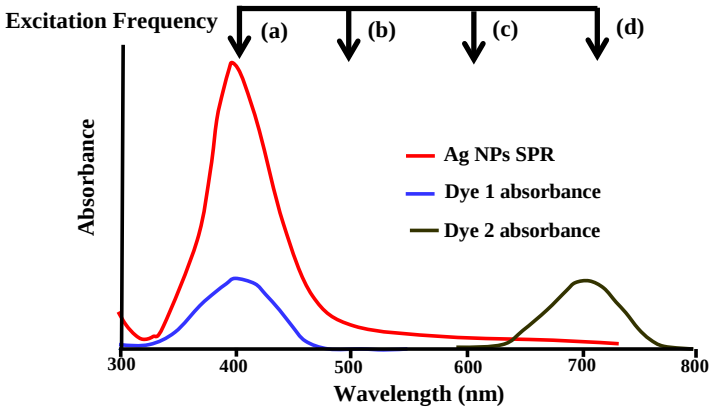

Figure 1.17. Schematic depiction of SERRS condition. (Adapted from ref.[121], 2005 Royal Society of Chemistry)

Excitation frequency (a) represents ideal excitation, (b), (c) and (d) represent non-ideal scenarios. Murgida et al. successfully investigated the structural changes occurring in Cyt-c protein adsorbed on carboxyl-terminated alkanethiols coated Ag electrodes using laser excitation of 413 nm. By setting up a close resonance between the SPR of the substrate, laser excitation, and vibrational frequencies of heme group of Cyt-c protein, they were able to selectively record Soret band of heme among several non-heme bonds.[123, 124] In another example demonstrated by Ros et al. Raman spectra of a heteroaromatic dye was recorded using three different laser excitation sources of 488, 514, and 785 nm on Au nanorods. It was found that the SERS signal

was highest at laser excitation wavelength resonant with the longitudinal plasmon mode of the Au nanorods.[125] Another advantage of SERRS over SERS is a huge difference in the obtained EFs. SERRS is known to yield EFs up to 10^{14}, strong enough for detecting analyte down to single molecule levels.[26] Till now it has been practically demonstrated by several groups that SERRS is a simple, sensitive, fast and reliable spectroscopic technique that yields very good detection limit.[126, 127]

1.3.1.3. Single molecule surface enhanced Raman scattering

Two independent reports by Nie and Emory[26] and Kneipp et al.[25] in 1997 demonstrated that it is possible to achieve single-molecule detection using SERS/SERRS. Single molecule measurements yield information that is washed out by ensemble methods, the appeal of achieving single molecule detection using SERS triggered enormous interest in the scientific community. Till now several approaches have been proposed for designing a SERS substrate that can detect a single molecule.

1.3.1.3.1. Ultra-low concentrations method

The pioneering studies on single molecule SERS detection[25, 26] relied on "ultralow concentration" approach for designing the SERS substrate. The simple idea behind this approach is to use the analyte in very low concentration, to the order of pM, such that the probability of finding more than one molecule in the scattering volume is negligible. While this approach gives an idea that a particular substrate can be used for single molecule detection. Since only a small proportion of the substrate contributes to the SERS signal doubts arise on its scalability as well as statistical reliability. Also, the strong fluctuations and shift in spectral position during the measurements hinder observation of one-step photobleaching, which is the direct proof of single molecule evidence as in the case of fluorescence measurements.[128] Furthermore, since it is difficult to find out the exact number of metal particles contributing to the highest intensity hotspot, determination of exact analyte concentration for single molecule measurements is very ambiguous.

1.3.1.3.2. Bi-analyte method

To overcome the problems associated with low concentration method Etchegoin group proposed the bi-analyte method.[129, 130] In this method, a mixture of two distinguishable Raman active analytes having similar Raman cross-sections is used for the SERS measurements. Three different types of Raman spectra can be obtained from the bi-analyte mixture, each of which corresponds to either pure

analytes or to a mixture. The observation of SERS signals of purely one analyte indicates that the signal is coming from a single molecule. This technique has been implemented in different variations, notably the isotopologue approach.[130] In this method, an isotopically labeled version of the analyte is used as the second SERS probe. The key advantage of isotopologues is that the two analytes will have identical surface binding chemistries and Raman cross-sections with distinguishable Raman signals.

The bi-analyte method although addresses the problem of uncertainty in quantifying the number of molecules contributing to SERS signal, works on the assumption that each hotspot yields an equivalent enhancement factor, which is practically not possible. Also, it does not provide control over placing the molecules exactly in the plasmonic hotspot.

1.3.1.3.3. Langmuir–Blodgett films

The Langmuir–Blodgett technique utilizes amphiphilic molecules with hydrophilic ‘‘heads’’ and hydrophobic tails such as fatty acids which can form a monolayer on subphase.[131, 132] The analyte molecules are first entrapped in this monolayer with a great deal of control over the dispersion. If a very low concentration of the analyte is used then the molecules get individually trapped in the layer. Further, the analyte containing layer is transferred to a substrate for SERS measurements. This method also does not provide control over placing the molecules exactly in the plasmonic hotspot and because of the low concentration of analyte, it is susceptible to poor statistics.

1.3.1.3.4. Nanogap enhanced Raman scattering

Plasmonic nanogap enhanced Raman scattering can be defined as Raman signal enhancement from plasmonic metallic nanoparticles arranged with an interparticle gap of few nanometers.[133] When nanoparticles are closely packed with interparticle gap of few nanometers, very intense electromagnetic field is generated in the conjunction region, commonly termed as “hotspots”.[134] These high intensity electromagnetic fields can generate strong enhancement in Raman signals of analyte placed in the nanogap.[135] The extent of enhancement in Raman signals is largely affected by the structural and compositional factors such as stoichiometry, interparticle gaps, type of metal nanostructure, and positioning of the probe molecule in the hotspot. Lee et al. investigated the effect of interparticle gap and size of metal nanoparticle on the SERS EFs using single DNA tethered Au-Ag core shell nanodumbbell designs.[136] They found that SERS EFs increased with decreasing interparticle gaps and were highest when the nanogap was > 1 nm. And the nanodumbbells generated the highest Raman signals with a combination of 50 nm Au

core and 514 nm laser excitation that is in close resonance with the Ag shell. Till now, there are several reports where plasmonic nanogap based SERS substrates have been used for multiplexed applications including biological and chemical sensing, bioimaging and theranostics [28, 137, 138] but are not employed for practical utility due to lack of reproducibility in Raman signals. It has been demonstrated by Fang et al. that out of 10^6 SERS active sites only 63 yields high enhancements accounting to 24% of the overall SERS intensity[139], so there is a pressing need for designing new SERS active substrates that can yield high enhancement factors (EFs), good reproducibility, and uniform response.

1.3.2. Plasmon enhanced fluorescence spectroscopy

Fluorescence is the emission of light from a substance that occurs after the absorption of electromagnetic radiation. The phenomenon of fluorescence was first observed by Sir John Frederick William Herschel from a quinine solution which on absorbing UV light from sunlight emits blue light.[140] The processes that occur between absorption and emission of light were later described by Professor Alexander Jablonski,[141] who is now regarded as the father of fluorescence spectroscopy. Fluorescence based spectroscopy and imaging techniques are powerful optical tools that have revolutionized the field of science and technology. The high sensitivity of this technique paved the way for choosing fluorescence as a means for carrying out single-molecule measurements. However, from the very first report on single molecule detection using a single fluorophore,[142] it was evident that technically it is a difficult task. Because despite using optical filters, purified solvents, and pulsed laser excitation the detected signal was 50 photons per molecule with up to 20 background counts. The initial publications on fluorescence based single molecule spectroscopy demonstrated the feasibility of detecting single molecules using basic techniques. Now single-molecule spectroscopy is a mature field, with highly established technology and methodology.

1.3.2.1. Fluorescent probes for single molecule studies

A good signal-to-noise ratio is very crucial for the success of any single-molecule detection technique. Most of the biomolecules, for instance, have very low intrinsic fluorescence that makes their intrinsic fluorescence-based single molecule detection difficult.[143] That's why most of the fluorescence based single molecule detection techniques rely on external labeling of non-fluorescent and weakly fluorescent species with a fluorescent probe. A fluorescence probe act as a reporter that reveals the information about the molecular state of the molecule. For getting a very high signal to noise ratio it is important that the fluorescent probes should be highly

photostable, have high quantum yield, non-invasive, and have a small size so that it doesn't affect the molecular functions. Generally, organic fluorophores or quantum dots are used as fluorescence probes for labeling the molecule of interest.

1.3.2.1.1. Organic fluorophores

Organic fluorophores are small fluorescent organic molecules that have a chromophoric group, a conjugated π- electron system that provides a stabilizing force and they absorb and emit light in the visible region (400-700 nm).[144] For example, the chromophoric unit of Rhodamine,

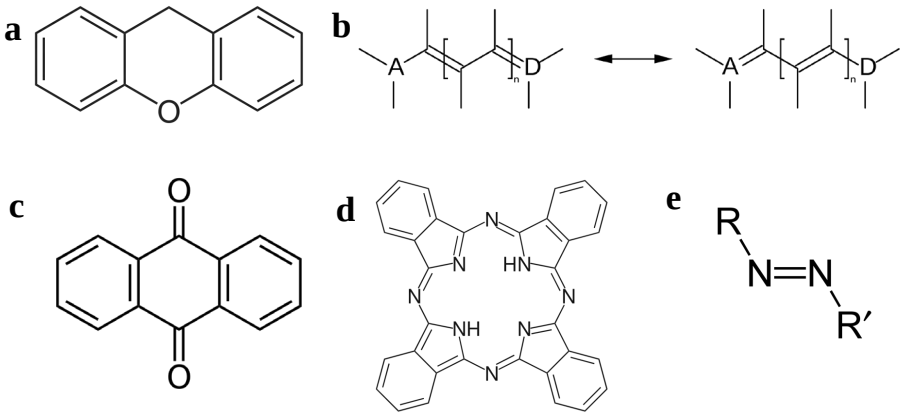

Figure 1.18. (a) Xanthene, (b) Polymethine, (c) Anthraquinone, (d) Phthalocyanine, and (e) Azo chromophoric groups.

Texas red, and Fluorescein dyes is xanthene group[145] and that of Cyanine dyes is polymethine group.[146] Chromophores of some of the commonly used dyes are given in figure 1.18. In addition to chromophores, organic dyes also have other groups, for example, hydroxyl, amino,

Table 1.1. List of organic fluorophores used for single molecule experiments

Dye	Excitation (nm)	Emission (nm)
Cy2	**489**	**506**
Atto 488	**498**	**520**
Alexa 488	**495**	**519**
Cy3	**550**	**565**
Atto550	**554**	**577**
Alexa555	**555**	**567**
Alexa647	**650**	**667**
ATTO647N	**644**	**664**
Cy5	**655**	**667**

sulfonic and carboxylic acid generally termed as auxochromes. Individually auxochromes are non-fluorescent, but when present in conjugation with a chromophore, they contribute to both the wavelength and intensity of its absorption. Auxochromes also assist in conjugating the organic fluorophores with the molecule of interest. For fluorescence based single molecule measurements, the first critical step is selection of the organic dye. An appropriate organic dye should have high quantum yield so that the desired signal to noise ratio can be achieved and highly photostable that allows the study of molecular dynamics for a long duration of time. Some of the commercially available fluorophores that are used for single molecule experiments are given in table 1.1.

Origin of blinking and photobleaching in organic fluorophores. A fluorophore upon absorbing light of appropriate wavelength gets excited and jumps from its ground state (S_0) to an excited state (S_1) as shown in figure 1.19. This transition is generally termed as HOMO to LUMO transition. An excited fluorophore can return to its ground state through radiative

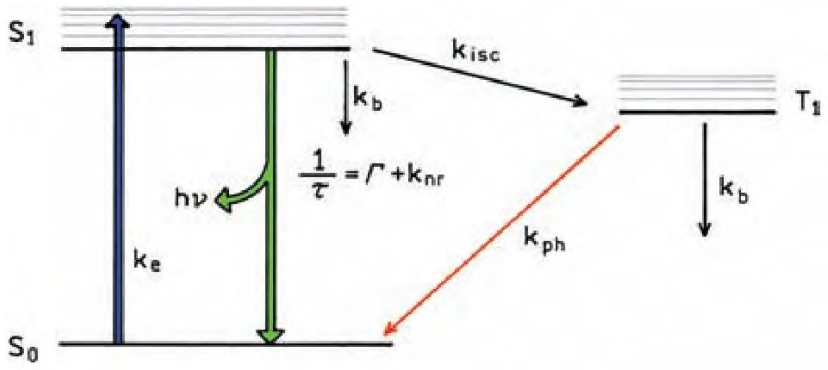

Figure 1.19. Jablonski diagram showing the origin of single-molecule blinking. (Reprinted with permission from ref.[30], 2006 Springer Science Business Media, LLC)

pathways or can enter non-fluorescent triplet excited state (T_1) via intersystem crossing which is the origin of fluorophore blinking. Blinking is defined as random switching of a fluorophore from ON (fluorescent) and OFF (non-fluorescent) states when illuminated continuously. It is believed that excursions to the triplet excited state reduce the rate of emission and opens the pathway to chemical degradation of dye commonly termed as photobleaching.[147] A organic fluorophore undergoes several ON-OFF cycles before undergoing irreversible photobleaching. The number of ON-OFF cycles is different for different fluorophores and is determined by the inverse of its photobleaching quantum yield.[30] Figure 1.20 shows fluorescence transients of single Cy3 dye showing blinking and photobleaching. A single step photobleaching as shown in

figure 1.20b is considered as a hallmark of an individual fluorophore. For single molecule experiments, the intensity of the laser is kept high to obtain a high photon emission rate. This results in the photodegradation of fluorophores limiting their utility for measurements that requires a longer observation time such as studying enzymatic kinetics and dynamics. The single photobleaching step of the fluorescent signal is a hallmark of an individual fluorophore.

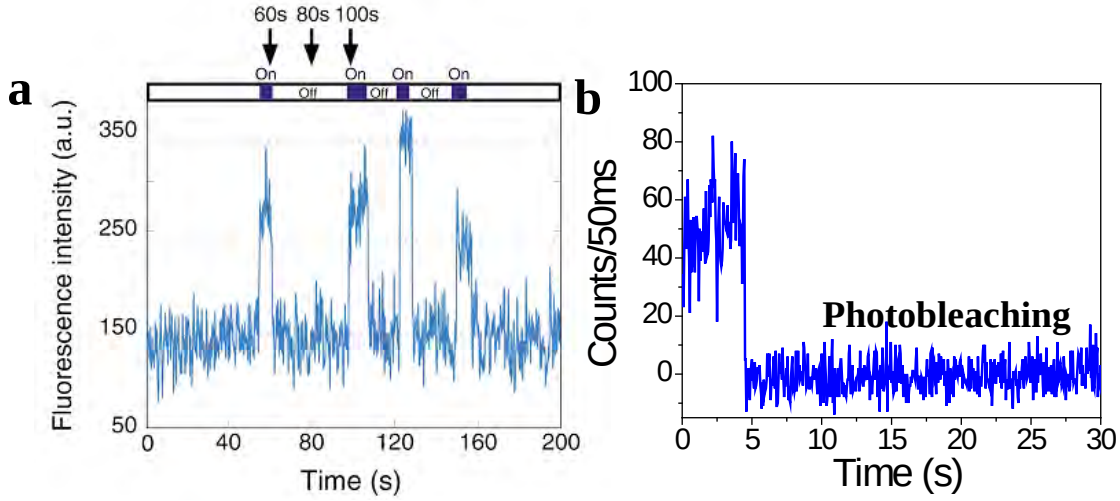

Figure 1.20. Fluorescence transients of single Cy3 dye showing (a) blinking (Reprinted with permission from ref.[148] 2001 Nature Publishing Group) and (b) photobleaching.

1.3.2.1.2. Quantum dots

Quantum dots (QDs) are small fluorescent particles or nanocrystals of a semiconducting material with diameters in the range of 2-10 nanometers, smaller than the Bohr exciton radius of the same bulk material. They were first discovered by Russian physicist Alexei Ekimov in 1980. QDs can be made from single-element materials, such as silicon or germanium, or from compound semiconductors, composed of elements from the periodic groups of II–VI (*e.g.*, CdTe and CdSe) and III–V (*e.g.*, InP).[149, 150] They display unusual optical properties such as broad excitation and tunable narrow emission spectra, broad absorption cross-sections, slow excited-state decay rates, and high photostability.[151, 152] These interesting optical properties are due to quantum confinement effects which occur when the size of the particle is too small to be comparable to the wavelength of the electron.[153]

In a bulk semiconductor crystal, the electrons exist in a range of energy levels termed as bands. The valance band is filled and the conduction band is completely empty at 0 K. The valence and conduction bands are separated by some finite energy gap characteristic of the material called

the "bandgap" (Figure 1.21).[154] With the absorption of a photon, if an electron attains sufficient energy, it jumps from the valence band to the conduction band across the bandgap, leaving behind a positively charged hole. The excited electron after a finite time comes back to the valence band and recombines with the hole. This process is often accompanied by the emission

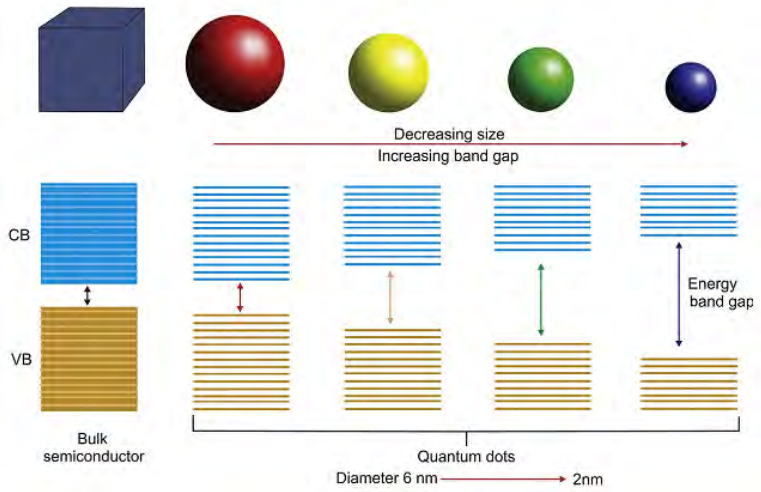

Figure 1.21. Energy band variation in quantum dots as the size is varied. (Reprinted with permission from ref.[155], 2018 Elsevier Ltd.)

of energy called radiative recombination. The distance between the electron-hole pair is called the Bohr exciton radius, which can vary depending on the material. As the particle size becomes of the order of the exciton Bohr radius or smaller, quantum confinement leads to a collapse of the continuous energy bands of bulk material into discrete, atomic like energy levels (Figure 1.21). The discrete structure of energy states causes the observed shift of the absorption edge to higher energies as the particle size decreases. With decreasing size, the energy difference between the filled states and the empty states increases or widen the bandgap of the semiconductor. As a result, the optical and electronic properties of semiconductors change drastically.[154]

Owing to these interesting optical properties, in recent years, semiconductor QDs have come up as a promising alternative to organic fluorophores.[156-158] The broad emission spectra of organic dyes limit their applicability for multicolor imaging purposes because of the simultaneous excitement of different fluorophores. QDs have a broad excitation and tunable narrow emission spectra, and thus emissions from many QDs can be resolved upon excitation with a single light source.[157, 159] Organic fluorophores usually require customized chemistry for conjugating them to biomolecules, however, a universal approach can be used for conjugating biomolecules to all

QDs. Most importantly, unlike organic fluorophores QDs have good stability toward photobleaching and chemical degradation, making them an ideal probe for fluorescence based measurements.

1.3.2.2. Plasmonic enhancement of single molecule fluorescence signals

In fluorescence based methods usually highly photostable fluorophore or quantum dot having high quantum-yield (> 0.1) are used for getting a high signal to noise ratio. Weakly emitting or non-emitting species requires labeling with highly emissive fluorophores which is not feasible for certain applications like sensing where analysis has to be done directly in the clinical samples.

Plasmonic nanoparticles can confine the propagating radiation into the nanoscale regime, thereby intensification and localization of electromagnetic fields in the near vicinity.[40] When a fluorophore/QD is placed in the near vicinity of a plasmonic metal nanoparticle its fluorescence emission get drastically enhanced, the phenomenon is generally termed as plasmon enhanced fluorescence.[160] Over thousand fold enhancement in fluorescence brightness of single molecule has been reported using nanoantennas fabricated by lithography[161, 162] or solution based techniques.[128, 163-165] Although the exact mechanism of metal enhanced fluorescence is not yet completely understood, but it is generally believed that enhancement in fluorescence signals could be because of increased rate of excitation and increased intrinsic radiative decay rates of the fluorophores.[166]

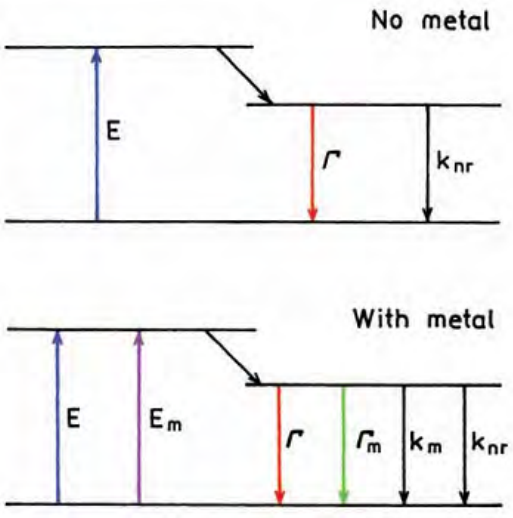

Figure 1.22. Jablonski diagram without and with the effects of near metal surfaces. (Reprinted with permission from ref.[167],2006 Springer Science Business Media, LLC)

Figure 1.22 shows Jablonski's diagram that includes the effect of metal on the fluorescence emission. Where Γ and k_{nr} denotes the radiative and non-radiative decay rates respectively. Γ_m stands for new rate that arises in presence of metal surface and increases the total radiative rate. The modified quantum yield and lifetime of fluorophore in presence of a metal nanoparticle are given by equation 1.5 and equation 1.6.

$$Q_m = \frac{\Gamma + \Gamma_m}{\Gamma + \Gamma_m + k_{nr}} \quad \text{Equation 1.5}$$

$$\tau_m = (\Gamma + \Gamma_m + k_{nr})^{-1} \quad \text{Equation 1.6}$$

With increasing value of Γ_m the quantum yield of the fluorophore increases while the lifetime decreases. Generally, a decrease in lifetime is accompanied by a decrease in the quantum yield. But in case of metal enhanced fluorescence the increase occurs because the fluorophores emit before they slip to non-radiative decay pathways thereby increasing the total decay rate.

Metal fluorophore interactions are highly dependent on certain factors such as distance between the metal surface and nanoparticle, nanoparticle size, geometry, and excitation wavelength. It has been found that the fluorescence emission of a molecule starts quenching when the metal fluorophore distance is reduced to < 2 nm and was maximum when the distance was ~ 5 nm.[168] It is important to note that the enhancement effects are confined only to about 10 nm of metal fluorophore distance. Further increasing the distance does not show any enhancement in the fluorescence emission. The SPR of the metal nanoparticle plays a crucial role in enhancing single-molecule fluorescence signals. As demonstrated by Khatua et al. fluorescence enhancement is maximum when there is a close overlap between the SPR wavelength, laser excitation, and the emission wavelength of the fluorophore.[165] Fluorescence enhancement also depends on the shape and size of nanoparticles. Due to increased scattering efficiency of large nanoparticles better enhancements are reported.[169] The enhancement of single molecule fluorescence signals is of great interest not only because it offers enhanced emissions but it allows an expansion of the field of fluorescence by incorporating weak quantum emitters which will ultimately result in imaging with resolutions significantly better than the diffraction limit.

The sensitivity of fluorescence based spectroscopic techniques can be significantly improved by the excitation enhancement of a QD coupled to a plasmonic antenna. The interaction between QDs and plasmonic nanoparticles has been investigated extensively over the past several years. It has been shown in several reports that the emission of QDs can be amplified in the proximity of metal nanoparticles.[170-172] Despite the advanced capabilities to produce the nanoantennas and

the QDs separately, merging a single QD with a single plasmonic nanoantenna is an ongoing challenge. In this regard, attempts were made to build the optical nanoantenna directly around the QD using lithography and chemical etching methods.[173, 174] Modest enhancements were achieved due to the degradation of QDs during harsh processing steps. In an alternative approach, single QD was directly targeted to the plasmonic hotspot using AFM probe.[175, 176] This method does not guarantee the exact positioning of the QD into the plasmonic hotspot. A slight shift of few nanometers of the delivery site from the targeted site can lead to quenching of photoluminescence. Zhang et al. investigated the enhancement in two-photon-excited luminescence of single CdSe/ZnS core–shell QD in the proximity of Au nanorods. They exploited the random diffusion of single QD around the Au nanorod for carrying out the enhancement studies.[177] Although the obtained EFs were high, this system cannot be used for applications where an intact QD-metal hybrid nanostructure is required for further analysis. Very recently, Nicoli et al. coupled single CdSeS/ZnS QD in between metal nanoparticle dimer structure using DNA origami technique. They further tested the functionality of the designed nanoantennas by measuring fluorescence enhancement of the QDs up to ~ 30 fold.

1.4. Fabrication of plasmonic nanoantennas

For designing a highly efficient plasmonic nanoantenna there are primarily two important challenges, first, the two nanoparticles have to be placed close to each other with a controlled nanogap. Second, the probe molecule has to be precisely placed in the conjunction region between the nanoparticles such that it experiences the highest electromagnetic field. Additionally, the fabrication technique should be generating nanoantennas with good reproducibility, scalability, and at a low cost. Fabrication of plasmonic nanoantennas follows one of two approaches, commonly termed as “top-down” and “bottom-up.”

1.4.1. Top-down approach

Top-down approach is a subtractive method in which bulk material is cut to yield nanostructures of controlled shape and size. The most frequently used top-down approach is electron-beam lithography (EBL)[178] and focused ion beam (FIB) etching.[179] In EBL, at first, an electron-beam resist is deposited on a substrate, and then a focused electron beam is made to scan over the surface. Exposure to an electron beam results in the development of the resist which results in its removal from the exposed portions. Further, a metal layer is deposited to generate patterned structures. FIB involves exposing a thin layer of metal to a focused ion beam that sputters off the metal locally. These techniques have been used for fabricating a variety of structures for

example bowtie antennas,[180] nanorings,[181] nanoprism array,[182] and dimer of pillars[183] with different interparticle gaps. Despite the sophistication and flexibility of lithographic techniques, there are significant number of associated limitations such as inability to produce structures having 3D shape and size below 5-10 nm, high cost of production and time consuming multistep synthesis procedure. Additionally, it is highly challenging to place the probe molecule exactly in the plasmonic hotspot using EBL.

1.4.2. Bottom-up approach

The bottom-up fabrications are solution based approaches that start with the colloidal synthesis of plasmonic nanoparticles and further self-assembling them using different techniques such as controlled evaporation of solvent,[184] or transferring nanoparticles dispersed in organic solvents to water which results in monolayer of nanoparticles after evaporation.[185] Solution based approaches for the fabrication of nanoantennas are highly desirable because they allow production of the targeted nanostructures in high yield. Further, it allows utilization of the synthesized nanoantennas for a variety of applications such as sensing, imaging, and therapeutics. Although a number of solution based approaches have been proposed for designing plasmonic nanoantennas, synthesis of nanoantennas with ultrasmall nanogaps and precise localization of probe in the hotspot remains challenging.[186, 187]

1.4.2.1. DNA origami for fabrication of plasmonic nanoantennas

DNA origami technique is a simple solution based bottom-up approach for fabrication of plasmonic nanoantennas that has stimulated enormous research interest owing to its ability to co-assemble different types of particles in complex geometries with precise control over interparticle gap, orientation, and stoichiometry.[128, 188, 189]

1.4.2.1.1. Structural DNA nanotechnology

"As with any craft material, the structural applications of DNA are limited only by the imagination" – Nadrian C. Seeman

The idea of using DNA as a construction material is a field that is commonly termed as structural DNA nanotechnology, was first demonstrated by Ned Seeman in the early 1980s. [190] It is a bottom-up fabrication technique that uses Deoxyribonucleic acid (DNA) as a structural component to assemble 1D, 2D, and 3D nanostructures. DNA is a biomolecule that carries genetic information necessary for the growth, development, and functioning of all living organisms. It is a long polymer that consists of repeating units called nucleotides.[191] Each DNA

nucleotide is composed of a 2-deoxyribose sugar, a phosphate group and one of the four types of nitrogen bases adenine (A), cytosine (C), guanine (G), and thymine (T). X-ray diffraction pattern of DNA obtained by Rosalind Franklin and her student R.G.Gosling (Figure 1.23a) indicated that DNA has a double helix structure.[192] Later Watson and Crick[193, 194] proposed that in all species the two polar polynucleotide chains hybridize to each other by hydrogen bond to form a double helix structure (Figure 1.23b) such that the distance between two consecutive nucleotides is 0.34 nm and a single helical pitch is composed of 10.5 nucleotides. The two polar polynucleotide chains in the double helix structure are bonded to each other with a double hydrogen bond between purine A and pyrimidine T and triple hydrogen bond between the purine G and pyrimidine C (Figure 1.23c). Each nucleobase binds covalently to its neighbor from the 5'-phosphate of its adjoining pentose sugar, to the 3'-hydroxyl group of the

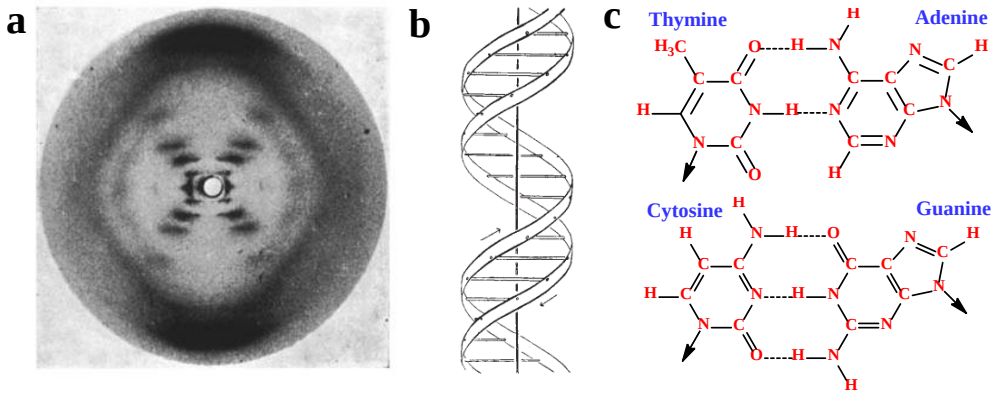

Figure 1.23. Structure of DNA.(a) X-ray fiber diffraction pattern of B-form DNA (Reprinted with permission from ref.[192], 1953 Springer Nature), (b) schematic depiction of double helix structure of B-form DNA with major and minor grooves (Reprinted with permission from ref.[194], 1953 Springer Nature). The ribbons represent the two phosphate-sugar chains while the horizontal rods illustrate the base pair, and (c) Watson-Crick base pairs showing hydrogen bonding between nitrogen bases.

neighboring ribose via a phosphodiester bond. Naturally occurring DNA is a linear molecule but it can form a range of branched structures by crossing DNA strands from one helix to another. A single crossover, called a Holliday junction, first proposed by British geneticist Robin Holliday,[195] is a cross-shaped structure that occurs in the process of genetic recombination. In a single holliday junction the four DNA strands are paired to form four double stranded DNA arms attached at a common branching point (Figure 1.24a). Multiple holliday junctions can be connected to each other via single-stranded overhangs at the end of a double helix, called

"sticky ends" (Figure 1.24b). This enables the formation of both 2D and 3D lattices (Figure 1.24c). [190, 196] The key features of DNA including nanometer dimensions, predictable base-pairing allowing numerous sequence possibilities, robustness, stiffness, convenient synthetic producibility, programmability to form branched structures and biocompatibility instigated the advent and fast-expanding of the field of structural DNA nanotechnology.[190, 197] Since Seeman and coworkers developed the background and basics of using DNA strands to build DNA nanostructures a series of advanced nanostructures have been constructed including tetrahedron, [198, 199] octahedron, [200] icosahedra,[201] 3D prisms,[202] complex wireframe networks,[203] and nanotubes.[204, 205]

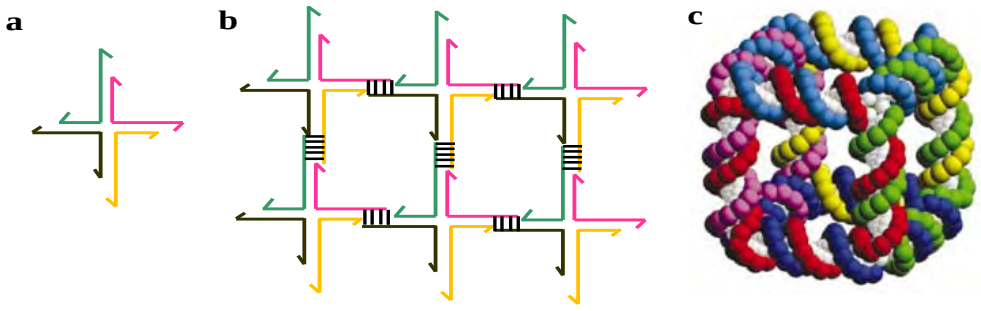

Figure 1.24. (a) Single Holliday junction with sticky-ends, (b) connected Holliday junction, and (c) 3D cube.

Developed DNA nanostructures laid the foundation of dynamic DNA nanotechnology which aims at creating smart nanomachines for various applications using dynamic DNA base pairing. DNA nanostructures have been used for creating stimuli responsive DNA devices,[206] DNA motors, [207-209], biosensors,[210-212] and drug delivery vehicles.[213, 214]

1.4.2.1.2. The DNA origami method

The synthetic strategy proposed by Ned Seeman[190] involves assembling of DNA nanostructures using short-staple DNA sequences combined in careful stoichiometry's. The assembly process requires a large number of reaction and purification steps which results in low yield of correctly assembled structures. In 2003, Yan et al. constructed a DNA barcode lattice by a self-assembly process of directed nucleation of DNA tiles around a scaffold DNA strand constructed by ligation.[215] Later, Shih et al. reported the synthesis of octahedron by controlled folding of a 1.7 kb long single DNA strand using five 40-mer synthetic oligonucleotides.[200] Inspired from a similar idea, Paul Rothemund in 2006, proposed a versatile 'one-pot' method for the synthesis of self-assembled DNA structures which he termed as 'scaffolded DNA origami'.[188] Origami is

a Japanese word in which "ori" means folding and "kami" stands for paper and describes the traditional Japanese art of folding into different shapes. Similarly, in DNA origami method 7249 nt long single-stranded genomic DNA of M13 bacteriophage is used as a scaffold and it is folded into arbitrary shapes by hundreds of short synthetic oligonucleotides complementary to

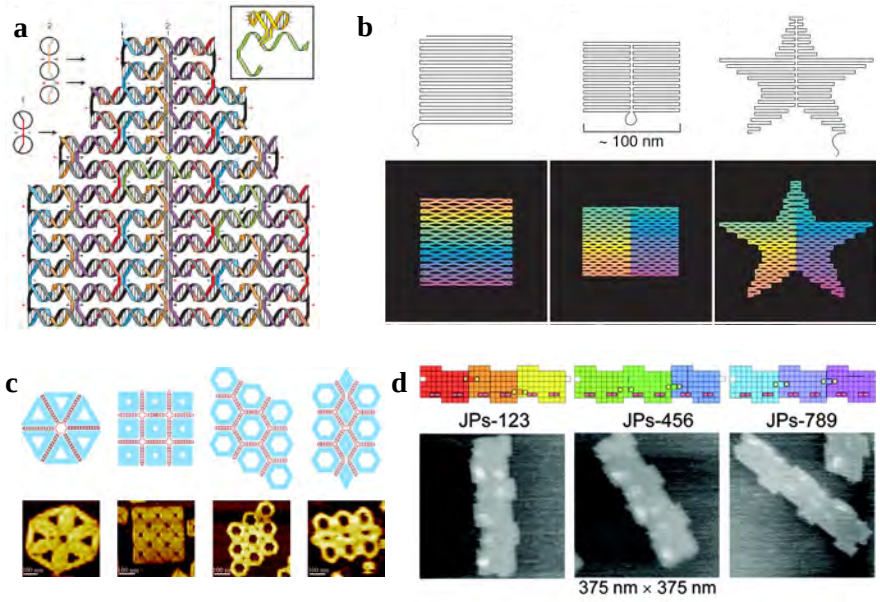

Figure 1.25. (a) Design of DNA origami, and (b) 2D DNA origami shapes developed by Rothemund (Reprinted with permission from ref.[188], 2006 Nature publishing group). (c) Two-dimensional structures developed by Yan and co-workers (Reprinted with permission from ref.[216], 2011 American Chemical Society). (d) DNA origami jigsaw pieces developed by Sugiyama and co-workers (Reprinted with permission from ref.[217], 2011 American Chemical Society).

the scaffold, usually called "staple strands". In designing a DNA origami, at first, the folding pattern of the scaffold is chosen such that the long scaffold DNA raster throughout the whole area of the structure. The adjacent portions of the scaffold are held together by a periodic array of scaffold crossovers (Figure 1.25a). These crossovers also help in the progression of the scaffold DNA from one helix to the adjacent helix and continue there. The position of scaffold crossovers can only be designated to places where the scaffold is placed at a tangent point between helices. So a periodic array of crossovers are arranged at every (n + 0.5) helical turn of the DNA (Figure 1.25a). The folding is assisted by staple strands running through adjacent helices either in an S-shaped or Z-shaped geometry. After successful hybridization of all staple strands to the scaffold, helices are bundled together by crossovers located after every 32 nt. In his publication, Paul Rothemund used genomic DNA of M13mp18 bacteriophage as the

scaffold (7249 nt) and folded it into different 2D shapes such as stars, squares, rectangle and disks using 200-250 staple sequences (Figure 1.25b). Later the idea of DNA origami was used for creating various 2D shapes such as a dolphin,[218] map of China,[219] and branched assemblies.[220] Further, 2D arrays of different length were constructed by joining individual origami structures using linking staple strands.[221-224] The size of designed DNA origami structures was small and was not sufficient for accommodating large molecules required for the preparation of DNA origami based devices. Keeping this in mind, several new routes were developed for constructing origami's with a size of few micrometers such as synthesis of large DNA origami tiles by linking preformed scaffold frames (Figure 1.25c),[216] supersized sheets by using long scaffold DNA, [225] DNA jigsaw puzzle (Figure 1.25d), [217, 224] 2D arrays, [221] and crystallization in two dimension by introducing loops on the surface.

Douglas et al. in 2009 reported synthesis of various 3D DNA origami designs such as 3D rectangular blocks, stacked cross, railed bridge, and genie bottle of varying cross-section

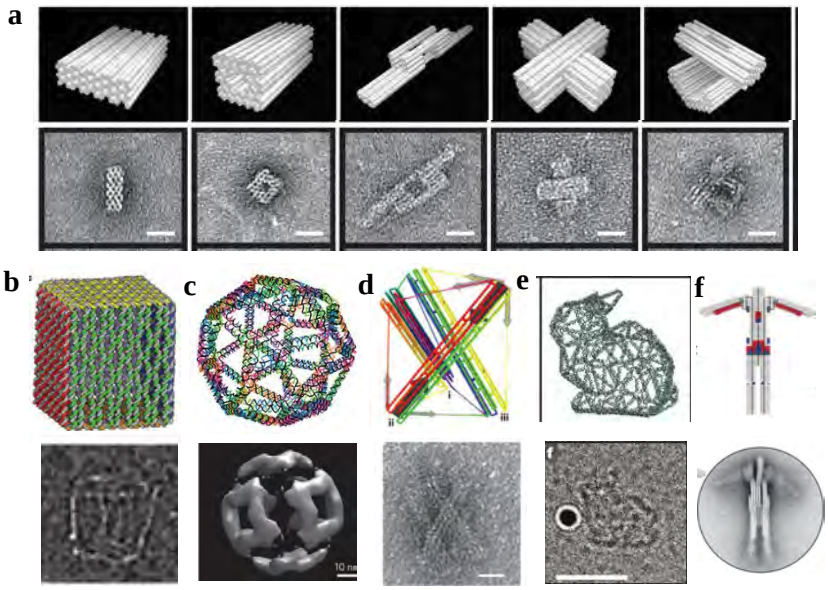

Figure 1.26. DNA origami designs. (a) 3D DNA origami shapes developed by Shih and co-workers (Reprinted with permission from ref.[226], 2009 Springer Nature).(b) 3D DNA origami box developed by Andersen et al. (Reprinted with permission from ref.[227], 2009 Springer Nature).(c) 3D wireframe Archimedean snub cube developed by Yan and co-workers (Reprinted with permission from ref.[228], 2015 Springer Nature). (d) 3D tensegrity prism designed by Liedl et al. (Reprinted with permission from ref.[229], 2010 Springer Nature). (e) A wireframe rabbit (Reprinted with permission from ref.[230], 2015 Springer Nature). (f) A robot (Reprinted with permission from ref.[231], 2015 American Association for the Advancement of Science).

dimensions by stacking sheets of parallel helices and honeycomb-pleat-based strategy (Figure 1.26a).[226, 232] The DNA origami designs were created using caDNAno open-source graphical interface designing program that allows designing new 2D and 3D DNA origami shapes in a user-friendly way. The first version of caDNAno software was developed in William Shih's laboratory. Several different strategies have been developed to construct 3D DNA origami structures. For example, Andersen et al. reported synthesis of nanoscale DNA box with a lid by connecting flat DNA origami sheets at their edges (Figure 1.26b).[227] Yan et al created complex 2D and 3D wireframe DNA origami networks with different types of multiarm junctions (Figure 1.26c).[228] Liedl et al. designed 3D 'tensegrity prism' using single stranded DNA segments of the scaffold as entropic springs, which helped in connecting rigid DNA origami beams under tension (Figure 1.26d).[229] Other 3D shapes developed so far includes nanoflask,[233] 3D gridiron,[234] wireframe rabbit (Figure 1.26e),[230] and a robot (Figure 1.26f).[231]

1.4.2.1.3. Applications of DNA origami

In DNA origami, the nucleic acids act as engineering material and building blocks. Each staple strand possesses a unique sequence and hence occupies a specific position in the folded origami nanostructure. This unique positioning and specificity of Watson–Crick base pairing allow site-specific positioning of organic and inorganic nanoparticles such as fluorophores,[235] quantum dots,[236] nanodiamonds,[237] metal nanoparticles,[238] and proteins[239, 240] in predefined geometries with nanometer precision. Composites assembled using DNA origami have been utilized for applications in diversified fields of research including structural biology, photonics, plasmonics, biosensing, and drug delivery.[241, 242]

1.4.2.1.4. DNA origami for assembling plasmonic nanostructures

A prerequisite for achieving efficient plasmonic coupling is that the nanoparticles have to be arranged with precisely controlled interparticle distances and relative orientation of the individual nanoparticles in space. [40] This can be achieved using DNA origami technique which offers binding sites at a resolution of ~ 6 nm, difficult to achieve using high-end methods such as electron-beam lithography.[243] In recent years, DNA origami technique has emerged as a powerful tool for the assembly of nanoparticles into different patterns with increasing complexities.[244-246] The ability to arrange nanoparticles on DNA origami templates with high accuracy and yield has opened new pathways to construct plasmonic structures with novel optical properties. Among all the metal nanoparticles, so far Au NPs have been the material of choice for self-assembly due to its facile conjugation with DNA oligonucleotides using Au-thiol

bond. [247, 248] Functional groups or labels are often incorporated into the DNA origami structures by modifying one of the staple strands.[249] In 2012, Liedl and Ding demonstrated the potential of DNA origami for construction of 3D plasmonic chiral nanostructures, exhibiting strong plasmon induced circular dichroism (CD) response.[243, 250] Since then, a vast number of examples are reported where DNA origami has been used as a template for assembling spherical[189, 251, 252] and anisotropic[253-255] nanoparticles in predefined patterns. The primary rationale behind using DNA origami as a template for fabrication of metal nanoparticles was concentration and manipulation

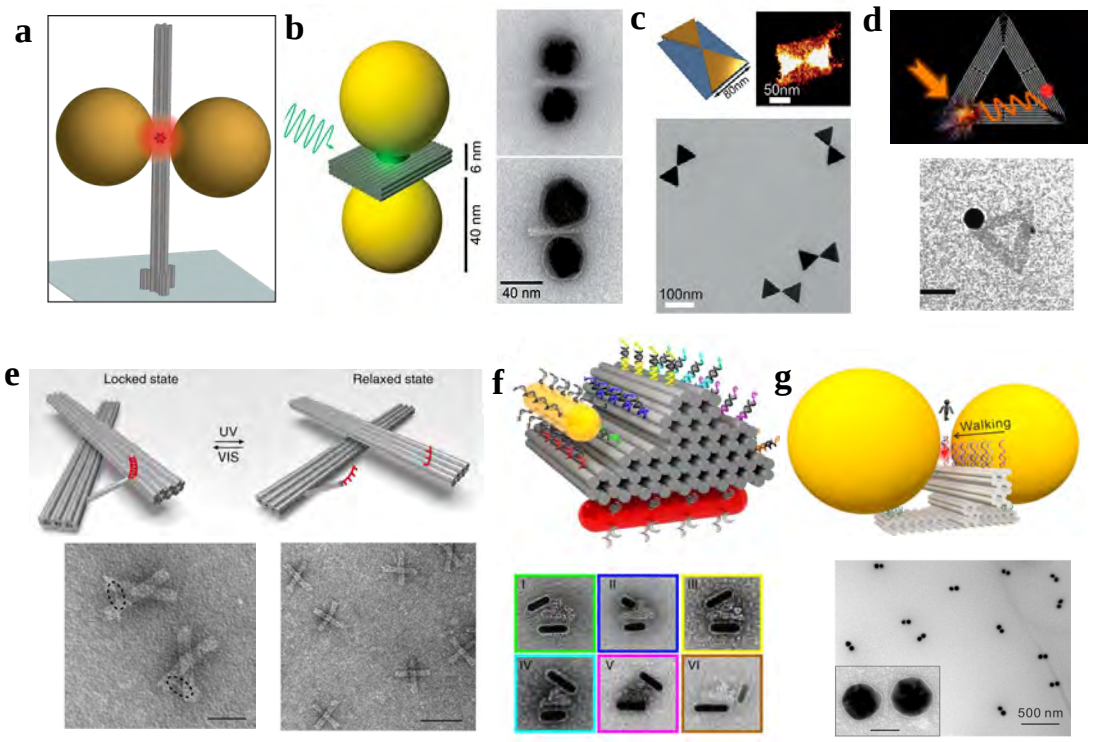

Figure 1.27. DNA origami based static and dynamic plasmonic assemblies. (a and b) DNA origami assembled Au NP dimers for fluorescence and Raman enhancement studies (Reprinted with permission from ref.[128] , 2012 American Association for the Advancement of Science and ref.[256], 2014 American Chemical Society) . (c) Bowtie nanoantenna on DNA origami (Reprinted with permission from ref.[257], 2018 Wiley-VCH Verlag GmbH & Co. KGaA).(d) DNA origami based spectroscopic ruler (Reprinted with permission from ref. [258], 2014 American Chemical Society). (e) Optically responsive plasmonic assembly (Reprinted with permission from ref.[259], 2016 Springer Nature).(f) Plasmonic walker on DNA origami (Reprinted with permission from ref.[260], 2015 Springer Nature).(g) Single fluorophore walking in plasmonic hotspot (Reprinted with permission from ref.[261], 2019 American Chemical Society).

of light into deep-subwavelength volumes. This was elegantly demonstrated by Tinnefeld and co-workers, who used DNA origami nanopillars to construct Au NP dimers which were further used for single molecule fluorescence enhancement studies (Figure 1.27a).[128, 163] Kuhler et al. and Zhan et al. demonstrated the utility of DNA origami assembled Au NP dimers (Figure 1.27b) and bowtie nanoantennas (Figure 1.27c) for SERS application.[256, 257] In other example, Liedl and co-workers, created right handed and left handed helical patterns of Au NPs using 24-helix bundle DNA origami found to be showing pronounced circular dichroism effects.[250] Samanta et al. investigated distance dependent quenching of CdTe/CdS quantum dot fluorescence emission by Au NPs using Au NP-QD hybrid constructed using triangular DNA origami (Figure 1.27d).[258] In a similar work Ko et al. investigated the effect of geometrical configuration of QD-Au NP conjugates on the lifetime and average photon count rate of QD.[262] Hemmig et al. demonstrated DNA origami can be used a platform for artificial light harvesting applications.[263] Several other examples are reported that highlights the utility of DNA origami plasmonic nanoparticle hybrid structures containing single emitters for enhanced fluorescence emission, Raman scattering, and increased Förster resonance energy transfer (FRET) rate studies.[256, 257, 264-266] Apart from static plasmonic assemblies, DNA origami technique has been used for the construction of dynamic plasmonic systems exhibiting optically controlled responses.[267] The Liedl group created a dynamic origami-templated chiral plasmonic assembly showing orientation dependent reversible CD spectra.[268] Kuzyk et al. designed reconfigurable chiral plasmonic nanostructures, exhibiting DNA regulated, [267] light induced (Figure 1.27e),[259] and pH responsive[269] reversible plasmonic chiroptical responses. Kuzyk et al.[260] (Figure 1.27f) and Urban et al.[270] demonstrated Au nanorod (Au NR)-DNA origami hybrid plasmonic walker system in which Au NR could perform directional walking on DNA origami. Very recently Zhan et al.[271] and Wang et al.[272] reported design of dynamic DNA assisted plasmonic assemblies showing reversible sliding motion powered by DNA fuels and optically responsive reconfigurable structural changes respectively. In another very recent report by Xin et al. a single fluorophore carried by a DNAzyme strand was guided to walk into the plasmonic hotspot (Figure 1.27g).[261] DNA origami assembled single fluorophore/QD-metal hybrid nanostructures will open the window to a new class of photostable probes for single-molecule spectroscopic applications.

1.4.2.1.5. DNA origami for single molecule detection

In DNA origami, the position of each folding staple is different, if extended with a single-stranded DNA sequence each staple acts as an individual capture site where any molecule or

particle that can be conjugated with DNA can be precisely placed. Immobilized single molecules can further be analyzed using a suitable single-molecule technique. For example, Sun et al. used DNA origami as a template for creating an enzyme cascade of single catalase and glucose oxidase and further monitored the moving trajectory of the proteins in real-time using total internal reflection fluorescence microscopy (TIRFM).[273] A spatial resolution of ~ 6 nm allows studying distance dependent properties of two or more different components localized at different positions. Rinker et al. captured single thrombin protein molecule on DNA origami using two thrombin specific aptamer DNA sequences. [274] They investigated the effect of distance between the aptamer sequences on thrombin binding. Acuna et al. used DNA origami for studying distance-dependent single-molecule photoluminescence quenching of an organic fluorophore by Au nanoparticle.[275] A major breakthrough was achieved when Voigt et al. demonstrated the applicability of DNA origami for analysis of single-molecule chemical coupling and cleavage reactions.[276] Later, Helmig et al. carried out distance-dependent oxidation of organic molecules using singlet oxygen generated from a single photosensitizer. The organic molecules and the photosensitizer were placed on the origami template.[277] The programmable nature of DNA origami not only allowed studying events at single molecule level but also acted as a lab bench for studying energy transfer processes. Stein et al. visualized energy transfer paths between an input dye (ATTO488) and two output dyes (ATTO647N and Alexa 750) using single molecule four color Foster resonance energy transfer (FRET) studies.[278] The energy transfer was directed with the help of a jumper dye (ATTO565) located in between the input and output dyes. This study demonstrated that DNA origami has the potential to be used as a circuit board for designing photonic devices. Strenuous efforts have been taken by the scientific community to create fully controlled artificial molecular systems such as cargo transporter,[279] bipedal motor,[280] and a molecular robot[281] using DNA origami as a building block.

The characteristics of DNA origami such as nanometer addressability, scalability, bio-compatibility, and easy synthesis makes it a promising technology for sensing applications especially single-molecule sensing that reflects in the several reported examples. Ke et al. created nucleic acid probe tiles using DNA origami and used them for label-free detection of RNA.[282] Koirala et al. demonstrated mechanochemical sensing of platelet-derived growth factor (PDGF) at the single-molecule level using designed 7-tile DNA origami nanostructure.[283] Kuzuya et al.[284] and Ke et al.[285] designed 3D dynamic DNA origami nanostructures that undergo considerable conformational changes upon binding of single target molecule. The designed structures were used for nucleic acid sensing. Recently, DNA origami has been

explored for creating nanopores as it provide control over the size of nanopore and localization of the analyte, difficult to achieve using high end techniques used for creating nanopores.[286, 287] Ainsa et al.[288] have shown that it is possible to do selective detection of ssDNA sequences using DNA nanopores, increasing the hope that DNA origami nanopores can be designed as a versatile chemical/biological sensors.

The ability of DNA origami to position functional biomolecules such as proteins and ligands along with nanoparticles makes it a promising candidate for designing plasmonic sensing devices.[289] Although there are considerable number of reports on DNA origami based single molecule sensing,[290, 291] only a handful of reports describe plasmonic sensing on DNA origami template. Tinnefeld and co-workers reported detection of Zika virus nucleic acid without prior amplification in the plasmonic hotspot of silver nanoparticles coupled to pillar DNA origami.[292] Heck et al. recently demonstrated SERS based detection of single streptavidin protein molecule labeled with alkyne groups positioned in the plasmonic hotspot.[293] Huang et al.[294] and Funck et al.[294] individually reported applicability of DNA origami based chiral plasmonic sensing devices for sensing of nucleoside bases and RNA with limit of detection of 20 μM and 100 pM respectively. Very recently, Masciotti et al. reported detection of specific DNA probe using designed DNA origami-Au NP hybrid plasmonic nanosensor.[295]

Although in recent years DNA origami has matured from the production of complex nanostructures to functional and sensing devices, the remarkable capability of the DNA origami technique has not been fully utilized to take the designed devices from research articles to commercial applications. There is still plenty of room for improvement.

1.5. Outline of the thesis

The research on the fabrication of novel self-assembled hybrid nanoantennas for enhancing single molecule signals has evolved manifold in recent times, because of the wide variety of advantages associated with single molecule detection. Development of highly sensitive and efficient single molecule detection techniques will not only benefit academic research in understanding fundamental biomolecular mechanisms but will also allow expansion of analytical technologies for medical diagnostics. The aim of the works included in this thesis was to develop novel self-assembled plasmonic nanoantenna materials and further explore their applicability for single molecule spectroscopic and sensing applications. DNA origami has been used as a template for assembling anisotropic metal nanoparticles with tunable nanogap and stoichiometry. A systematic approach has been presented to study the effect of interparticle

gaps, stoichiometry, and negative curvature of Au nanostars and Au@Ag nanostars on the single molecule SERS EFs. Various characterization techniques have been used for the structural and optical characterization of all the nanostructures used for assembling the plasmonic nanoantennas. AFM correlated Raman measurements were done for recording single molecule SERS signals. The thesis is divided into seven chapters including this one.

Chapter 2 is the description of the synthesis methods and characterization techniques used for carrying out the work included in this thesis. Synthesis of Au nanostars, Au@Ag nanostars, Au nanoclusters, quantum dots, DNA origami, and self-assembly of plasmonic nanoantennas (with tunable interparticle gaps and stoichiometry) on DNA origami is discussed in detail. The basic principle and instrumentation of different characterization techniques such as different microscopy (Transmission electron microscopy (TEM), Atomic force microscopy (AFM)), single molecule AFM correlated Raman measurements, X-ray diffraction (XRD), UV-Visible spectroscopy, Time correlated single photon counting (TCSPC), Fourier transform infrared spectroscopy (FTIR), Dynamic light scattering (DLS) study and Photoluminescence spectroscopy has been discussed in this chapter.

Chapter 3 discusses the design of Au nanostar (Au NS) dimer structures with tunable interparticle gap and stoichiometry using the DNA origami technique. The effect of the interparticle gap, stoichiometry and negative curvature site of Au NSs on the Raman enhancement of single Texas red (TR) dye molecule has been investigated. Single TR dye molecule which acts as a Raman reporter molecule was precisely positioned in the junction of the dimerized DNA origami by modifying one of the branching staples of the DNA origami template with the dye molecule. AFM correlated Raman measurements were used for recording single-molecule SERS spectra.

Chapter 4 reports the synthesis and strong broadband field enhancement effects of nanoantennas designed using Au@Ag bimetallic nanostars. The effect of Au@Ag bimetallic nanostars on the SERS signals of single FAM, Cy3, and TR dye molecules corresponding to different regions of the visible spectrum has been investigated. Au@Ag NSs were synthesized by coating a thin layer of Ag on the surface of Au NSs, without compromising on the sharpness of the tips. Au@Ag NS dimers with different interparticle gaps (5 and 10 nm) and monomer were assembled on dimerized rectangular DNA origami. Further, the applicability of designed Au@Ag NS dimer nanoantennas for single molecule fluorescence enhancement and label-free detection of bacterial biomarker pyocyanin has been discussed.

Chapter 5 discusses the synthesis and immobilization of Silicon quantum dots (Si QDs) on DNA origami. A simple one-pot, green, cost-effective and energy efficient approach for the synthesis of blue emitting Si QDs has been proposed. Si QDs were synthesized at room temperature using 3-aminopropyltriethoxysilane (APTES) as the silicon source and a commonly available sugar, glucose, as a reducing and stabilizing agent. The as synthesized hydrophilic Si QDs have been exploited as a reducing agent for the reduction of Au^{3+} ions to Au NPs leading to the formation of Au NP-Si QD nanocomposite. Also, the catalytic abilities of the Au NP-Si QD nanocomposite have been exploited for the reduction of nitroarenes.

This chapter also demonstrates the generation of white light emitting mixture (WLEM) by controlled mixing of as synthesized blue emitting Si QDs with orange red emitting Au nanoclusters (Au NCs). Further, the generated WLEM was utilized for fast, sensitive, and selective reversible sensing of Hg^{+2} ions and thiol containing amino acid Cysteine with a limit of detection of 10 nM.

The last part of this chapter discusses the immobilization of single Si QD on the DNA origami and their use in single molecule fluorescence enhancement studies.

Chapter 6 explores the applicability of the designed Au@Ag NS dimer nanoantennas for the sensing of single thrombin protein molecule. Specific binding of single thrombin protein in the conjunction region between the Au@Ag NSs was achieved by incorporating thrombin binding aptamers on the DNA origami template. After binding of thrombin protein molecule in the plasmonic hotspot we were able to record Raman vibrational bands at 1140, 1540, and 1635 cm^{-1} which are characteristic bands of the protein. The designed plasmonic nanoantenna has the potential to be used as label free sensor for detection of single protein molecules.

Chapter 7 discusses the relevance of the works done by us as well as their scope for future applications.

References

1. X. S. Xie and J. K. Trautman, *Annual Review of Physical Chemistry*, 1998, **49**, 441-480.
2. B. P. English, W. Min, A. M. van Oijen, K. T. Lee, G. Luo, H. Sun, B. J. Cherayil, S. C. Kou and X. S. Xie, *Nature Chemical Biology*, 2006, **2**, 87-94.
3. H. P. Lu, L. Xun and X. S. Xie, *Science*, 1998, **282**, 1877-1882.
4. W. E. Moerner and L. Kador, *Physical Review Letters*, 1989, **62**, 2535-2538.
5. M. Orrit and J. Bernard, *Physical Review Letters*, 1990, **65**, 2716-2719.
6. E. Betzig and R. J. Chichester, *Science*, 1993, **262**, 1422-1425.
7. J. K. Trautman, J. J. Macklin, L. E. Brus and E. Betzig, *Nature*, 1994, **369**, 40-42.
8. T. Funatsu, Y. Harada, M. Tokunaga, K. Saito and T. Yanagida, *Nature*, 1995, **374**, 555-559.
9. D. M. Rissin, C. W. Kan, T. G. Campbell, S. C. Howes, D. R. Fournier, L. Song, T. Piech, P. P. Patel, L. Chang, A. J. Rivnak, E. P. Ferrell, J. D. Randall, G. K. Provuncher, D. R. Walt and D. C. Duffy, *Nature Biotechnology*, 2010, **28**, 595-599.
10. Z. Földes-Papp, U. Demel and G. P. Tilz, *Proceedings of the National Academy of Sciences*, 2001, **98**, 11509-11514.
11. W. E. Moerner, *The Journal of Physical Chemistry B*, 2002, **106**, 910-927.
12. M. F. Juette, D. S. Terry, M. R. Wasserman, Z. Zhou, R. B. Altman, Q. Zheng and S. C. Blanchard, *Current Opinion in Chemical Biology*, 2014, **20**, 103-111.
13. J. Eid, A. Fehr, J. Gray, K. Luong, J. Lyle, G. Otto, P. Peluso, D. Rank, P. Baybayan, B. Bettman, A. Bibillo, K. Bjornson, B. Chaudhuri, F. Christians, R. Cicero, S. Clark, R. Dalal, A. deWinter, J. Dixon, M. Foquet, A. Gaertner, P. Hardenbol, C. Heiner, K. Hester, D. Holden, G. Kearns, X. Kong, R. Kuse, Y. Lacroix, S. Lin, P. Lundquist, C. Ma, P. Marks, M. Maxham, D. Murphy, I. Park, T. Pham, M. Phillips, J. Roy, R. Sebra, G. Shen, J. Sorenson, A. Tomaney, K. Travers, M. Trulson, J. Vieceli, J. Wegener, D. Wu, A. Yang, D. Zaccarin, P. Zhao, F. Zhong, J. Korlach and S. Turner, *Science*, 2009, **323**, 133-138.
14. H. P. Lu, *Chemical Society Reviews*, 2014, **43**, 1118-1143.
15. P. R. Banerjee and A. A. Deniz, *Chemical Society Reviews*, 2014, **43**, 1172-1188.
16. B. Prevo and E. J. G. Peterman, *Chemical Society Reviews*, 2014, **43**, 1144-1155.
17. S. Hohng, S. Lee, J. Lee and M. H. Jo, *Chemical Society Reviews*, 2014, **43**, 1007-1013.
18. M. B. J. Roeffaers, B. F. Sels, H. Uji-i, F. C. De Schryver, P. A. Jacobs, D. E. De Vos and J. Hofkens, *Nature*, 2006, **439**, 572-575.
19. L. E. Weiss, L. Milenkovic, J. Yoon, T. Stearns and W. E. Moerner, *Proceedings of the National Academy of Sciences*, 2019, **116**, 5550-5557.
20. E. Betzig, *Angewandte Chemie International Edition*, 2015, **54**, 8034-8053.
21. W. E. Moerner, *Angewandte Chemie International Edition*, 2015, **54**, 8067-8093.
22. J. Todd, B. Freese, A. Lu, D. Held, J. Morey, R. Livingston and P. Goix, *Clinical Chemistry*, 2007, **53**, 1990-1995.
23. B. N. G. Giepmans, S. R. Adams, M. H. Ellisman and R. Y. Tsien, *Science*, 2006, **312**, 217-224.
24. S. E. J. Bell and N. M. S. Sirimuthu, *Journal of the American Chemical Society*, 2006, **128**, 15580-15581.
25. K. Kneipp, Y. Wang, H. Kneipp, L. T. Perelman, I. Itzkan, R. R. Dasari and M. S. Feld, *Physical Review Letters*, 1997, **78**, 1667-1670.
26. S. Nie and S. R. Emory, *Science*, 1997, **275**, 1102-1106.
27. H. Liu, L. Zhang, X. Lang, Y. Yamaguchi, H. Iwasaki, Y. Inouye, Q. Xue and M. Chen, *Scientific Reports*, 2011, **1**, 112.
28. L. M. Almehmadi, S. M. Curley, N. A. Tokranova, S. A. Tenenbaum and I. K. Lednev, *Scientific Reports*, 2019, **9**, 12356.
29. A. R. L. Marshall, M. Roberts, J. Gierschner, J.-S. G. Bouillard and A. M. Adawi, *ACS Applied Polymer Materials*, 2019, **1**, 1175-1180.
30. in *Principles of Fluorescence Spectroscopy*, ed. J. R. Lakowicz, Springer US, Boston, MA, 2006, DOI: 10.1007/978-0-387-46312-4_23, pp. 757-795.
31. M. J. Levene, J. Korlach, S. W. Turner, M. Foquet, H. G. Craighead and W. W. Webb, *Science*, 2003, **299**, 682-686.
32. J. Wenger and H. Rigneault, *Int J Mol Sci*, 2010, **11**, 206-221.

33. P. Holzmeister, G. P. Acuna, D. Grohmann and P. Tinnefeld, *Chemical Society Reviews*, 2014, **43**, 1014-1028.
34. S. Nie, D. Chiu and R. Zare, *Science*, 1994, **266**, 1018-1021.
35. D. Axelrod, *Traffic*, 2001, **2**, 764-774.
36. J. Lee, Y. Miyanaga, M. Ueda and S. Hohng, *Biophys J*, 2012, **103**, 1691-1697.
37. G. M. J. Segers-Nolten, C. Wyman, N. Wijgers, W. Vermeulen, A. T. M. Lenferink, J. H. J. Hoeijmakers, J. Greve and C. Otto, *Nucleic Acids Research*, 2002, **30**, 4720-4727.
38. R. M. Dickson, D. J. Norris, Y.-L. Tzeng and W. E. Moerner, *Science*, 1996, **274**, 966-968.
39. F. Karim, T. B. Smith and C. Zhao, *Journal of Nanophotonics*, 2017, **12**, 1-15, 15.
40. J. A. Schuller, E. S. Barnard, W. Cai, Y. C. Jun, J. S. White and M. L. Brongersma, *Nature Materials*, 2010, **9**, 193-204.
41. S. A. Maier and H. A. Atwater, *Journal of Applied Physics*, 2005, **98**, 011101.
42. P. Sharma, S. Brown, G. Walter, S. Santra and B. Moudgil, *Advances in Colloid and Interface Science*, 2006, **123-126**, 471-485.
43. F. Tao, L. Nguyen and S. Zhang, in *Metal Nanoparticles for Catalysis: Advances and Applications*, The Royal Society of Chemistry, 2014, DOI: 10.1039/9781782621034-00001, pp. 1-5.
44. O. V. Salata, *J Nanobiotechnology*, 2004, **2**, 3-3.
45. C. A. P. Louis, Olivier, *Gold Nanoparticles for Physics, Chemistry and Biology*.
46. M. Faraday, *Philosophical Transactions of the Royal Society of London*, 1857, **147**, 145-181.
47. British Museum-The Lycurgus Cup, https://research.britishmuseum.org/.
48. J. Kunckels, *Nuetliche Observationes oder Anmerkungen von Auro und Argento Potabili*, Hamburg, Schutzens, 1676.
49. S. Horinouchi, Y. Yamanoi, T. Yonezawa, T. Mouri and H. Nishihara, *Langmuir*, 2006, **22**, 1880-1884.
50. A. Bej, K. Ghosh, A. Sarkar and D. W. Knight, *RSC Advances*, 2016, **6**, 11446-11453.
51. S. Dadashi, R. Poursalehi and H. Delavari, *Procedia Materials Science*, 2015, **11**, 722-726.
52. D. L. Huber, *Small*, 2005, **1**, 482-501.
53. M. B. Gawande, A. Goswami, F.-X. Felpin, T. Asefa, X. Huang, R. Silva, X. Zou, R. Zboril and R. S. Varma, *Chemical Reviews*, 2016, **116**, 3722-3811.
54. D. Huang, F. Liao, S. Molesa, D. Redinger and V. Subramanian, *Journal of The Electrochemical Society*, 2003, **150**, G412-G417.
55. M.-C. Daniel and D. Astruc, *Chemical Reviews*, 2004, **104**, 293-346.
56. L. Dykman and N. Khlebtsov, *Chemical Society Reviews*, 2012, **41**, 2256-2282.
57. A. Corma and H. Garcia, *Chemical Society Reviews*, 2008, **37**, 2096-2126.
58. L. M. Liz-Marzán, *Materials Today*, 2004, **7**, 26-31.
59. G. Mie, *Annalen der Physik*, 1908, **330**, 377-445.
60. R. Gans, *Annalen der Physik*, 1915, **352**, 270-284.
61. G. C. Papavassiliou, *Progress in Solid State Chemistry*, 1979, **12**, 185-271.
62. U. Kreibig and M. Vollmer, *Optical properties of metal clusters*, Springer, Berlin; New York, 1995.
63. R. H. Ritchie, *Physical Review*, 1957, **106**, 874-881.
64. in *Physics at Surfaces*, ed. A. Zangwill, Cambridge University Press, Cambridge, 1988, DOI: DOI: 10.1017/CBO9780511622564.009, pp. 163-182.
65. K. L. Kelly, E. Coronado, L. L. Zhao and G. C. Schatz, *The Journal of Physical Chemistry B*, 2003, **107**, 668-677.
66. M. E. Stewart, C. R. Anderton, L. B. Thompson, J. Maria, S. K. Gray, J. A. Rogers and R. G. Nuzzo, *Chemical Reviews*, 2008, **108**, 494-521.
67. K. A. Willets and R. P. V. Duyne, *Annual Review of Physical Chemistry*, 2007, **58**, 267-297.
68. J. Krajczewski, K. Kołątaj and A. Kudelski, *RSC Advances*, 2017, **7**, 17559-17576.
69. C. F. Bohren and D. R. Huffman, *Absorption and Scattering of Light by Small Particles*, Wiley, 1983.
70. M. Kerker and E. M. Loebl, *The Scattering of Light and Other Electromagnetic Radiation*, Elsevier Science, 2016.
71. A. J. Haes, C. L. Haynes, A. D. McFarland, G. C. Schatz, R. P. Van Duyne and S. Zou, *MRS Bulletin*, 2011, **30**, 368-375.

72. S. Link and M. A. El-Sayed, *The Journal of Physical Chemistry B*, 1999, **103**, 8410-8426.
73. E. K. Payne, K. L. Shuford, S. Park, G. C. Schatz and C. A. Mirkin, *The Journal of Physical Chemistry B*, 2006, **110**, 2150-2154.
74. J. Cao, T. Sun and K. T. V. Grattan, *Sensors and Actuators B: Chemical*, 2014, **195**, 332-351.
75. S. Link, M. B. Mohamed and M. A. El-Sayed, *The Journal of Physical Chemistry B*, 1999, **103**, 3073-3077.
76. E. Prodan, C. Radloff, N. J. Halas and P. Nordlander, *Science*, 2003, **302**, 419-422.
77. F. Hao, C. L. Nehl, J. H. Hafner and P. Nordlander, *Nano Letters*, 2007, **7**, 729-732.
78. S. Barbosa, A. Agrawal, L. Rodríguez-Lorenzo, I. Pastoriza-Santos, R. A. Alvarez-Puebla, A. Kornowski, H. Weller and L. M. Liz-Marzán, *Langmuir*, 2010, **26**, 14943-14950.
79. N. Halas, *MRS Bulletin*, 2011, **30**, 362-367.
80. C. Loo, A. Lin, L. Hirsch, M.-H. Lee, J. Barton, N. Halas, J. West and R. Drezek, *Technology in Cancer Research & Treatment*, 2004, **3**, 33-40.
81. K. D. Gilroy, A. Ruditskiy, H.-C. Peng, D. Qin and Y. Xia, *Chemical Reviews*, 2016, **116**, 10414-10472.
82. W. Zhang and X. Lu, *Journal*, 2013, **2**, 487.
83. K. K. Haldar, S. Kundu and A. Patra, *ACS Applied Materials & Interfaces*, 2014, **6**, 21946-21953.
84. S. Pande, S. K. Ghosh, S. Praharaj, S. Panigrahi, S. Basu, S. Jana, A. Pal, T. Tsukuda and T. Pal, *The Journal of Physical Chemistry C*, 2007, **111**, 10806-10813.
85. A. M. Fales, H. Yuan and T. Vo-Dinh, *The Journal of Physical Chemistry C*, 2014, **118**, 3708-3715.
86. Y. Yang, J. Shi, G. Kawamura and M. Nogami, *Scripta Materialia*, 2008, **58**, 862-865.
87. M. Osawa, K.-I. Ataka, K. Yoshii and Y. Nishikawa, *Applied Spectroscopy*, 1993, **47**, 1497-1502.
88. Z.-Q. Tian, B. Ren, J.-F. Li and Z.-L. Yang, *Chemical Communications*, 2007, DOI: 10.1039/B616986D, 3514-3534.
89. P. L. Stiles, J. A. Dieringer, N. C. Shah and R. P. V. Duyne, *Annual Review of Analytical Chemistry*, 2008, **1**, 601-626.
90. J.-F. Li, C.-Y. Li and R. F. Aroca, *Chemical Society Reviews*, 2017, **46**, 3962-3979.
91. W. L. Barnes, A. Dereux and T. W. Ebbesen, *Nature*, 2003, **424**, 824-830.
92. J. O. Arroyo and P. Kukura, *Nature Photonics*, 2015, **10**, 11.
93. H. Yu, Y. Peng, Y. Yang and Z.-Y. Li, *npj Computational Materials*, 2019, **5**, 45.
94. C. Zhan, X.-J. Chen, J. Yi, J.-F. Li, D.-Y. Wu and Z.-Q. Tian, *Nature Reviews Chemistry*, 2018, **2**, 216-230.
95. J. Reguera, J. Langer, D. Jiménez de Aberasturi and L. M. Liz-Marzán, *Chemical Society Reviews*, 2017, **46**, 3866-3885.
96. C. V. Raman and K. S. Krishnan, *Nature*, 1928, **121**, 501-502.
97. H. K. Lee, Y. H. Lee, C. S. L. Koh, G. C. Phan-Quang, X. Han, C. L. Lay, H. Y. F. Sim, Y.-C. Kao, Q. An and X. Y. Ling, *Chemical Society Reviews*, 2019, **48**, 731-756.
98. M. Fleischmann, P. J. Hendra and A. J. McQuillan, *Chemical Physics Letters*, 1974, **26**, 163-166.
99. S. Schlücker, *Angewandte Chemie International Edition*, 2014, **53**, 4756-4795.
100. M. F. Cardinal, E. Vander Ende, R. A. Hackler, M. O. McAnally, P. C. Stair, G. C. Schatz and R. P. Van Duyne, *Chemical Society Reviews*, 2017, **46**, 3886-3903.
101. I. Bruzas, W. Lum, Z. Gorunmez and L. Sagle, *Analyst*, 2018, **143**, 3990-4008.
102. B. Sharma, R. R. Frontiera, A.-I. Henry, E. Ringe and R. P. Van Duyne, *Materials Today*, 2012, **15**, 16-25.
103. P. Kambhampati, C. M. Child, M. C. Foster and A. Campion, *The Journal of Chemical Physics*, 1998, **108**, 5013-5026.
104. a. H Metiu and P. Das, *Annual Review of Physical Chemistry*, 1984, **35**, 507-536.
105. E. L. Ru and P. Etchegoin, *Principles of Surface-Enhanced Raman Spectroscopy: and Related Plasmonic Effects*, Elsevier Science, 2008.
106. E. C. Le Ru and P. G. Etchegoin, *Chemical Physics Letters*, 2006, **423**, 63-66.
107. S.-Y. Ding, J. Yi, J.-F. Li, B. Ren, D.-Y. Wu, R. Panneerselvam and Z.-Q. Tian, *Nature Reviews Materials*, 2016, **1**, 16021.

108. R. Esteban, A. Zugarramurdi, P. Zhang, P. Nordlander, F. J. García-Vidal, A. G. Borisov and J. Aizpurua, *Faraday Discussions*, 2015, **178**, 151-183.
109. W. Zhu, R. Esteban, A. G. Borisov, J. J. Baumberg, P. Nordlander, H. J. Lezec, J. Aizpurua and K. B. Crozier, *Nature Communications*, 2016, **7**, 11495.
110. J. Nelayah, M. Kociak, O. Stéphan, F. J. García de Abajo, M. Tencé, L. Henrard, D. Taverna, I. Pastoriza-Santos, L. M. Liz-Marzán and C. Colliex, *Nature Physics*, 2007, **3**, 348-353.
111. L. Rodríguez-Lorenzo, R. A. Álvarez-Puebla, I. Pastoriza-Santos, S. Mazzucco, O. Stéphan, M. Kociak, L. M. Liz-Marzán and F. J. García de Abajo, *Journal of the American Chemical Society*, 2009, **131**, 4616-4618.
112. H. Yuan, C. G. Khoury, H. Hwang, C. M. Wilson, G. A. Grant and T. Vo-Dinh, *Nanotechnology*, 2012, **23**, 075102.
113. L. Rodríguez-Lorenzo, R. de la Rica, R. A. Álvarez-Puebla, L. M. Liz-Marzán and M. M. Stevens, *Nature Materials*, 2012, **11**, 604.
114. W. Niu, Y. A. A. Chua, W. Zhang, H. Huang and X. Lu, *Journal of the American Chemical Society*, 2015, **137**, 10460-10463.
115. A. Campion and P. Kambhampati, *Chemical Society Reviews*, 1998, **27**, 241-250.
116. J. R. Lombardi, R. L. Birke, T. Lu and J. Xu, *The Journal of Chemical Physics*, 1986, **84**, 4174-4180.
117. L.-B. Zhao, R. Huang, M.-X. Bai, D.-Y. Wu and Z.-Q. Tian, *The Journal of Physical Chemistry C*, 2011, **115**, 4174-4183.
118. M. Osawa, N. Matsuda, K. Yoshii and I. Uchida, *The Journal of Physical Chemistry*, 1994, **98**, 12702-12707.
119. J. A. Creighton, *Surface Science*, 1986, **173**, 665-672.
120. W.-H. Park and Z. H. Kim, *Nano Letters*, 2010, **10**, 4040-4048.
121. D. Cunningham, R. E. Littleford, W. E. Smith, P. J. Lundahl, I. Khan, D. W. McComb, D. Graham and N. Laforest, *Faraday Discussions*, 2006, **132**, 135-145.
122. G. McNay, D. Eustace, W. E. Smith, K. Faulds and D. Graham, *Applied Spectroscopy*, 2011, **65**, 825-837.
123. D. H. Murgida and P. Hildebrandt, *The Journal of Physical Chemistry B*, 2001, **105**, 1578-1586.
124. D. Hobara, K. Niki and T. M. Cotton, *Biospectroscopy*, 1998, **4**, 161-170.
125. I. Ros, T. Placido, V. Amendola, C. Marinzi, N. Manfredi, R. Comparelli, M. Striccoli, A. Agostiano, A. Abbotto, D. Pedron, R. Pilot and R. Bozio, *Plasmonics*, 2014, **9**, 581-593.
126. C. McLaughlin, D. MacMillan, C. McCardle and W. E. Smith, *Analytical Chemistry*, 2002, **74**, 3160-3167.
127. K. Faulds, R. P. Barbagallo, J. T. Keer, W. E. Smith and D. Graham, *Analyst*, 2004, **129**, 567-568.
128. G. P. Acuna, F. M. Möller, P. Holzmeister, S. Beater, B. Lalkens and P. Tinnefeld, *Science*, 2012, **338**, 506-510.
129. E. C. Le Ru, M. Meyer and P. G. Etchegoin, *The Journal of Physical Chemistry B*, 2006, **110**, 1944-1948.
130. E. Blackie, E. C. Le Ru, M. Meyer, M. Timmer, B. Burkett, P. Northcote and P. G. Etchegoin, *Physical Chemistry Chemical Physics*, 2008, **10**, 4147-4153.
131. C. J. L. Constantino, T. Lemma, P. A. Antunes and R. Aroca, *Analytical Chemistry*, 2001, **73**, 3674-3678.
132. P. J. G. Goulet, N. P. W. Pieczonka and R. F. Aroca, *Journal of Raman Spectroscopy*, 2005, **36**, 574-580.
133. J.-M. Nam, J.-W. Oh, H. Lee and Y. D. Suh, *Accounts of Chemical Research*, 2016, **49**, 2746-2755.
134. D. L. Jeanmaire and R. P. Van Duyne, *Journal of Electroanalytical Chemistry and Interfacial Electrochemistry*, 1977, **84**, 1-20.
135. H. Lee, G.-H. Kim, J.-H. Lee, N. H. Kim, J.-M. Nam and Y. D. Suh, *Nano Letters*, 2015, **15**, 4628-4636.
136. J.-H. Lee, J.-M. Nam, K.-S. Jeon, D.-K. Lim, H. Kim, S. Kwon, H. Lee and Y. D. Suh, *ACS Nano*, 2012, **6**, 9574-9584.
137. J. W. Kang, P. T. C. So, R. R. Dasari and D.-K. Lim, *Nano Letters*, 2015, **15**, 1766-1772.

138. J. Li, Z. Zhu, B. Zhu, Y. Ma, B. Lin, R. Liu, Y. Song, H. Lin, S. Tu and C. Yang, *Analytical Chemistry*, 2016, **88**, 7828-7836.
139. Y. Fang, N.-H. Seong and D. D. Dlott, *Science*, 2008, **321**, 388-392.
140. J. F. W. Herschel, *Philosophical Transactions of the Royal Society of London*, 1845, **135**, 143-145.
141. A. Jabłoński, *Zeitschrift fur Physik*, 1935, **94**, 38-46.
142. E. Brooks Shera, N. K. Seitzinger, L. M. Davis, R. A. Keller and S. A. Soper, *Chemical Physics Letters*, 1990, **174**, 553-557.
143. A. C. Croce and G. Bottiroli, *European Journal of Histochemistry*, 2014, **58**.
144. E. N. Abrahart, *Dyes and Their Intermediates*, Edward Arnold, 1977.
145. in *Advances in Photochemistry*, DOI: 10.1002/9780470133491.ch4, pp. 315-394.
146. A. S. Tatikolov, *Journal of Photochemistry and Photobiology C: Photochemistry Reviews*, 2012, **13**, 55-90.
147. Q. Zheng, M. F. Juette, S. Jockusch, M. R. Wasserman, Z. Zhou, R. B. Altman and S. C. Blanchard, *Chemical Society Reviews*, 2014, **43**, 1044-1056.
148. H. Taguchi, T. Ueno, H. Tadakuma, M. Yoshida and T. Funatsu, *Nature Biotechnology*, 2001, **19**, 861-865.
149. T. Rajh, O. I. Micic and A. J. Nozik, *The Journal of Physical Chemistry*, 1993, **97**, 11999-12003.
150. B. A. Kairdolf, A. M. Smith and S. Nie, *Journal of the American Chemical Society*, 2008, **130**, 12866-12867.
151. M. L. Steigerwald and L. E. Brus, *Accounts of Chemical Research*, 1990, **23**, 183-188.
152. N. Chestnoy, T. D. Harris, R. Hull and L. E. Brus, *The Journal of Physical Chemistry*, 1986, **90**, 3393-3399.
153. A. P. Alivisatos, *The Journal of Physical Chemistry*, 1996, **100**, 13226-13239.
154. A. M. Smith and S. Nie, *Accounts of Chemical Research*, 2010, **43**, 190-200.
155. D. Sumanth Kumar, B. Jai Kumar and H. M. Mahesh, in *Synthesis of Inorganic Nanomaterials*, eds. S. Mohan Bhagyaraj, O. S. Oluwafemi, N. Kalarikkal and S. Thomas, Woodhead Publishing, 2018, DOI: https://doi.org/10.1016/B978-0-08-101975-7.00003-8, pp. 59-88.
156. U. Resch-Genger, M. Grabolle, S. Cavaliere-Jaricot, R. Nitschke and T. Nann, *Nature Methods*, 2008, **5**, 763-775.
157. W. C. W. Chan, D. J. Maxwell, X. Gao, R. E. Bailey, M. Han and S. Nie, *Current Opinion in Biotechnology*, 2002, **13**, 40-46.
158. J. P. Wolfgang, G. Daniele, P. Teresa, Z. Daniela, M. Christine, C. W. Shara, B. Rosanne, A. L. G. Mark, A. L. Carolyn and A. P. Alivisatos, *Nanotechnology*, 2003, **14**, R15.
159. X. Michalet, F. Pinaud, T. D. Lacoste, M. Dahan, M. P. Bruchez, A. P. Alivisatos and S. Weiss, *Single Molecules*, 2001, **2**, 261-276.
160. J. R. Lakowicz, *Anal Biochem*, 2005, **337**, 171-194.
161. D. Punj, M. Mivelle, S. B. Moparthi, T. S. van Zanten, H. Rigneault, N. F. van Hulst, M. F. García-Parajó and J. Wenger, *Nature Nanotechnology*, 2013, **8**, 512.
162. A. Kinkhabwala, Z. Yu, S. Fan, Y. Avlasevich, K. Müllen and W. E. Moerner, *Nature Photonics*, 2009, **3**, 654-657.
163. A. Puchkova, C. Vietz, E. Pibiri, B. Wünsch, M. Sanz Paz, G. P. Acuna and P. Tinnefeld, *Nano Letters*, 2015, **15**, 8354-8359.
164. D. Punj, R. Regmi, A. Devilez, R. Plauchu, S. B. Moparthi, B. Stout, N. Bonod, H. Rigneault and J. Wenger, *ACS Photonics*, 2015, **2**, 1099-1107.
165. S. Khatua, P. M. R. Paulo, H. Yuan, A. Gupta, P. Zijlstra and M. Orrit, *ACS Nano*, 2014, **8**, 4440-4449.
166. J. R. Lakowicz, *Anal Biochem*, 2001, **298**, 1-24.
167. in *Principles of Fluorescence Spectroscopy*, ed. J. R. Lakowicz, Springer US, Boston, MA, 2006, DOI: 10.1007/978-0-387-46312-4_25, pp. 841-859.
168. P. Anger, P. Bharadwaj and L. Novotny, *Physical Review Letters*, 2006, **96**, 113002.
169. F. Tam, G. P. Goodrich, B. R. Johnson and N. J. Halas, *Nano Letters*, 2007, **7**, 496-501.
170. O. Kulakovich, N. Strekal, A. Yaroshevich, S. Maskevich, S. Gaponenko, I. Nabiev, U. Woggon and M. Artemyev, *Nano Letters*, 2002, **2**, 1449-1452.

171. Y. Chen, K. Munechika, I. J.-L. Plante, A. M. Munro, S. E. Skrabalak, Y. Xia and D. S. Ginger, *Applied Physics Letters*, 2008, **93**, 053106.
172. K. Munechika, Y. Chen, A. F. Tillack, A. P. Kulkarni, I. J.-L. Plante, A. M. Munro and D. S. Ginger, *Nano Letters*, 2010, **10**, 2598-2603.
173. O. L. Muskens, V. Giannini, J. A. Sánchez-Gil and J. Gómez Rivas, *Nano Letters*, 2007, **7**, 2871-2875.
174. L. Sapienza, M. Davanço, A. Badolato and K. Srinivasan, *Nature Communications*, 2015, **6**, 7833.
175. D. Ratchford, F. Shafiei, S. Kim, S. K. Gray and X. Li, *Nano Letters*, 2011, **11**, 1049-1054.
176. J. N. Farahani, D. W. Pohl, H. J. Eisler and B. Hecht, *Physical Review Letters*, 2005, **95**, 017402.
177. W. Zhang, M. Caldarola, X. Lu and M. Orrit, *ACS Photonics*, 2018, **5**, 2960-2968.
178. C. Vieu, F. Carcenac, A. Pépin, Y. Chen, M. Mejias, A. Lebib, L. Manin-Ferlazzo, L. Couraud and H. Launois, *Applied Surface Science*, 2000, **164**, 111-117.
179. A. Joshi-Imre and S. Bauerdick, *Journal of Nanotechnology*, 2014, **2014**, 26.
180. A. Kinkhabwala, Z. Yu, S. Fan, Y. Avlasevich, K. Müllen and W. E. Moerner, *Nature Photonics*, 2009, **3**, 654.
181. R. Near, C. Tabor, J. Duan, R. Pachter and M. El-Sayed, *Nano Letters*, 2012, **12**, 2158-2164.
182. L. Petti, R. Capasso, M. Rippa, M. Pannico, P. La Manna, G. Peluso, A. Calarco, E. Bobeico and P. Musto, *Vibrational Spectroscopy*, 2016, **82**, 22-30.
183. P. Sadeghi, K. Wu, T. Rindzevicius, A. Boisen and S. Schmid, *Journal*, 2017, **7**, 497.
184. T. P. Bigioni, X.-M. Lin, T. T. Nguyen, E. I. Corwin, T. A. Witten and H. M. Jaeger, *Nature Materials*, 2006, **5**, 265-270.
185. A. Tao, P. Sinsermsuksakul and P. Yang, *Nature Nanotechnology*, 2007, **2**, 435-440.
186. G. Yang, J. Nanda, B. Wang, G. Chen and D. T. Hallinan, *ACS Applied Materials & Interfaces*, 2017, **9**, 13457-13470.
187. Y.-W. Wang, K.-C. Kao, J.-K. Wang and C.-Y. Mou, *The Journal of Physical Chemistry C*, 2016, **120**, 24382-24388.
188. P. W. K. Rothemund, *Nature*, 2006, **440**, 297-302.
189. Y. Tian, T. Wang, W. Liu, H. L. Xin, H. Li, Y. Ke, W. M. Shih and O. Gang, *Nature Nanotechnology*, 2015, **10**, 637.
190. N. C. Seeman, *Journal of Theoretical Biology*, 1982, **99**, 237-247.
191. W. Saenger, *Principles of nucleic acid structure*, Springer-Verlag, 1984.
192. R. E. Franklin and R. G. Gosling, *Nature*, 1953, **171**, 740-741.
193. J. D. Watson and F. H. C. Crick, *Nature*, 1953, **171**, 964-967.
194. J. D. Watson and F. H. C. Crick, *Nature*, 1953, **171**, 737-738.
195. R. Holliday, *Genetical Research*, 2009, **5**, 282-304.
196. C. Mao, W. Sun and N. C. Seeman, *Journal of the American Chemical Society*, 1999, **121**, 5437-5443.
197. N. C. Seeman and P. S. Lukeman, *Reports on Progress in Physics*, 2004, **68**, 237-270.
198. Y. He, T. Ye, M. Su, C. Zhang, A. E. Ribbe, W. Jiang and C. Mao, *Nature*, 2008, **452**, 198-201.
199. R. P. Goodman, I. A. T. Schaap, C. F. Tardin, C. M. Erben, R. M. Berry, C. F. Schmidt and A. J. Turberfield, *Science*, 2005, **310**, 1661-1665.
200. W. M. Shih, J. D. Quispe and G. F. Joyce, *Nature*, 2004, **427**, 618-621.
201. D. Bhatia, S. Mehtab, R. Krishnan, S. S. Indi, A. Basu and Y. Krishnan, *Angewandte Chemie International Edition*, 2009, **48**, 4134-4137.
202. F. A. Aldaye and H. F. Sleiman, *Journal of the American Chemical Society*, 2007, **129**, 13376-13377.
203. W. Wang, S. Chen, B. An, K. Huang, T. Bai, M. Xu, G. Bellot, Y. Ke, Y. Xiang and B. Wei, *Nature Communications*, 2019, **10**, 1067.
204. P. W. K. Rothemund, A. Ekani-Nkodo, N. Papadakis, A. Kumar, D. K. Fygenson and E. Winfree, *Journal of the American Chemical Society*, 2004, **126**, 16344-16352.
205. F. Mathieu, S. Liao, J. Kopatsch, T. Wang, C. Mao and N. C. Seeman, *Nano Letters*, 2005, **5**, 661-665.
206. Y. Yu, B. Jin, Y. Li and Z. Deng, *Chemistry – A European Journal*, 2019, **25**, 9785-9798.

207. D. Zhu, H. Pei, G. Yao, L. Wang, S. Su, J. Chao, L. Wang, A. Aldalbahi, S. Song, J. Shi, J. Hu, C. Fan and X. Zuo, *Advanced Materials*, 2016, **28**, 6860-6865.
208. J. Pan, F. Li, T.-G. Cha, H. Chen and J. H. Choi, *Current Opinion in Biotechnology*, 2015, **34**, 56-64.
209. T.-G. Cha, J. Pan, H. Chen, J. Salgado, X. Li, C. Mao and J. H. Choi, *Nature Nanotechnology*, 2013, **9**, 39.
210. A. R. Chandrasekaran, J. A. Punnoose, L. Zhou, P. Dey, B. K. Dey and K. Halvorsen, *Nucleic Acids Research*, 2019, DOI: 10.1093/nar/gkz580.
211. C. Li, X. Hu, J. Lu, X. Mao, Y. Xiang, Y. Shu and G. Li, *Chemical Science*, 2018, **9**, 979-984.
212. P. Zhang, J. Jiang, R. Yuan, Y. Zhuo and Y. Chai, *Journal of the American Chemical Society*, 2018, **140**, 9361-9364.
213. X. Liu, L. Wu, L. Wang and W. Jiang, *Talanta*, 2018, **179**, 356-363.
214. S. Wang, M. Xia, J. Liu, S. Zhang and X. Zhang, *ACS Sensors*, 2017, **2**, 735-739.
215. H. Yan, T. H. LaBean, L. Feng and J. H. Reif, *Proceedings of the National Academy of Sciences*, 2003, **100**, 8103-8108.
216. Z. Zhao, Y. Liu and H. Yan, *Nano Letters*, 2011, **11**, 2997-3002.
217. A. Rajendran, M. Endo, Y. Katsuda, K. Hidaka and H. Sugiyama, *ACS Nano*, 2011, **5**, 665-671.
218. E. S. Andersen, M. Dong, M. M. Nielsen, K. Jahn, A. Lind-Thomsen, W. Mamdouh, K. V. Gothelf, F. Besenbacher and J. Kjems, *ACS Nano*, 2008, **2**, 1213-1218.
219. L. Qian, Y. Wang, Z. Zhang, J. Zhao, D. Pan, Y. Zhang, Q. Liu, C. Fan, J. Hu and L. He, *Chinese Science Bulletin*, 2006, **51**, 2973-2976.
220. E. Pound, J. R. Ashton, H. A. Becerril and A. T. Woolley, *Nano Letters*, 2009, **9**, 4302-4305.
221. W. Liu, H. Zhong, R. Wang and N. C. Seeman, *Angewandte Chemie International Edition*, 2011, **50**, 264-267.
222. G. Tikhomirov, P. Petersen and L. Qian, *Nature*, 2017, **552**, 67.
223. R. Wang, K. Gorday, C. Nuckolls and S. J. Wind, *Chemical Communications*, 2016, **52**, 1610-1613.
224. M. Endo, T. Sugita, Y. Katsuda, K. Hidaka and H. Sugiyama, *Chemistry – A European Journal*, 2010, **16**, 5362-5368.
225. H. Zhang, J. Chao, D. Pan, H. Liu, Q. Huang and C. Fan, *Chemical Communications*, 2012, **48**, 6405-6407.
226. S. M. Douglas, H. Dietz, T. Liedl, B. Högberg, F. Graf and W. M. Shih, *Nature*, 2009, **459**, 414.
227. E. S. Andersen, M. Dong, M. M. Nielsen, K. Jahn, R. Subramani, W. Mamdouh, M. M. Golas, B. Sander, H. Stark, C. L. P. Oliveira, J. S. Pedersen, V. Birkedal, F. Besenbacher, K. V. Gothelf and J. Kjems, *Nature*, 2009, **459**, 73-76.
228. F. Zhang, S. Jiang, S. Wu, Y. Li, C. Mao, Y. Liu and H. Yan, *Nature Nanotechnology*, 2015, **10**, 779.
229. T. Liedl, B. Högberg, J. Tytell, D. E. Ingber and W. M. Shih, *Nature Nanotechnology*, 2010, **5**, 520-524.
230. E. Benson, A. Mohammed, J. Gardell, S. Masich, E. Czeizler, P. Orponen and B. Högberg, *Nature*, 2015, **523**, 441.
231. T. Gerling, K. F. Wagenbauer, A. M. Neuner and H. Dietz, *Science*, 2015, **347**, 1446-1452.
232. S. M. Douglas, A. H. Marblestone, S. Teerapittayanon, A. Vazquez, G. M. Church and W. M. Shih, *Nucleic acids research*, 2009, **37**, 5001-5006.
233. D. Han, S. Pal, J. Nangreave, Z. Deng, Y. Liu and H. Yan, *Science*, 2011, **332**, 342-346.
234. D. Han, S. Pal, Y. Yang, S. Jiang, J. Nangreave, Y. Liu and H. Yan, *Science*, 2013, **339**, 1412-1415.
235. R. Schreiber, J. Do, E.-M. Roller, T. Zhang, V. J. Schüller, P. C. Nickels, J. Feldmann and T. Liedl, *Nature Nanotechnology*, 2013, **9**, 74.
236. D. Huang, M. Freeley and M. Palma, *Scientific Reports*, 2017, **7**, 45591.
237. T. Zhang, A. Neumann, J. Lindlau, Y. Wu, G. Pramanik, B. Naydenov, F. Jelezko, F. Schüder, S. Huber, M. Huber, F. Stehr, A. Högele, T. Weil and T. Liedl, *Journal of the American Chemical Society*, 2015, **137**, 9776-9779.
238. S. Tanwar, K. K. Haldar and T. Sen, *Journal of the American Chemical Society*, 2017, **139**, 17639-17648.

239. B. Saccà, R. Meyer, M. Erkelenz, K. Kiko, A. Arndt, H. Schroeder, K. S. Rabe and C. M. Niemeyer, *Angewandte Chemie International Edition*, 2010, **49**, 9378-9383.
240. K. Zhou, Y. Ke and Q. Wang, *Journal of the American Chemical Society*, 2018, **140**, 8074-8077.
241. A. A. Arora and C. de Silva, *Nano Reviews & Experiments*, 2018, **9**, 1430976.
242. P. Wang, T. A. Meyer, V. Pan, P. K. Dutta and Y. Ke, *Chem*, 2017, **2**, 359-382.
243. X. Shen, C. Song, J. Wang, D. Shi, Z. Wang, N. Liu and B. Ding, *Journal of the American Chemical Society*, 2012, **134**, 146-149.
244. J. Chao, Y. Lin, H. Liu, L. Wang and C. Fan, *Materials Today*, 2015, **18**, 326-335.
245. S. J. Tan, M. J. Campolongo, D. Luo and W. Cheng, *Nature Nanotechnology*, 2011, **6**, 268-276.
246. X. Lan and Q. Wang, *NPG Asia Materials*, 2014, **6**, e97-e97.
247. J. Sharma, R. Chhabra, C. S. Andersen, K. V. Gothelf, H. Yan and Y. Liu, *Journal of the American Chemical Society*, 2008, **130**, 7820-7821.
248. B. Ding, Z. Deng, H. Yan, S. Cabrini, R. N. Zuckermann and J. Bokor, *Journal of the American Chemical Society*, 2010, **132**, 3248-3249.
249. J. J. Schmied, M. Raab, C. Forthmann, E. Pibiri, B. Wünsch, T. Dammeyer and P. Tinnefeld, *Nature Protocols*, 2014, **9**, 1367.
250. A. Kuzyk, R. Schreiber, Z. Fan, G. Pardatscher, E.-M. Roller, A. Högele, F. C. Simmel, A. O. Govorov and T. Liedl, *Nature*, 2012, **483**, 311-314.
251. W. Liu, J. Halverson, Y. Tian, A. V. Tkachenko and O. Gang, *Nature Chemistry*, 2016, **8**, 867.
252. X. Shen, A. Asenjo-Garcia, Q. Liu, Q. Jiang, F. J. García de Abajo, N. Liu and B. Ding, *Nano Letters*, 2013, **13**, 2128-2133.
253. A. Cecconello, L. V. Besteiro, A. O. Govorov and I. Willner, *Nature Reviews Materials*, 2017, **2**, 17039.
254. X. Lan, Z. Chen, G. Dai, X. Lu, W. Ni and Q. Wang, *Journal of the American Chemical Society*, 2013, **135**, 11441-11444.
255. C. Rao, Z.-G. Wang, N. Li, W. Zhang, X. Xu and B. Ding, *Nanoscale*, 2015, **7**, 9147-9152.
256. P. Kühler, E.-M. Roller, R. Schreiber, T. Liedl, T. Lohmüller and J. Feldmann, *Nano Letters*, 2014, **14**, 2914-2919.
257. P. Zhan, T. Wen, Z.-g. Wang, Y. He, J. Shi, T. Wang, X. Liu, G. Lu and B. Ding, *Angewandte Chemie International Edition*, 2018, **57**, 2846-2850.
258. A. Samanta, Y. Zhou, S. Zou, H. Yan and Y. Liu, *Nano Letters*, 2014, **14**, 5052-5057.
259. A. Kuzyk, Y. Yang, X. Duan, S. Stoll, A. O. Govorov, H. Sugiyama, M. Endo and N. Liu, *Nature Communications*, 2016, **7**, 10591.
260. C. Zhou, X. Duan and N. Liu, *Nature Communications*, 2015, **6**, 8102.
261. L. Xin, M. Lu, S. Both, M. Pfeiffer, M. J. Urban, C. Zhou, H. Yan, T. Weiss, N. Liu and K. Lindfors, *ACS Photonics*, 2019, **6**, 985-993.
262. S. H. Ko, K. Du and J. A. Liddle, *Angewandte Chemie International Edition*, 2013, **52**, 1193-1197.
263. E. A. Hemmig, C. Creatore, B. Wünsch, L. Hecker, P. Mair, M. A. Parker, S. Emmott, P. Tinnefeld, U. F. Keyser and A. W. Chin, *Nano Letters*, 2016, **16**, 2369-2374.
264. N. Aissaoui, K. Moth-Poulsen, M. Käll, P. Johansson, L. M. Wilhelmsson and B. Albinsson, *Nanoscale*, 2017, **9**, 673-683.
265. J. Prinz, C. Heck, L. Ellerik, V. Merk and I. Bald, *Nanoscale*, 2016, **8**, 5612-5620.
266. T. Zhang, N. Gao, S. Li, M. J. Lang and Q.-H. Xu, *The Journal of Physical Chemistry Letters*, 2015, **6**, 2043-2049.
267. A. Kuzyk, R. Schreiber, H. Zhang, A. O. Govorov, T. Liedl and N. Liu, *Nature Materials*, 2014, **13**, 862.
268. R. Schreiber, N. Luong, Z. Fan, A. Kuzyk, P. C. Nickels, T. Zhang, D. M. Smith, B. Yurke, W. Kuang, A. O. Govorov and T. Liedl, *Nature Communications*, 2013, **4**, 2948.
269. A. Kuzyk, M. J. Urban, A. Idili, F. Ricci and N. Liu, *Science Advances*, 2017, **3**, e1602803.
270. M. J. Urban, C. Zhou, X. Duan and N. Liu, *Nano Letters*, 2015, **15**, 8392-8396.
271. P. Zhan, S. Both, T. Weiss and N. Liu, *Nano Letters*, 2019, **19**, 6385-6390.
272. M. Wang, J. Dong, C. Zhou, H. Xie, W. Ni, S. Wang, H. Jin and Q. Wang, *ACS Nano*, 2019, DOI: 10.1021/acsnano.9b06734.
273. L. Sun, Y. Gao, Y. Xu, J. Chao, H. Liu, L. Wang, D. Li and C. Fan, *Journal of the American Chemical Society*, 2017, **139**, 17525-17532.

274. S. Rinker, Y. Ke, Y. Liu, R. Chhabra and H. Yan, *Nature Nanotechnology*, 2008, **3**, 418-422.
275. G. P. Acuna, M. Bucher, I. H. Stein, C. Steinhauer, A. Kuzyk, P. Holzmeister, R. Schreiber, A. Moroz, F. D. Stefani, T. Liedl, F. C. Simmel and P. Tinnefeld, *ACS Nano*, 2012, **6**, 3189-3195.
276. N. V. Voigt, T. Tørring, A. Rotaru, M. F. Jacobsen, J. B. Ravnsbæk, R. Subramani, W. Mamdouh, J. Kjems, A. Mokhir, F. Besenbacher and K. V. Gothelf, *Nature Nanotechnology*, 2010, **5**, 200-203.
277. S. Helmig, A. Rotaru, D. Arian, L. Kovbasyuk, J. Arnbjerg, P. R. Ogilby, J. Kjems, A. Mokhir, F. Besenbacher and K. V. Gothelf, *ACS Nano*, 2010, **4**, 7475-7480.
278. I. H. Stein, C. Steinhauer and P. Tinnefeld, *Journal of the American Chemical Society*, 2011, **133**, 4193-4195.
279. H. Gu, J. Chao, S.-J. Xiao and N. C. Seeman, *Nature*, 2010, **465**, 202-205.
280. M. Liber, T. E. Tomov, R. Tsukanov, Y. Berger and E. Nir, *Small*, 2015, **11**, 568-575.
281. K. Lund, A. J. Manzo, N. Dabby, N. Michelotti, A. Johnson-Buck, J. Nangreave, S. Taylor, R. Pei, M. N. Stojanovic, N. G. Walter, E. Winfree and H. Yan, *Nature*, 2010, **465**, 206-210.
282. Y. Ke, S. Lindsay, Y. Chang, Y. Liu and H. Yan, *Science*, 2008, **319**, 180-183.
283. D. Koirala, P. Shrestha, T. Emura, K. Hidaka, S. Mandal, M. Endo, H. Sugiyama and H. Mao, *Angewandte Chemie International Edition*, 2014, **53**, 8137-8141.
284. A. Kuzuya, Y. Sakai, T. Yamazaki, Y. Xu and M. Komiyama, *Nature Communications*, 2011, **2**, 449.
285. Y. Ke, T. Meyer, W. M. Shih and G. Bellot, *Nature Communications*, 2016, **7**, 10935.
286. N. A. W. Bell and U. F. Keyser, *FEBS Letters*, 2014, **588**, 3564-3570.
287. D. Branton, D. W. Deamer, A. Marziali, H. Bayley, S. A. Benner, T. Butler, M. Di Ventra, S. Garaj, A. Hibbs, X. Huang, S. B. Jovanovich, P. S. Krstic, S. Lindsay, X. S. Ling, C. H. Mastrangelo, A. Meller, J. S. Oliver, Y. V. Pershin, J. M. Ramsey, R. Riehn, G. V. Soni, V. Tabard-Cossa, M. Wanunu, M. Wiggin and J. A. Schloss, *Nature Biotechnology*, 2008, **26**, 1146-1153.
288. S. Hernández-Ainsa, N. A. W. Bell, V. V. Thacker, K. Göpfrich, K. Misiunas, M. E. Fuentes-Perez, F. Moreno-Herrero and U. F. Keyser, *ACS Nano*, 2013, **7**, 6024-6030.
289. B. Shen, M. A. Kostiainen and V. Linko, *Langmuir*, 2018, **34**, 14911-14920.
290. H. K. K. Subramanian, B. Chakraborty, R. Sha and N. C. Seeman, *Nano Letters*, 2011, **11**, 910-913.
291. M. Tintoré, I. Gállego, B. Manning, R. Eritja and C. Fàbrega, *Angewandte Chemie*, 2013, **125**, 7901-7904.
292. S. E. Ochmann, C. Vietz, K. Trofymchuk, G. P. Acuna, B. Lalkens and P. Tinnefeld, *Analytical Chemistry*, 2017, **89**, 13000-13007.
293. C. Heck, Y. Kanehira, J. Kneipp and I. Bald, *Angewandte Chemie International Edition*, 2018, **57**, 7444-7447.
294. Y. Huang, M.-K. Nguyen, A. K. Natarajan, V. H. Nguyen and A. Kuzyk, *ACS Applied Materials & Interfaces*, 2018, **10**, 44221-44225.
295. V. Masciotti, L. Piantanida, D. Naumenko, H. Amenitsch, M. Fanetti, M. Valant, D. Lei, G. Ren and M. Lazzarino, *Nano Research*, 2019, **12**, 2900-2907.

Chapter 2

Methodology

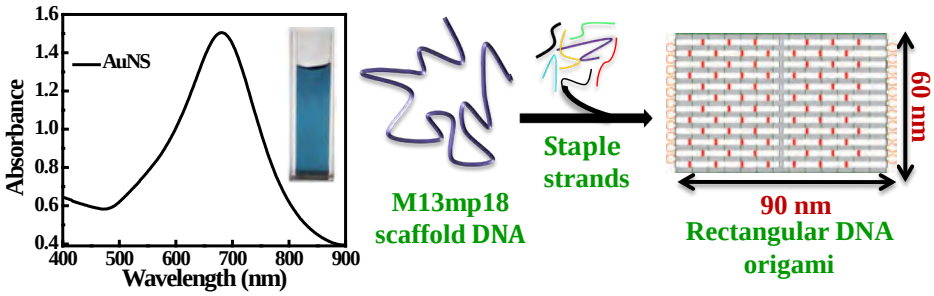

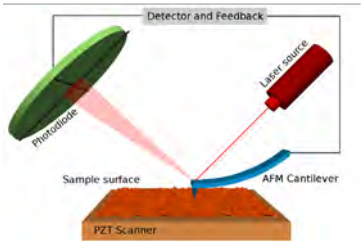

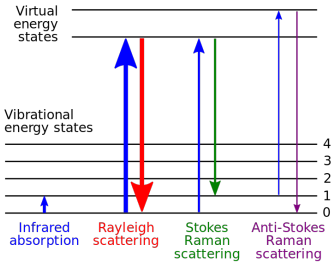

This chapter describes the synthesis of anisotropic shaped metal nanoparticles, DNA origami, fluorescent gold nanoclusters, and quantum dots. Further, a brief overview of the basic principles and theories of the characterization tools and the spectroscopic techniques used for carrying out the work included in this thesis has been given.

2.1. Synthesis of Au nanoparticles

In 1857 Michael Faraday described the synthetic protocol for the production of colloidal Au nanoparticles. He used white phosphorus for the reduction of gold salt and carbon disulfide was used as a stabilizing agent.[1] In 1951, Turkevich et al. proposed a method for the synthesis of spherical Au nanoparticles using citrate as reducing agent [2-4] which was further refined by Frens.[5] It is now a widespread method is most commonly called citrate reduction method. Since then a number of synthetic methods have been proposed for the synthesis of spherical and anisotropic shaped gold nanoparticles.

2.1.1. Synthesis of anisotropic shaped metal nanoparticles

The synthetic strategies adopted for the synthesis of anisotropic shaped nanoparticles can be classified into two main groups: 1) top-down, and 2) bottom-up.[6] The top-down approach involves carving of nanoscale structures from larger or bulk materials by controlled removal which is achieved through lithographic techniques[7, 8] or chemical based routes.[9, 10] Although this strategy has contributed to the growth of the field, its success is limited by associated key issues such as high cost of fabrication, varied particle shape and geometry, and broad size distribution.[11] Wet chemical synthesis is potential bottom-up method for the synthesis of anisotropic shaped nanoparticles which provides control over the morphology and polydispersity. In bottom-up method, at first, nucleation takes place which is followed by thermodynamically or kinetically controlled growth mechanisms. Simple reduction of metal salts tends to nucleate and grow into thermodynamically stable nanoparticles which results in the formation of minimum energy spherical or near-spherical structures. In the case of kinetically controlled growth, directional growth over low energy crystallographic facets results in the anisotropic growth. This is achieved by selective adsorption of polymers, ligands, surfactants or ions on selective facets.[12] Lofton and Sigmund proposed that the presence of twin planes in the metal seeds results in anisotropic growth of nanoparticles.[13]

Till now different chemical synthetic approach has been used for the synthesis of anisotropic shaped metal nanoparticles such as seed-mediated synthesis,[14, 15] polyol synthesis,[16] template

mediated synthesis,[17] electrochemical,[18] and photoinduced synthesis.[19] Among all, seed-mediated approach is the most widely used method that resulted in metal nanostructures of different shapes such as rods, wires, triangles, stars, and flowers.

2.1.1.1. Seed mediated synthesis

Seed mediated synthesis was first demonstrated by Jana et al for the synthesis of Au nanorods (Au NRs).[20, 21] Since then it has been used for the synthesis of metal nanoparticles of different shapes such as nanorods, nanostars, nanocube and so on. A typical seed mediated method generally involves two steps, at first, small spherical nanoparticles (seeds) are synthesized by reduction of metal salts using a strong reducing agent. This is followed by the second step which involves the growth of seed nanoparticles into the desired shape in the presence of a surfactant or shape directing agent and a mild reducing agent such as ascorbic acid. The role of surfactant in the growth solution is to go and preferentially bind to certain crystal faces of the seed, thus inhibiting growth at those facets. Poly(vinylpyrrolidone) (PVP) and hexadecylcetyltrimethylammonium bromide (CTAB) are the most widely used surfactants for the synthesis anisotropic shaped nanoparticles. [22-25] Among all the anisotropic shapes synthesis of Au nanostars has been driven by the interest on their structural and optical properties.[26] Thus, in last few years a number of wet chemical synthesis methods for the synthesis of Au nanostars have been proposed. [27] Some of the proposed methods are inspired by the well-known seeded growth process employed for the synthesis of Au NRs. For example, Kumar et al. used poly(vinylpyrrolidone) (PVP) in combination with *N*,*N*-dimethylformamide (DMF) for the seeded growth of Au nanostars.[22] Here, preformed PVP capped Au seeds restricted the growth along the (110) direction that resulted in flower like morphology. With decreasing concentration of Au seeds in the growth solution the nanostars were getting smaller with a lower number of spikes. Wu et al. reported a seed mediated synthesis of Au nanostars having five symmetrical branches using cetyltrimethylammonium chloride surfactant as a shape directing agent.[28] Use of surfactant limits the application of Au nanostars due to associated toxicity, aggregation after washing, and difficult bioconjugation. Therefore, Au nanostars synthesized using surfactant-free methods are of particular interest for the development of further applications. Yuan et al.[29] proposed a simple surfactant free seed mediated wet chemistry method for the synthesis of highly monodisperse Au nanostars (Shown in scheme 2.1). $HAuCl_4$ is reduced using ascorbic acid in the presence of $AgNO_3$ and Au seeds under acidic conditions. In the growth solution presence of silver nitrate ($AgNO_3$) and chloride ions due to hydrochloric acid assisted in the formation of Au nanostars.[30, 31] The size of the nanostars was found to be tunable by varying the

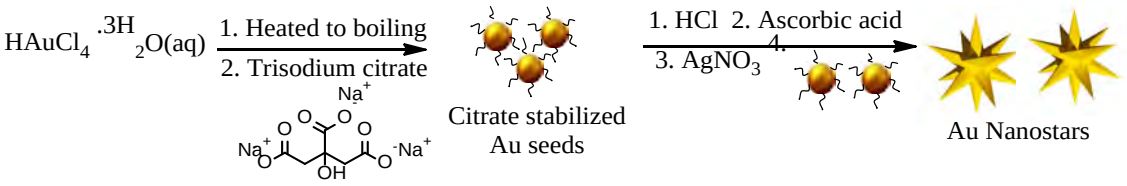

Scheme 2.1. Schematic depiction of surfactant-free seed mediated synthesis of Au nanostars.

concentration of seeds in the growth solution.

For carrying out the work included in this thesis, surfactant free seed mediated synthesis has been used for the synthesis of Au nanostars and Au@Ag nanostars.

2.1.2. Synthesis of Au nanoclusters

Owing to their strong luminescence, low toxicity, good biocompatibility, ultrasmall size and increased lifetime of Au NCs, till now several synthetic routes have been developed for their synthesis.[32, 33] Synthetic strategies used for the synthesis of Au−thiolate NCs are generally grouped into two routes: "Atoms to Clusters" and "Nanoparticles to Clusters". The nanoparticles to clusters route is basically a top to bottom strategy that involves etching of larger Au NPs to small nanoclusters using ligands such as phosphines, thiols, amines, and polymers.[33-35] This method resulted in Au NCs with high quantum yield but due to slow decomposition kinetics, the reaction generally requires a longer time for completion. The other route termed as "atoms to clusters" involves direct reduction of gold precursor using a strong reducing agent such as $NaBH_4$,[36, 37] and a series of templates such as dendrimers,[38] proteins,[39, 40] polymers,[41, 42] and DNA.[43, 44]

Glutathione (GSH), is a tripeptide (N-γ-glutamyl-cysteinyl-glycine) that has been used for preparing water soluble, highly stable and luminescent Au NCs.[37, 45] Luo et al. reported the synthesis of luminescent Au NCs using GSH as reducing-cum-protecting agent.[46] The reaction mechanism can be divided into three stages (Scheme 2.2). During the first stage of reaction, Au(III) is reduced to Au(I) by the thiol group of GSH [47, 48] followed by coordination of Au(I) to thiol group of GSH to form Au(I)-thiolate complex and Au(I)-X complexes where X stands for carbonyl group of GSH or small anions such as chloride present in the solution. In the second stage Au(I)-X complex reduces to Au(0) atoms followed by formation of Au(0)-on-Au(I)−thiolate intermediates due to high affinity between Au(0) atoms and Au(I).[46] In the last stage, Au(0)-on-Au(I)-thiolate intermediates by collision and fusion leads to the formation of highly luminescent Au(0) core and Au(I) −thiolate nanoclusters.

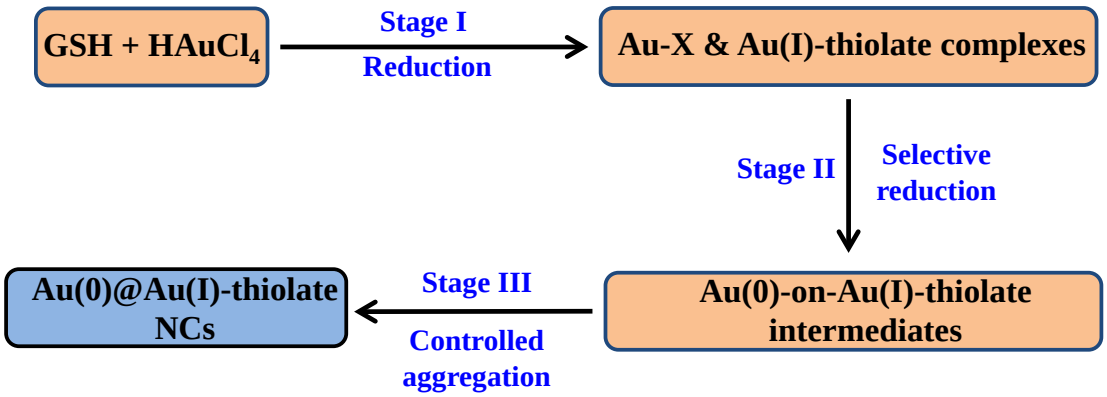

Scheme 2.2. Schematic of synthesis of highly luminescent Au(0)@Au(I)−thiolate nanoclusters. (Adapted with permission from ref.[46] 2012, American Chemical Society)

Similar protocol has been followed for the synthesis of GSH capped Au NCs and is reported in chapter 5 of this thesis.

2.2. Synthesis of quantum dots (QDs)

The synthetic routes used for the synthesis of QDs can be broadly classified into two categories "Top – Down" and "Bottom-Up" approach. Top-down approaches involves thinning down a bulk semiconductor to nanoscale size using high end techniques like electron beam lithography, reactive ion etching or wet chemical etching. [49] High cost of the synthesis and inability to introduce structural imperfections are some of the major drawbacks of these techniques.[49] Bottom-up approaches for the QD synthesis are further divided into two sub-categories wet chemical synthesis and vapor phase methods. In wet chemical methods two or more solutions are mixed together followed by nucleation and limited growth of the nanocrystals. Size, shape, composition, and emission properties of the QDs can be varied by changing several parameters such as temperature, precursor concentration, stabilizers and solvent system. The processes commonly included in this category are microemulsion based synthesis, sol-gel synthesis, and heat up decomposition. [49, 50] Heating-up methods, first described by Murray et al.,[51] are now widely used for the synthesis of monodisperse QDs. In this method reaction mixtures are prepared at room temperatures and further heated to high temperatures which result in highly monodisperse QDs. Scheme 2.3. illustrates the formation mechanism of QDs using heating-up methods. At first, with thermal decomposition of the reactants, small crystal nuclei's are formed a process generally termed as nucleation. As the reaction progresses, small sized nanocrystals are formed followed by their further growth and finally stopping when the maximum level is attained.

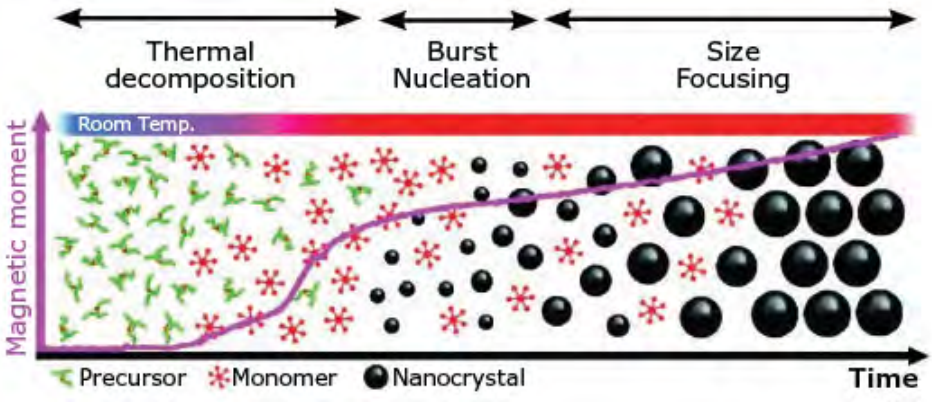

Scheme 2.3. Scheme depicting the formation mechanism of QDs using heating-up methods. (Adapted from ref.[52], 2007 American Chemical Society)

Among all the developed methods aqueous phase synthesis is important for biological applications where the synthesized QDs are required to be further modified. Due to toxicity associated with heavy metal chalcogenides based QDs,[53] methods are being developed to synthesize biocompatible and non-toxic quantum dots such as carbon and silicon QDs. In this thesis, Silicon QDs were synthesized by heating up the reaction mixture hydrothermally and is reported in chapter 5.

2.3. Synthesis of rectangular DNA origami

To assemble rectangular DNA origami, M13mp18 single stranded bacteriophage genomic DNA having 7249 nucleotides was used as a scaffold DNA and 213 short staple DNA sequences were used to direct the folding of the scaffold DNA (Scheme 2.4). The design was the same as the one outlined by Paul Rothemund in his first paper on DNA origami. [54]

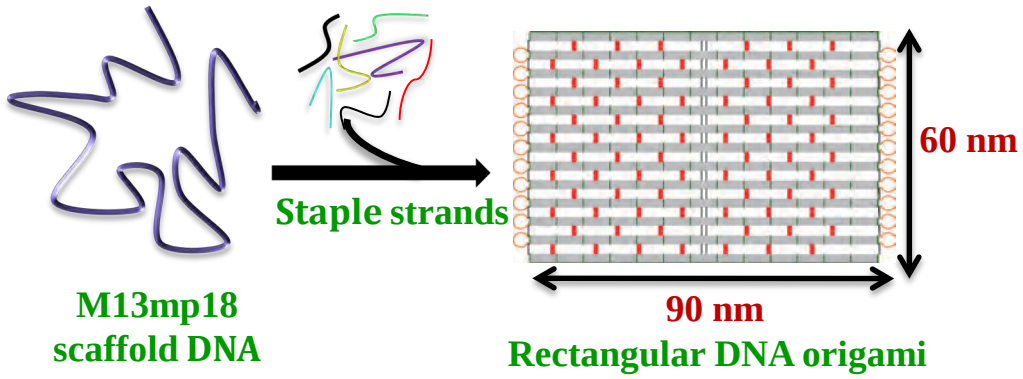

Scheme 2.4. Schematic depiction of the synthesis of rectangular DNA origami.

Self-assembly of DNA origami structures was done using thermal annealing method. The reaction was a one-pot reaction in which scaffold DNA along with folding staple strands was at first heated to 90 ºC followed by cooling down to 20 ºC. A single-stranded scaffold DNA has numerous internal secondary and tertiary structures owing to existence of random complementary bases.[55] These structures hinder the binding of the staple strands at their predesigned positions at room temperature. Heating the reaction mixture at 90 ºC removes all the internal structures leaving the scaffold DNA stretched.[56] On slow cooling, all the staples go and bind to scaffold DNA to reach the designed structure with the minimum energy configuration. Folding of the DNA origami structures was carried out in a Bio-Rad PCR thermocycler (Model no.C1000 Touch) with a 1.5-hour folding program. The volume of folding reaction mixture was 50 µl in which the final concentration of scaffold DNA, modified and unmodified staple strands were 2, 10, and 20 nM respectively in 1xTAE-Mg^{2+} buffer (40 mM Tris, 20 mM Acetic acid, 2 mM EDTA and 12.5 mM Magnesium chloride, pH 8.0). The concentration of folding staples was taken in excess with respect to the scaffold concentration so that all the scaffold strands have access to all required staple strands, resulting in the high throughput of correctly folded structures. The presence of divalent cations such as Mg^{+2} in 10–20 mM range helps in the folding of origami structures by counteracting the negative charges of the phosphates in the DNA backbone thereby reducing the repulsion between scaffold and staple strands.[56] For rectangular DNA origami 12.5 mM of Mg^{+2} concentration is generally considered suitable for folding.

Rectangle DNA origami has many parallel blunt-ends along their left and right edges. Due to strong stacking interactions on blunt-ended helices, DNA origami structures get aggregated.[54] To avoid unwanted stacking the edge staples (12 each side) can be omitted out, this leaves the scaffold DNA unfolded along the edges but prevents aggregation.[57] Another possible solution is to add poly Thymine hairpin loops to edge staples. The incorporation of poly T sequences in edge staples disaggregates DNA nanostructures by reducing interorigami π-stacking interactions.[58] In our case, we wanted to dimerize rectangular DNA origami, so to block one side of monomer leaving the other end free we have used poly T modified edge staples. The details of edge sequences are given in tables 2 and 3 of appendix A.

2.3.1. Dimerization of rectangular DNA origami

The size of individual DNA origami structures is determined by the size of scaffold DNA. For assembling large nanoparticles with different stoichiometry and interparticle gaps

polymerization of DNA origami is required. Among all the different strategies adopted [57, 59] one demonstrated by Rajendran et al.[58] appeared to be the most efficient approach because it enabled assembly without an intertile gap and in high yield. The scheme of dimerization is illustrated in scheme 2.5. The two origami monomers A and B are connected by introducing 24 bridging staples. A part of each bridging strand was complementary to the scaffold sequence on one edge of the origami rectangle and another part to the opposing edge, which enables the seaming of two origami units without any gap. To avoid uncontrolled polymerization, the edges of the origami unit opposite the junction side were blocked using poly T modified edge staples. We have used the same strategy previously reported by Liber et al.[60] for the dimerization of rectangular DNA origami for carrying out the work included in this thesis.

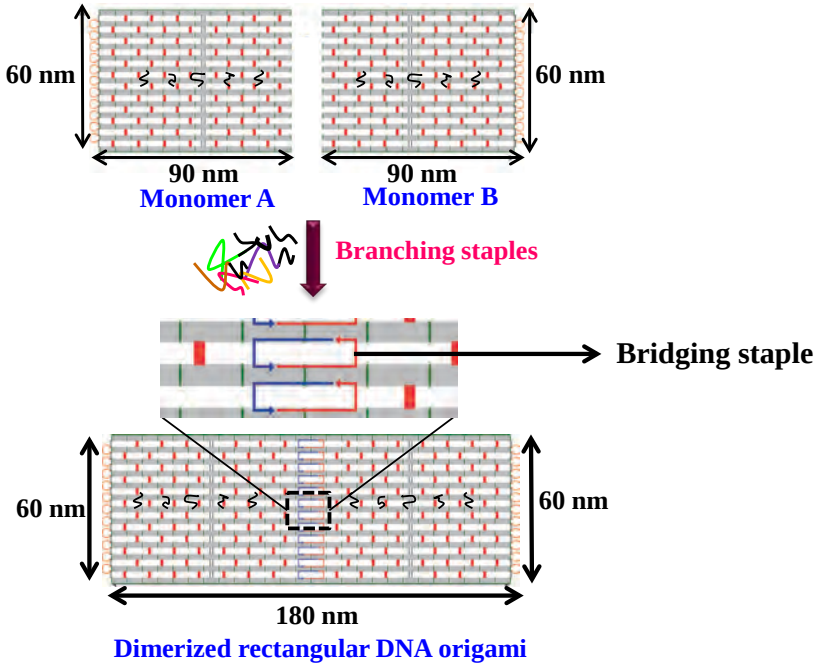

Scheme 2.5. Schematic depiction of the dimerization of rectangular DNA origami.

2.4. Fabrication of plasmonic nanoantennas

Till now several top-down to bottom-up fabrication techniques have been used for the fabrication of plasmonic nanoantennas. [6, 61-63] Since its inception, DNA origami has emerged as a powerful technique to self- assemble plasmonic nanoparticles in a programmable fashion.[64] In DNA origami, the sequence of each folding staple is different and its position is designed to bind to a specific location along the scaffold.[65] Each folding staple sequence can be modified and extended to produce an independent binding site on the template.[66] Nanoparticles functionalized with

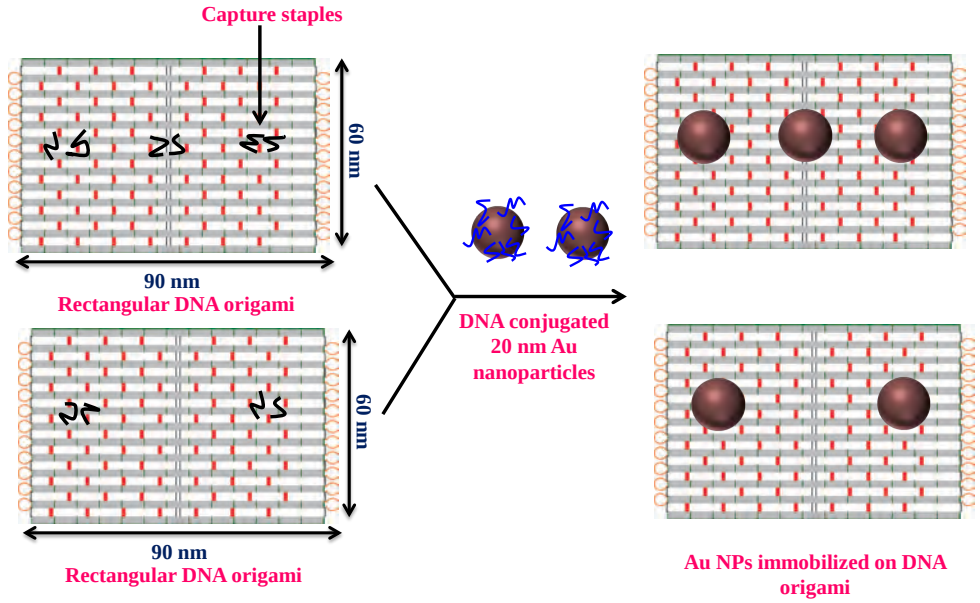

Scheme 2.6. Schematic depiction of immobilization of Au nanoparticles on DNA origami with different interparticle gaps and stoichiometry.

complementary sequence to the linker DNA go and bind to the specific position on pre-assembled DNA origami template. By changing the position of capture sequences, interparticle gap sizes and stoichiometry can be very easily tuned (as shown in scheme 2.6). Because of this versatility, DNA origami has been used as a pegboard to assemble metallic nanoparticles,[67-69] quantum dots [70, 71] and biomacromolecules[72, 73] in predefined geometries.

In this thesis, dimerized rectangular DNA origami was used for designing Au nanostar and Au@Ag nanostar dimer nanostructures which were further used for single molecule spectroscopic applications. Single dye molecule was incorporated in the conjunction region between the nanostars by modifying one the branching staples as described in chapter 3 and chapter 4. Single thrombin protein was immobilized on the origami template by introducing thrombin binding aptamers on the origami template by modifying the branching staples in chapter 6.

2.5. Characterization techniques

2.5.1. UV-Vis spectroscopy

UV-Vis spectroscopy is a quantitative analytical characterization technique concerned with a sample containing species that absorb light in the near-ultraviolet (180–390 nm) or visible (390–780 nm). The wavelength of absorption depends on the energy required for exciting the

molecules from the ground state to the excited state. When less energy is required, the wavelength of absorption is higher and the wavelength is lower if more energy is needed for the excitation. UV-Vis spectrophotometer principle follows the Beer-Lambert law. This law states that whenever a beam of monochromatic light is passed through a solution with an absorbing substance, the decreasing rate of the radiation intensity along with the thickness of the absorbing solution is actually proportional to the concentration of the solution and the incident radiation.

Beer-Lambert law is expressed through equation 2.1.

$$A = log_{10}\left(\frac{I_0}{I}\right) = \varepsilon cl \qquad \text{Equation 2.1}$$

Where A is the measured absorbance, I_o is the intensity of the incident light upon a sample cell, I is the transmitted intensity, *l* is the path length through the sample, *c* the concentration of the absorbing species and ε is a constant known as molar absorptivity or extinction coefficient. This constant is a fundamental molecular property in a given solvent, at a particular temperature and pressure, and has units of $M^{-1}cm^{-1}$.

The electrons in a molecule can be of one of three types: namely σ (single bond), π (multiple-bond), or non-bonding (n-caused by lone pairs). Upon shining with ultraviolet or visible light

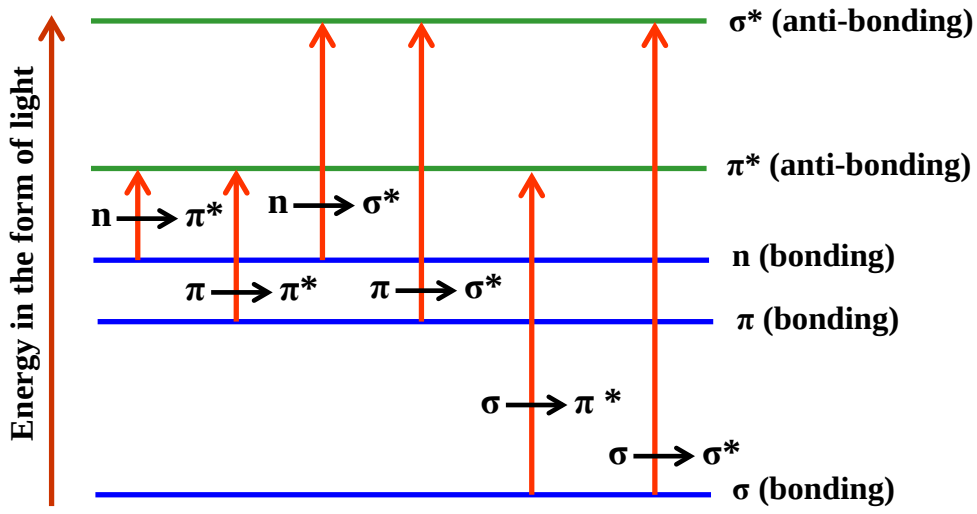

Figure 2.1. Electronic transitions between the bonding and anti-bonding electronic states.

these molecules can absorb energy and excite these electrons from the highest occupied molecular orbital (HOMO) to the lowest unoccupied molecular orbital (LUMO). There are four possible types of transitions (π–π*, n–π*, σ–σ*, and n–σ*) that take place when light energy is

absorbed in UV-Visible range (Figure 2.1). A UV-Vis spectrophotometer records the degree of absorption by a sample at different wavelengths and the resulting plot of absorbance (A) versus wavelength (λ) is known as a spectrum. The wavelength at which the sample absorbs the maximum amount of light is known as λ_{max}.

In this thesis, UV-visible spectroscopy was used for recording UV-visible absorption spectra of spherical Au nanoparticles, Au nanostars, Au@Ag bimetallic nanostars, and Au nanoclusters. It was also used for determining time-dependent absorption spectra for the conversion of p-nitrophenol to p-aminophenol. All the UV−Vis spectra were recorded using a Shimadzu UV-2600 spectrophotometer.

2.5.2. Dynamic light scattering (DLS) study

Dynamic light scattering also referred to as photon correlation spectroscopy or quasi-elastic light scattering technique is used for measuring the size and size distribution of molecules and particles typically in the submicron region. Dynamic light scattering (DLS) measures the Brownian motion of dispersed particles and relates this to the size of the particles. Brownian motion is the random movement of particles which can be described as: when particles are dispersed in a liquid they move randomly in all directions and are constantly colliding with solvent molecules. These collisions result in transferring of energy among the particles, which induces particle movement. This energy transfer has a greater effect on smaller particles as a result, smaller particles move at higher speeds than larger particles. The velocity of the Brownian motion is defined by a property known as the translational diffusion coefficient (usually given the symbol, D). The relation between the speed of the particles and the particle size is given by the Stokes-Einstein equation (Equation 2.2).

$$d(H) = \frac{kT}{3\pi\eta D} \qquad \text{Equation 2.2}$$

Where d(H) is the hydrodynamic diameter, k is Boltzmann's constant, D is translational diffusion coefficient, η is the viscosity of sample medium, and T stands for temperature of the system. A typical DLS instrument (Figure 2.2) consists of a single frequency laser which is directed to the sample contained in a cuvette. The incident laser gets scattered in all directions and is detected at a certain angle over time. The scattered light is used for determining the diffusion coefficient and the particle size by the Stokes-Einstein equation (Equation 2.2).

In the present thesis, dynamic light scattering (DLS) measurements were performed to determine the hydrodynamic diameter and size distribution of Au nanoparticles and Si QDs.

Dynamic light scattering (DLS) measurements were performed on a Malvern zetasizer nano ZSP instrument with a HeNe laser.

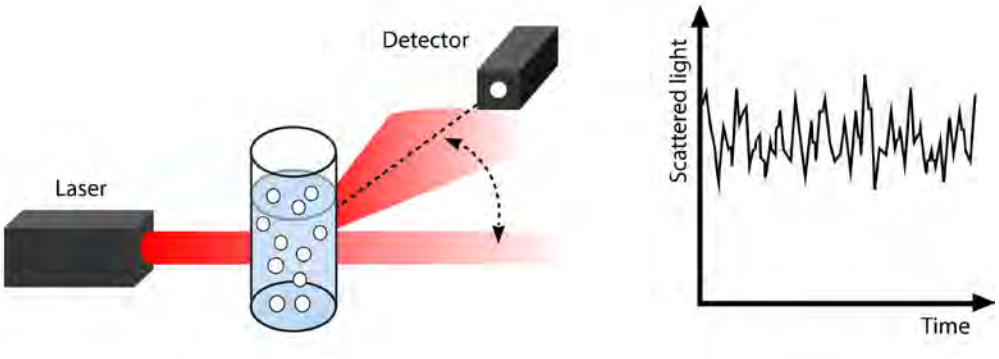

Figure 2.2. Setup of a DLS measurement system.[74]

2.5.3. Photoluminiscence (PL) spectroscopy

Photoluminescence spectroscopy, often referred to as PL, is emission of light or luminescence from any form of matter after the absorption of photons. The transition of electrons between electronic states that occur between the absorption and emission of light is usually explained by the Jablonski diagram (Figure 2.3).[75] In figure 2.3 S_0, S_1, S_2, and T_1 denote the singlet ground, first, and second and first triplet electronic states respectively. After absorption of light, a fluorophore is excited from the ground state to higher vibrational levels of the first S_1 or second S_2 singlet energy state in about 10^{-15} s. Following light absorption, several processes usually occur with varying probabilities.

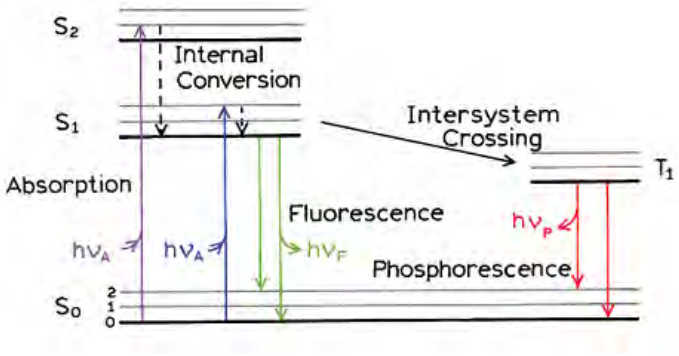

Figure 2.3. Jablonski diagram showing possible electronic transitions. (Reprinted with permission from Ref.[75]*, 2006, Springer Science Business Media, LLC)*

Fluorescence emission occurs predominantly from the lowest singlet state (S_1), so electrons excited to higher singlet states will be relaxed to lowest vibrational energy level of the first

excited state i.e. S_1. This process is known as internal conversion or vibrational relaxation and generally occurs in a 10^{-12} s or less. After coming down to lowest excited singlet state a molecule finally relaxes to ground state, if the relaxation process is accompanied by emission of a photon, the process is formally described as fluorescence. Fluorescence lifetimes are typically near 10^{-8} s. Fluorescence typically occurs at lower energies or longer wavelengths. This phenomenon was first observed by Sir. G. G. Stokes in 1852 at the University of Cambridge and is called as Stokes shift.[76] Several other relaxation pathways compete with the fluorescence emission process, the excited fluorophore can collide with another molecule undergo a spin conversion to the first triplet state T_1 by phenomenon known as intersystem crossing. Transitions from the triplet excited state to the singlet ground state results in emission of a photon through process called phosphorescence. The average lifetime for phosphorescence ranges from 10^{-4}–10^{4} s. Phosphorescence is generally shifted to longer wavelengths relative to the fluorescence. The emission spectrum of a fluorophore is usually a mirror image of its absorption spectrum. This is due to the fact that the spacing between the vibrational levels of excited state and ground state are similar and electronic transition from the ground state to excited state does not alter the geometry of the nucleus. The end result is that PL emission spectra display similar, but reversed, vibrational structures to those observed in the absorption spectra.

In this thesis, emission spectra of Texas red (TR), Fluorescein (FAM), Cyanine 3 (Cy3) dye, Au NCs, and Si QDs were recorded using an FS5 steady state fluorescence spectrometer from Edinburg Instruments.

2.5.4. Total internal reflection fluorescence microscopy (TIRFM)

TIRFM is a well-established single molecule detection technique that utilizes the phenomenon of total internal reflection for inducing an evanescent wave or field in a nanometer regime of the sample near to the interface. An incoming light gets totally reflected from an interface when it enters a medium having a less refractive index at an incident angle greater than the critical angle. The physics behind total internal reflection can be explained using figure 2.4a. The angle of incidence of the incident light is Θ_I, n_2 and n_1 are the refractive indexes of the glass slide and water respectively.

The critical angle (Θ_c) is given by equation 2.3.

$$\Theta_c = sin^{-1}\left(\frac{n_1}{n_2}\right) \qquad \text{Equation 2.3}$$

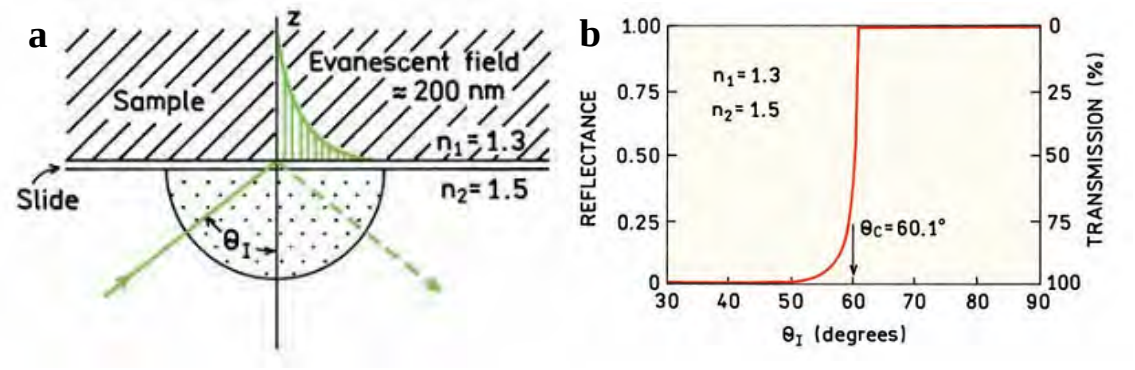

Figure 2.4. (a) Optical geometry for total internal reflection and (b) calculated reflectance and transmittance for n_2 = 1.5 and n_1 = 1.3. (Reprinted with permission from ref. [77]2006 Springer Science Business Media, LLC)

When $\Theta_I < \Theta_c$ most of the incident light gets transmitted. Total internal reflection occurs when $\Theta_I > \Theta_c$. Despite getting totally reflected the incident beam penetrates a short distance into the sample at the glass water interface. This restricted illumination of the sample along the z -axis reduces the observing volume making single molecule detection feasible. The intensity of the penetrating light is given by equation 2.4.

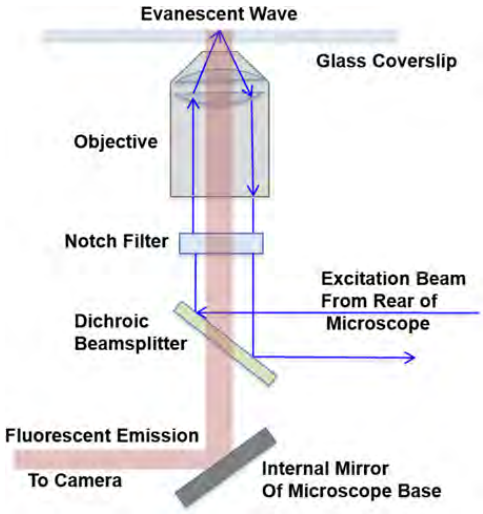

Figure 2.5. Optical setup of a TIRFM. (Reprinted with permission from ref.[78], 2016 Morgan & Claypool Publishers)

$$I(z) = I(0)\exp(-\frac{z}{d}) \qquad \text{Equation 2.4}$$

The decay constant is given by equation 2.5.

$$d = \frac{\lambda_0}{4\pi}(n_2^2 sin\theta_2 - n_1^2)^{-\frac{1}{2}}$$ Equation 2.5

Figure 2.4b shows the calculated reflectance and transmittance as a function of the incident angle of light of wavelength 600 nm. For an incident angle of 70º d can be calculated as 73.3 nm. Figure 2.5 shows the schematic of a typical TIRF microscope. The sample is excited using laser through a prism such that it undergoes total internal reflection illuminating a small region of the sample. The emitted light is collected by an objective and an image is created using a CCD camera.

In this thesis, TIRF microscope was used for carrying out single molecule fluorescence enhancement studies as described in chapter 4. Single molecule measurements were done using oil immersion Nikon TIRF objective (100× magnification) mounted on a custom built inverted optical microscope using 532 nm laser excitation. For separating the excitation and emission light a 532 nm high pass dichroic (AHF Analysentechnik) was used. Single molecule photon events were recorded using Andor EMCCD iXon Ultra at the frame rate of 17 MHz and exposure time of 50 ms. The time trajectories were recorded and analyzed using the Andor Solis Software. The image area of only 128 × 128 pixels was taken from the total 512 × 512 pixels of the whole sensor of EMCCD.

2.5.5. Raman spectroscopy

Raman spectroscopy named after Indian physicist C.V.Raman is a spectroscopic technique based on inelastic scattering of monochromatic light usually from a laser source. When light interacts with matter, the incoming photons may get absorbed, scattered or may not interact with

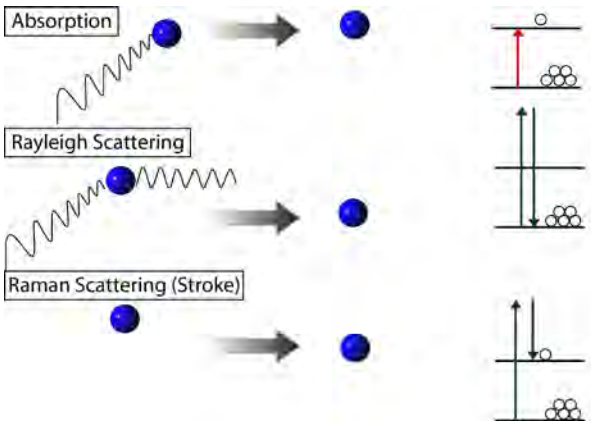

Figure 2.6. Schematic depiction of absorption, Rayleigh, and Raman scattering phenomenon.

the material (Figure 2.6). If the scattered photons have almost the same energy as that of incident photons, this scattering process is regarded as elastic scattering and is termed as Rayleigh scattering. If during the scattering process nuclear motion is induced, energy is transferred from the incident photon to the molecule or from the molecule to the scattered

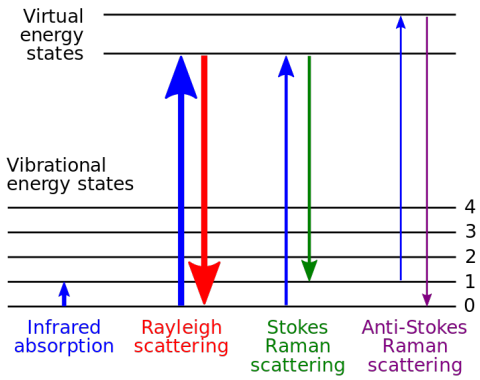

Figure 2.7. Energy level diagram showing the states involved in Raman spectra. (Image taken from Wikipedia).

photon. As a result the photons scatter inelastically i.e the energy of the scattered photon is less or more than that of the incident photons. This scattering process is termed as Raman scattering (Figure 2.7). If the resulting frequency of the scattered photon is reduced it is called stokes frequency and if it goes up it is called antistokes frequency. Raman scattering is an inherently weak process in that only one in every 10^6 –10^8 photons which scatter is Raman scattered. Not every molecule or vibrations are Raman active, vibrations that result in a change in the polarizability ellipsoid show intense Raman scattering. Usually, symmetric vibrations cause the largest changes and give the greatest scattering.

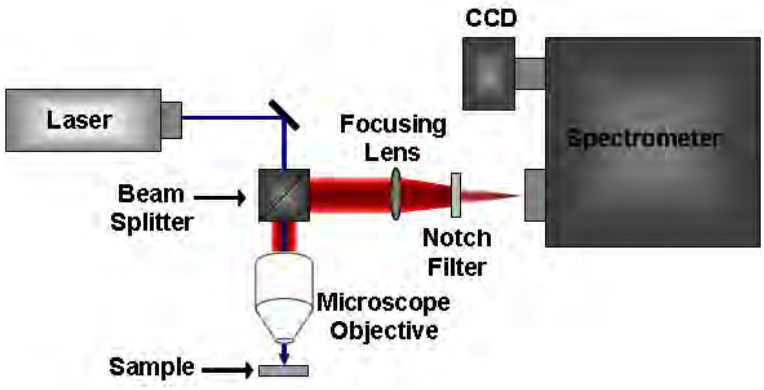

Figure 2.8. Components of a Raman microscope.[79]

A Raman system typically consists of four major components (Figure 2.8) namely, a laser excitation source, sample illumination system and light collection optics, wavelength selector (filter or spectrophotometer), and detector (photodiode array, CCD or PMT). A sample is normally illuminated with a laser beam in the ultraviolet (UV), visible (Vis) or near infrared (NIR) range. Scattered light is collected with a lens and is sent through interference filter or spectrophotometer to obtain Raman spectrum of a sample.

In this thesis, confocal Raman microscope was used for carrying out all the single molecule surface enhanced Raman spectroscopic measurements. Confocal Raman microscope (Witec alpha 300 R) equipped with an upright optical microscope (Zeiss) was used throughout this study. The measurements were performed in air using lasers having wavelength of 532 and 633 nm using 100 × objective (NA = 0.9).

2.5.6. Time correlated single photon counting (TCSPC)

Time-correlated single photon counting (TCSPC) is a well-established technique to measure fluorescence lifetime. In TCSPC measurements, a single photon coming from the sample is detected and its time of arrival is correlated to the pulsed laser used for excitation. By using a pulsed laser with a high repetition rate, this process can be repeated many times so that a photon distribution and the spatial coordinates are built up over time. Figure 2.9 describes the principle

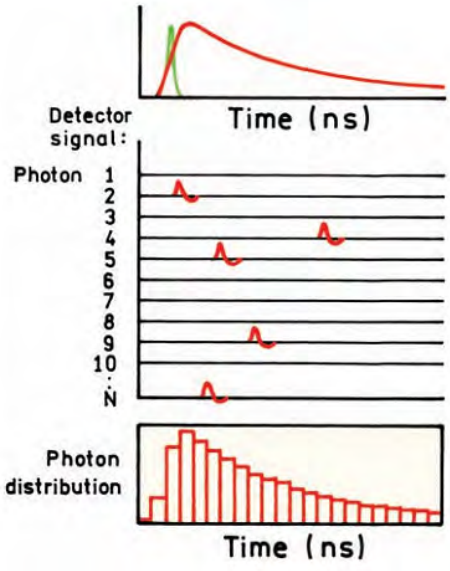

Figure 2.9. Principle of TCSPC. (Reprinted with permission from Ref.[75],2006 Springer Science Business Media, LLC)

of TCSPC. The sample is excited with a pulse of light, resulting in the waveform shown at the top of the figure 2.9. This waveform is due to simultaneous excitation of many fluorophores and detection of numerous photons. However, for TCSPC measurements the conditions are adjusted such that only one photon or less than one photon is detected per pulse of the laser. In fact, the detection rate is typically 1 photon per 100 excitation pulses. The time is measured between the excitation pulse and the observed photon and stored in a histogram. Time resolved fluorescence measurements were performed using a picosecond time correlated single photon counting (TCSPC) system from Edinburgh instruments (Model: FL920). A picosecond diode laser (Model: EPL375) with an excitation wavelength of 375 nm was used to excite the sample. The repetition rate was 5 MHz. The signals were collected using a PMT detector. The system has a pulse width of 60.4 ps. The fluorescence decay was described as a sum of exponential functions (Equation 2.6):

$$D(t) = \sum_{i=1}^{n} a_i \exp\left(\frac{-t}{\tau_i}\right) \qquad \text{Equation 2.6}$$

Where $D(t)$ is the normalized fluorescence decay, τ_i are the fluorescence lifetimes of various fluorescent components and a_i are the normalized pre-exponential factors. The amplitude weighted lifetime is given by equation 2.7.

$$\langle \tau \rangle = \sum_{i=1}^{n} a_i \tau_i \qquad \text{Equation 2.7}$$

The quality of the fit was judged by reduced Chi square (χ^2) values and the corresponding residual distribution. To obtain the best fitting in all of the cases, χ^2 was kept near to unity. Temperature dependent lifetime measurements of Si QDs were done using Horiba Scientific, U.K. (model, FluoroHub)with TBX PMT detection system. The laser used was 375 nm diode laser with 1 MHz rep rate. Low temperature TCSPC measurements were done using Horiba Scientific, U.K. (model, FluoroHub) with TBX PMT detection system.

2.5.7. Powder X-ray diffraction (XRD)

X-ray powder diffraction (XRD) is a rapid analytical technique primarily used for determining the atomic and molecular structure of a crystal. When an X-ray beam is incident on a crystalline sample, the crystalline structure causes the incident X-rays to diffract into many specific directions. By measuring the angles and intensities of these diffracted beams,

a crystallographer can produce a three-dimensional picture of the density of electrons within the crystal. From this electron density, the mean positions of the atoms in the crystal, their chemical bonds, crystallographic disorder, and various other information are determined.

Bragg's law

Lawrence Bragg explained the diffraction of X-rays by a crystal by modeling the crystal as a set of discrete parallel planes separated by a constant parameter *d*. He proposed that when a X-ray radiation of wavelength comparable to the atomic spacings ~2–3 A˚ is incident on a crystalline system, it gets scattered from the lattice planes separated by the interplanar distance *d*. When the scattered waves undergo constructive interference a Bragg's peak is observed. Constructive interference means the path lengths of the two waves is equal to an integer multiple of the wavelength of incident X-rays. The path difference between the two waves undergoing interference is given by $2d\sin\theta$, where θ is the glancing angle (Figure 2.10). Bragg's law (Equation 2.8) describes the condition on θ for the constructive interference to be at its strongest.

$$2dsin\theta = n\lambda \qquad \text{Equation 2.8}$$

Where n is a positive integer and λ is the wavelength of the incident wave. The X-ray wavelength commonly employed is the characteristic $K\alpha$ radiation, λ = 1.5418 A, emitted by Cu. In this thesis, powder XRD was used for recording X-ray diffraction pattern of Si QDs and Au NPs synthesized using Si QDs as a reducing agent. X-ray diffraction (XRD) patterns were recorded using a Bruker Eco D8 setup using Cu Kα radiation (λ = 0.154056 nm).

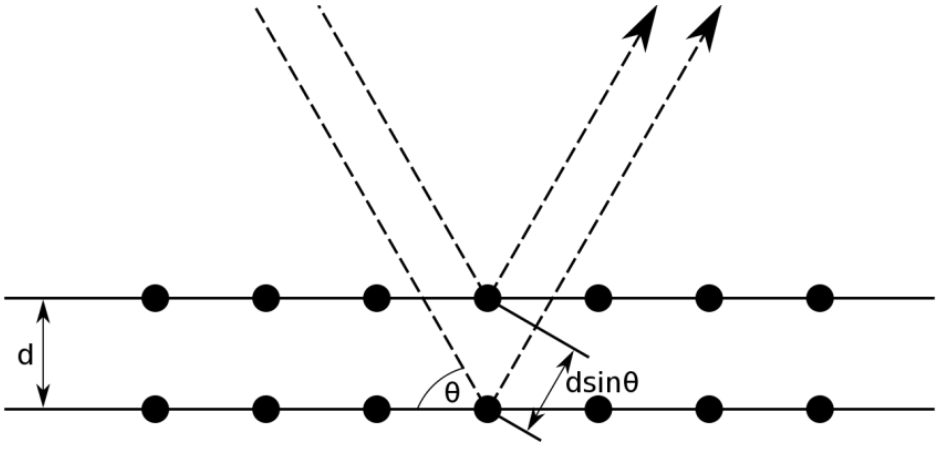

Figure 2.10. Bragg's law of diffraction. (Taken from Wikipedia)

2.5.8. Fourier transform infrared (FTIR) spectroscopy

Infrared spectroscopy (IR) is a well-established technique for the identification and structural analysis of chemical compounds. Infrared radiation is electromagnetic radiation that extends from 700 nm to 1 mm wavelength of the electromagnetic spectrum. Infrared region is divided into three regions; near IR 12500-4000 cm^{-1} (0.8–2.5 μm), mid IR 4000-400 cm^{-1} (2.5–25 μm) and far IR 400-10 cm^{-1} (25–1000 μm). An IR spectrum is a molecular vibrational spectrum. When molecules are exposed to infrared radiation, radiation of specific wavelength is absorbed, which results in a change of the dipole moment of the molecules. When the frequency of the absorbed radiation matches with the vibrational frequencies a peak comes in the IR spectrum.

The frequency of vibration is given by equation 2.9.

$$\gamma = \frac{1}{2\pi}\sqrt{\frac{k}{\mu}} \qquad \text{Equation 2.9}$$

Where k is the force constant and μ is the reduced mass. The peaks in the IR spectrum of a sample represent the excitation of vibrational modes of the chemical bonds and functional groups present in the molecules. Thus, the IR spectrum of a compound is characteristic of its structure and is often regarded as its "fingerprint". Normally an IR spectrum is recorded from 4000-400 cm^{-1} because most of the inorganic and organic compounds show absorption in this region. Most molecules are infrared active except for several homonuclear diatomic molecules such as O_2, N_2 and Cl_2 due to the net-zero dipole moment.

FTIR spectrometers are the third generation IR spectrometer that collects high-spectral-resolution data over a wide spectral range. Some of the advantages of FTIR spectrometers are high signal to noise ratio, high accuracy of wavenumber with an error in the range of ± 0.01 cm^{-1}, lower scan time, and wide scan range.

In this thesis, FTIR was used for determining the surface functionalities of the synthesized Si QDs. FTIR measurements were performed using a Cary 600 series spectrometer from Agilent technologies.

2.5.9. X-ray photoelectron spectroscopy

X-ray photoelectron spectroscopy (XPS) is a surface characterization spectroscopic technique that reveals which chemical elements are present at the surface and the nature of the chemical bond that exists between these elements. XPS works on the principles of the photoelectric

effect. When x-rays beam bombards a sample, if the photon energy is more than the binding energy of the core electron, the core electrons become excited and escape from the atom and emit out of the surface. The binding energy of solids is determined by equation 2.10.

$$BE = h\upsilon - KE - (\phi) \qquad \text{Equation 2.10}$$

Where, BE is the binding energy of atom from where the electron has ejected, KE is the kinetic energy of the electron and Φ is the work function. An XPS spectrum is obtained by plotting the number of electrons ejected with respect to their binding energy. A set of peaks emerge in an XPS spectrum that further helps in determining the chemical state and electronic state of the material under observation. A commercially made XPS system (Figure 2.11) comprises of a source of X-rays, an ultra-high vacuum (UHV) stainless steel chamber with UHV pumps, an electron collection lens, an electron energy analyzer, Mu-metal magnetic field shielding, an electron detector system, a moderate vacuum sample introduction chamber, sample mounts, a sample stage, and a set of stage manipulators.

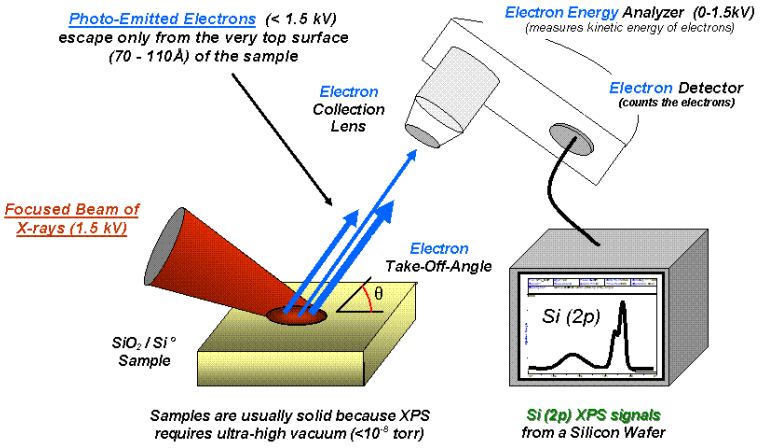

Figure 2.11. Schematic showing components of an XPS spectrometer. (Taken from Wikipedia)

XPS spectrum of Si QDs was recorded using a PHI 5000 Versaprobe-II system of ULVAC-PHI, Inc.

2.5.10. Transmission electron microscopy (TEM)

Transmission electron microscopy is a structural characterization technique in which a high energy beam of electrons is bombarded on a sample and the transmitted electrons are used for forming an image. Due to the resolution limit proposed by Ernst Abbe (Equation 2.11), visible

light can result in an approximated resolution limit of about 200 nm. In equation 2.11, λ and NA correspond to the wavelength of light and numerical aperture respectively.

$$d = \frac{1.22\lambda}{2NA} \qquad \text{Equation 2.11}$$

So for getting a resolution in nm, electrons represent an appropriate source. According to Louis de Broglie, the wavelength of electrons (λ_e) is related to their kinetic energy *E* (Equation 2.12).

$$\lambda_e = \frac{\mathrm{h}}{\sqrt{2m_o E\left(1+\frac{E}{2m_o c^2}\right)}} \qquad \text{Equation 2.12}$$

Where, *h* = Planck constant, m_0 = electron rest mass, *c* = speed of light. By using different accelerating voltages, electrons of different wavelengths and hence different resolutions are obtained. For biological samples accelerating voltages in the range of 80-120 kV are used. For less sensitive samples higher voltages can be used.

TEMs are the most efficient structural characterization tools for analyzing materials spanning from atomic scale to the nanometer regime up to the micrometer level and beyond. It utilizes energetic transmitted electrons (electrons which are passing through the sample) to create an image. As the electron beam passes through the sample, along with the morphology it provides compositional and crystallographic information on samples.

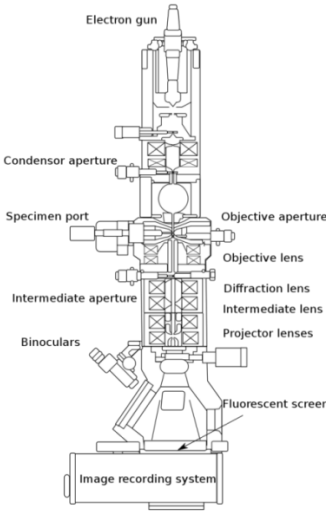

Figure 2.12. Design of a basic TEM showing the optical components. (Image taken from Wikipedia).

A TEM consists of three essential systems (shown in Figure 2.12):

(1) Illumination system- It consists of an electron gun and the condenser system. The electron gun generates an electron beam which falls on the sample. In all the modern days TEM lanthanum hexaboride (LaB_6) crystal is used as the electron source. The condenser system focuses the generated electron beam onto the sample.

(2) Image producing system- It consists of objective, condenser, intermediate, and projector lenses and movable specimen stage. A condenser lens is responsible for primary beam formation, while the objective lens is used for initial magnification of the image, intermediate lenses magnify the image coming from the objective lens. At last, projector lens expands the beam onto a phosphor screen.

(3) Image recording system- The image recording system of a TEM comprises of a fluorescent screen on which the sample is viewed and a CCD camera that converts the electron image into a digital image.

To prevent uncontrolled deflection of electrons a vacuum system consisting of pumps and their associated gauges and valves, and power supplies are required. A TEM can record high-resolution transmission electron microscopy (HRTEM) images of a sample which help in studying properties of materials on the atomic scale. A scanning transmission electron microscope (STEM) is a type TEM equipped with additional scanning coils and detectors. It helps in determining the surface properties. First Fourier Transformation pattern (FFT) or selected area electron diffraction patterns (SAED) provide information about the crystalline phases of the nanocrystals.

In the present thesis, TEM has been used for determining the morphology and size of synthesized Au nanoparticles, DNA origami, Si quantum dots, and Si QD-Au NP hybrid nanoparticles. Since the scattering effect is proportional to the square of the atomic number it is difficult to image biological samples without staining. So for imaging DNA origami negative staining with uranyl acetate was done. The TEM, HRTEM, EDX, STEM-EDX, and SAED measurements were carried out with a JEOL model 2100 instrument operated at an accelerating voltage of 200 kV for nanoparticles and 120 kV for DNA origami. STEM-EDS mapping images were obtained using a JEOL JEM 2100F system at an accelerating voltage of 200 kV.

2.5.11. Atomic force microscopy (AFM)

Atomic force microscope is one kind of scanning probe microscopes (SPM) used for analyzing surface properties of materials such as height, friction, morphology with a probe. The basic

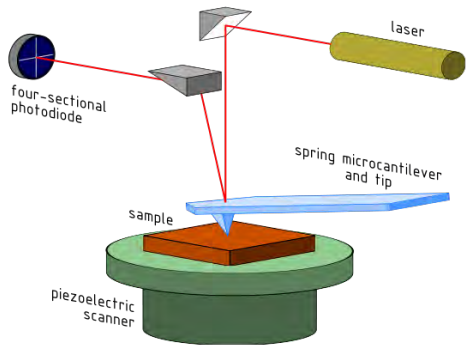

Figure 2.13. Schematic of an atomic force microscope.

working principle of an AFM is to scan the surface of the sample by a tip that has a curvature radius in the nanometer range. As the tip approaches the surface, the close-range, attractive forces bring the cantilever towards the surface and when the distance between the two further reduces repulsive forces take over and the cantilever is deflected away from the sample surface. A laser beam is used to detect cantilever deflections towards or away from the surface. The position of the reflected laser beam is detected on two or four closely spaced photodiodes and then translated into an image. A schematic of the components of an AFM is given in figure 2.13. An AFM is usually operated in three different modes contact, non-contact, and tapping mode. The main difference between these three types of modes can be explained using Lennard-Jones potential (shown in Figure 2.14). The force associated with AFM is an interatomic force

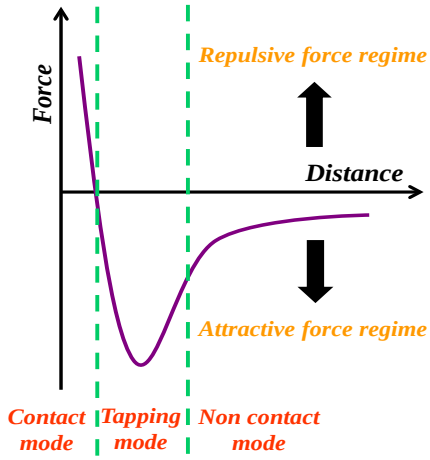

Figure 2.14. A Lennard-Jones-type potential. Van der Waals force versus distance.

called the Van der Waals force. In the contact mode, the cantilever is held very close to the sample (~ 10^{-10} m from the sample) as a result the interatomic force between the sample and the

cantilever is repulsive. In non-contact mode, the distance between the cantilever and the sample surface is on the order of tens to hundreds of Å, the interatomic forces are attractive. Tapping mode is an intermittent mode that fluctuates between the contact and non-contact regions.

In this thesis, AFM imaging of all the samples was done in tapping mode. AFM samples were prepared on mica disk (V1 quality) and Si wafer. Bruker Multimode 8 scanning probe microscope with silicon cantilever from Bruker and Budget sensors (Tap150Al-G) with a force constant of 5 N m^{-1} have been used for imaging DNA origami and the designed plasmonic nanoantennas.

2.5.12. Agarose gel electrophoresis

Electrophoresis is a simple technique in which negatively charged molecules move towards positively charged cathode under the influence of an electric field. Depending on the size and charge the running speed of macromolecules differs, as a result, they get separated. A matrix (such as agarose or polyacrylamide) must be used to conduct heat evenly and provide an extra sieving effect. In case of agarose gel electrophoresis, agarose is used as a matrix. It is usually used for separation of DNA (single-stranded, double-stranded, and supercoiled) and RNA. Figure 2.15 shows a schematic depiction of a typical gel electrophoresis system. Depending on

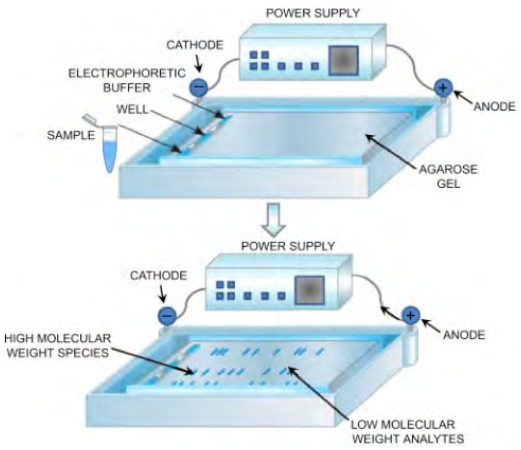

2.15. Agarose gel electrophoresis system.[80]

the size of the molecule to be separated the percentage of agarose gel is determined for example, a gel of 0.7 % is sufficient for good resolution of 5-10 kb DNA fragments and 2% for 0.2-1kb fragments. The mobility of DNA strands in the gel depends on a number of factors such as the pore size of the gel, molecular weight/size of the DNA strands, running voltage and concentration of running buffer. Small DNA strands travel faster than large DNA strands due to

differences in their molecular weights. Further, folded structures tend to move faster due to their compact size as compared to relaxed DNA. DNA and RNA are optically transparent molecules so for their visualization ethidium bromide is used as a staining agent. Ethidium bromide is an intercalating DNA that binds to the major grooves of DNA and fluoresces under UV light illumination. Other commonly used staining dyes are SYBR green, Nile blue, methylene blue, and crystal violet. The separated DNA/RNA strands can be extracted from the agarose gel matrix for further use.

In this thesis, agarose gel electrophoresis was used for the purification of rectangular DNA origami monomer and dimer. Ethidium bromide dye was used for the visualization of bands corresponding to DNA origami structures. After running the gel in Bio-Rad horizontal electrophoresis system, the bands were visualized and imaged using ChemiDoc XRS+ molecular imager with image lab software.

References

1. M. Faraday, *Philosophical Transactions of the Royal Society of London*, 1857, **147**, 145-181.
2. J. Turkevich, P. C. Stevenson and J. Hillier, *Discussions of the Faraday Society*, 1951, **11**, 55-75.
3. B. V. Enustun and J. Turkevich, *Journal of the American Chemical Society*, 1963, **85**, 3317-3328.
4. J. Turkevich, *Gold Bulletin*, 1985, **18**, 125-131.
5. G. Frens, *Nature Physical Science*, 1973, **241**, 20-22.
6. A. Biswas, I. S. Bayer, A. S. Biris, T. Wang, E. Dervishi and F. Faupel, *Advances in Colloid and Interface Science*, 2012, **170**, 2-27.
7. S. Kawata, H.-B. Sun, T. Tanaka and K. Takada, *Nature*, 2001, **412**, 697-698.
8. Z. Tang and A. Wei, *ACS Nano*, 2012, **6**, 998-1003.
9. H.-D. Yu, M. D. Regulacio, E. Ye and M.-Y. Han, *Chemical Society Reviews*, 2013, **42**, 6006-6018.
10. M. J. Mulvihill, X. Y. Ling, J. Henzie and P. Yang, *Journal of the American Chemical Society*, 2010, **132**, 268-274.
11. P. R. Sajanlal, T. S. Sreeprasad, A. K. Samal and T. Pradeep, *Nano Reviews*, 2011, **2**, 5883.
12. G. Berhault, M. Bausach, L. Bisson, L. Becerra, C. Thomazeau and D. Uzio, *The Journal of Physical Chemistry C*, 2007, **111**, 5915-5925.
13. C. Lofton and W. Sigmund, *Advanced Functional Materials*, 2005, **15**, 1197-1208.
14. A. Gole and C. J. Murphy, *Chemistry of Materials*, 2004, **16**, 3633-3640.
15. Y. Xiong and Y. Xia, *Advanced Materials*, 2007, **19**, 3385-3391.
16. X. Lu, M. Rycenga, S. E. Skrabalak, B. Wiley and Y. Xia, *Annual Review of Physical Chemistry*, 2009, **60**, 167-192.
17. Z. Huo, C.-k. Tsung, W. Huang, X. Zhang and P. Yang, *Nano Letters*, 2008, **8**, 2041-2044.
18. Yu, S.-S. Chang, C.-L. Lee and C. R. C. Wang, *The Journal of Physical Chemistry B*, 1997, **101**, 6661-6664.
19. R. Jin, Y. Charles Cao, E. Hao, G. S. Métraux, G. C. Schatz and C. A. Mirkin, *Nature*, 2003, **425**, 487-490.
20. N. R. Jana, L. Gearheart and C. J. Murphy, *Chemical Communications*, 2001, DOI: 10.1039/B100521I, 617-618.
21. N. R. Jana, L. Gearheart and C. J. Murphy, *The Journal of Physical Chemistry B*, 2001, **105**, 4065-4067.
22. P. Senthil Kumar, I. Pastoriza-Santos, B. Rodríguez-González, F. Javier García de Abajo and L. M. Liz-Marzán, *Nanotechnology*, 2007, **19**, 015606.
23. C. J. Murphy, T. K. Sau, A. M. Gole, C. J. Orendorff, J. Gao, L. Gou, S. E. Hunyadi and T. Li, *The Journal of Physical Chemistry B*, 2005, **109**, 13857-13870.
24. B. Nikoobakht and M. A. El-Sayed, *Chemistry of Materials*, 2003, **15**, 1957-1962.
25. T. K. Sau and C. J. Murphy, *Langmuir*, 2004, **20**, 6414-6420.
26. C. Hrelescu, T. K. Sau, A. L. Rogach, F. Jäckel, G. Laurent, L. Douillard and F. Charra, *Nano Letters*, 2011, **11**, 402-407.
27. A. Guerrero-Martínez, S. Barbosa, I. Pastoriza-Santos and L. M. Liz-Marzán, *Current Opinion in Colloid & Interface Science*, 2011, **16**, 118-127.
28. H.-L. Wu, C.-H. Chen and M. H. Huang, *Chemistry of Materials*, 2009, **21**, 110-114.
29. H. Yuan, C. G. Khoury, H. Hwang, C. M. Wilson, G. A. Grant and T. Vo-Dinh, *Nanotechnology*, 2012, **23**, 075102.
30. M. Grzelczak, J. Pérez-Juste, P. Mulvaney and L. M. Liz-Marzán, *Chemical Society Reviews*, 2008, **37**, 1783-1791.
31. M. Grzelczak, A. Sánchez-Iglesias, B. Rodríguez-González, R. Alvarez-Puebla, J. Pérez-Juste and L. M. Liz-Marzán, *Advanced Functional Materials*, 2008, **18**, 3780-3786.
32. L. Jin, L. Shang, S. Guo, Y. Fang, D. Wen, L. Wang, J. Yin and S. Dong, *Biosensors and Bioelectronics*, 2011, **26**, 1965-1969.
33. X. Qu, Y. Li, L. Li, Y. Wang, J. Liang and J. Liang, *Journal of Nanomaterials*, 2015, **2015**, 23.

34. C.-A. J. Lin, T.-Y. Yang, C.-H. Lee, S. H. Huang, R. A. Sperling, M. Zanella, J. K. Li, J.-L. Shen, H.-H. Wang, H.-I. Yeh, W. J. Parak and W. H. Chang, *ACS Nano*, 2009, **3**, 395-401.
35. C. Zhou, C. Sun, M. Yu, Y. Qin, J. Wang, M. Kim and J. Zheng, *The Journal of Physical Chemistry C*, 2010, **114**, 7727-7732.
36. M. Zhu, E. Lanni, N. Garg, M. E. Bier and R. Jin, *Journal of the American Chemical Society*, 2008, **130**, 1138-1139.
37. Y. Negishi, Y. Takasugi, S. Sato, H. Yao, K. Kimura and T. Tsukuda, *Journal of the American Chemical Society*, 2004, **126**, 6518-6519.
38. J. Zheng, J. T. Petty and R. M. Dickson, *Journal of the American Chemical Society*, 2003, **125**, 7780-7781.
39. J. Xie, Y. Zheng and J. Y. Ying, *Journal of the American Chemical Society*, 2009, **131**, 888-889.
40. C.-L. Liu, H.-T. Wu, Y.-H. Hsiao, C.-W. Lai, C.-W. Shih, Y.-K. Peng, K.-C. Tang, H.-W. Chang, Y.-C. Chien, J.-K. Hsiao, J.-T. Cheng and P.-T. Chou, *Angewandte Chemie International Edition*, 2011, **50**, 7056-7060.
41. Y. Chen, X. Zheng, X. Wang, C. Wang, Y. Ding and X. Jiang, *ACS Macro Letters*, 2014, **3**, 74-76.
42. L. Maya, G. Muralidharan, T. G. Thundat and E. A. Kenik, *Langmuir*, 2000, **16**, 9151-9154.
43. G. Liu, Y. Shao, K. Ma, Q. Cui, F. Wu and S. Xu, *Gold Bulletin*, 2012, **45**, 69-74.
44. S. Chakraborty, S. Babanova, R. C. Rocha, A. Desireddy, K. Artyushkova, A. E. Boncella, P. Atanassov and J. S. Martinez, *Journal of the American Chemical Society*, 2015, **137**, 11678-11687.
45. T. G. Schaaff and R. L. Whetten, *The Journal of Physical Chemistry B*, 2000, **104**, 2630-2641.
46. Z. Luo, X. Yuan, Y. Yu, Q. Zhang, D. T. Leong, J. Y. Lee and J. Xie, *Journal of the American Chemical Society*, 2012, **134**, 16662-16670.
47. C. F. Shaw, M. P. Cancro, P. L. Witkiewicz and J. E. Eldridge, *Inorganic Chemistry*, 1980, **19**, 3198-3201.
48. P. L. Witkiewicz and C. F. Shaw, *Journal of the Chemical Society, Chemical Communications*, 1981, DOI: 10.1039/C39810001111, 1111-1114.
49. A. Valizadeh, H. Mikaeili, M. Samiei, S. M. Farkhani, N. Zarghami, M. Kouhi, A. Akbarzadeh and S. Davaran, *Nanoscale Res Lett*, 2012, **7**, 480-480.
50. D. Bera, L. Qian, T.-K. Tseng and P. H. Holloway, *Materials (Basel)*, 2010, **3**, 2260-2345.
51. C. B. Murray, D. J. Norris and M. G. Bawendi, *Journal of the American Chemical Society*, 1993, **115**, 8706-8715.
52. S. G. Kwon, Y. Piao, J. Park, S. Angappane, Y. Jo, N.-M. Hwang, J.-G. Park and T. Hyeon, *Journal of the American Chemical Society*, 2007, **129**, 12571-12584.
53. M. Bottrill and M. Green, *Chemical Communications*, 2011, **47**, 7039-7050.
54. P. W. K. Rothemund, *Nature*, 2006, **440**, 297-302.
55. H. K. Nguyen and E. M. Southern, *Nucleic Acids Res*, 2000, **28**, 3904-3909.
56. J. J. Schmied, M. Raab, C. Forthmann, E. Pibiri, B. Wünsch, T. Dammeyer and P. Tinnefeld, *Nature Protocols*, 2014, **9**, 1367.
57. R. Jungmann, M. Scheible, A. Kuzyk, G. Pardatscher, C. E. Castro and F. C. Simmel, *Nanotechnology*, 2011, **22**, 275301.
58. A. Rajendran, M. Endo, Y. Katsuda, K. Hidaka and H. Sugiyama, *ACS Nano*, 2011, **5**, 665-671.
59. W. Liu, H. Zhong, R. Wang and N. C. Seeman, *Angewandte Chemie International Edition*, 2011, **50**, 264-267.
60. M. Liber, T. E. Tomov, R. Tsukanov, Y. Berger and E. Nir, *Small*, 2015, **11**, 568-575.
61. G. Yang, J. Nanda, B. Wang, G. Chen and D. T. Hallinan, *ACS Applied Materials & Interfaces*, 2017, **9**, 13457-13470.
62. Y.-W. Wang, K.-C. Kao, J.-K. Wang and C.-Y. Mou, *The Journal of Physical Chemistry C*, 2016, **120**, 24382-24388.
63. A. Kinkhabwala, Z. Yu, S. Fan, Y. Avlasevich, K. Müllen and W. E. Moerner, *Nature Photonics*, 2009, **3**, 654.
64. P. Wang, T. A. Meyer, V. Pan, P. K. Dutta and Y. Ke, *Chem*, 2017, **2**, 359-382.
65. T. Tørring, N. V. Voigt, J. Nangreave, H. Yan and K. V. Gothelf, *Chemical Society Reviews*, 2011, **40**, 5636-5646.

66. S. Takabayashi, W. P. Klein, C. Onodera, B. Rapp, J. Flores-Estrada, E. Lindau, L. Snowball, J. T. Sam, J. E. Padilla, J. Lee, W. B. Knowlton, E. Graugnard, B. Yurke, W. Kuang and W. L. Hughes, *Nanoscale*, 2014, **6**, 13928-13938.
67. F. N. Gür, F. W. Schwarz, J. Ye, S. Diez and T. L. Schmidt, *ACS Nano*, 2016, **10**, 5374-5382.
68. S. Pal, Z. Deng, B. Ding, H. Yan and Y. Liu, *Angewandte Chemie International Edition*, 2010, **49**, 2700-2704.
69. R. Schreiber, J. Do, E.-M. Roller, T. Zhang, V. J. Schüller, P. C. Nickels, J. Feldmann and T. Liedl, *Nature Nanotechnology*, 2013, **9**, 74.
70. D. Huang, M. Freeley and M. Palma, *Scientific Reports*, 2017, **7**, 45591.
71. K. Du, S. H. Ko, G. M. Gallatin, H. P. Yoon, J. Alexander Liddle and A. J. Berglund, *Chemical Communications*, 2013, **49**, 907-909.
72. Y. Ke, S. Lindsay, Y. Chang, Y. Liu and H. Yan, *Science*, 2008, **319**, 180-183.
73. K. Vogele, J. List, F. C. Simmel and T. Pirzer, *Langmuir*, 2018, **34**, 14780-14786.
74. The principles of dynamic light scattering, https://wiki.anton-paar.com/en/the-principles-of-dynamic-light-scattering/).
75. J. R. Lakowicz, *Principles of fluorescence spectroscopy*, Springer, New York, 2006.
76. G. G. Stokes, *Philosophical Transactions of the Royal Society of London*, 1852, **142**, 463-562.
77. in *Principles of Fluorescence Spectroscopy*, ed. J. R. Lakowicz, Springer US, Boston, MA, 2006, DOI: 10.1007/978-0-387-46312-4_23, pp. 757-795.
78. S. K. Sarkar, in *Single Molecule Biophysics and Poisson Process Approach to Statistical Mechanics*, Morgan & Claypool Publishers, 2016, DOI: 10.1088/978-1-6817-4116-1ch2, pp. 2-1-2-14.
79. A. R. Barron, Surface-Enhanced Raman Spectroscopy for the Study of Surface Chemistry, https://cnx.org/contents/-KGSWHOc@1/Surface-Enhanced-Raman-Spectroscopy-for-the-Study-of-Surface-Chemistry).
80. A. Drabik, A. Bodzoń-Kułakowska and J. Silberring, in *Proteomic Profiling and Analytical Chemistry (Second Edition)*, eds. P. Ciborowski and J. Silberring, Elsevier, Boston, 2016, DOI: https://doi.org/10.1016/B978-0-444-63688-1.00007-0, pp. 115-143.

Chapter 3

Design of Au nanostar dimers for single molecule surface enhanced Raman scattering

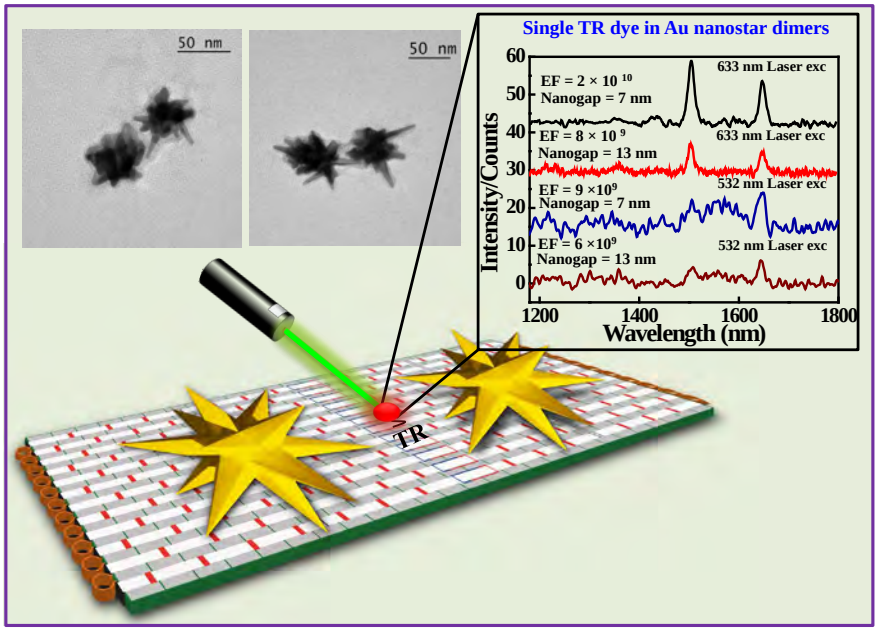

3.1. Introduction

Developing single molecule detection platforms with high sensitivity and specificity is the seminal goal of the scientific community because of their ability to transform the fields of imaging, biophysics, and optical sensing.[1, 2] In the past few decades, Surface enhanced Raman spectroscopy (SERS) has emerged as a highly sensitive and non-invasive spectroscopic technique capable of detecting molecules with single-molecule sensitivity.[3-5] Till now, numerous reports have been published showing applicability of SERS for detecting physical, chemical, and biological entities at the micro/nanoscale.[6-11] In SERS, enhancement factor (EF) is directly proportional to the fourth power of the intensity of the EM field,[7] therefore, in order to efficiently harness the strong EM field, considerable interest has been shifted towards coupled plasmonic systems such as dimers and trimers with ultrasmall nanojunctions,[6, 12] commonly addressed as plasmonic nanoantennas. Plasmonic nanoantennas act as a miniaturized optical device that can confine the propagating optical radiation into nanometer regime,[13] where due to strong plasmonic coupling the generated extrinsic hotspots can result in EFs as high as 10^{10}.[18, 19] The field enhancement effects are more pronounced in case of anisotropic metal nanostructures bearing sharp corners[14, 15] or tips[16, 17] due to lightning rod effect, which results in accumulation of high intensity electromagnetic fields at their sharp edges.[18] Among all the anisotropic shapes, Au nanostars are especially attractive due to their particular structural and optical properties, including strong localized plasmonic fields at their sharp edged tips, and tunable NIR resonances for their use in sensing, SERS, biological imaging, and biomedical applications.[19, 20] The strong electromagnetic field generated at the sharp tips of Au nanostars can lead to an extraordinary field enhancement[21] and also the plasmons focused at the core couples with the tips in Au nanostar structures,[17] making it an outstanding candidate for numerous spectroscopic applications. For achieving single molecule sensitivity, the plasmonic nanoantennas should be capable of enhancing Raman signals with minimum EFs to the order of 10^6–10^8.[22] It has been shown both experimentally and theoretically that apart from the shape and size of nanoparticles, EFs strongly depends on the interparticle gaps.[23] The excited surface plasmons decay rapidly as $1/d^{12}$,[24, 25] as a result, the enhancement effects are highest near to the metal surface where the maximum EM field is experienced. Therefore, the primary prerequisite conditions for designing SM-SERS active substrates are, maintaining the interparticle gap in the range of 2-10 nm, precise positioning of a single Raman active probe in the plasmonic hotspot and close resonance between the LSPR and absorption maxima of the Raman reporter molecule a condition called surface enhanced resonant Raman scattering (SERRS).[26] Till now several strategies have been adopted for producing high intensity hotspots and positioning of a single analyte predominantly

at SERS hot spots. Nie and Emory[4] used ultra-low concentrations of R6G dye such that single colloidal Ag nanoparticle was expected to contain either one or zero dye molecule contributing to SERS signal. Although the obtained EFs were in the order of 10^{14} to 10^{15}, only a small proportion of the SERS substrate contributed to detectable Raman signals which raise questions on its scalability. Aroca et al. used fatty acid Langmuir-Blodgett films for trapping the bis(benzimidazo)perylene (AzoPTCD) dye molecules, which were further transferred to Ag island films.[27, 28] This approach also provided poor statistics which made interpretation of results difficult. Tip-enhanced Raman spectroscopy is another approach where the Raman probe resides on a substrate and a metallic tip placed above the substrate amplifies the Raman signal.[29, 30] The drawback of placing a single molecule precisely at the hotspot remained the same. Despite so many advances and efforts being made to improve the sensitivity of SERS substrates down to single molecule level significant improvements are required for the utility of SERS substrates for commercial applications.

Owing to its programmability and structural plasticity, DNA origami has emerged as a promising and versatile platform for designing complex 2 and 3-dimensional [31, 32] assemblies for carrying out single molecule analysis. Since the first report of the DNA origami method by Paul Rothemund, this versatile technique has been utilized extensively for precise arrangement of nanoparticles of arbitrary size at a predefined interparticle distance with sub-nm accuracy, controlled spatial orientation, and tunable stoichiometry.[31, 33, 34] In light of these fascinating properties of DNA origami, many examples have been shown in past that used DNA origami as a template for fabricating novel plasmonic nanoantennas.[35-37] Kühler et al. reported the synthesis of Au nanoparticle dimers prepared by DNA origami and their use as efficient SERS substrate.[38] Zhan et al. assembled Au bowtie structures with nanoscale precision on DNA origami template to study the effect of localized EM fields on enhancement of single molecule Raman signals.[39] Heck et al. synthesized Au-Ag core shell nanoparticle dimers using DNA origami as a template and further showed its applicability for SM-SERS. [40] Prinz et al. demonstrated SERS from Au NP dimer on DNA origami substrates for the identification of specific Raman bands of single TAMRA molecules attached to the DNA origami. [41] DNA origami technique provides sequence defined binding sites to place analyte molecules of interest specifically in the hotspot region, and this unique feature marks a clear advantage compared to other methods that rely on random adsorption of molecules to the nanoantenna gap.

This chapter demonstrates the design of Au nanostar dimer plasmonic nanoantennas with tunable interparticle gaps and stoichiometry assembled on dimerized rectangular DNA origami.

Further, the designed nanoantennas have been employed for SM SERS measurements. Single Texas red (TR) dye molecule was precisely positioned in the conjunction region between the nanostars by modifying one of the branching staples of the DNA origami template with the dye molecule. The effect of the interparticle gap, stoichiometry, and negative curvature of nanostars on the Raman EF of single TR dye has been investigated. To detect the Raman signal from each dye molecule, AFM correlated Raman spectroscopy was used.

3.2. Experimental section

3.2.1. Materials

Gold chloride trihydrate ($HAuCl_4$. $3H_2O$), trisodium citrate, L-ascorbic acid, silver nitrate (Ag NO_3), ethylenediaminetetraacetic acid disodium salt (EDTA), trizma base, tris-(carboxyethyl)phosphine hydrochloride (TCEP), and sodium chloride (NaCl) were purchased from Sigma-Aldrich and $MgCl_2.6H_2O$ from SRL. M13mp18 single stranded DNA was procured from New England Biolabs and was used without further treatment. All unmodified staple strands were purchased from Integrated DNA Technologies, Inc. (IDT) in unpurified form (standard desalting). 5′-thiol modified single stranded DNA was purchased from IDT after HPLC purification. Sephacryl S-300 HR resin was purchased from GE Healthcare. All of these reagents were used without further purification. Amicon filters with 0.5 ml centrifugal volume, 100 KDa molecular weight were purchased from Sigma-Aldrich. Freeze N Squeeze spin columns were purchased from Bio-Rad. Milli-Q (MQ) water was used for all the experiments.

3.2.2. Buffers

DNA origami samples were annealed in 1× TAE buffer (40 mM Tris a, 20 mM Acetic acid, 1 mM EDTA) containing 12.5 mM magnesium chloride, pH 8.0.

3.2.3. Experimental procedures

3.2.3.1. Synthesis of Au nanostars

To facilitate the assembling of Au nanostars on DNA origami for SM SERS measurements, a surfactant free synthesis in aqueous media that produces high yield monodisperse Au nanostars with sharp edges was of particular interest. In literature different synthesis protocols using poly(*N*-vinylpyrrolidone) (PVP)[42] or cetyltrimethylammonium bromide (CTAB)[43] have been proposed for the synthesis of Au nanostars. Unfortunately, the use of these nanostars for bioapplications has been limited due to difficulty in removal of excess of surfactant prior to bio-

conjugation and cytotoxicity associated with surfactants.[44, 45] Keeping all these factors in mind, Au nanostars were synthesized using seed mediated method (as shown in Scheme 3.1) in aqueous medium without any surfactant.[46] Au nanostars were synthesized using previously

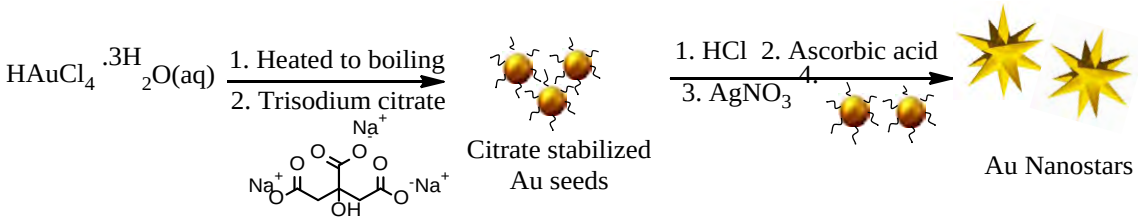

Scheme 3.1. Schematic depiction of the synthesis of Au nanostars.

reported method after slight modifications.[46]Au nanostars were prepared based on a seed-mediated growth method. At first, citrate stabilized Au nanoparticles seed solution was synthesized by following a well-known citrate reduction method.[47] Briefly, to a 12.5 mL boiling solution of 1 mM $HAuCl_4$, 2 mL of 1.5% trisodium citrate was added under vigorous stirring. The color of the solution changes from light yellow to red due to the formation of Au nanoparticles (Au NPs) within 5−10 min. The solution was stirred continuously with heating for another 20 min. Finally, the solution was cooled to room temperature under stirring.

Au nanostars were prepared by adding 150 μL of the above synthesized seed solution to growth solution containing 10 mL of 0.15 mM $HAuCl_4$ with 10 μL of 1 M HCl under mild stirring. It was followed by simultaneous addition of 40 μL of 0.01 M $AgNO_3$, 50 μL of 0.01 M ascorbic acid, and 20 μL of 0.01 M SDS solution, respectively. To halt the process of nucleation, the Au nanostar solution was immediately given one centrifugal wash at 4000g for 15 min, followed by resuspension in water (MQ). Seed solutions were ultrasonicated for 10 min before addition to growth solution at a frequency of 53 kHz.

3.2.3.2. Functionalization of Au nanostars with DNA oligonucleotides

The thiolated DNA oligonucleotides were reduced by incubating them with 0.2 M TCEP (1:200 molar ratio of DNA: TCEP) in water (MQ) for 3 h. The DNA functionalization of Au nanostars was performed by following the method reported by Mirkin et al.[48] with the following DNA sequence containing a thiol modification at the 5′end: 5 ′-thiol CGTCGTATTCGATAGCTTAG-3′. The DNA functionalized Au nanostars were washed using 100 kDa amicon filter to remove excess unbound oligonucleotides and were finally resuspended in 0.5× TAE-Mg^{2+} buffer.

3.2.3.3. Synthesis of rectangular DNA origami

The rectangular DNA origami structure was synthesized by following the method described by Rothemund.[31] M13mp18 single-stranded DNA was used as the scaffold. Briefly, the rectangular DNA origami was self-assembled using a long single-stranded M13mp18 viral genomic DNA folded by a set of ~200 short staple strands using a 1.5 h annealing program. Annealing was performed in 1× TAE buffer with scaffold concentration of 2 nM, 10-fold excess of regular staples, and 20-fold excess of modified staples. Sequence of all the short staple sequences and edge staples are given in table 1, 2, and table 3 of the appendix A respectively.

3.2.3.4. Purification of rectangular DNA origami monomer

Annealed DNA origami monomer was purified using amicon filter (100 kDa) that was filled with 50 μL of PCR mixture and 450 μL of 1×TAE buffer (pH 8) with 12.5 mM $MgCl_2$ and spun at 14000g for 5 min at 4° C. This was followed by three times washing with 500 μL of 1× TAE, 12.5 mM $MgCl_2$ buffer. Finally, an amicon filter was inverted in a fresh micro centrifuge tube and spun at 5000g for 10 min to collect purified origami.

3.2.3.5. Dimerization of rectangular DNA origami

Dimerization of rectangular DNA origami was done according to previously reported protocol.[49] To an equimolar mixture of unpurified origami A and origami B solution, 24 branching staples were added in 40-fold excess and the mixture was incubated at room temperature for 24 h in 50× TAE with 12.5 mM $MgCl_2$. The edges of each origami monomer were extended with 24 T-loop edge staples of various lengths in the opposite side of the junction to restrict the uncontrolled polymerization into ribbons of nonuniform lengths (shown in Scheme 3.2).[50] Details of branching staples are given in table 4 and 5 of the appendix A.

3.2.3.6. Purification of rectangular DNA origami dimer

Dimerized rectangular DNA origami was purified using Sephacryl S-300 HR resin. Polypropylene columns were hand packed with 750 μL of liquid resin and then spun at 1400 g at 10 °C for 2 min. The column was further washed with 500 μL of 1× TAE buffer (pH 8) with 11 mM $MgCl_2$ and spun at 1400g for 2 min. This procedure was repeated thrice to completely equilibrate the column. After addition of dimerized rectangular DNA origami solution, column was spun at 1400g for 5 min at 10°C. Collected purified origami was used for atomic force microscopy (AFM) and transmission electron microscopy (TEM) imaging and also for immobilization of DNA functionalized Au nanostars. The monomer and dimerized rectangular

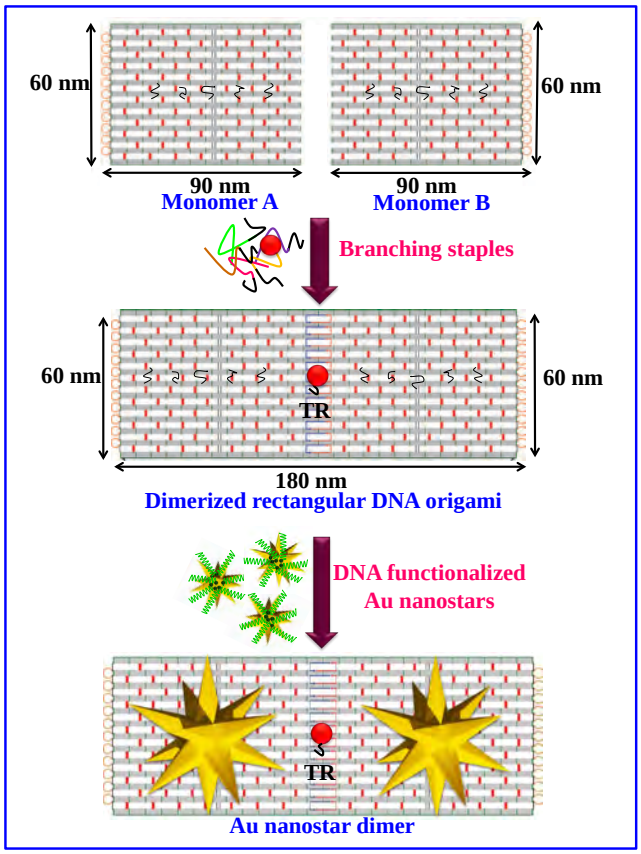

Scheme 3.2. Schematic design of Au nanostar dimers on dimerized rectangular DNA origami structures.

DNA origami structures were also purified using gel electrophoresis. For gel electrophoresis, 1% agarose in 1× TAE buffer was heated to boiling and cooled to 50°C followed by addition of 1 M $MgCl_2$ (final concentration of 12.5 mM $MgCl_2$) to provide stability to DNA origami nanostructures during the run. Staining was done using ethidium bromide. Gel lanes were filled with 25 µL of unpurified dimerized DNA origami and 5 µL of loading buffer. For running the gel, a voltage of 70 V was applied for 2 h. Gel assembly was kept in an ice bath during 2 h of run time to prevent denaturation of DNA origami because of heat. After running the gel, the bands were visualized and imaged using ChemiDoc XRS+ molecular imager with image lab software and extracted using Freeze N Squeeze spin columns.

3.2.3.7. Incorporation of single Texas red dye in DNA origami

Texas red (TR) is a red fluorescent dye that is extensively used for staining cell specimens in biology and also in single-molecule fluorescence resonance energy transfer studies.[51, 52] For the incorporation of single TR dye molecule in the center of the dimerized rectangular DNA

origami, we have modified one branching staple by attaching with a TR moiety at the 3 ′ end. Usual unmodified branching staple was replaced by the dye modified staple during dimerization step. The rest of the dimerization conditions and concentrations were similar to those mentioned in section 3.2.3.5. Sequence of dye labeled staple is given in table 6 of the appendix A.

3.2.3.8. Hybridization between Au nanostars and DNA origami

The dimerized DNA origami was mixed with DNA-functionalized Au nanostars at a molar ratio of 1:2 in 0.5× TAE Mg^{2+} with 0.3 M NaCl. The mixture was heated repeatedly between 40 and 20°C for 12 h, being kept in a PCR thermocycler (Bio-rad C1000). This thermocycling resulted in immobilization of Au nanostars on DNA origami (as shown in Scheme 3.2). The final product was used for TEM imaging and Raman measurements.

3.2.3.9. Transmission Electron Microscopy (TEM) imaging

For recording TEM images of DNA origami and Au nanostars-DNA origami hybrid nanostructures, at first, the carbon coated grids were activated using 1 M $MgCl_2$ solution. After that purified DNA origami (6 μL) solution was dropped onto the grid for 3 min followed by negative staining using (2% w/v) uranyl acetate for 2 min. For Au nanostars, TEM grid was prepared by the drop-casting method.

3.2.3.10. Atomic Force Microscopy (AFM) imaging

AFM imaging of DNA origami samples was done on mica sheets of V1 quality with silicon cantilever (Bruker) in tapping mode analysis. At first, mica sheet was fixed on round metal plate (Dia-1.5 mm) using transparent nail polish and freshly cleaved 5−6 times. It was then incubated with 50 μM $MgCl_2$ solution for 5 min followed by washing 3−4 times with H_2O. After drying the substrate in air, 10 μL of purified origami was placed on mica substrate for 10 min, followed by washing with water and drying using a gentle breeze of N_2.

Immobilization of Au nanostars on Si wafer for AFM correlated Raman measurements. Si wafer pieces (1 × 1 cm^2 size) were oxygen plasma cleaned (using Plasma bonder from Omicron scientific equipment Co.) for 5 min to ensure hydrophilicity of the wafer surface. The wafers were then washed twice with 1:1 solution of ethanol and distilled water followed by incubation with dilute solution of Au nanostars−DNA origami structure in 10× TAE with 200 mM $MgCl_2$ for 20 min. This was followed by washing with MQ and drying with gentle breeze of N_2 to ensure uniform and complete coverage of surface.

3.2.3.11. Raman measurements and calculation of the enhancement factor (EF)

Raman measurements were performed in air using laser light at 532 and 633 nm lasers using 100 × objective (NA = 0.9) to a diffraction-limited spot of about 1 μm^2 on Si wafer. The laser power was set to 1 mW with integration time 4 s (for TR dye bound to Au nanostar-DNA origami structures) or 10 s for TR bound to DNA origami structures and bulk dye. Reference Raman measurements of the TR were performed with a bulk solution at 1.5 mM concentration. AFM correlated Raman measurements were performed by introducing a prominent feature (a scratch in Si wafer samples) and scanning almost the same area by AFM imaging and confocal Raman microscopy and then overlapping the images by manually relocating the pronounced feature in both images. The SERS enhancement factor was calculated using equation 3.1.[53-56]

$$EF = \frac{N_{bulk}}{N_{SERS}} \frac{I_{SERS}}{I_{bulk}}$$ Equation 3.1

Optical characterization of as synthesized Au nanoparticles, Au nanostars, DNA origami, Au nanostar-DNA origami hybrid structures were performed by dynamic light scattering (DLS) study, UV-Vis spectrophotometer, photoluminescence spectrophotometer, TEM, AFM, and confocal Raman microscope as described in chapter 2 of this thesis.

3.3. Results and discussion

3.3.1. Characterization of Au nanostars

Optical characterization of as synthesized Au NPs using UV-Vis spectroscopy showed an SPR band around 518 nm corresponding to Au NPs (Figure 3.1a). Structural characterization using TEM microscopy revealed formation of spherical Au NPs with an average size of 15±2 nm (Figure 3.1b and 3.1c). As synthesized Au NPs were then added to growth solution having hydrochloric acid, ascorbic acid, and $AgNO_3$. Where ascorbic acid act as a reducing agent and $AgNO_3$ assisted in directed growth that led to the formation of sharp tips. Initially, Au nanostars were synthesized using 100 µL of the Au seeds solution, the UV-Vis spectrum (Figure 3.1d) showed presence of longitudinal surface plasmon resonance (LSPR) band at 742 nm along with a very weak hump at 522 nm. The UV-Vis spectrum indicated formation of anisotropic shaped Au nanostructures. Further identification of these structures with TEM imaging confirmed formation of Au nanostars with sharp tips with an average size of 100 ± 10 nm (TEM images shown in Figure 3.1e and 3.1f). To achieve strong plasmonic coupling with a red emitting dye like TR, it was required to blue shift the LSPR of synthesized nanostars to the red region. The

plasmon band and the size of the nanostars were further tuned by varying the concentration of Ag^+ ions and seeds concentration in the growth solution. Figure 3.1g shows the UV-visible

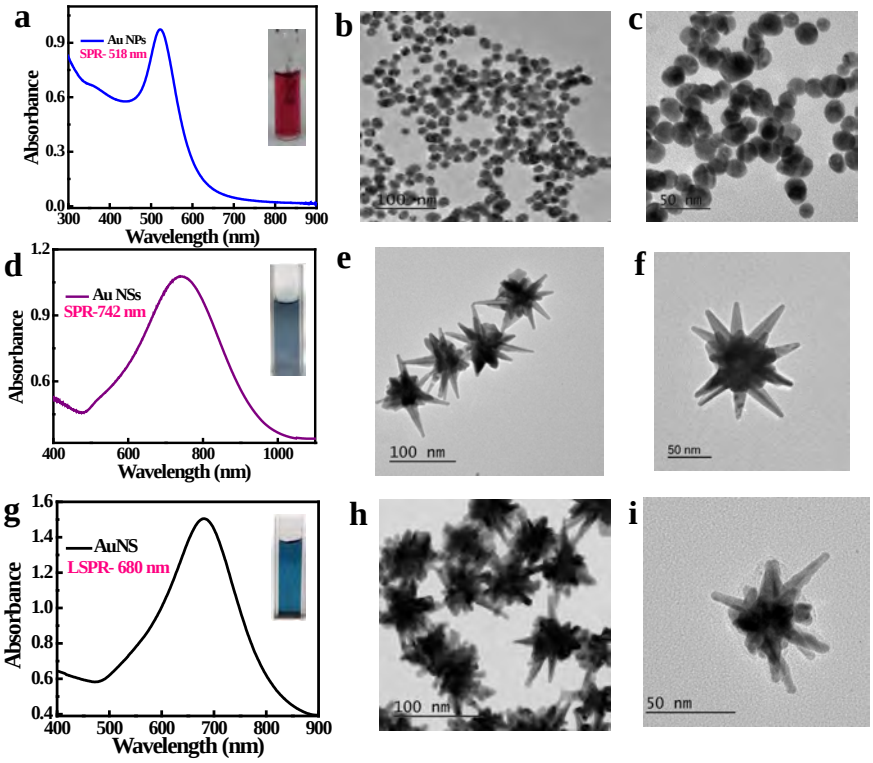

Figure 3.1. (a) UV-Vis spectrum and (b and c) TEM images of the as synthesized Au NPs. (d) UV-Vis spectrum and (e and f) TEM images of Au nanostar synthesized using 100 µL of the seeds solution. (g) UV-Vis spectrum and (h and i) TEM images of the Au nanostars synthesized using 150 µL of the seeds solution (Insets show the digital images of the Au NPs and Au nanostars solution).

spectrum of the nanostars used throughout this study. The LSPR of the nanostars was centered at 680 nm and the average size was found to be 70 ± 5 nm (TEM images shown in Figure 3.1h and 3.1i). Such Au nanostars with sharp and uniform tips giving LSPR centered at 680 nm can strongly couple with a red-emitting dye like TR and were expected to give highly enhanced SERS signal.

3.3.2. DNA functionalization of the Au nanostars

After successful aqueous medium synthesis of the nanostars, next step was to conjugate these nanostars with DNA oligonucleotides. DNA functionalization of as synthesized Au nanostars was carried out using a well-established protocol of salt aging.[48] The density of DNA

oligonucleotides on surface of Au nanoparticles depends on the final concentration of NaCl that can reduce the phosphate backbone repulsion between oligonucleotides. Thus, to achieve uniform and dense DNA coating on Au nanostar surface, the concentration of NaCl was increased slowly from 0 to 750 mM during the functionalization step (Figure 3.2a). UV−Vis absorption spectra showed no significant change in the position of LSPR band of Au nanostars after DNA functionalization (Figure 3.2b), suggesting no morphological changes after DNA modification. These DNA-functionalized Au nanostars were also found to be stable in high salt concentration of 500 mM NaCl (shown in Figure 3.2c), which reveals their stability in high salt concentration that is required for the immobilization of Au nanostars on DNA origami.

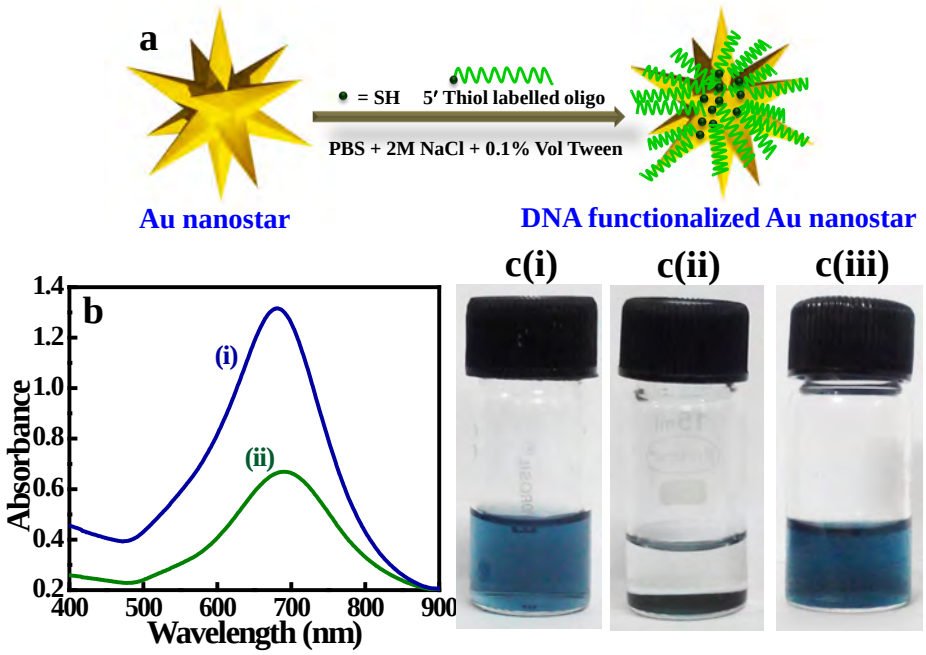

Figure 3.2. (a) Schematic representation of DNA functionalization of Au nanostars. (b) UV−visible spectra of Au nanostars before (curve (i)) and after DNA functionalization (curve (ii)). (c) Photographs of Au nanostars solution without salt (i), Au nanostars solution without DNA functionalization with PBS −500 mM NaCl buffer (ii), and DNA-functionalized Au nanostars solution with PBS −500 mM NaCl (iii).

3.3.3. Characterization of DNA origami

The folded rectangular DNA origami monomers were run on an agarose gel electrophoresis setup along with scaffold DNA and 1 Kb DNA ladder (Figure 3.3a). The applied voltage resulted in the migration of DNA origami structures and excess staple strands with different

speeds because of different length and size. There were only two bands in the lane having DNA origami, the fast and the slow band corresponded to excess staples and DNA origami structures respectively. Absence of any other slow band which could be because of aggregates as well as defective structures indicated that the DNA origami structures are assembling in high yield. AFM and TEM studies further revealed the formation of high yield of DNA origami monomer (>95%). Figure 3.3b shows the AFM images of rectangular DNA origami monomer of dimension of ~90 × 60 nm, with a height of ~ 2 nm (Figure 3.3c). TEM images further confirmed the formation of rectangular DNA origami of dimension of ~90 × 60 nm, which can hold only a large Au nanostar (Figure 3.3d and 3.3e). The size of individual DNA origami structures is limited by the size of the scaffold so, for the synthesis of Au nanostar dimer, two rectangular DNA origami monomers were linked together to form dimerized rectangular DNA origami (presented in Scheme 3.2). For the dimerization, rectangular DNA origami monomer A and monomer B were mixed together with 24 branching staples which weaved the two origami

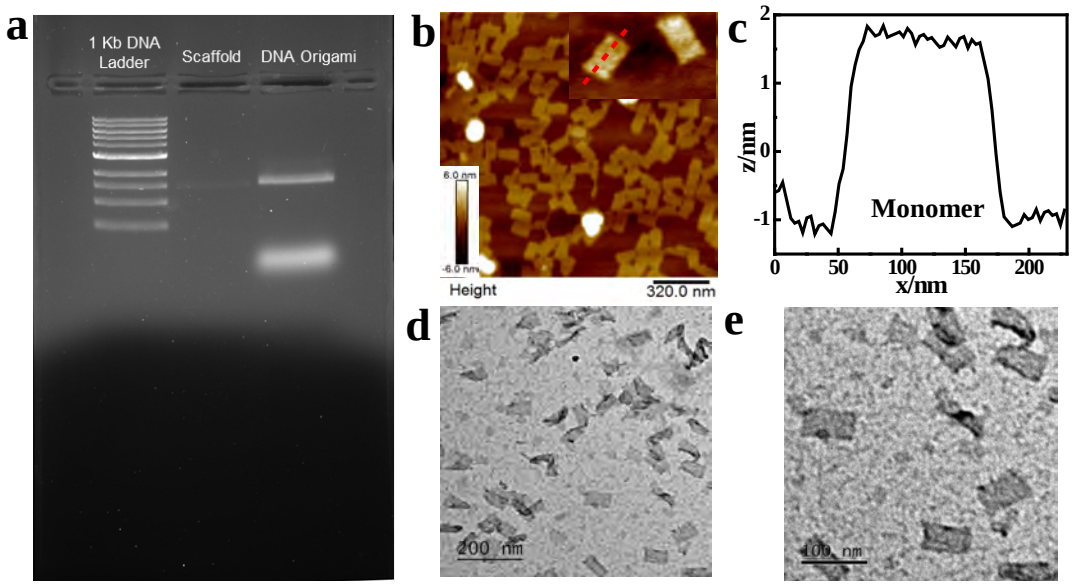

Figure 3.3. (a) Gel electrophoresis image, (b and c) AFM images and corresponding height profile, and (d and e) TEM images of rectangular DNA origami monomer.

units through their edges. The branching staples were designed in such a way that three fourth of each sequence was complementary to the scaffold of one origami monomer and remaining one-fourth of the sequence to the scaffold of the second monomer, as described by Liber et al.[49] Gel electrophoresis image (Figure 3.4a) indicated the formation of dimers. AFM and TEM studies (Figure 3.4b,c,d,e) further revealed the formation of dimerized rectangular DNA origami

with a dimension of ~ 180 × 60 nm that is capable of holding two Au nanostars. Single TR dye was incorporated into the dimerized rectangular DNA origami template by replacing one of

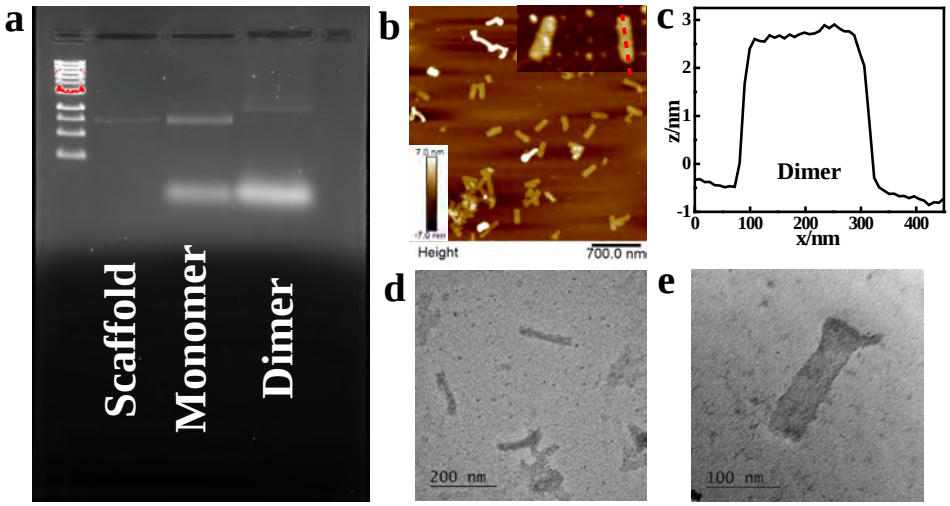

Figure 3.4. (a) Gel electrophoresis image, (b and c) AFM images and corresponding height profile, and (d and e) TEM images of rectangular DNA origami dimer.

the branchings staples with dye modified staple. To ensure the successful incorporation of a single TR dye molecule in the center of the DNA origami dimer (shown in Scheme 3.2), fluorescence spectra of the dye-bound DNA origami dimer was recorded. Before recording the fluorescence spectra, the DNA origami structures were purified using Sephacryl S-300 resin to remove excess unbound dye-labeled staple strands. The emission spectrum of the dye centered at 614 nm upon excitation with 594 nm (shown in Figure 3.5) suggested successful incorporation of dye inside the origami structure.

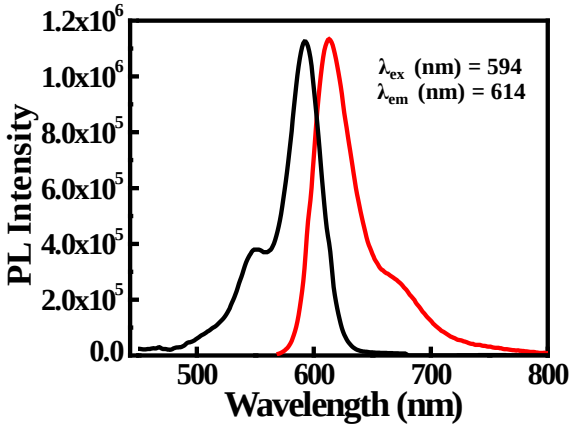

Figure 3.5. Fluorescence spectra of Texas red dye incorporated in DNA origami.

3.3.4. Assembly of Au nanostars on dimerized origami with tunable nanogap and stoichiometry

The procedure of coupling two Au nanostars on dimerized rectangular origami is schematically shown in scheme 3.2. A set of five staples of each origami monomer unit were extended at the 3′ end in order to bind complimentarily to the thiolated oligonucleotides that were conjugated on the surface of Au nanostars using Au-thiol chemistry. In this way, after annealing together each monomer origami can bind to a single Au nanostar specifically through the hybridization interactions between complementary oligonucleotides, overall resulting in dimer of Au nanostars on dimeric origami (presented in Scheme 3.2). In order to study the effect of interparticle gap on SERS efficiency, Au nanostar dimer structures with two different average gaps were synthesized. The interparticle gap was varied by changing the position of the 5 capture staple sequences on each monomeric unit. A schematic sketch of rectangular DNA origami design showing positions of capturing staples and dye labeled staple is presented in scheme 3.3.

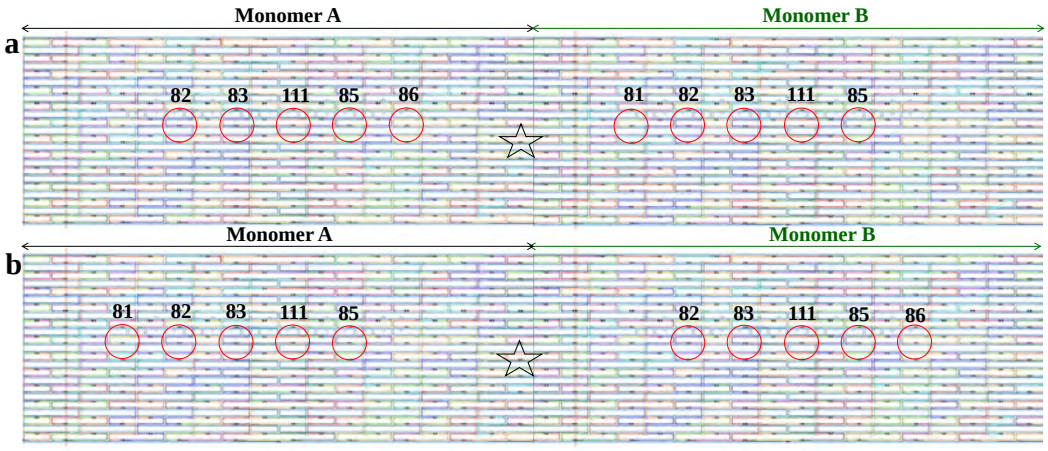

Scheme 3.3. Dimerized rectangular DNA origami design for synthesis of Au nanostar dimer with interparticle gap of (a) 7 nm and (b) 13 nm. Staple modifications for capturing Au nanostars are indicated by red colored circles. Position of Texas red dye is represented by black colored star.

For getting less interparticle gap, capturing staple strands were taken at the position of 82,83,111,85,86 of monomer A and 81,82,83,111,85 of monomer B. Similarly, for larger gap, capturing staples used were 81,82,83,111,85 and 82,83,111,85,86 for monomers A and B, respectively. To study the effect of stoichiometry on the electromagnetic field enhancement in

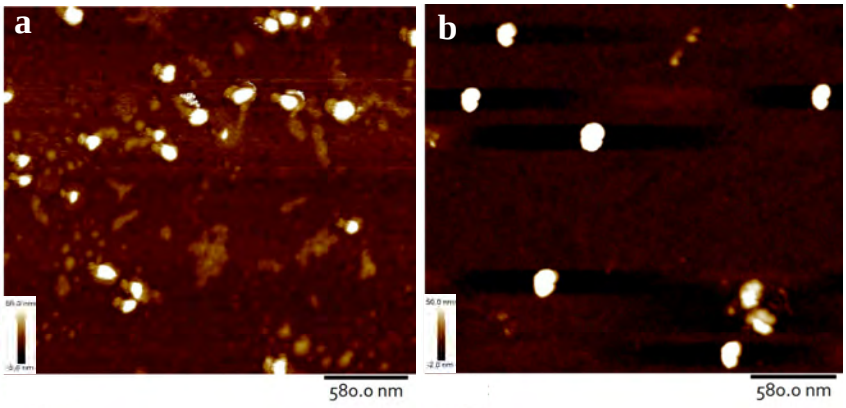

Figure 3.6. AFM images of (a) Au nanostar monomer on DNA origami and (b) Au nanostar dimer on DNA origami.

the hotspot, Au nanostar monomers were prepared by removing capture strands from one monomer unit. AFM imaging (shown in Figure 3.6a,b) confirmed the formation of Au nanostar monomer and dimer structures on DNA origami. In case of Au nanostar monomer (Figure 3.6a),

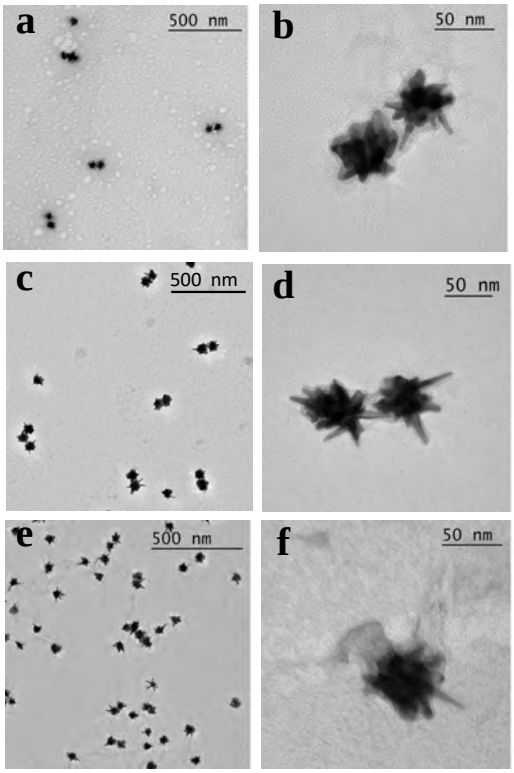

Figure 3.7. (a−d) TEM images of Au nanostar dimers on DNA origami with different interparticle gaps: (a,b) average interparticle gap of 13 nm and (c,d) gap of 7 nm. (e,f) TEM images of Au nanostar monomer on DNA origami.

DNA origami template was clearly visible. However, in case of Au nanostar dimer (Figure 3.6b) DNA origami template probably got hidden behind the Au nanostar dimer. The interparticle gap of the Au nanostar dimer could not be resolved with AFM so to determine the exact interparticle gaps TEM imaging was done. From TEM measurements of the dimer samples (shown in Figure 3.7a,b,c,d), average gaps of 13 ±1 and 7 ± 1 nm (Au nanostar core to core) were obtained. In the TEM images of Au nanostar monomer (shown in Figure 3.7e,f) the origami template is clearly visible, which further confirms successful immobilization of nanostars on origami template. We have also calculated the tip-to tip distances (d) in the conjunction region that is present between tips and cores of two nanostars after considering several TEM images of nanostar dimer structures. The tip-to tip distances were found to lie in the ranges of ~1 nm ≤ d ≤ 4 nm and ~2 nm ≤ d ≤ 4.8 nm for 7 and 13 nm nanogap dimer structures, respectively.

3.3.5. AFM correlated single-molecule Raman measurements

After the synthesis and careful characterization of our Au nanostar dimer and monomer structures, we investigated for their potential to be used in single-molecule SERS measurements. In this study, we have used two different laser sources of 532 and 633 nm wavelength for studying the dependence of SERS EFs on laser excitation wavelength. Before starting single molecule SERS measurements we recorded the reference Raman spectrum of TR

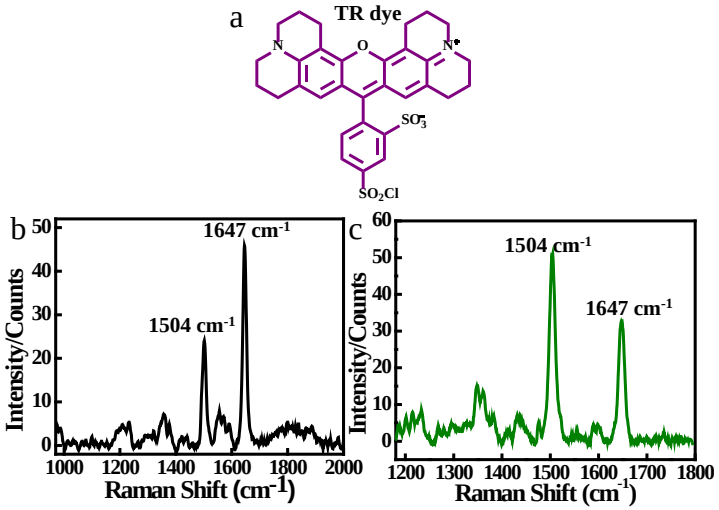

Figure 3.8. (a) Structure of Texas red dye (b and c) reference Raman spectrum of TR dye measured on the surface of 50 nm Au NPs using 532 nm and 633 nm laser excitation source respectively.

dye to determine its Raman signatures which helped us in concluding that the recorded signals are characteristic of the dye molecule. Reference Raman spectrum was (shown in Figure 3.8) was obtained by casting the TR solution (0.5 μM) on the surface of 50 nm spherical Au nanoparticles uniformly distributed over Si substrate with 532 and 632 nm laser sources. The obtained two peaks at 1504 and 1647 cm^{-1} can be assigned to aromatic ring stretching and NH deformation modes, respectively.[57] The change in the relative ratio of the intensity of the two peaks with change in the laser excitation source is also consistent with the previous reports.[58] For single molecule measurements, the nanoantennas were immobilized on Si wafer as

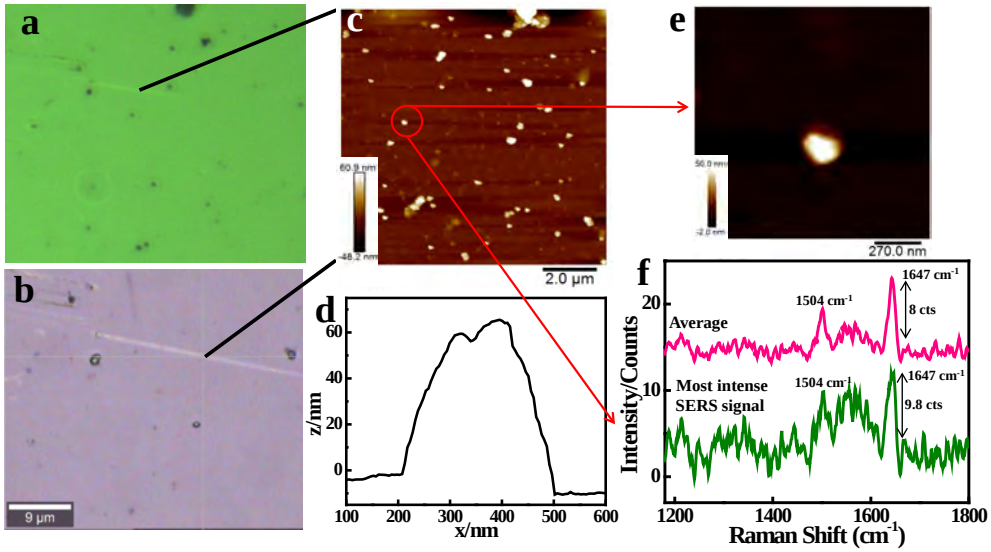

Figure 3.9. AFM-correlated Raman measurements using 532 nm laser source. (a) Optical image taken using 10× objective of AFM. (b) Optical image taken using 100× objective of confocal Raman microscope. (c) AFM images of Au nanostar dimer with interparticle gap of 7 nm and (d) corresponding height profile. (e) AFM image of single Au nanostar dimer nanostructure. (f) Average and most intense SERS spectra of TR dye bound to Au nanostar dimer on DNA origami.

described in methods section followed by AFM correlated Raman measurements. In this spectroscopic setup, almost same area is scanned by AFM imaging and confocal Raman microscopy. At first, images taken by optical microscope of AFM and confocal Raman microscope as shown in Figures 3.9a,b and 3.10a,b were overlapped by identification of pronounced features in images with precise accuracy. This was followed by scanning that particular area by AFM (Figures 3.9c and 3.10c) and then doing Raman measurements of the same area. Figures 3.9d and 3.10d represent the height profile of the recorded AFM images

shown in Figures 3.9c and 3.10c which confirm the presence of Au nanostar dimer structures on origami. Figures 3.9e and 3.10e are the AFM images of single Au nanostar dimer nanostructures. The average and most intense AFM correlated SERS spectra of TR dye bound to Au nanostar dimer on DNA origami with nanogap of 7 nm using laser excitation wavelengths of 532 and 633 nm are shown in Figures 3.9f and 3.10f, respectively. To get fair comparison of the results, during all the measurements, several instrument factors like integration time,

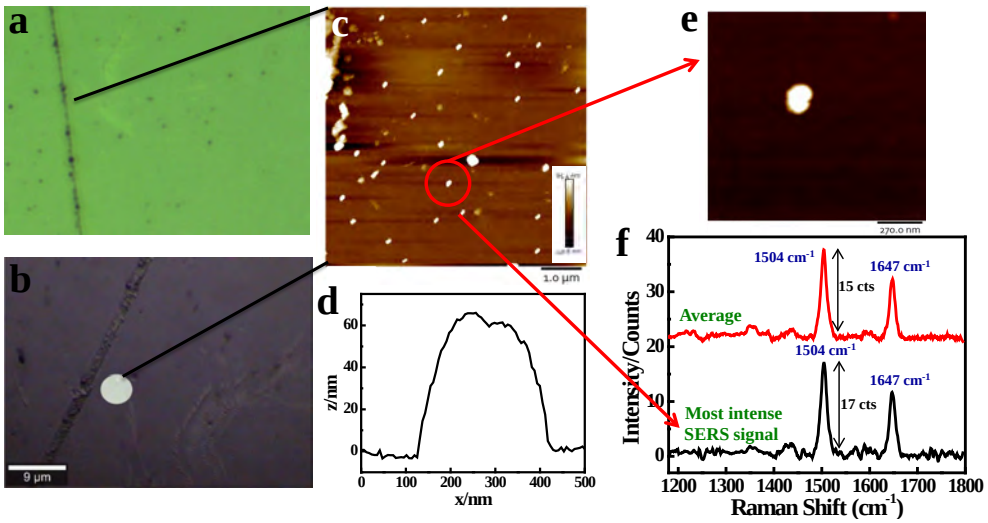

Figure 3.10. AFM-correlated Raman measurements using 633 nm laser source. (a) Optical image taken using 10× objective of AFM. (b) Optical image taken using 100× objective of confocal Raman microscope. (c) AFM images of Au nanostar dimer with interparticle gap of 7 nm and (d) corresponding height profile. (e) AFM image of single Au nanostar dimer nanostructure.(f) Average and most intense SERS spectra of TR dye bound to bound to Au nanostar dimer on DNA origami.

number of accumulations, spectral range, and laser power were kept same. The laser power was kept low to 1 mW to avoid disintegration of DNA origami structures due to heat generated at high laser powers. After identifying the desired area using AFM imaging the same area was scanned under confocal Raman microscope for recording Raman signatures of TR dye. Raman spectra of TR dye bound to different dimer structures immobilized at different regions of Si wafer were recorded. From the Raman spectra acquired at different regions of selected area, we found that the peak intensity does not remains same for all the structures but the difference was very less indicating that the gap between our structures was uniform throughout the sample (Figures 3.9f and 3.10f). Overlaid single-molecule Raman spectra of TR dye from 12 different Au nanostar dimer nanostructures (nanogap ~7 nm with 633 nm laser excitation) showing slight

change in Raman intensity and corresponding AFM images are shown in figure 3.11. Mean enhancement factor was calculated by taking ~25 different spectra acquired from 25 different structures of selected area. For calculating SERS EF, I_{SERS} was taken from the strongest Raman peaks of the TR dye, which are 1647 and 1504 cm^{-1} for 532 and 633 nm laser excitation, respectively.[53, 59] The EFs were calculated using equation 3.1 given in the experimental

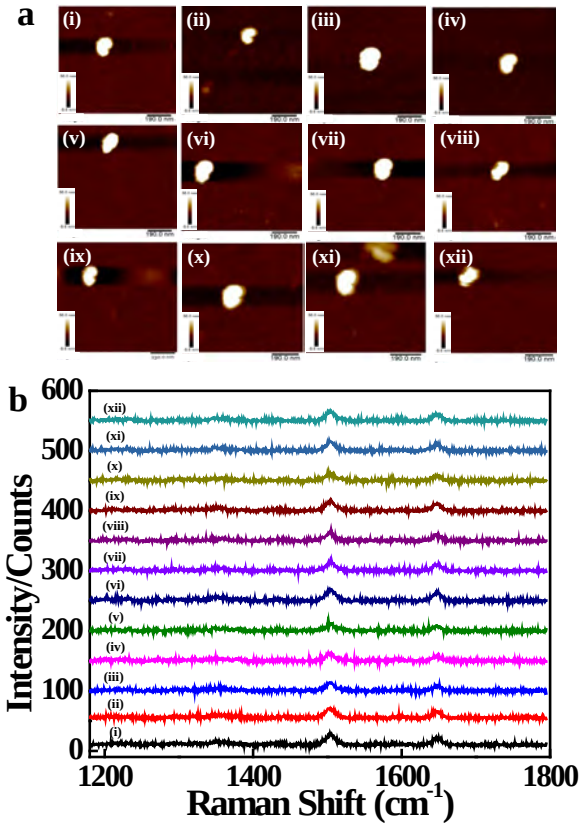

Figure 3.11. (a) AFM images of 12 different Au nanostar dimer nanostructures (7 nm nanogap), and (b) corresponding single molecule SERS spectra acquired using 633 nm laser excitation.

procedures section of this chapter. In the equation, I_{bulk} was determined by recording normal Raman spectrum of 1.5 mM solution of TR dye keeping all the instrument parameters same as to the SERS measurements. N_{Bulk} was calculated to be 5.34×10^8 by determining the number of molecules coming in the average probed volume of focused laser beam (1 μm^3).[53, 55] It has been assumed that TR dye molecules form well defined monolayer on the silicon surface for the estimation of the number of molecules being probed during Raman measurement. In an attempt to identify the total number of TR molecules contributing in the SERS signal (I_{SERS}), we considered the laser focal area of 1 μm^2.[40] After careful examination of the AFM images (shown

in 3.9c and 3.10c), we have found that only one Au nanostar dimer (assembled on DNA origami) structure is resided in the laser focal area. Now each origami structure (Au NS dimer) contains a single TR dye specifically bound in the origami, so there will be one dye present in the focal spot, and hence one independent single TR molecule is contributing in the Raman

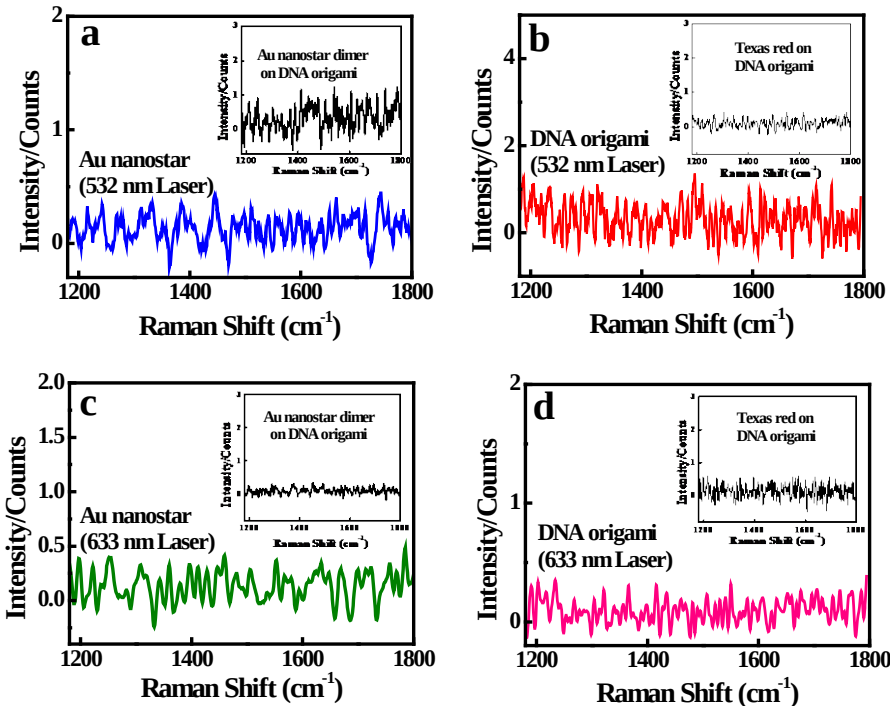

Figure 3.12. Raman spectra of (a) Au nanostar using 532 nm laser source (Au nanostar dimer on DNA origami without TR dye is shown in inset profile); (b) DNA origami using 532 nm laser source (TR dye on DNA origami without Au nanostar is shown in inset profile); (c) Au nanostar using 633 nm laser source (Au nanostar dimer on DNA origami without TR dye is shown in inset profile); and (d) DNA origami using 633 nm laser source (TR dye on DNA origami without Au nanostar is shown in inset profile).

signal. The corresponding Raman spectra of a single TR dye bound to Au nanostar dimer are shown in figures 3.9f and 3.10f with different laser excitation. As a control experiment, Raman spectra of samples comprising Au nanostars, Au nanostar dimer on DNA origami, and DNA origami without any TR dye were recorded by using both 532 and 633 nm laser excitation sources. No Raman peaks were obtained for Au nanostars only (Figure 3.12a,c) and DNA origami without any TR dye (Figure 3.12b,d). The Raman spectrum of Au nanostar dimer on DNA origami without any TR dye showed no peak with both 532 and 633 nm laser source in almost all the Raman spectra (inset of Figure 3.12a,c). However, when measurement was done with much higher laser power (~1.8 mW) two new peaks appeared as represented in figure

3.13. The peaks observed at 1331 and 1568 cm $^{-1}$ can be ascribed to DNA surrounding the Au nanostars[41] and were originated due to the electromagnetic field enhancement generated by the sharp tips of Au nanostars providing SERS enhancement for the DNA located in the hotspot.[41]

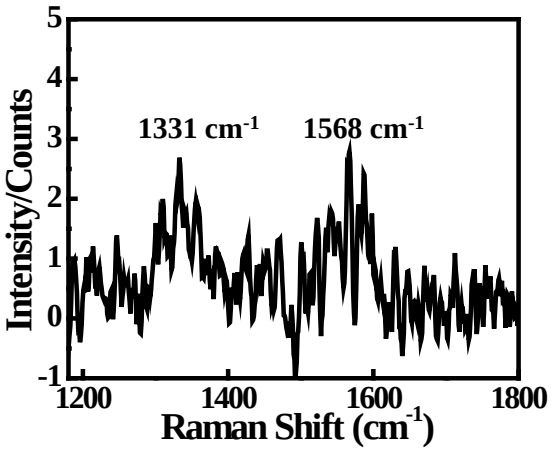

Figure 3.13. Raman spectrum of Au nanostar dimer on DNA origami (laser power used ~1.8 mW).

It is interesting to note that no Raman signals corresponding to TR dye were observed for TR dye bound to DNA origami in absence of Au nanostar even with a high laser power of 1 mW for both 532 and 633 nm laser excitation (inset of Figure 3.12b,d).

3.3.6. Effect of interparticle gap, stoichiometry, and laser wavelength on the SERS EFs

Single molecule Raman spectra of TR dye bound to Au nanostar dimers on DNA origami with different nanogaps and Au nanostar monomer and the corresponding EFs are shown in figure 3.14 and table 3.1 respectively. The strongest Raman bands of TR dye, located at 1647 and 1504 cm $^{-1}$, are clearly visible in the SERS spectra of TR for both monomer and dimer nanostars and become even more pronounced for dimer nanostar. We found that the intensity of peaks corresponding to TR dye slightly decreased upon increasing the interparticle distance from 7 to 13 nm. The mean enhancement factors of TR dye were found to be 9×10^9 and 6×10^9 using 532 nm laser excitation and 2×10^{10} and 8×10^9 using 633 nm laser excitation for Au nanostar dimers with gaps of 7 and 13 nm, respectively (shown in Table 3.1), which are sufficient enough for single TR molecule detection. It is clearly seen in the present study that the magnitude of electromagnetic field enhancement in the conjunction region decreases with increasing interparticle distance of nanostar dimer, revealing less SERS enhancement for both the lasers used. At lower interparticle gap (7 nm), the signal increases prominently due to much

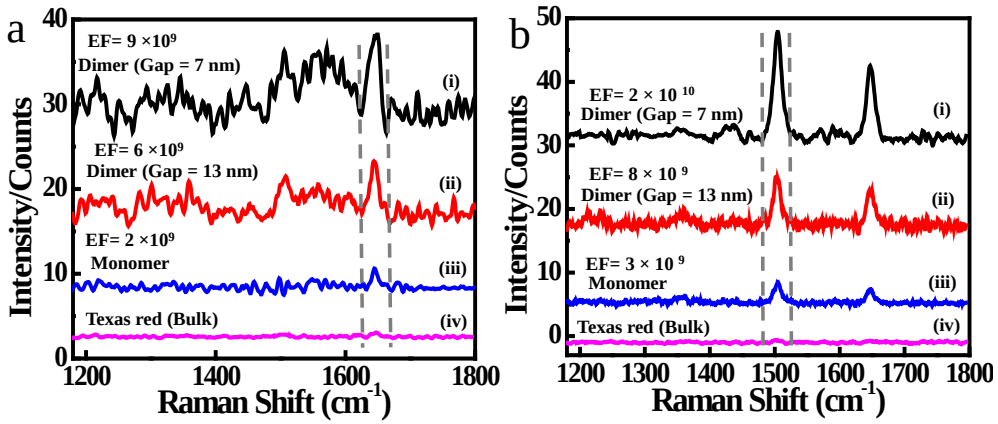

Figure 3.14. (a) SERS spectra of TR dye bound to Au nanostar dimers with average gaps of 7 nm (curve (i)) and 13 nm (curve (ii)), and TR dye bound to Au nanostar monomer on DNA origami (curve (iii)) and bulk TR dye (curve (iv)) recorded using 532 nm laser. (b) SERS spectra of TR dye bound to Au nanostar dimers with average gaps of 7 nm (curve (i)) and 13 nm (curve (ii)), and TR dye bound to Au nanostar monomer on DNA origami (curve (iii)) and bulk TR dye (curve (iv)) recorded using 633 nm laser.

stronger plasmon coupling between sharp tips and cores of two Au nanostars in the wide conjunction region. The order of distance dependence of EF was found to be in good agreement with previous results.[53, 59] It is very well evident from previous reports that lesser the interparticle gap between the plasmonic structures better the enhancements in Raman signals.[60] So, we tried to reduce the interparticle gap by choosing capture staples (83,111,85,86,87 for monomer A and 80,81,82,83,111 for monomer B) located towards the junction of the two origami units. However, it was found from TEM study of such Au nanostar dimer structures

Table 3.1. Experimentally obtained data from SERS measurements

Systems	Average interparticle gap	Raman peak Intensity of TR dye (1647 cm^{-1})	Mean Enhancement Factor (532 nm laser)	Raman peak Intensity of TR dye (1504 cm^{-1})	Mean Enhancement Factor (633 nm laser)
Au nanostar monomer	-	2.4	2×10^9	3.2	3×10^9
Au nanostar dimer	13 nm	6.43	6×10^9	7.7	8×10^9
Au nanostar dimer	7 nm	9.86	9×10^9	17	2×10^{10}

that the tips are touching to each other in the conjunction region between two nanostars and core-to-core distance between two nanostars becomes ~4 nm (shown in Figure 3.15a). Raman measurement of this dimer structure showed no enhancement of Raman signal of TR dye molecule and even the characteristic peaks were also not visible in the SERS spectrum as presented in figure 3.15b. It has been described by Aizpurua et al. that when the interparticle gap is reduced to subnanometer ($d \leq 0.3-0.4$ nm) level the plasmon modes of the dimers progressively diminishes and the charge transfer plasmon modes gradually emerge. At this point

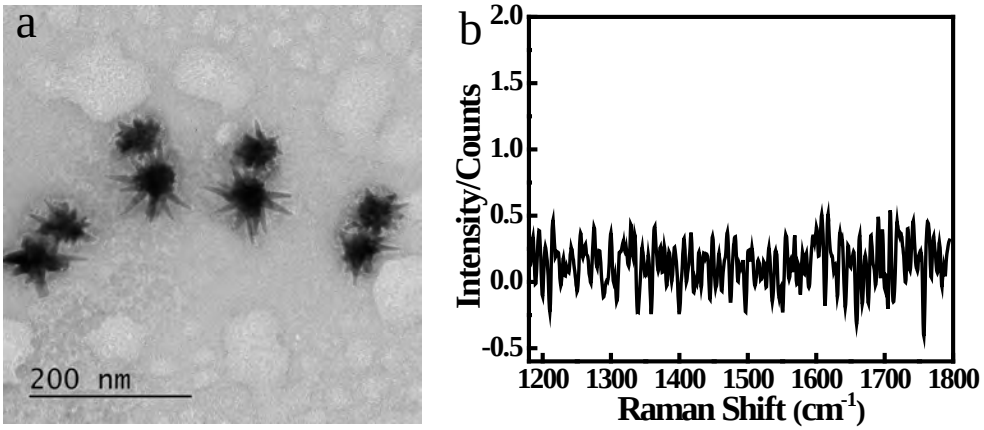

Figure 3.15. (a) TEM images of Au nanostar dimers on DNA origami with touching tips, and (b) corresponding Raman spectrum of TR dye placed in between two nanostars on DNA origami by using 633 nm laser excitation.

the two particles gets conductively connected through electron tunneling which leads to quenching of the electric near field enhancement.[61 62] In this case, there is no gap between tips of two particles in the conjunction region which leads to quantum tunnelling and results in no enhancement of Raman signal of TR which is placed in between two nanostars in the conjunction region. In a recent theoretical study, Abajo et al. also mentioned that the SERS signal enhancement can be quenched when tips and valleys are closely intertwined.[63]When we changed the stoichiometry of the structure from Au nanostar dimer to monomer the intensities of various peaks were almost halved from Au nanostar dimer to monomer due to the absence of plasmon coupling in monomer providing less SERS enhancement of TR dye for monomer. For TR dye bound to Au nanostar monomer, calculated averaged EF is 2×10^9 when 532 nm laser used. The mean EF of TR is increased by a factor of ~4 in case of 532 nm laser and by a factor of ~5 in case of 633 nm laser from monomer nanostar to dimer nanostar (gap = 7 nm). It is well reported that mean EF of Raman reporters increases from monomer to dimer due to the presence of hotspot in the dimeric junction. Ma et al. showed the similar trend of SERS

intensity enhancement of 4-ATP in Au nanostar dimer structures compared to single nanostar,[64] which agrees very well with our findings. It has been very recently demonstrated by Bukasov et al. that the EF increases upon dimerization by 1−2 orders of magnitude relative to the mean EF of single NPs.[65] The ratio of the mean intensity or mean EF of dimers to the mean intensity or mean EF of monomers (I_d/ I_m or EF_d/EF_m) for NPs on substrates depends on the nature of NPs, substrates and the position of the LSPR frequencies relative to the frequency of the exciting laser.[65] They have observed that the mean EF of 2-ATP molecule measured on Si surface was increased by a factor of 4.8 when placed in the hotspot of 60 nm sized Au NPs dimer to single Au NP whereas the mean EF ratios were 1.61 and 1.42 for Ag and Au surfaces, respectively. Our experimental findings yield the increase of mean EF of TR dye measured on Si surface by a factor of ∼5 from monomer nanostar to dimer nanostar (gap = 7 nm) which corroborates the results reported by Bukasov et al. Further, calculated EFs were found to be higher for 633 nm laser than 532 nm laser by a factor of ∼2. Higher value of EF for 633 nm laser can be attributed due to close resonance between wavelength of laser source and LSPR of Au nanostars. Hence, finding the proper excitation wavelength range to resonantly excite the plasmonic modes is important for obtaining the highest SERS signal. In SERS enhancement factor calculation error can result from different molecular orientation. We have estimated the error in mean EFs calculation by taking intensity of characteristic Raman peaks of different SERS spectra and was found to be ∼17%.

3.3.7. Effect of changing the negative curvature site on SERS EF

The negative curvature of the nanostars can be changed either by changing metal core size or by changing the number of branches of the stars (as shown in scheme 3.4). It is previously reported that by changing the negative curvature site of metal nanostructure ,the plasmon coupling and the local field enhancement can be controlled. In the present study, we have increased the negative curvature regions of Au nanostars by decreasing the number of branches of the nanostars to study its influence on the SERS responses of the nanostar dimer structures. We have measured the SERS activities of Au nanostar dimers (7 nm nanogap as shown in Figure 3.16a) with nanostar having lesser number of tips (radius of curvature of tips ∼4−6 nm, number of branches ∼6 −7) and the corresponding SERS spectrum is shown in Figure 3.16. It was found that the EF decreases by a factor of ∼13 for nanostar dimer structures with higher negative curvature. This is due to the increase of separation distance between tips in the nanostar which can decrease the coupling between the tips and minimize the local field enhancement as

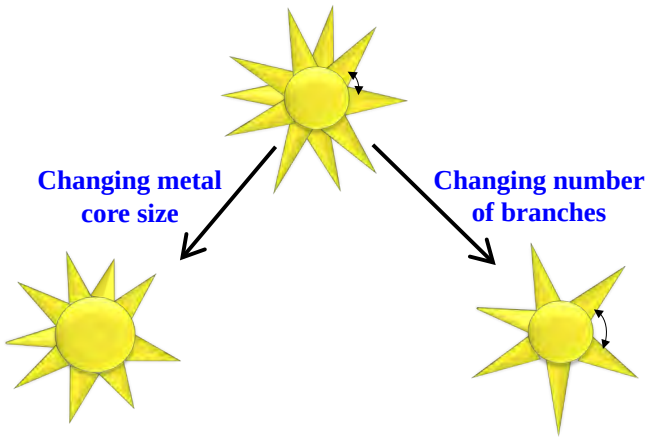

Scheme 3.4. Tuning the negative curvature of Au nanostars.

mentioned by Odom et al.[66] for Au nanocrescent type of structures. Our experimental findings confirm that the SERS-based detection of single TR molecule is possible after placing the dye in the center of the conjunction region of Au nanostar dimer bound to DNA origami structure. Moreover, in a remarkable observation, it was noted that the highly enhanced electromagnetic

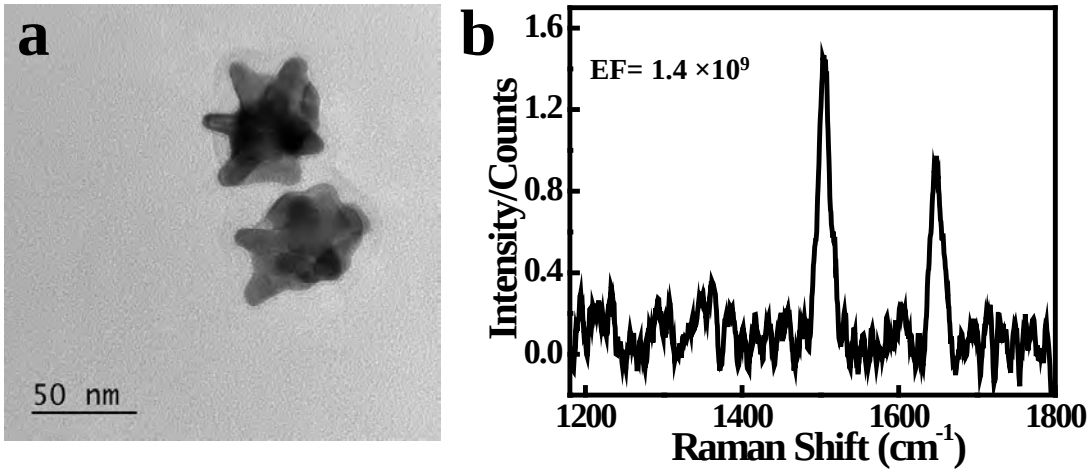

Figure 3.16. (a) TEM images of Au nanostar dimer with interparticle gap 7 nm, and (b) SERS spectrum of TR dye bound to origami in the hotspot of Au nanostar dimer with blunt tips. Laser excitation used was 633 nm.

field generated by the coupling of sharp tips of Au nanostars exhibits excellent SERS sensitivity even at an interparticle separation distance of 13 nm. Thus, the Au nanostar dimeric structures on origami have highly SERS-active wide conjunction region that can provide enough space for the accommodation of large biomolecule of interest (such as protein) to enable its specific detection via single-molecule SERS.

3.4. Conclusion

In this chapter, the synthesis of Au nanostar dimer with tunable interparticle gap and controlled stoichiometry has been demonstrated. Rectangular DNA origami has been used as a template for self-assembling the plasmonic nanoantennas. DNA origami technique provides a reliable fabrication method to build probes of strongly coupled nanostructure dimers with precisely controlled particle spacing with sub nm accuracy, spatial orientation, and well-defined geometry in order to create plasmonic hotspots of tunable strength. In this study, TR dye was used as a Raman probe which was specifically placed in the center of the conjunction region between the Au nanostar-DNA origami hybrid structures with different nanogaps and stoichiometry. We found that the most intense Raman bands of TR dye can be clearly identified in the SERS spectra of single TR dye molecules in both monomer and dimer nanostars on DNA origami substrates. The mean EFs of TR dye were obtained to be in the order of 10^{10}, which are high enough for single-analyte detection. Consequently, the detection of single analyte molecules with much lower Raman cross sections might be feasible by using these structures. Such hybrid nanoantennas assembled on DNA origami with controlled interparticle distance and stoichiometry act as excellent SERS substrates and will have potential applications as a cost-effective and reproducible platform for single-molecule sensing. Importantly, DNA origami offers several sequence-specific binding sites where a wide variety of biomolecules can be attached specifically at the hotspot region with great precision, and this may allow molecules to be targeted at a single-molecule level.

Note:

- The permission has been granted by authors and corresponding author of the published paper prior to adopting in the present thesis. The associated relevant publication is:

Swati Tanwar, Krishna Kanta Haldar, and Tapasi Sen "DNA origami directed Au nanostar dimers for single-molecule surface-enhanced Raman scattering" ***Journal of the American Chemical Society***, 2017, 139 (48), 17639-17648.

References

1. H. P. Lu, L. Xun and X. S. Xie, *Science*, 1998, **282**, 1877-1882.
2. P. Holzmeister, G. P. Acuna, D. Grohmann and P. Tinnefeld, *Chemical Society Reviews*, 2014, **43**, 1014-1028.
3. N. P. W. Pieczonka and R. F. Aroca, *Chemical Society Reviews*, 2008, **37**, 946-954.
4. S. Nie and S. R. Emory, *Science*, 1997, **275**, 1102-1106.
5. K. Kneipp, Y. Wang, H. Kneipp, L. T. Perelman, I. Itzkan, R. R. Dasari and M. S. Feld, *Physical Review Letters*, 1997, **78**, 1667-1670.
6. J. M. McMahon, S. Li, L. K. Ausman and G. C. Schatz, *The Journal of Physical Chemistry C*, 2012, **116**, 1627-1637.
7. E. C. Le Ru and P. G. Etchegoin, *Chemical Physics Letters*, 2006, **423**, 63-66.
8. S. Yang, X. Dai, B. B. Stogin and T.-S. Wong, *Proceedings of the National Academy of Sciences*, 2016, **113**, 268-273.
9. A. P. Craig, A. S. Franca and J. Irudayaraj, *Annual Review of Food Science and Technology*, 2013, **4**, 369-380.
10. T. Vo-Dinh, *Sensors and Actuators B: Chemical*, 1995, **29**, 183-189.
11. R. A. Halvorson and P. J. Vikesland, *Environmental Science & Technology*, 2010, **44**, 7749-7755.
12. P. H. C. Camargo, M. Rycenga, L. Au and Y. Xia, *Angewandte Chemie International Edition*, 2009, **48**, 2180-2184.
13. L. Novotny and N. van Hulst, *Nature Photonics*, 2011, **5**, 83-90.
14. M. J. Mulvihill, X. Y. Ling, J. Henzie and P. Yang, *Journal of the American Chemical Society*, 2010, **132**, 268-274.
15. Q. Zhang, N. Large and H. Wang, *ACS Applied Materials & Interfaces*, 2014, **6**, 17255-17267.
16. L. Rodríguez-Lorenzo, R. A. Álvarez-Puebla, F. J. G. de Abajo and L. M. Liz-Marzán, *The Journal of Physical Chemistry C*, 2010, **114**, 7336-7340.
17. S. Barbosa, A. Agrawal, L. Rodríguez-Lorenzo, I. Pastoriza-Santos, R. A. Alvarez-Puebla, A. Kornowski, H. Weller and L. M. Liz-Marzán, *Langmuir*, 2010, **26**, 14943-14950.
18. P. F. Liao and A. Wokaun, *The Journal of Chemical Physics*, 1982, **76**, 751-752.
19. C. G. Khoury and T. Vo-Dinh, *The Journal of Physical Chemistry C*, 2008, **112**, 18849-18859.
20. A. Shiohara, J. Langer, L. Polavarapu and L. M. Liz-Marzán, *Nanoscale*, 2014, **6**, 9817-9823.
21. C. L. Nehl, H. Liao and J. H. Hafner, *Nano Letters*, 2006, **6**, 683-688.
22. E. C. Le Ru, E. Blackie, M. Meyer and P. G. Etchegoin, *The Journal of Physical Chemistry C*, 2007, **111**, 13794-13803.
23. H. Xu, E. J. Bjerneld, M. Käll and L. Börjesson, *Physical Review Letters*, 1999, **83**, 4357-4360.
24. A. Campion and P. Kambhampati, *Chemical Society Reviews*, 1998, **27**, 241-250.
25. G. Kumari, J. Kandula and C. Narayana, *The Journal of Physical Chemistry C*, 2015, **119**, 20057-20064.
26. G. McNay, D. Eustace, W. E. Smith, K. Faulds and D. Graham, *Applied Spectroscopy*, 2011, **65**, 825-837.
27. C. J. L. Constantino, T. Lemma, P. A. Antunes and R. Aroca, *Analytical Chemistry*, 2001, **73**, 3674-3678.
28. P. J. G. Goulet, N. P. W. Pieczonka and R. F. Aroca, *Journal of Raman Spectroscopy*, 2005, **36**, 574-580.
29. R. M. Stöckle, Y. D. Suh, V. Deckert and R. Zenobi, *Chemical Physics Letters*, 2000, **318**, 131-136.
30. B. Pettinger, B. Ren, G. Picardi, R. Schuster and G. Ertl, *Physical Review Letters*, 2004, **92**, 096101.
31. P. W. K. Rothemund, *Nature*, 2006, **440**, 297-302.
32. E. S. Andersen, M. Dong, M. M. Nielsen, K. Jahn, R. Subramani, W. Mamdouh, M. M. Golas, B. Sander, H. Stark, C. L. P. Oliveira, J. S. Pedersen, V. Birkedal, F. Besenbacher, K. V. Gothelf and J. Kjems, *Nature*, 2009, **459**, 73-76.
33. A. Samanta, Y. Zhou, S. Zou, H. Yan and Y. Liu, *Nano Letters*, 2014, **14**, 5052-5057.
34. G. P. Acuna, M. Bucher, I. H. Stein, C. Steinhauer, A. Kuzyk, P. Holzmeister, R. Schreiber, A. Moroz, F. D. Stefani, T. Liedl, F. C. Simmel and P. Tinnefeld, *ACS Nano*, 2012, **6**, 3189-3195.

35. G. P. Acuna, F. M. Möller, P. Holzmeister, S. Beater, B. Lalkens and P. Tinnefeld, *Science*, 2012, **338**, 506-510.
36. V. V. Thacker, L. O. Herrmann, D. O. Sigle, T. Zhang, T. Liedl, J. J. Baumberg and U. F. Keyser, *Nature communications*, 2014, **5**, 3448.
37. S. Simoncelli, E. M. Roller, P. Urban, R. Schreiber, A. J. Turberfield, T. Liedl and T. Lohmuller, *Acs Nano*, 2016, **10**, 9809-9815.
38. P. Kühler, E.-M. Roller, R. Schreiber, T. Liedl, T. Lohmüller and J. Feldmann, *Nano Letters*, 2014, **14**, 2914-2919.
39. P. Zhan, T. Wen, Z.-g. Wang, Y. He, J. Shi, T. Wang, X. Liu, G. Lu and B. Ding, *Angewandte Chemie International Edition*, 2018, **57**, 2846-2850.
40. J. Prinz, C. Heck, L. Ellerik, V. Merk and I. Bald, *Nanoscale*, 2016, **8**, 5612-5620.
41. J. Prinz, B. Schreiber, L. Olejko, J. Oertel, J. Rackwitz, A. Keller and I. Bald, *The Journal of Physical Chemistry Letters*, 2013, **4**, 4140-4145.
42. *Nanotechnology*, 2008, **19**.
43. Z. Kereselidze, V. H. Romero, X. G. Peralta and F. Santamaria, *J Vis Exp*, 2012, DOI: 10.3791/3570, 3570.
44. L. Wang, X. Jiang, Y. Ji, R. Bai, Y. Zhao, X. Wu and C. Chen, *Nanoscale*, 2013, **5**, 8384-8391.
45. J. Li, B. Zhu, Z. Zhu, Y. Zhang, X. Yao, S. Tu, R. Liu, S. Jia and C. J. Yang, *Langmuir*, 2015, **31**, 7869-7876.
46. H. Yuan, C. G. Khoury, H. Hwang, C. M. Wilson, G. A. Grant and T. Vo-Dinh, *Nanotechnology*, 2012, **23**, 075102.
47. J. Turkevich, P. C. Stevenson and J. Hillier, *Discussions of the Faraday Society*, 1951, **11**, 55-75.
48. C. A. Mirkin, R. L. Letsinger, R. C. Mucic and J. J. Storhoff, *Nature*, 1996, **382**, 607-609.
49. M. Liber, T. E. Tomov, R. Tsukanov, Y. Berger and E. Nir, *Small*, 2015, **11**, 568-575.
50. R. Jungmann, M. Scheible, A. Kuzyk, G. Pardatscher, C. E. Castro and F. C. Simmel, *Nanotechnology*, 2011, **22**, 275301.
51. R. Liu, D. Hu, X. Tan and H. P. Lu, *Journal of the American Chemical Society*, 2006, **128**, 10034-10042.
52. J. Liu, A. Stace-Naughton, X. Jiang and C. J. Brinker, *Journal of the American Chemical Society*, 2009, **131**, 1354-1355.
53. J. Kumar and K. G. Thomas, *The Journal of Physical Chemistry Letters*, 2011, **2**, 610-615.
54. S. Harmsen, M. A. Bedics, M. A. Wall, R. Huang, M. R. Detty and M. F. Kircher, *Nature Communications*, 2015, **6**, 6570.
55. D. Jana, A. Mandal and G. De, *ACS Applied Materials & Interfaces*, 2012, **4**, 3330-3334.
56. D. Paital, T. Sen, A. Patra and K. Haldar, *Gold Bulletin $V 50*, 2017, 313-317.
57. D. K. Corrigan, N. Gale, T. Brown and P. N. Bartlett, *Angewandte Chemie International Edition*, 2010, **49**, 5917-5920.
58. G. Moula and R. F. Aroca, *Analytical Chemistry*, 2011, **83**, 284-288.
59. M. Shanthil, R. Thomas, R. S. Swathi and K. George Thomas, *The Journal of Physical Chemistry Letters*, 2012, **3**, 1459-1464.
60. G. J. Kovacs, R. O. Loutfy, P. S. Vincett, C. Jennings and R. Aroca, *Langmuir*, 1986, **2**, 689-694.
61. R. Esteban, A. Zugarramurdi, P. Zhang, P. Nordlander, F. J. García-Vidal, A. G. Borisov and J. Aizpurua, *Faraday Discussions*, 2015, **178**, 151-183.
62. W. Zhu, R. Esteban, A. G. Borisov, J. J. Baumberg, P. Nordlander, H. J. Lezec, J. Aizpurua and K. B. Crozier, *Nature Communications*, 2016, **7**, 11495.
63. D. M. Solís, J. M. Taboada, F. Obelleiro, L. M. Liz-Marzán and F. J. García de Abajo, *ACS Photonics*, 2017, **4**, 329-337.
64. W. Ma, M. Sun, L. Xu, L. Wang, H. Kuang and C. Xu, *Chemical Communications*, 2013, **49**, 4989-4991.
65. S. Sergiienko, K. Moor, K. Gudun, Z. Yelemessova and R. Bukasov, *Physical Chemistry Chemical Physics*, 2017, **19**, 4478-4487.
66. T. W. Odom, E.-A. You and C. M. Sweeney, *The Journal of Physical Chemistry Letters*, 2012, **3**, 2611-2616.

Chapter 4

Au@Ag bimetallic nanostar dimer nanoantennas for single molecule SERS and fluorescence enhancement

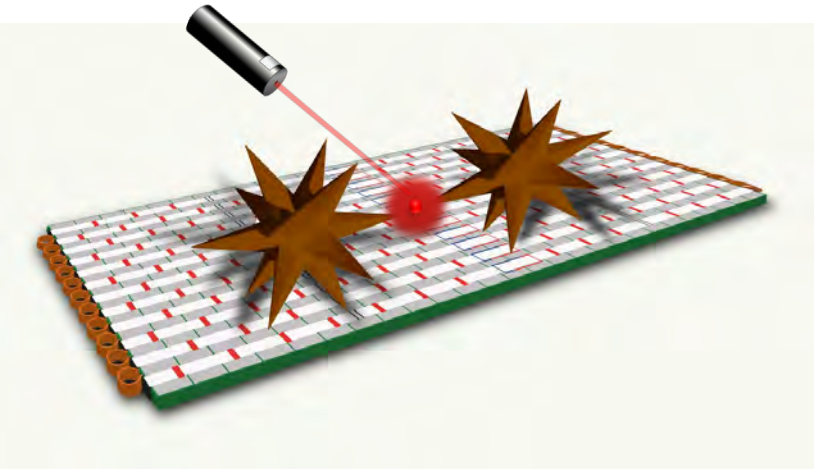

Au@Ag nanostar dimer on DNA origami

4.1. Introduction

Surface-enhanced Raman spectroscopy (SERS), owing to its unique features such as molecular specificity and extremely high sensitivity,[1, 2] has progressed its applications from ensemble systems to highly sophisticated single molecule systems.[3-7] But, as demonstrated by Fang et al., out of 10^6 SERS active sites only 63 yields high enhancements accounting to 24% of the overall SERS intensity[8], there is a pressing need for designing new SERS active substrates that can yield high enhancement factors (EFs), good reproducibility and uniform response. Considerable efforts are being put to identify new plasmonic materials and methods of fabrication to optimize SERS active substrate and configure them to yield highest EFs.[9] Among all plasmonic metal nanoparticles, Au and Ag nanoparticles (NPs) occupy the center stage in SERS based research due to their fascinating optical and electronic properties.[10, 11] In comparison with Ag, Au NPs are chemically stable, highly biocompatible and offer easy surface modification but yield lower EFs in the visible region.[12, 13] On the other hand, Ag NPs have high plasmonic efficiency and are more effective in terms of EFs but are prone to oxidation.[14-16]

To meet this end, bimetallic Au@Ag nanoparticles have come up as an alternative that combines the best of both metals i.e. enhanced plasmonic properties (high extinction coefficient) of Ag, and chemical stability of Au in one structure.[17] They also provide control over tuning the position of surface plasmon resonance (SPR) band by simply changing the thickness of the Ag coating,[18, 19] which makes them well suited for surface enhanced resonant Raman scattering studies (SERRS). It is very well known that SERRS results in better EFs than SERS and can detect analyte down to a single molecule level.[20, 21] Fan et al.[16] and Freeman et al.[20] carried out a comparative analysis of SERS efficiency of Au@Ag bimetallic nanoparticles with pure Au and Ag NPs, they found bimetallic nanoparticles are resulting in a better enhancement in SERS signals. In addition to contribution of the properties from the individual components, a unique electronic transfer from the Au core to the Ag shell imparts intriguing properties such as biocompatibility and stability against oxidation to the Au@Ag bimetallic structure.[22-24] It is important to note that electronic interactions between the Au core and Ag shell depend on the thickness of the Ag shell, the thicker the Ag shell weaker the interactions become.[23] Very recently Feng et al. found that an Ag shell thickness of 2.4 nm is optimum for getting the highest charge transfer effects and biocompatibility (both in vitro and in vivo).[25] Another important aspect of Au@Ag bimetallic system which gives them an edge over other bimetallic systems is similar lattice parameters (0.40786 nm for Au and 0.40862 nm for Ag) which leads to epitaxial growth of Ag over Au NP core providing a high degree of control over

shape and size of the nanoparticles.[26] In view of their multifunctional properties, Au@Ag bimetallic systems have been widely explored for a diversified range of SERS and non-SERS based applications.[27-31] Recently, Lim et al. used gap tailored Au-Ag core shell nanodumbbells for single molecule SERS studies and obtained a EF factor to the order of 10^{12}.[32] In another report, Heck et al. used Au-Ag core shell nanoparticles for single molecule SERS enhancement of two different dye molecules i.e. Cy3 and TAMRA and obtained EFs to the order of 10^{8} to 10^{10}.[33] As compared to metal nanospheres, anisotropic shaped metal nanoparticles are believed to yield higher enhancements due to high intensity EM field generated near the vicinity of sharp edges.[34] Among them, multi-branched Au nanostars (Au NSs) display superior performances for SERS compared to other morphologies, due to the strong electromagnetic field enhancement around the tips and the tunable localized SPR absorption band from the visible to near infrared (NIR) region.[35-37] Anisotropic Au@Ag bimetallic nanostructures comprise of a powerful combination of excellent plasmonic effects and higher EM field intensity due to the sharp edges.[38, 39] There are numerous reports where different anisotropic shaped Au@Ag bimetallic nanoparticles have been used for ensemble SERS applications. [13, 18, 40] To the best of our knowledge till now there are no reports of Ag coated Au bimetallic nanostars (Au@Ag NSs) being used for single molecule SERS enhancement studies. Very recently, William et al. carried out single molecule SERS studies using sprouted potato-shaped Au-Ag bimetallic nanoparticles.[41] Although the obtained limit of detection for Raman active molecules was lower than fM, the system lack precise localization of target analyte in the hotspot which is imperative for designing efficient plasmonic nanoantennas.

An abundance of molecular biomarkers exist on diseased cells and tissues, and a number of them are eventually released by pathogens into their surrounding mediums thereby forming promising non-invasive and real-time surrogates for diagnosis. They act as representative readouts and offer a unique route for the assessment of associated clinical conditions, monitoring their prognosis, and providing effective treatment.[42] One of the clinically important bacterial biomarkers which require immediate attention is pyocyanin. It is a toxin released from gram negative bacterium *Pseudomonas aeruginosa*, known to cause respiratory tract infections.[43] Normally it is identified using bacteriological culture methods that require at least 24 hours for reliable results. So, it is highly desirable to develop fast label-free detection methods that can detect pyocyanin directly in the biological samples with high sensitivity and selectivity. The unprecedented ability of SERS to identify a specific analyte from a complex

mixture with high sensitivity has fueled research for the development of SERS based sensors.[44-46]

The first part of this chapter demonstrates that plasmonic nanoantennas designed using Au@Ag bimetallic nanostars can be used for enhancing single molecule SERS signals of FAM, Cy3 and TR dye molecules corresponding to different regions of visible spectrum. The programmable nature of DNA origami has given it an edge over other solution[47, 48] and lithography[49] based methods and it has emerged as a powerful method of nanofabrication to achieve control over the self-assembly of nanoparticles into complex plasmonic nanoantenna designs such as Au nanostar dimers,[50] bowtie nanoantenna,[51] assembling Au nanolenses,[52] and localizing the desired target molecule in the hot spot of plasmonic nanoantenna.[53-55] DNA origami was used as a template for self-assembling Au@Ag NSs with different interparticle gaps and stoichiometry and positioning single FAM, Cy3, and TR dye molecules in the plasmonic hotspot. Further, we have demonstrated that the designed nanoantennas can be used as a high-performance optical sensor for the sensing of bacterial biomarker pyocyanin with a limit of detection (LOD) of 500 pM.

Fluorescence based spectroscopy and imaging techniques are powerful optical tools that have revolutionized the field of science and technology. The high sensitivity of this technique paved the way for the development of fluorescence based single molecule detection methods. Due to diffraction-limited resolution (approx. 250 nm), single-molecule fluorescence measurements can only be performed in a limited concentration range from roughly 1 pM to 1 nM.[56] Due to which optimum signal to noise ratio required for single molecule detection is lost. To overcome the concentration limit, light must be confined toward the nanometer scale, far below the classical wavelength size set by the diffraction limit. Plasmonic nanoantennas offer extremely promising strategies to enhance the brightness of the fluorescent marker in single-molecule fluorescence measurement and breach the limitations set by diffraction.[57] The extent of fluorescence enhancement is strongly dependent on the particle size, shape, spectral overlap, and separation distance between the chromophores and metal NPs.[58] Several examples are reported that highlights the utility of DNA origami assembled plasmonic nanoantennas for single molecule fluorescence enhancement studies. For example, Acuna et al. used pillar DNA origami for designing Au nanoparticles dimer structures showing upto 5000 fold enhancement in single molecule fluorescence signals.[59, 60] Vietz et al. demonstrated that DNA origami-Ag nanoparticle dimer structures can enhance fluorescence signals by more than 2 orders of magnitude for dyes throughout the visible spectral range.[61] Zhang et al. created a series of plasmon coupled Au nanorod dimer structures using DNA origami and investigated the effect of

different gap sizes on fluorescence enhancement at single particle level. A maximum enhancement factor of 470-fold was achieved for the gap size of 6.1 nm. The second part of this chapter demonstrates the utility of designed Au@Ag NS dimer structures with interparticle gap of 5 nm for single molecule fluorescence enhancement studies.

4.2. Experimental section

4.2.1. Materials

Magnesium chloride hexahydrate ($MgCl_2.6H_2O$), ethylenediaminetetraacetic acid disodium (EDTA), HEPES buffer solution (pH=5), gold chloride trihydrate ($HAuCl_4.3H_2O$, purity ≥ 99.9%), trisodium citrate dihydrate ($Na_3C_6H_5O_7$) , L-Ascorbic acid, silver nitrate ($AgNO_3$), sodium dodecyl sulphate (SDS), tris(hydroxymethyl)aminomethane (Tris base), tris-(carboxyethyl) phosphine hydrochloride (TCEP.HCl), 1 M Potassium phosphate monobasic solution (KH_2PO_4), 1 M potassium phosphate dibasic solution (K_2HPO_4), pyocyanin, phosphate buffer saline (PBS) tablets, biotin labeled bovine albumin, and sodium chloride (NaCl) were purchased from Sigma-Aldrich and used without further purification. Ammonium hydroxide (NH_4OH, 25%), hydrochloric acid (HCl), Tween 20 and acetic acid (CH_3COOH) were purchased from Merck. Hydrofluoric acid was purchased from Central Drug House fine chemicals. NeutrAvidin protein and Lab-Tek chambered coverglass were purchased from Thermo Fisher Scientific. M13mp18 single stranded DNA was purchased from New England Biolabs and was used without further purification. All modified and unmodified staple strands were purchased from Integrated DNA Technologies (IDT). Thiol, Cy3, FAM, Texas red (TR) dye and biotin labeled DNA oligonucleotides were purchased from IDT with HPLC purification. Sephacryl S-300 high resolution resin was bought from GE Healthcare. Carbon coated Cu TEM grids were procured from Ted Pella. AFM mica discs of V1 quality were bought from Agar Scientific. Si wafer (double side polished with resistivity 1-10 ohm.cm) was purchased from Ekta Marketing corporation. Micro bio spin chromatography columns for packing of resin were purchased from Bio-Rad. All the experiments were carried out in type 1 ultrapure water.

4.2.2. Experimental procedures

4.2.2.1. Synthesis of Au@Ag NSs

Au NSs were synthesized according to previously reported protocol.[50] Ag coated Au NSs were prepared by the subsequent addition of 1 µL of 0.1 M $AgNO_3$, 1 µL of 0.1M ascorbic acid and 2

µL of NH_4OH solution to 1 mL solution of Au NSs. After stirring for 2 minutes, the color of solution changed from blue to purple indicating the coating of Ag on Au NSs. A 40 µL aliquot of 0.1 M SDS solution was then added to the solution and further stirred for 5 minutes. The solution was then centrifuged at 4000 rcf for 10 min and redispersed in 5 mM HEPES buffer (pH-3). Figure 4.1 shows the schematic diagram of the synthesis of Au@Ag NSs.

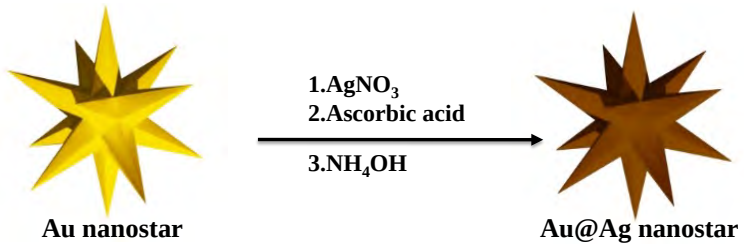

Figure 4.1. Schematic depiction of the synthesis of Au@Ag NSs.

4.2.2.2. DNA functionalization of Au@Ag NSs

The DNA conjugates of Au@Ag NSs with thiolated DNA oligonucleotides were prepared by pH assisted fast binding of oligonucleotides to nanoparticles followed by stepwise salt addition. [62, 63] At first, the disulphide protected thiol group of DNA oligonucleotides was deprotected using TCEP.HCl. The thiol protected DNA oligonucleotides were incubated with TCEP.HCl with a molar ratio of 1:200 for 3 hours. Deprotected DNA oligonucleotides were then incubated with Au@Ag NSs suspended in HEPES buffer (pH=3) for 30 minutes. This was followed by addition of 10% Tween 20 solution and 4:5 mixture of KH_2PO_4 and K_2HPO_4 buffers with a time gap of 15 minutes. The mixture was kept for overnight stirring. Further, the salt concentration of solution was slowly increased to 750 mM by gradual addition of PBS, 2M NaCl, 0.1% Vol Tween 20 buffer solution. After salt addition, the reaction mixture was further kept for overnight stirring. The Au@Ag NSs DNA conjugates were purified by 3 times centrifugation at a rate of 5,000 × g, 10 min for each time. The supernatant was carefully removed and the nanoparticles were finally resuspended in 0.5×TAE buffer.

4.2.2.3. Assembly of DNA origami

The rectangular DNA origami template was assembled in a PCR thermocycler by mixing M13mp18 scaffold DNA, staple sequences and modified sequences to a final concentration of 2 nM, 10 nM, and 20 nM respectively in 1× TAE buffer having 12.5 mM $MgCl_2$. The thoroughly

mixed reaction mixture was subjected to a folding program comprising of heating to 95 ºC followed by cooling down to 20 ºC in a duration of 1.5 hours.

Dimerization of rectangular DNA origami was done according to previously reported protocol.[50] Unpurified solutions of monomer A and monomer B were mixed with 24 branching staples to a final concentration of 40 nm in 50 × TAE buffer with 12.5 mM $MgCl_2$. The reaction mixture was kept at room temperature for 24 hours. Dimerized rectangular DNA origami was purified using Sephacryl S-300 HR resin.

The rectangular DNA origami structures used for preparing sample for single molecule fluorescent enhancement studies were assembled using 4 biotin labeled DNA sequences. The regular staples were replaced by biotinylated DNA strands in the preassembly used for assembling the origami structures. Biotin modifications were done at the 5' end of the DNA oligo's so that the biotin group comes on the origami face opposite to the face having capture DNA sequences. The details of biotin labeled DNA sequences are given in table 9 of appendix A. Dimerization of rectangular DNA origami was done using 23 regular branching staples (table 4 and 5 of appendix A) and 1 modified branching staple having ~ 100 mixed DNA sequences (given in table 10 of appendix A). After purification, the dimerized DNA origami structures were incubated with Cy3 dye labeled DNA having sequence complementary to the modified branching staple for 6 hours (sequence given in table 10 of appendix A). The dye modified origami structures were then purified and used for incubation with DNA functionalized Au@Ag NSs.

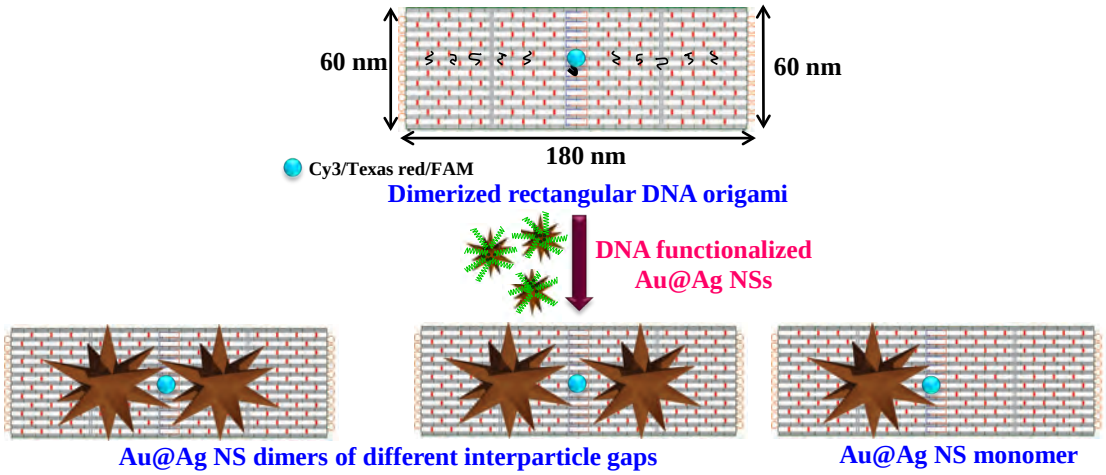

Scheme 4.1. A scheme illustrating the synthetic strategy adopted for self-assembling Au@Ag NSs DNA origami hybrid nanostructures with different interparticle gaps and stoichiometry.

4.2.2.4. Synthesis of Au@Ag NSs-DNA origami hybrid nanostructures

DNA conjugated Au@Ag NSs were mixed with purified dimerized rectangular DNA origami in a molar ratio of 2:1 in 0.5 × TAE buffer with 6.25 mM $MgCl_2$ and 300 mM NaCl. The mixture was kept in PCR thermocycler and repeatedly heated from 40°C to 20°C for 12 hours with a ramp rate of - 0.1°C/s. Scheme 4.1 illustrates the synthetic strategy adopted for self-assembling the Au@Ag NSs DNA origami hybrid nanoantennas. The final product was used for TEM imaging and AFM correlated Raman measurements.

4.2.2.5. Transmission electron microscopy (TEM) imaging

(a) DNA origami and Au@Ag NSs-DNA origami hybrid nanostructures. The hydrophilicity of carbon coated Cu grids was increased by treating them with 1 M $MgCl_2$ solution. This was followed by drop casting purified DNA origami (6µL) Au@Ag NSs DNA origami hybrid nanostructures onto TEM grid for 3 minutes. Uranyl acetate (2%w/v) was used for doing negative staining of DNA origami.

(b) Au NSs and Au@Ag NSs. Nanostars solution was directly drop-casted onto carbon coated Cu grids followed by drying in a vacuum desiccator. TEM imaging was done using a JEOL 2100 microscope at an accelerating voltage of 200 kV. Size distribution of nanoparticles was analyzed using Image J software. STEM EDX mapping of Au@Ag nanostar dimer nanostructures was done using (IACS Kolkata TEM details).

4.2.2.6. AFM imaging

(a) DNA origami. AFM imaging of DNA origami nanostructures was done on mica sheets of V1 quality. At first, mica discs were fixed on round metal plates (Diameter 1.5 cm) using transparent nail polish. Before putting the sample, mica discs were mechanically cleaved at least 5 to 6 times using scotch tape for getting a clean and flat surface. To make the surface hydrophilic, mica discs were incubated with 50 µM $MgCl_2$ solution for 10 minutes followed by washing with water. The substrate was dried with N_2 gas after that 20 µL of purified origami was dropped on it for 10 minutes. This was followed by washing with water and drying using a gentle breeze of N_2 to get an even distribution of origami nanostructures on the substrate.

(b) Au@Ag NSs DNA origami hybrid nanostructures. Si wafer was cut into small pieces of 1 × 1 cm^2 size followed by oxygen plasma cleaning (using Plasma bonder from Omicron scientific equipment Co.) for 10 min to make the surface hydrophilic. After cleaning the wafers

with 1:1 solution of ethanol and distilled water, they were incubated with a dilute solution of Au@Ag NSs DNA origami hybrid nanostructures in 10× TAE with 200 mM $MgCl_2$ for 2 hours. Wafers were washed with MQ water 3 to 4 times to remove excess salt and unbound material. To ensure uniform and complete coverage Si wafer surface was dried with a gentle breeze of N_2 gas.

Silicon cantilever's (Bruker) and TAP 150-Al-G cantilevers (Budget sensor) were used for imaging DNA origami and Au@Ag NSs hybrid nanostructures respectively.

4.2.2.7. Single molecule SERS measurements

Single molecule SERS signals were recorded using AFM correlated measurements as described previously.[50] Briefly, at first the Si substrate with immobilized nanoantennas was scanned using AFM and an area having sparsely distributed nanoantennas such that in the laser confocal area of 1 μm^2 only one nanoantenna resides was located. The area was then relocated using a confocal Raman optical microscope using optically visible features on the substrate and was scanned for Raman signals.

4.2.2.8. Calculation of enhancement factor (EF)

Enhancement factor was calculated using the same equation as described previously.[50]

$$EF = \frac{N_{bulk}}{N_{SERS}} \frac{I_{SERS}}{I_{bulk}} \qquad \text{Equation 4.1}$$

Where,

I_{bulk} = Normal Raman scattering intensity of dye (concentration 1.5 mM),

I_{SERS} = SERS intensity of dye,

N_{bulk} = Number of molecules contributing to normal Raman signal of dye,

N_{SERS}= Number of molecules contributing to SERS signal.

4.2.2.9. SERS based Pyocyanin detection

The Au@Ag NSs dimer nanoantennas were immobilized on Si wafer in a similar manner as described above. After successful identification of the desired area using AFM, the immobilized dimer structures were incubated with different concentrations of pyocyanin solution to form a monolayer over the dimer structures. After 30 minutes of incubation, the excess sample was

wicked and washed followed by scanning the substrate under a confocal Raman microscope for scattering signals.

4.2.2.10. Single molecule fluorescence enhancement measurements

The Au@Ag NS dimer structures with nanogap of 5 nm assembled on biotin modified DNA origami template were immobilized in Lab-Tek chambers for single molecule fluorescence measurements. For immobilization, at first, the Lab-Tek chambers were cleaned using a 10% HF solution for ten minutes to remove any impurities present on the surface of Lab-Tek. After washing the chambers 5 to 6 times with water, the Lab-Tek were incubated with 200 µL of 0.5 mg/mL BSA-biotin solution for overnight being kept at 4 ºC. The BSA-biotin solution was removed and three times washing with PBS buffer was given. Then, 200 µL of 0.5 mg/mL neutravidin solution was added in the BSA-biotin modified chambers for 2 hours. The chambers were three times washed with PBS buffer to remove unbound protein. The synthesized Au@Ag NS dimer antennas were then diluted in 200 µL PBS buffer having 12.5 mM of $MgCl_2$ and incubated in Lab-Tek chambers. After getting an ideal concentration of the structures on the surface of Lab-Tek supernatant solution was slowly removed and the chamber was refilled with 200 µL of PBS-12.5 mM $MgCl_2$. Single molecule fluorescence measurements were done using 532 nm laser excitation.

As synthesized Au@Ag NSs, DNA origami, Au@Ag NSs-DNA origami hybrid structures were characterized by, UV-Vis spectrophotometer, photoluminescence spectrophotometer, TEM, AFM, total internal reflection fluorescence microscope (TIRFM) and confocal Raman microscope as described in chapter 2 of this thesis.

4.3. Results and discussion

4.3.1. Design of DNA origami-Au@Ag NS hybrid plasmonic nanoantennas

The bimetallic Au@Ag NSs were synthesized by the epitaxial growth of Ag over premade Au NSs. This approach has been successfully used for synthesizing different anisotropic shaped Au core Ag shell nanoparticles such as nanoprisms,[64] nanocubes,[65] and nanorods.[15, 66] During the synthesis of the Au@Ag NSs, the major challenge was to achieve a uniform coating of Ag over the previously synthesized Au NSs such that the sharpness of the tips remains unaltered. However, the aforementioned challenge was overcomed by very precisely controlling the concentration of Ag in the coating solution. The Au NSs used for the synthesis were prepared according to a previously published report.[50] In the coating solution, Ag NO_3 was the precursor

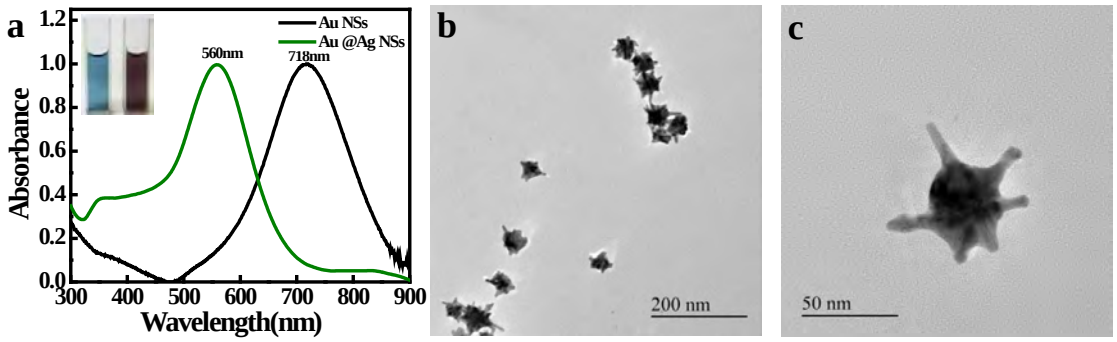

Figure 4.2. (a) UV-Vis spectra of Au NSs and Au@Ag NSs (inset shows digital images of nanostar solutions, and (b and c) TEM images of Au@Ag NSs.

of Ag and ascorbic acid acted as a reducing agent. The reduction of Ag^{+} ions to Ag^{0} by ascorbic acid was commenced on adding NH_4OH which increased the pH of the reaction mixture as evidenced by a change in color of the solution from blue to pinkish purple (inset of Figure 4.2a). The overlapping UV-Vis spectra of the Au NSs before and after Ag coating (Figure 4.2a) shows a blue shifting of surface plasmon band (SPR) of Au NSs from 718 nm to 560 nm covering almost the entire visible region. The blue shift with no change in the shape of the spectrum indicated a successful coating of Ag over the Au NSs with no change in the morphology. This was further confirmed using TEM, from the TEM images of NSs (Figure 4.2b and 4.2c) it was evident that Ag is getting deposited on the surface of Au NSs and no separate nucleation is taking place. Due to significant similarity in the lattice fringe width of both the metals[67] Ag was deposited uniformly over the Au NSs leaving the sharpness of tips unaltered (as shown in Figure 4.2b and 4.2c). The average size of Au@Ag NSs, calculated using 20 different structures

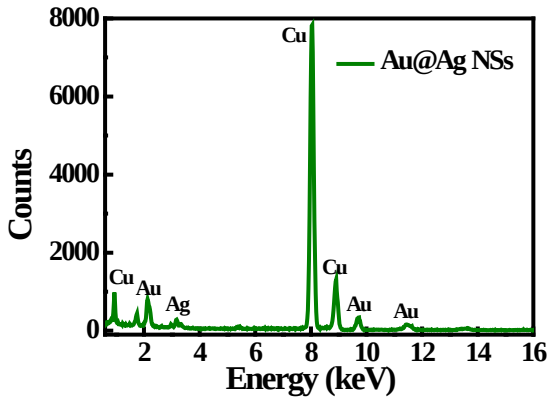

Figure 4.3. EDX spectrum of Au@Ag NSs.

was found to be 70 ± 6 nm. Energy dispersive X-ray (EDX) analysis of the nanostructures further confirmed the presence of Ag over Au NSs (Figure 4.3). A careful examination of the TEM images of Au@Ag NSs revealed the thickness of Ag coating around the Au core is around 1.5 nm. As reported elsewhere, lesser the thickness of Ag coating better is the stability of Au@Ag bimetallic structure,[23] the designed structures were expected to be stable and have pronounced plasmonic enhancement effects. After successful synthesis of the Au@Ag NSs, the

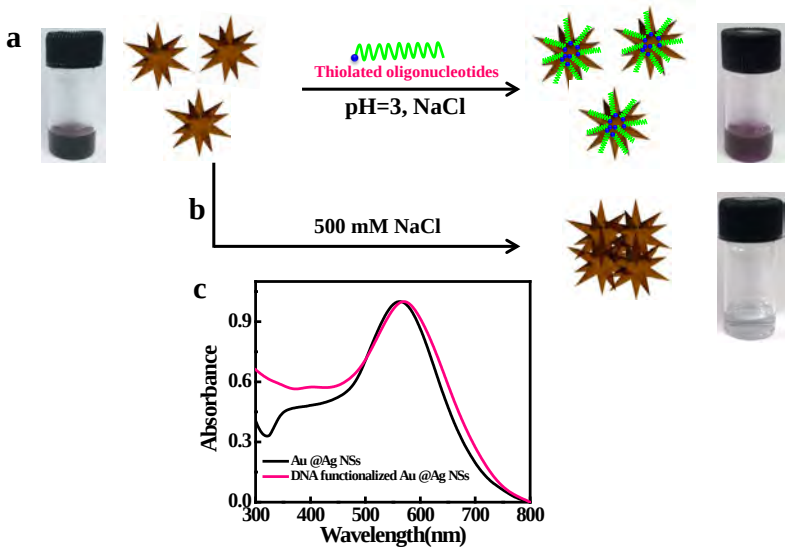

Figure 4.4. (a) Schematic depiction of synthesis of DNA conjugated Au@Ag NSs, (b) Au@Ag NSs in PBS having 500 mM NaCl, and (c) UV-Vis spectra of Au@Ag NSs before and after DNA functionalization.

nanostars were functionalized with thiolated ssDNA oligonucleotides. The DNA functionalization was carried out using the well-established method of salt aging with some modifications (Schematic is shown in figure 4.4a). The initial step of attachment of thiolated DNA to Au@Ag NSs was carried out at pH 3 to overcome the problem of low adsorption of DNA on the Ag surface at neutral pH.[68] Charge repulsion between phosphate backbones of adjacent DNA oligonucleotides was further reduced by increasing the salt concentration of solution to 750 mM in very slow steps. Normally, during the immobilization of NPs on DNA origami, buffer solutions having a high salt concentration of around 500 mM NaCl is used. So it was necessary to check the stability of the as synthesized Au@Ag NSs in high salt concentration. We found that the DNA conjugated Au@Ag NSs solutions were able to withstand high salt concentration conditions required for immobilization on DNA origami (Figure 4.4b). The UV-Vis spectra (Figure 4.4c) of Au@Ag NSs before and after DNA

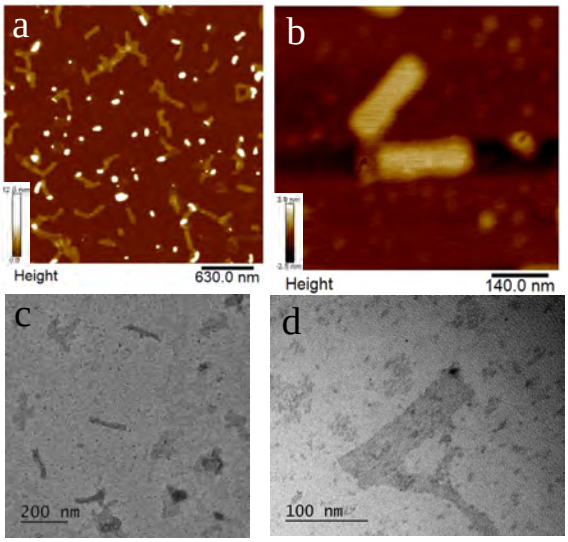

Figure 4.5. (a and b) AFM images, and (c and d) TEM images of dimerized rectangular DNA origami.

functionalization showed a slight red shift of ~ 8 nm, which usually happens due to a change in the dielectric constant of the surrounding medium after conjugation. Further, the DNA functionalized Au@Ag NSs were self-assembled on dimerized rectangular DNA origami with

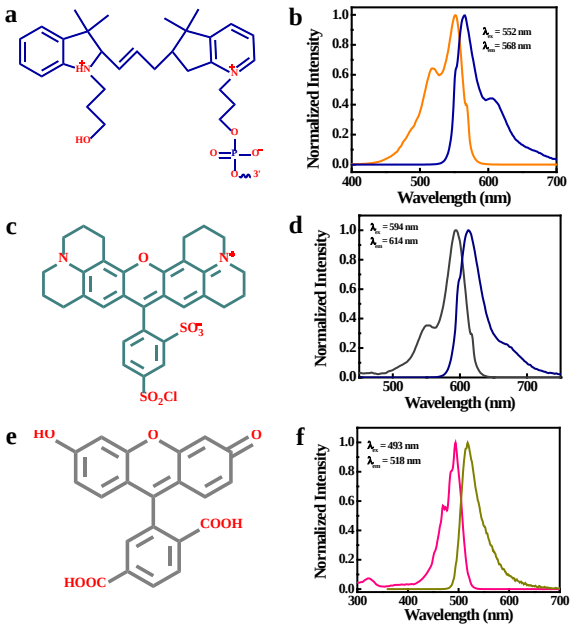

Figure 4.6. Chemical structure and fluorescence spectra of (a and b) Cy3, (c and d) TR, and (e and f) FAM dye molecules.

different interparticle gaps and stoichiometry as shown in scheme 4.1. It has been shown previously that dimerized rectangular DNA origami, not only provides enough space for co-assembling large metal nanoparticles of size ~ 70 nm but also allows tuning of the interparticle gap. [50] So, for assembling the Au@Ag NSs dimer and monomer nanoantennas dimerized rectangular origami was used. The AFM and TEM images of dimerized rectangular DNA are incorporated in figure 4.5. Single dye molecule was positioned at the center of the interparticle gap by replacing one of the branching staples with dye modified staple. To check the enhancement efficiency of the designed nanoantenna across the visible region, we used three different dye molecules: FAM, Cy3, and TR approximately corresponding to the blue, green, and red regions of the visible spectrum respectively. Fluorescence spectra of the dye molecules recorded after incorporating them on DNA origami (Figure 4.6) confirmed their successful

Table 4.1. Position of capture staple sequences

Interparticle gap	Monomer A	Monomer B
10 nm	81,82,83,111,85	82,83,111,85,86
5 nm	82,83,111,85,86	81,82,83,111,85

incorporation. Details of dye labeled sequences can be found in table 8 of appendix A. Two attachment sites were created on the dimerized DNA origami for assembling Au@Ag NSs on the DNA origami template. Each attachment site comprised of 5 capture sequences created by extending staples in 3ˈdirection with DNA sequence complementary to the DNA sequence used

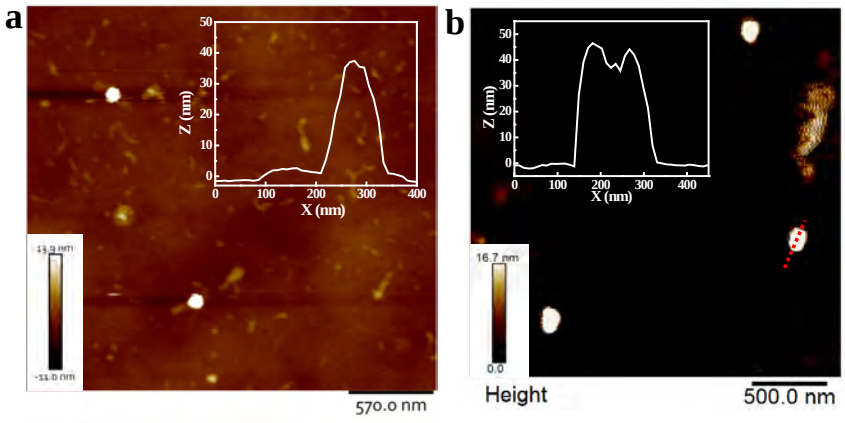

Figure 4.7. AFM images of Au@Ag NS (a) monomer and (b) dimer. The inset shows the height profile of the constructs.

for functionalizing Au@Ag NSs. By changing the position of capture sequences, Au@Ag NS dimer constructs of two different interparticle gap sizes and monomer were synthesized. The details of the position of the capture staples are given in table 4.1. The interparticle gap of the dimer construct cannot be fully resolved using AFM, but the AFM images (Figure 4.7a and 4.7b) confirmed that the Au@Ag NSs are getting assembled on DNA origami. The height profile of the nanoantennas (as shown inset) matched well with the size of nanostars. In order to calculate the interparticle gap, TEM images of the dimer nanoantennas were recorded (Figure 4.8) the average interparticle gap of dimers was measured to be 10 ± 1 nm and 5 ± 1 nm. As

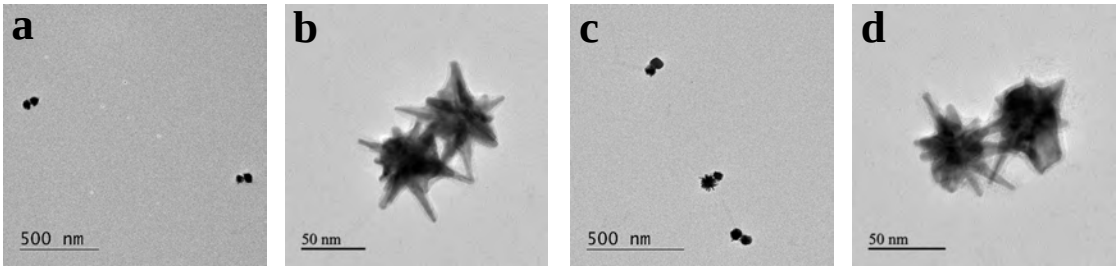

Figure 4.8. TEM images of Au@Ag NSs dimers of an average interparticle gap of (a and b) 5 nm, and (c and d) 10 nm on DNA origami.

mentioned in chapter 3 of this thesis, [50] when we tried to reduce the interparticle gap of Au nanostar dimer below 7 nm by changing the position of capture sequences, the tips of nanostars were found to be touching with each other resulting in no enhancement in Raman signals due to quantum confinement effect. With our present system by coating the particles with Ag, we were able to reduce the interparticle gap without changing the position of capture sequences. The

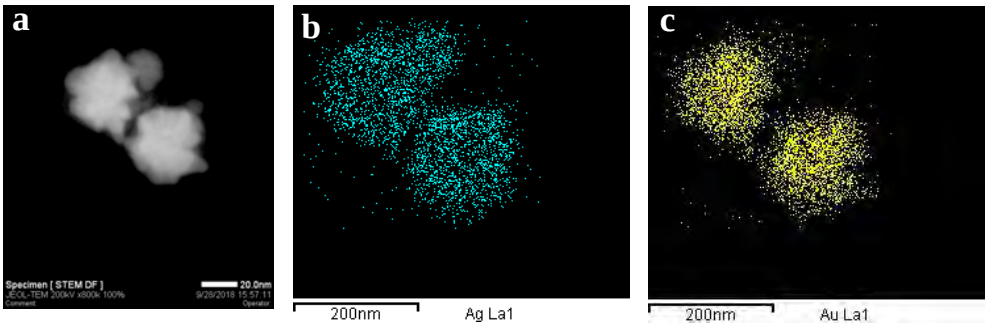

Figure 4.9. (a) Dark field STEM mapping image of Au@Ag NS dimer of an average interparticle gap of 10 nm, and (b and c) the corresponding elemental mapping images.

STEM EDX mapping (Figure 4.9) of the dimer nanoantenna further confirmed the presence of Ag over the Au NSs, indicating that the coating of Ag is getting stabilized after DNA functionalization and is not getting removed during the fabrication procedure.

4.3.2. Single molecule SERS measurements

In order to investigate the plasmonic abilities of the designed nanoantenna, we then performed single molecule AFM correlated Raman measurements.[50] Briefly, at first, the nanoantennas

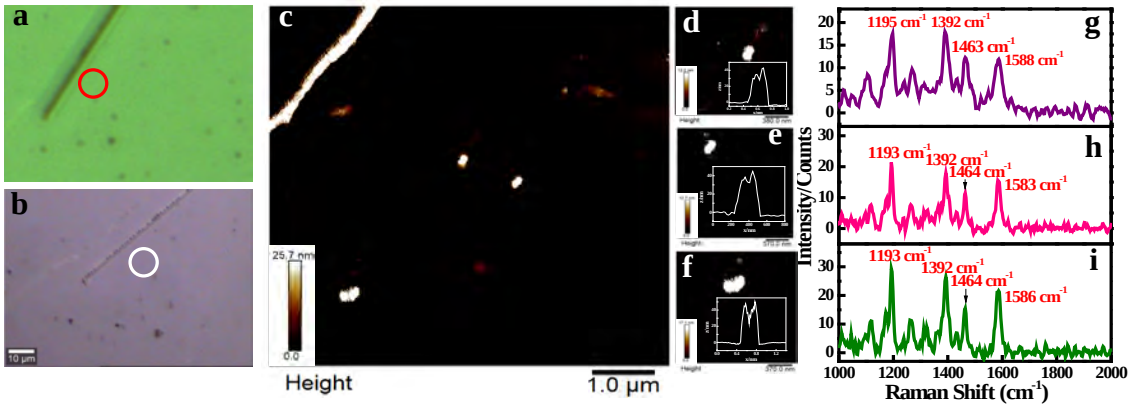

Figure 4.10. Single molecule SERS measurements of Cy3 dye in Au@Ag NS dimer nanoantenna of 5 nm interparticle gap. (a and b) Optical images recorded using AFM and confocal Raman microscopes (red and white circle shows the scanned area). (c) AFM images of the nanoantenna structures. (d,e and f) High resolution AFM image of single nanoantenna structure with their height profiles. (g,h, and i) Corresponding single molecule SERS spectra.

were immobilized on the surface of Si wafer for AFM imaging. After identification of the desired area, the same area was scanned using confocal Raman microscope for collecting Raman signals. For each of the three dyes used in this study three different samples i.e. Au@Ag NS dimer gap 5 nm, Au@Ag NS dimer gap 10 nm, and Au@Ag NS monomer were prepared. Figure 4.10 shows the correlated AFM images and SERS spectra of Au@Ag NS dimer (gap= 5 nm) nanoantennas having Cy3 dye molecule. From the single molecule SERS signals (figure 4.10g, 4.10h, and 4.10i) we noted a slight shift in the spectral position of some of the peaks along with the intensity. The change in spectral position can be ascribed to different molecular orientations in the plasmonic hotspot. To account for the slight conformational variations in individual nanoantenna and random orientation of the dye in the hotspot, the averaged EFs were calculated considering SERS signals from 15 different structures. All the Raman measurements were carried out using laser excitation of 633 nm. The characteristic Raman fingerprints of all

three dyes were determined by recording the reference Raman spectrum using spherical Ag NPs of 50 nm size (Figure 4.11). The fingerprint peaks for the three dyes were found to be: Cy3 - 1195, 1392, 1463 and 1586 cm^{-1}, TR - 1502 and 1647 cm^{-1} and FAM- 1180, 1330, 1476, 1505, 1569, and 1636 cm^{-1}. For FAM, Cy3, and TR highest intensity Raman peaks i.e. 1330 cm^{-1}, 1195 cm^{-1}, and 1502 cm^{-1} were identified for calculating the EFs. Figure 4.12 shows the

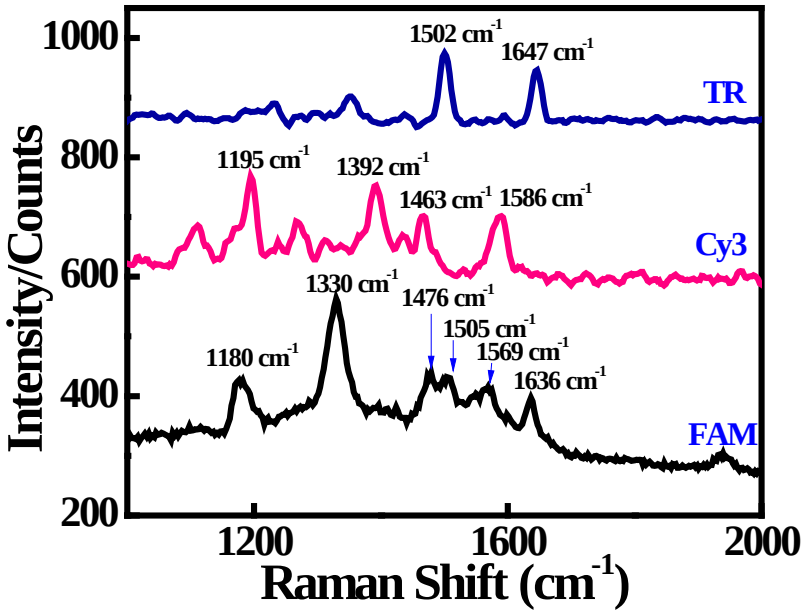

Figure 4.11. Reference Raman spectra of TR, Cy3, and FAM dye molecules recorded on 50 nm Ag NPs.

averaged SERS spectra of all three dyes for the three different structures. We found that the EFs were highest for Cy3 dye followed by that of TR and FAM respectively. It is very well known that SERS EFs are maximum when there is a close resonance between the electronic transition of probe molecule, laser excitation wavelength and the surface plasmon resonance of the metal nanoparticles, a condition commonly termed as SERRS.[69] From practical point of view it is quite difficult and restricting to exactly match all the three parameters. Experimentally it has been found that SERRS works quite well with two possible arrangements, first, the molecular absorbance and SPR wavelength coincide with each other while the excitation wavelength is away from absorbance and plasmon maximum. Second, the molecular absorbance and the SPR band position do not coincide with each other but the laser excitation is at the molecular absorbance maximum.[70] The absorption maxima of the dyes used are as follows: FAM: 493 nm, Cy3: 552 nm, TR: 594 nm. The SPR band position is at 560 nm and laser excitation

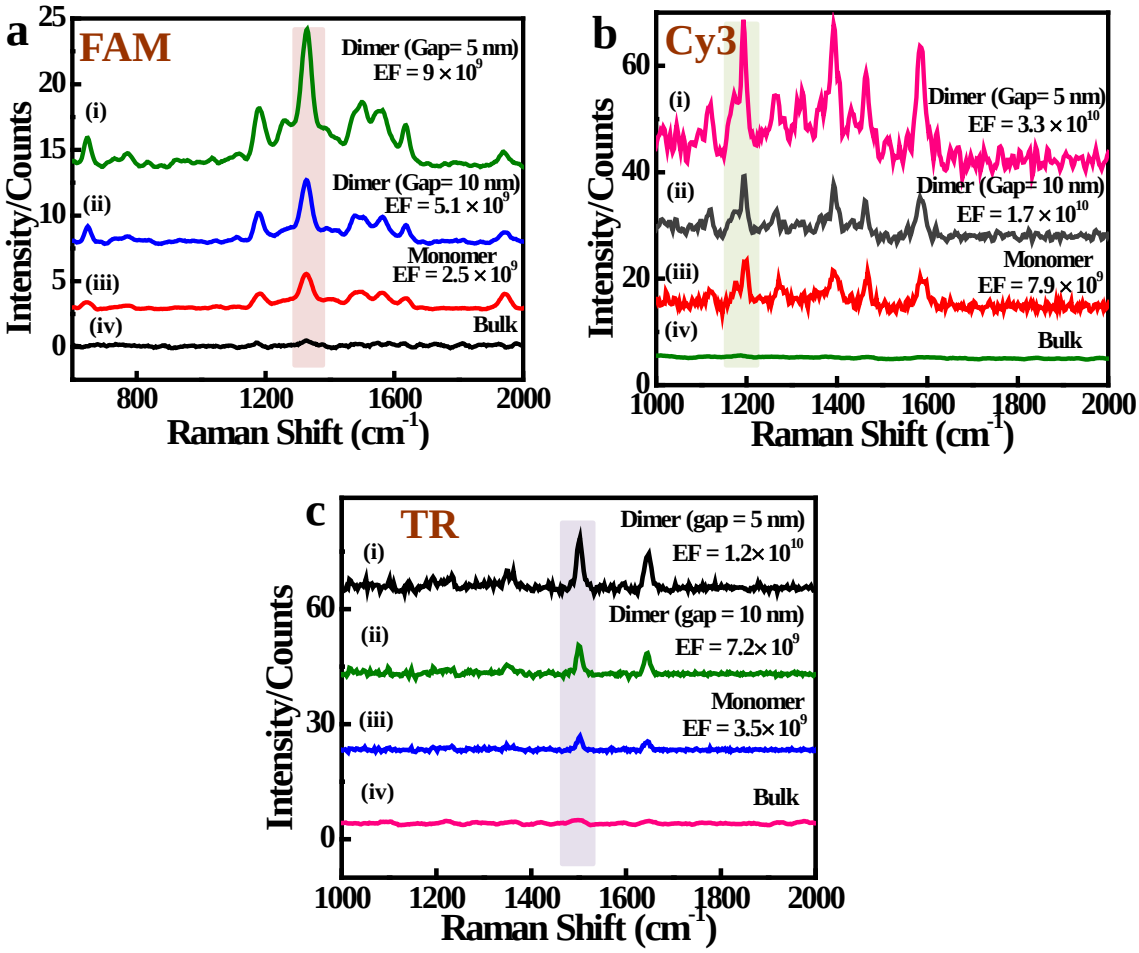

Figure 4.12. (a) Single molecule SERS spectra of FAM dye in plasmonic hotspot of Au@Ag NSs dimer of interparticle gap (i) 5 nm and (ii) 10 nm, (iii) Au@Ag NSs monomer, and (iv) bulk FAM dye. (b) Single molecule SERS spectra of Cy3 dye in plasmonic hotspot of Au@Ag NSs dimer of interparticle gap (i) 5 nm and (ii) 10 nm, (iii) Au@Ag NSs monomer, and (iv) bulk Cy3 dye. (c) Single molecule SERS spectra of TR dye in plasmonic hotspot of Au@Ag NSs dimer of interparticle gap (i) 5 nm and (ii) 10 nm, (iii) Au@Ag NSs monomer, and (iv) bulk TR dye.

is at 633 nm. The overlapping absorption spectra of all the three dyes and SPR absorption spectrum of Au@Ag NSs (Figure 4.13) indicate that the absorption maximum of Cy3 dye is closest to the SPR of the Au@Ag NSs fulfilling the SERRS condition. Thus, the higher EFs for Cy3 dye can be attributed to SERRS and high Raman cross-section of Cy3 dye in the hotspot.[33] In case of TR dye, the laser excitation wavelength was close to its molecular absorbance which resulted in EFs higher than that of FAM dye. The non-resonant SERS experiments for FAM still resulted in EFs to the order of 10^9, which are sufficient enough for single molecule detection.[32]

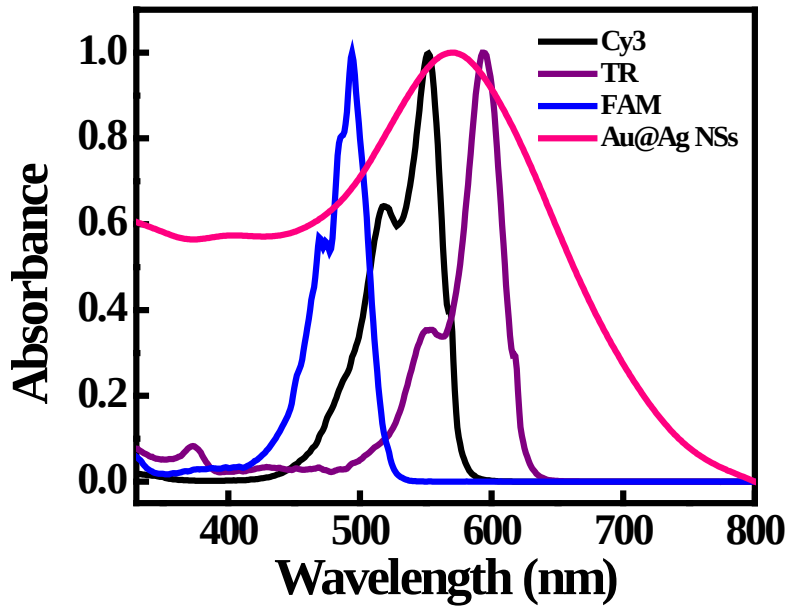

Figure 4.13. Overlapped absorption spectra of Cy3, TR, and FAM dye and SPR absorption spectrum of Au@Ag NSs.

We further found that for all the three dyes, the average EFs were highest for an interparticle gap of 5 nm followed by that of 10 nm and monomer nanoantenna (Table 4.2). The excited surface plasmons decay rapidly as $1/d^{12}$,[71, 72] as a result, the enhancement effects are highest when the probe

Table 4.2. Experimentally obtained EFs of FAM, Cy3, and TR dye molecules

	FAM dye	**Cy3 dye**	**TR dye**
System /Peaks	**(EF) 1330 cm^{-1}**	**(EF) 1195 cm^{-1}**	**(EF) 1502 cm^{-1}**
5 nm gap dimer	9.0×10^{9}	3.3×10^{10}	1.2×10^{10}
10 nm gap dimer	5.1×10^{9}	1.7×10^{10}	7.2×10^{9}
Monomer	2.5×10^{9}	7.9×10^{9}	3.5×10^{9}

molecule is close to the surface and almost no enhancement in Raman signals is observed at distances larger than 20 nm.[72] The overall change in the pattern of SERS intensity with a decrease in the interparticle gap and change in stoichiometry is in good agreement with the previous works.[50] The summarized results are plotted in the scattering graph (Figure 4.14). Variation in the intensity of SERS signal could be attributed to several factors such as slight

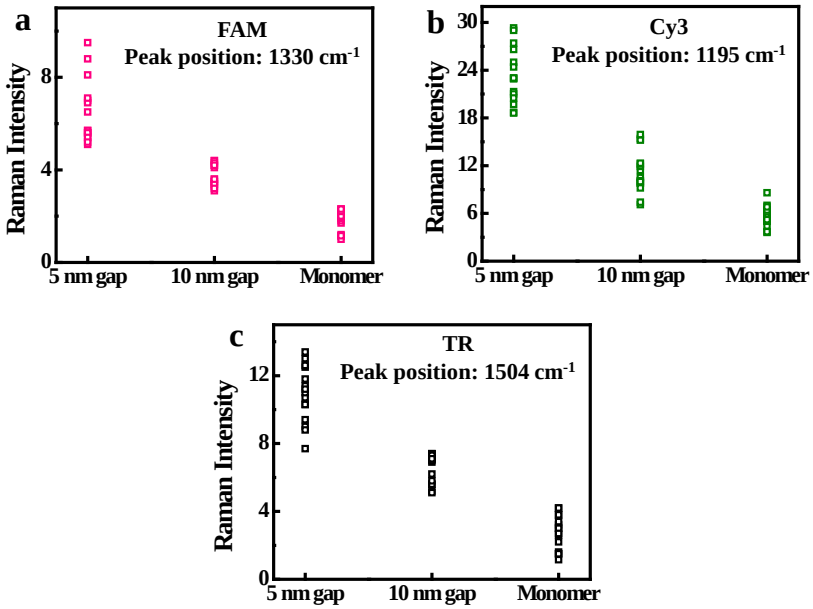

Figure 4.14. Scattering intensity plot showing single molecule SERS signals of (a) FAM, (b) Cy3, and (c) TR dye molecules recorded from 15 different individual nanoantennas.

variation in the interparticle gap, orientation of dye molecule and a slight change in the size of NPs. To confirm that the measured SERS signals are originating from the dye molecule placed in the hotspot, we recorded the Raman spectra of all the dyes incorporated on origami without the nanostars, DNA origami, Au@Ag NSs, and Au@AgNSs assembled on origami without the

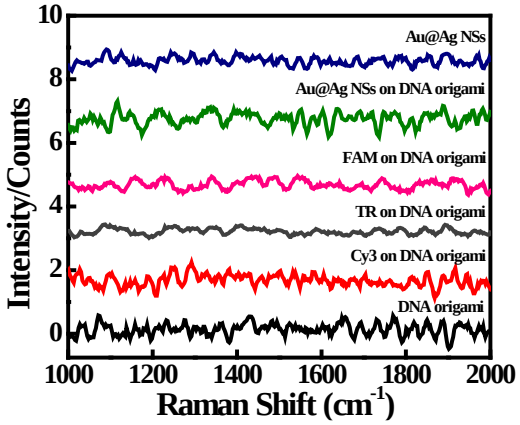

Figure 4.15. Raman spectra of DNA origami, TR dye on DNA origami, Cy3 dye on DNA origami, Au@Ag NSs, and Au@Ag NSs on DNA origami.

dye (Figure 4.15). It is interesting to note that no Raman peaks were observed in all the Raman measurements carried out as a control experiment.

4.3.3. Nanoantenna based label-free bacterial biomarker detection

After obtaining significant enhancement in Raman signals of single dye molecules, the designed nanoantenna structures were employed for label-free Raman enhancement-based detection of bacterial biomarker pyocyanin. Figure 4.16a illustrates the schematic depiction of the sensing of

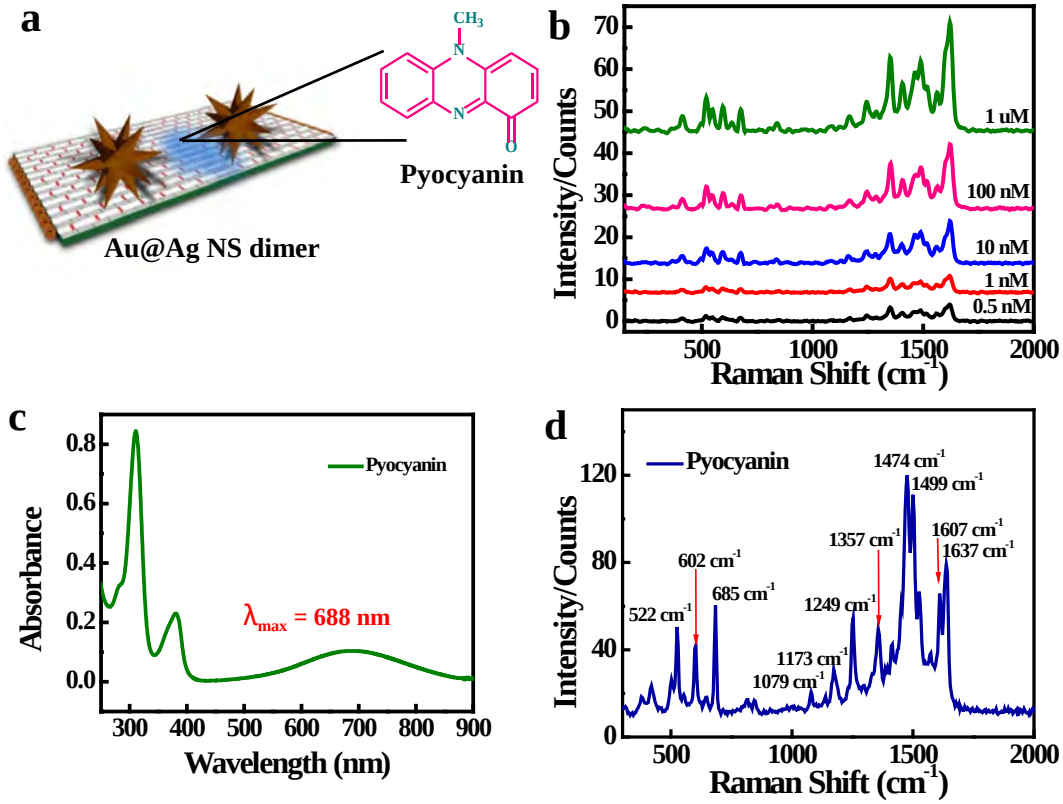

Figure 4.16. (a) Schematic depiction of pyocyanin sensing on the Au@Ag NSs dimer nanoantenna, (b) concentration-dependent SERS spectra of pyocyanin, (c) UV-Vis absorption spectrum of pyocyanin, and (d) reference Raman spectrum of pyocyanin recorded on 50 nm Ag NPs.

pyocyanin on Au@Ag NSs dimer nanoantennas. The dimer nanoantennas immobilized on Si wafer were incubated with different concentrations of pyocyanin to form a monolayer on the dimer structures. The SERS based sensing experiments were carried out using Au@Ag NS dimer nanoantennas with an interparticle gap of 10 nm and laser excitation of 633 nm. We were able to detect pyocyanin with a LOD of 500 pM with our nanoantenna structures (Figure 4.16b) which is better than some of the previous reports.[73, 74] Although there are several reports where LOD is lower than our system, they used costly fabrication techniques like lithography for making a micropatterned SERS active substrate. [75, 76] In our case, we were able to get a

sensitivity of 500 pM with a single nanoantenna structure. The UV-Vis absorption spectrum of pyocyanin shows a broad absorption band in the visible region (Figure 4.16c) with λ_{max} around 688 nm which is close to the laser excitation wavelength of 633 nm. Therefore, the Raman spectra recorded using the designed Au@Ag NS dimer nanoantennas were actually due to SERRS rather than SERS. Before carrying out the SERRS experiments the Raman fingerprints of pyocyanin were identified by recording the SERS spectrum of pyocyanin on 50 nm Ag NPs

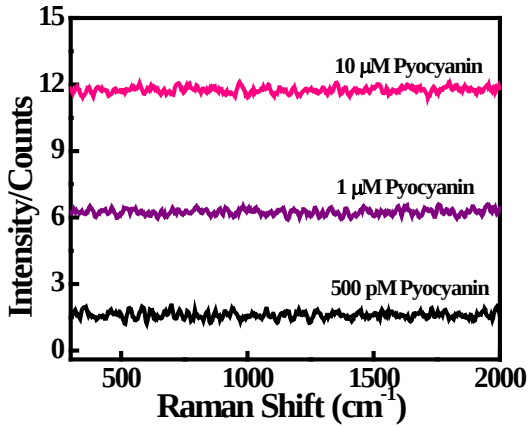

Figure 4.17. Normal Raman spectra of 10, 1, and 0.5 µM pyocyanin.

(Figure 4.16d). Further, to ascertain that the recorded SERS signals were coming from the pyocyanin molecules present on the Au@Ag NSs dimer nanoantennas, normal Raman spectra of pyocyanin with different concentrations of 10 µM, 1µM, and 500 pM was recorded (Figure 4.17). No Raman signal was detected for all the three concentrations which confirm that the obtained SERS signals were due to pyocyanin molecules present in the plasmonic hotspot. We emphasize that the LOD can further be lowered by immobilizing a target capturing probe molecule into the plasmonic hotspot.

4.3.4. Single molecule fluorescence enhancement measurements

As the designed Au@Ag dimer nanoantennas were showing significant enhancement in the single molecule SERS signals, fluorescence enhancement studies were also carried out using designed Au@Ag NS dimers having the interparticle gap of 5 nm. Fluorescence images and transient profiles recorded for single Cy3 dye immobilized on DNA origami and in the plasmonic hotspot of Au@Ag NS dimer of gap 5 nm are shown in figure 4.18. Preliminary results showed that the nanoantennas are showing 10-fold enhancement in the fluorescence signals of a single Cy3 dye molecule. For analysis, spots showing single step bleaching which is the characteristic feature of single molecules were considered. The results shown are for highest

intensity signal obtained during one measurement. More measurements are required for estimating the average enhancement factor by which designed nanoantennas can enhance single molecule fluorescence signals.

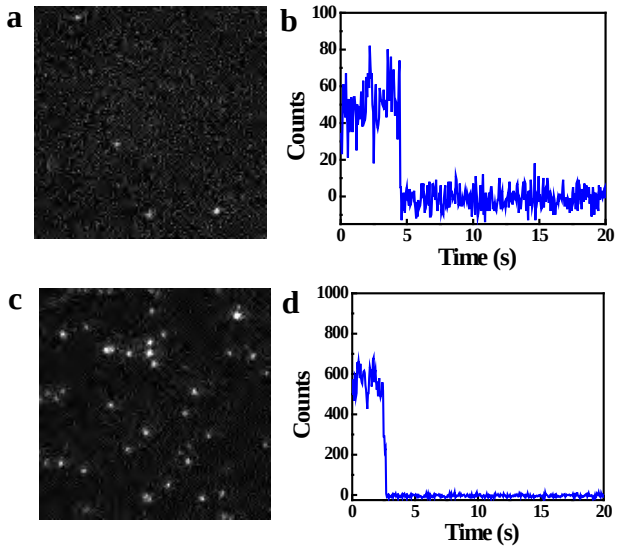

Figure 4.18. Fluorescence images (frame size 20 µM by 20 µM) and transients of single Cy3 dye on (a) DNA origami, and (b) positioned in the plasmonic hotspot of Au@Ag NS dimer nanoantenna (gap 5 nm).

4.4. Conclusion

This chapter demonstrates the strong broadband field enhancement effects of nanoantennas designed using Au@Ag bimetallic nanostars. Au@Ag NS dimers of different interparticle gap sizes and monomer structures were assembled using the DNA origami technique. The designed nanoantennas were found to be significantly enhancing SERS signals of single FAM, Cy3, and TR dye molecules, used as Raman probe in this study. The enhancement effect was highest for Cy3 dye because of close resonance between the SPR of Au@Ag NSs and the absorption maximum of Cy3 dye. The EFs for TR and FAM dye molecules were also in the order of 10^9-10^{10}, which are sufficient for single molecule detection. The obtained results show that the designed nanoantennas can be used as a broadband nanoantenna for enhancing Raman signals from all dyes corresponding to different regions of the visible spectrum. This is the first report where a single nanoantenna is shown as a broadband single molecule Raman signal enhancer. This chapter further demonstrates the applicability of the designed nanoantennas for label free ultrasensitive detection of bacterial biomarker pyocyanin with a LOD of 500 pM. The last part

of this chapter shows that the designed Au@Ag NS dimer nanoantennas (nanogap 5 nm) were showing a 10-fold enhancement in the fluorescence signals of single Cy3 dye molecule localized in the plasmonic hotspot. The results suggest that the designed Au@Ag NS dimer nanoantennas can be used for label-free plasmonic sensing of clinically important molecules.

References

1. E. C. L. Ru and P. G. Etchegoin, *Annual Review of Physical Chemistry*, 2012, **63**, 65-87.
2. L. Rodríguez-Lorenzo, R. A. Álvarez-Puebla, I. Pastoriza-Santos, S. Mazzucco, O. Stéphan, M. Kociak, L. M. Liz-Marzán and F. J. García de Abajo, *Journal of the American Chemical Society*, 2009, **131**, 4616-4618.
3. K. Zhang, Y. Liu, Y. Wang, J. Zhao and B. Liu, *Chemical Science*, 2019, **10**, 1741-1745.
4. R. A. Halvorson and P. J. Vikesland, *Environmental Science & Technology*, 2010, **44**, 7749-7755.
5. M. Y. Sha, H. Xu, M. J. Natan and R. Cromer, *Journal of the American Chemical Society*, 2008, **130**, 17214-17215.
6. X. M. Qian and S. M. Nie, *Chemical Society Reviews*, 2008, **37**, 912-920.
7. Y. Wang and J. Irudayaraj, *Philos Trans R Soc Lond B Biol Sci*, 2012, **368**, 20120026-20120026.
8. Y. Fang, N.-H. Seong and D. D. Dlott, *Science*, 2008, **321**, 388-392.
9. K. M. Kosuda, J. M. Bingham, K. L. Wustholz and R. P. Van Duyne, in *Comprehensive Nanoscience and Technology*, eds. D. L. Andrews, G. D. Scholes and G. P. Wiederrecht, Academic Press, Amsterdam, 2011, DOI: https://doi.org/10.1016/B978-0-12-374396-1.00110-0, pp. 263-301.
10. S. Sánchez-Cortés, J. V. García-Ramos and G. Morcillo, *Journal of Colloid and Interface Science*, 1994, **167**, 428-436.
11. C. G. Blatchford, J. R. Campbell and J. A. Creighton, *Surface Science*, 1982, **120**, 435-455.
12. E. C. Dreaden, A. M. Alkilany, X. Huang, C. J. Murphy and M. A. El-Sayed, *Chemical Society Reviews*, 2012, **41**, 2740-2779.
13. Y. Cui, B. Ren, J.-L. Yao, R.-A. Gu and Z.-Q. Tian, *The Journal of Physical Chemistry B*, 2006, **110**, 4002-4006.
14. R. Jiang, H. Chen, L. Shao, Q. Li and J. Wang, *Advanced Materials*, 2012, **24**, OP200-OP207.
15. M. Fernanda Cardinal, B. Rodríguez-González, R. A. Alvarez-Puebla, J. Pérez-Juste and L. M. Liz-Marzán, *The Journal of Physical Chemistry C*, 2010, **114**, 10417-10423.
16. M. Fan, F.-J. Lai, H.-L. Chou, W.-T. Lu, B.-J. Hwang and A. G. Brolo, *Chemical Science*, 2013, **4**, 509-515.
17. M. Lismont and L. Dreesen, *Materials Science and Engineering: C*, 2012, **32**, 1437-1442.
18. A. M. Fales, H. Yuan and T. Vo-Dinh, *The Journal of Physical Chemistry C*, 2014, **118**, 3708-3715.
19. S. Pande, J. Chowdhury and T. Pal, *The Journal of Physical Chemistry C*, 2011, **115**, 10497-10509.
20. S. Nie and S. R. Emory, *Science*, 1997, **275**, 1102-1106.
21. D. Cunningham, R. E. Littleford, W. E. Smith, P. J. Lundahl, I. Khan, D. W. McComb, D. Graham and N. Laforest, *Faraday Discussions*, 2006, **132**, 135-145.
22. S. Nishimura, A. T. N. Dao, D. Mott, K. Ebitani and S. Maenosono, *The Journal of Physical Chemistry C*, 2012, **116**, 4511-4516.
23. D. M. Mott, D. T. N. Anh, P. Singh, C. Shankar and S. Maenosono, *Advances in Colloid and Interface Science*, 2012, **185-186**, 14-33.
24. C. Shankar, A. T. N. Dao, P. Singh, K. Higashimine, D. M. Mott and S. Maenosono, *Nanotechnology*, 2012, **23**, 245704.
25. Y. Feng, G. Wang, Y. Chang, Y. Cheng, B. Sun, L. Wang, C. Chen and H. Zhang, *Nano Letters*, 2019, **19**, 4478-4489.
26. Y. Sun and Y. Xia, *Nano Letters*, 2003, **3**, 1569-1572.
27. Y. Yang, J. Shi, G. Kawamura and M. Nogami, *Scripta Materialia*, 2008, **58**, 862-865.
28. A. K. Samal, L. Polavarapu, S. Rodal-Cedeira, L. M. Liz-Marzán, J. Pérez-Juste and I. Pastoriza-Santos, *Langmuir*, 2013, **29**, 15076-15082.
29. R. G. Freeman, M. B. Hommer, K. C. Grabar, M. A. Jackson and M. J. Natan, *The Journal of Physical Chemistry*, 1996, **100**, 718-724.
30. K. K. Haldar, S. Kundu and A. Patra, *ACS Applied Materials & Interfaces*, 2014, **6**, 21946-21953.

31. S. Pande, S. K. Ghosh, S. Praharaj, S. Panigrahi, S. Basu, S. Jana, A. Pal, T. Tsukuda and T. Pal, *The Journal of Physical Chemistry C*, 2007, **111**, 10806-10813.
32. D.-K. Lim, K.-S. Jeon, H. M. Kim, J.-M. Nam and Y. D. Suh, *Nature Materials*, 2009, **9**, 60.
33. J. Prinz, C. Heck, L. Ellerik, V. Merk and I. Bald, *Nanoscale*, 2016, **8**, 5612-5620.
34. J. Reguera, J. Langer, D. Jiménez de Aberasturi and L. M. Liz-Marzán, *Chemical Society Reviews*, 2017, **46**, 3866-3885.
35. C. G. Khoury and T. Vo-Dinh, *The Journal of Physical Chemistry C*, 2008, **112**, 18849-18859.
36. J. D. Smith, Z. J. Woessner and S. E. Skrabalak, *The Journal of Physical Chemistry C*, 2019, **123**, 18113-18123.
37. S. K. Dondapati, T. K. Sau, C. Hrelescu, T. A. Klar, F. D. Stefani and J. Feldmann, *ACS Nano*, 2010, **4**, 6318-6322.
38. B. W. Boote, R. A. A. Ferreira, W. Jang, H. Byun and J.-H. Kim, *Nanotechnology*, 2015, **26**, 345701.
39. W. Zhang, J. Liu, W. Niu, H. Yan, X. Lu and B. Liu, *ACS Applied Materials & Interfaces*, 2018, **10**, 14850-14856.
40. K.-K. Liu, S. Tadepalli, G. Kumari, P. Banerjee, L. Tian, P. K. Jain and S. Singamaneni, *The Journal of Physical Chemistry C*, 2016, **120**, 16899-16906.
41. R. V. William, G. M. Das, V. R. Dantham and R. Laha, *Scientific Reports*, 2019, **9**, 10771.
42. *Clinical Pharmacology & Therapeutics*, 2001, **69**, 89-95.
43. T. A. Webster, H. J. Sismaet, J. L. Conte, I. p. J. Chan and E. D. Goluch, *Biosensors and Bioelectronics*, 2014, **60**, 265-270.
44. C. Hamon and L. M. Liz-Marzán, *Journal of Colloid and Interface Science*, 2018, **512**, 834-843.
45. V. M. Szlag, R. S. Rodriguez, J. He, N. Hudson-Smith, H. Kang, N. Le, T. M. Reineke and C. L. Haynes, *ACS Applied Materials & Interfaces*, 2018, **10**, 31825-31844.
46. K. C. Bantz, A. F. Meyer, N. J. Wittenberg, H. Im, Ö. Kurtuluş, S. H. Lee, N. C. Lindquist, S.-H. Oh and C. L. Haynes, *Physical Chemistry Chemical Physics*, 2011, **13**, 11551-11567.
47. G. Yang, J. Nanda, B. Wang, G. Chen and D. T. Hallinan, *ACS Applied Materials & Interfaces*, 2017, **9**, 13457-13470.
48. Y.-W. Wang, K.-C. Kao, J.-K. Wang and C.-Y. Mou, *The Journal of Physical Chemistry C*, 2016, **120**, 24382-24388.
49. A. Kinkhabwala, Z. Yu, S. Fan, Y. Avlasevich, K. Müllen and W. E. Moerner, *Nature Photonics*, 2009, **3**, 654.
50. S. Tanwar, K. K. Haldar and T. Sen, *Journal of the American Chemical Society*, 2017, **139**, 17639-17648.
51. P. Zhan, T. Wen, Z.-g. Wang, Y. He, J. Shi, T. Wang, X. Liu, G. Lu and B. Ding, *Angewandte Chemie International Edition*, 2018, **57**, 2846-2850.
52. C. Heck, J. Prinz, A. Dathe, V. Merk, O. Stranik, W. Fritzsche, J. Kneipp and I. Bald, *ACS Photonics*, 2017, **4**, 1123-1130.
53. C. Heck, Y. Kanehira, J. Kneipp and I. Bald, *Angewandte Chemie International Edition*, 2018, **57**, 7444-7447.
54. F. Nicoli, T. Zhang, K. Hübner, B. Jin, F. Selbach, G. Acuna, C. Argyropoulos, T. Liedl and M. Pilo-Pais, *Small*, 2019, **15**, 1804418.
55. I. Kaminska, J. Bohlen, S. Mackowski, P. Tinnefeld and G. P. Acuna, *ACS Nano*, 2018, **12**, 1650-1655.
56. P. Holzmeister, G. P. Acuna, D. Grohmann and P. Tinnefeld, *Chemical Society Reviews*, 2014, **43**, 1014-1028.
57. D. Punj, R. Regmi, A. Devilez, R. Plauchu, S. B. Moparthi, B. Stout, N. Bonod, H. Rigneault and J. Wenger, *ACS Photonics*, 2015, **2**, 1099-1107.
58. O. Stranik, R. Nooney, C. McDonagh and B. D. MacCraith, *Plasmonics*, 2007, **2**, 15-22.
59. A. Puchkova, C. Vietz, E. Pibiri, B. Wünsch, M. Sanz Paz, G. P. Acuna and P. Tinnefeld, *Nano Letters*, 2015, **15**, 8354-8359.
60. G. P. Acuna, F. M. Möller, P. Holzmeister, S. Beater, B. Lalkens and P. Tinnefeld, *Science*, 2012, **338**, 506-510.
61. C. Vietz, I. Kaminska, M. Sanz Paz, P. Tinnefeld and G. P. Acuna, *ACS Nano*, 2017, **11**, 4969-4975.
62. C. Vietz, B. Lalkens, G. P. Acuna and P. Tinnefeld, *New Journal of Physics*, 2016, **18**, 045012.

63. X. Zhang, M. R. Servos and J. Liu, *Chemical Communications*, 2012, **48**, 10114-10116.
64. C. Xue, J. E. Millstone, S. Li and C. A. Mirkin, *Angewandte Chemie International Edition*, 2007, **46**, 8436-8439.
65. Y. Liu, J. Zhou, B. Wang, T. Jiang, H.-P. Ho, L. Petti and P. Mormile, *Physical Chemistry Chemical Physics*, 2015, **17**, 6819-6826.
66. Liu and P. Guyot-Sionnest, *The Journal of Physical Chemistry B*, 2004, **108**, 5882-5888.
67. B. Rodríguez-González, A. Burrows, M. Watanabe, C. J. Kiely and L. M. Liz Marzán, *Journal of Materials Chemistry*, 2005, **15**, 1755-1759.
68. Z. Luo, X. Yuan, Y. Yu, Q. Zhang, D. T. Leong, J. Y. Lee and J. Xie, *Journal of the American Chemical Society*, 2012, **134**, 16662-16670.
69. G. McNay, D. Eustace, W. E. Smith, K. Faulds and D. Graham, *Applied Spectroscopy*, 2011, **65**, 825-837.
70. C. Rodger, W. E. Smith, G. Dent and M. Edmondson, *Journal of the Chemical Society, Dalton Transactions*, 1996, DOI: 10.1039/DT9960000791, 791-799.
71. A. Campion and P. Kambhampati, *Chemical Society Reviews*, 1998, **27**, 241-250.
72. G. Kumari, J. Kandula and C. Narayana, *The Journal of Physical Chemistry C*, 2015, **119**, 20057-20064.
73. V. Montes-García, S. Rodal-Cedeira, M. J. Cordero-Ferradás, B. Gómez, L. García-Río, I. Pastoriza-Santos and J. Pérez-Juste, *Israel Journal of Chemistry*, 2018, **58**, 1251-1260.
74. F. Jia, E. Barber, H. Turasan, S. Seo, R. Dai, L. Liu, X. Li, A. K. Bhunia and J. L. Kokini, *Journal of Agricultural and Food Chemistry*, 2019, **67**, 4603-4610.
75. G. Bodelón, V. Montes-García, V. López-Puente, E. H. Hill, C. Hamon, M. N. Sanz-Ortiz, S. Rodal-Cedeira, C. Costas, S. Celiksoy, I. Pérez-Juste, L. Scarabelli, A. La Porta, J. Pérez-Juste, I. Pastoriza-Santos and L. M. Liz-Marzán, *Nature Materials*, 2016, **15**, 1203.
76. C. Hanske, E. H. Hill, D. Vila-Liarte, G. González-Rubio, C. Matricardi, A. Mihi and L. M. Liz-Marzán, *ACS Applied Materials & Interfaces*, 2019, **11**, 11763-11771.

Chapter 5

Synthesis and immobilization of single Si QD on DNA origami for sensing and imaging applications

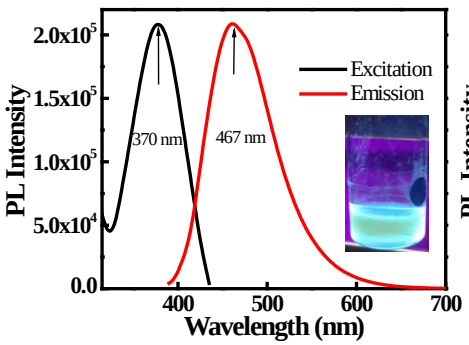

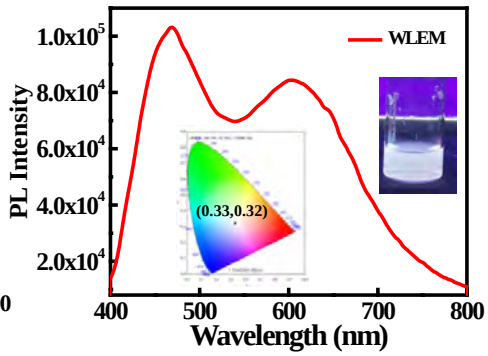

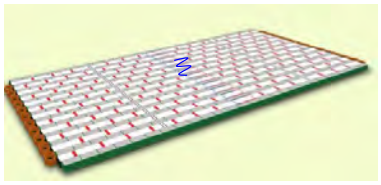

DNA functionalized Si QD

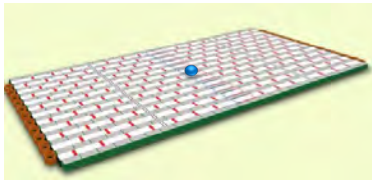

Rectangular DNA origami

DNA origami- Si QD hybrid structure

5.1. Introduction

Quantum dots (QDs) have attracted a great deal of scientific research interest due to their promising candidature in a plethora of applications ranging from solar cells to biology.[1-3] QDs have been utilized as ideal fluorescent probes for multicolor and multiplexing applications in molecular biology because of their novel optical properties such as narrow, symmetric emission and broad excitation spectra and stability towards photobleaching.[4, 5] Conventionally used QDs are semiconductor nanocrystals composed of elements from the periodic groups of II–VI (*e.g.*, CdTe and CdSe) and III–V (*e.g.*, InP) [6, 7] and have been extensively investigated due to their excellent quantum yield, high photostability, and strong tunable emission. In particular, heavy metal chalcogenide-based QDs such as CdSe and CdTe have been extensively investigated due to their excellent quantum yield, high photostability, and strong tunable emission. However, despite being used in a myriad of applications ranging from solar cells to biology, [1-3, 8] heavy metal chalcogenide-based QDs have limited applications in biology due to the toxicity associated with heavy metal ions such as Cd^{2+} and Pb^{+2}. [9, 10] Therefore, synthesis of biocompatible and non-toxic QDs has been a focal point of research. Recently, research interest has been shifted toward functional Si nanoparticles (NPs) owing to their magnificent optical, electronic, and mechanical properties, tailorable surface, and excellent biocompatibility. [11-18]Si NPs have promised to overcome the leaching problem of highly toxic heavy metal ions in chalcogenide-based QDs and also provide robust surface chemistry for easy conjugation with biomolecules. [19] Similar to conventional QDs, Si QDs are also resistant to photobleaching and have a wide emission range from visible to infrared region with relatively high quantum yields. Zhong et al. have shown that fluorescent Si NPs are better for long term in vitro imaging due to their high photostability with respect to FITC fluorescent labels that completely disappear after short-time irradiation of 3 minutes.[17] Further, it was found by Pramanik et al. that Si QDs doesn't have any effect on the viability of bacterial cells, whereas CdSe QDs exhibited considerable toxicity even at lower doses.[20] Despite having potential as a sustainable alternative to transition metal-based QDs, studies on Si NPs are limited due to the complicated synthetic procedures, use of costly equipments, and harsh experimental conditions involved in the synthesis. [21-23] For example, Liao et al. have described a one pot synthetic strategy for water dispersible Si QDs, but the process involved hydrothermal etching of Si powder. [24, 25] Furthermore, the QDs produced are generally hydrophobic, rendering their bioconjugation difficult, and require surface modifications to make them hydrophilic. [26-30] Therefore, simple and green synthetic strategies which eliminate the use of hazardous chemicals as well as energy exhaustive processes that lead to hydrophilic Si QDs without any surface modification are highly desirable.

The first part of this chapter demonstrates a one-pot, green, cost effective, and energy-efficient synthetic strategy for the synthesis of blue emitting Si QDs using 3-aminopropyltriethoxysilane (APTES) as the silicon source and a commonly available sugar, glucose, as reducing agent at room temperature. Several optical and structural characterizations have been done to confirm that the as synthesized QDs are of Si and are crystalline in nature. Stability studies have been carried out by subjecting the synthesized Si QDs to different ionic strength, temperature, and pH conditions. The presence of oxygen containing surface functionalities such as −OH and −COOH on the as-synthesized Si QDs were further used for reducing Au^{+3} ions at room temperature thereby forming Au NP-Si QD nanocomposite structures. The combination of two or more NPs with different functionalities leads to formation of composite NP system. Such hybrid structures are known to have properties superior to those of the single NP system due to synergistic effect between the two NPs. [31-36] The formation of a hybrid NP system, especially a QD−metal NP hybrid system leads to enhanced optoelectronic property of the QDs because of the presence of localized surface plasmon resonance (LSPR) of the metal NPs. Such hybrid nanostructures are known to have potential applications in photocatalysis, plasmon enhanced spectroscopy, solar energy harvesting, and bioimaging. [37-41] Till now most of the studied hybrid systems consist of metal NPs and Cd or Pb chalcogenides, but for applications related to energy and optoelectronic devices, metal NP hybridization with Si QDs is preferred. [15, 42] There are only a handful of reports showing the formation of Si QD−metal NP composite. [42-45] The as-synthesized Au NP-Si QD hybrid NPs were found to be showing excellent catalytic activity towards reduction of nitroarenes. Further, the catalytic activity of different sized Au NP-Si QD hybrid NPs, synthesized using different concentrations of Si QDs, towards reduction of *p*-nitrophenol to *p*-aminophenol has been demonstrated. Room temperature development of a hybrid system comprising the optical properties of both Si QDs and Au NPs is a promising step toward the design of a biocompatible and multifunctional hybrid NP system.

The second part of this chapter demonstrates a solution phase synthesis of white light emitting mixture (WLEM) by controlled mixing of blue emitting Si QDs and orange red emitting Au nanoclusters (Au NCs). The emission of white light from various organic, inorganic and hybrid materials is a highly desired phenomenon of immense interest due to its prospective applications in displays or light-emitting devices. [46] In recent years, organic light-emitting diodes (OLEDs) have emerged as an alternative to incandescent lamps in the development of solid state lighting due to their long lifetime, small size, and low energy consumption and hence reducing the pressure on fossil fuels for generation of energy. [47] The major drawback of

commercial WLEDs [48, 49] is their poor stability which leads to a change in chromaticity and color rendering with time.[50] Therefore development of novel, energy efficient, and reliable white light emitting sources remains a great challenge. Till now several strategies have been adopted for the generation of white light emission using different materials such as polymers, [51] metal–organic frameworks, [52, 53] semiconducting quantum dots, [54, 55] lanthanide co-doped systems, [56, 57] organic molecules [58, 59] etc. The development of white light emitting mixtures in solution phase is important because of their possible applications due to easy device fabrication on different types of substrates. Several reports exist on various composites such as carbon dots, silica hybrids or boronate microparticles which were exploited as white light emitting materials owing to their easy solution phase synthesis, good stability, bio-compatibility, cost effectiveness and non-toxicity. [60-64] Few reports exist on fluorescent Au NCs used as light emitting sources in optoelectronic devices. For example, Barman et al. reported the composite of carbon dots and dye encapsulated BSA-protein-capped Au NCs for white light generation. [65] Goswami et al. demonstrated the formation of white light emission by combining the blue and green fluorescence of green fluorescent protein (GFP)-expressing bacteria and orange luminescence of Au NCs. [66] Mandani et al. demonstrated the solution based synthesis of white light emitting system by controlled mixing of carbon dots with rhodamine B dye. [67] In a very recent study, Bose et al. demonstrated the production of white light by mixing green luminescent Si NPs with blue emitting Si NPs and red luminescent Au NCs.[23] Tu et al. [68] and Ghosh et al. [69] mixed red emitting Si QDs with green and blue emitting REE phosphors and poly[*N*,*N* '-bis(4-butylphenyl)-*N*,*N* '-bis(phenyl)benzidine] film respectively for the generation of white light. In most of the previous studies, the generation of white light emission was performed by combining different types of dyes or mixing dye with fluorescent NPs or mixing different types of NPs/NCs, which consist of three components. Such systems can suffer from self-absorption, color ageing, non-radiative energy transfer and unwanted changes in the chromaticity coordinates. [42, 43] In the present study, we have generated WLEM in solution phase by mixing as-synthesized blue emitting Si QDs with orange red emitting Au NCs. The WLEM mixture was incorporated in a gel, thin film as well as solid forms that will have potential utilities in designing solid state devices. Furthermore, the as obtained WLEM was employed for the reversible and selective detection of analyte molecules such as mercuric (Hg^{2+}) ions and cysteine amino acid (Cys).

The third part of this chapter discusses DNA functionalization and immobilization of single Si QD on DNA origami for single molecule fluorescence enhancement studies. Single molecule

measurements have significant advantages over ensemble average methods like ultrahigh sensitivity, low sample consumption, rapid analysis time, and ability to reveal hidden heterogeneities in a complex system.[70] It is very well known that plasmonic resonances in a metallic nanoparticle can be used to enhance the emission of fluorophores positioned a few nanometers from their surface and are widely employed in several ensemble-averaged biosensors[71, 72] and has been extended to the single-molecule regime.[73] Recently, DNA origami technique has emerged as an extremely powerful and versatile platform for designing plasmonic nanoantennas owing to its control over the spacing, stoichiometry and precise localization of particles at a well-defined position.[74] Till now most of the DNA origami assembled plasmonic nanoantennas have been targeted to enhance fluorescence signals of organic fluorophores,[75-77] relatively fewer nanoantennas have been proposed to enhance the fluorescence of QDs. Considering high quantum yield and photostability of QDs, designing plasmonic nanoantennas for enhancing fluorescence signals from single QD will enable the development of single QD-based nanosensors that will have extremely high sensitivity. For this reason, development of plasmonic nanoantennas capable of enhancing the performance of QDs is highly desirable. Recently, Nicoli et al. assembled a gold NP dimer with a single CdSeS/ZnS QD positioned in between and achieved an enhancement in fluorescence signals of the QDs up to ~30-fold.[78] The enhancement in fluorescence signals is higher in the case of anisotropic shaped nanoparticles due to their sharp edges.[79] This study demonstrates immobilization of single Si QD on DNA origami. As synthesized Si QDs were conjugated with amine labeled DNA oligonucleotides using well-established method of EDC-NHS coupling. Further, they were captured on DNA origami at a predefined position using Watson and Crick complementary base pairing.

5.2. Green synthesis of Si QDs and catalytic Au NP – Si QD nanocomposite

5.2.1. Experimental section

5.2.1.1. Materials

3-aminopropyltriethoxysilane (APTES), gold(III) chloride trihydrate, and sodium borohydride were purchased from Sigma-Aldrich. D-glucose and quinine sulfate were purchased from Himedia. Sodium hydroxide, nitric acid, and sodium chloride were procured from Merck, India. *p*-nitrophenol was procured from SRL chemicals, India. Dialysis membrane with a molecular weight cut off of 0.5-1 kDa was purchased from Spectra labs. All the reagents were of analytical grade and were used as received. All the experiments were performed using Milli-Q water.

5.2.1.2. Experimental procedures

5.2.1.2.1. Preparation of blue emitting Si QDs

Si QDs were synthesized using glucose as reductant at room temperature. In a typical synthesis, 450 mg of D-glucose was dissolved in 4 mL of water followed by slow addition of 0.5 mL of APTES under stirring. The stirring was continued for 48 hour at room temperature until the colorless solution became dark brown. The solution was dialyzed against Milli-Q water for 6 hour and stored for further use.

5.2.1.2.2. Preparation of Au NP − Si QD hybrid NPs

For the preparation of Au NP-Si QD hybrid NPs, the dialyzed Si QDs solution was first diluted. In a typical synthesis, 0.1 mL of the dialyzed Si QDs was added to 1.9 mL of water, followed by the addition of $HAuCl_4$ solution such that the final concentration of $HAuCl_4$ was 6×10^{-4} M. Within 30 min the solution color turned into red from light yellow at room temperature.

5.2.1.2.3. Catalytic activity of Au NP-Si QD hybrid NPs

The catalytic activity of Au NP-Si QD hybrid nanoparticles was studied by carrying out the reduction of *p*-nitrophenol to *p*-aminophenol by using $NaBH_4$ as reductant. In a quartz cuvette (1 cm path length), 2.5 mL of *p*-nitrophenol (0.12 mM) was mixed with 5 mg of $NaBH_4$ and 0.05 mL of as-synthesized Au NP-Si QD hybrid NPs. The mixture was characterized with a UV−visible spectrometer by recording the absorbance spectra every 2 min in the wavelength range of 200 −500 nm.

As synthesized Si QDs and Au NP-Si QD hybrid NPs were characterized by TEM, dynamic light scattering (DLS) study, UV-Vis spectrophotometer, FTIR, X-ray photoelectron spectroscopy (XPS), X-ray powder diffraction (XRD), photoluminescence spectrophotometer, and TCSPC measurements as described in chapter 2 of this thesis.

5.2.2. Results and discussion

5.2.2.1. Optical studies of Si QDs

Si QDs were synthesized by a facile one-pot green synthetic protocol, an aqueous solution of

APTES and glucose was stirred at room temperature for 48 hours. Where, APTES was used as source of Si and glucose as reducing and stabilizing agent. The appearance of a dark brown color from the colorless reaction mixture (Figure 5.1a), indicated the formation of Si QDs. The

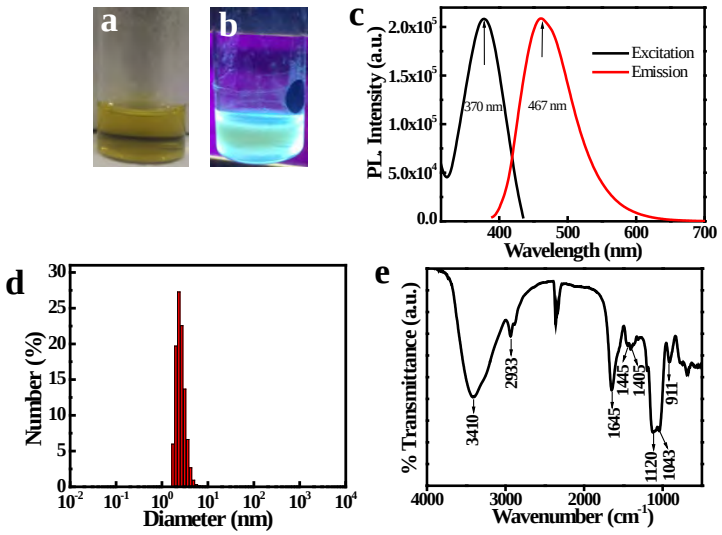

Figure 5.1. (a and b) Digital images of the as prepared Si QDs under daylight and under UV excitation (λ_{exc} = 365 nm), respectively. (c) Excitation and emission spectra of the Si QDs, (d) DLS size distribution histogram of the as prepared Si QDs, and (e) FTIR spectrum of the Si QDs.

solution when observed under a hand-held UV lamp with an excitation wavelength of 365 nm showed intense blue color fluorescence (Figure 5.1b), suggesting the formation of blue emitting Si QDs. Excitation and emission spectra of the resultant Si QDs (Figure 5.1c) showed emission centered at 467 nm upon excitation at 370 nm with symmetrical excitation and emission peaks. The PL spectra indicated that the synthesized Si QDs possess good photoluminescence properties. The photoluminescence quantum yield of the as synthesized Si QDs was calculated to be 3.1% using quinine sulfate as a reference, which was significantly higher than those of Si QDs synthesized using APTES and catechol.[80] The hydrodynamic size distribution obtained using DLS studies showed only a single peak corresponding to Si QDs with a diameter of 3.6 nm (Figure 5.1d). Absence of any other peak above 100 nm indicated that the formed particles are stable and are non-aggregated. To get insights into the nature of surface functionalities surrounding the Si QD, FTIR measurements were performed. The FTIR spectrum of the Si QDs is shown in figure 5.1e in the range of 4000−500 cm^{-1}. The FTIR spectrum showed a broad peak at 3410 cm^{-1} for Si QDs which may be attributed to O−H stretching vibration. The peaks at 2933 and 1445 cm^{-1} were assigned to the C−H stretching and bending vibrations, respectively. While the strong intensity peak at 1645 cm^{-1} could be assigned to the C=O stretching of the carboxylic group, the band at 1405 cm^{-1} was originated from C−O–H bending

vibrations. The peak at 1120 cm^{-1} was due to Si–C asymmetric deformation, and the peak at 1043 cm^{-1} was attributed to Si−O−Si stretching vibrations. Additionally, a peak due to Si−O stretching of the Si−O−H group at 911 cm^{-1} was observed. These results confirm the presence of plenty of hydrophilic oxygenated functional groups on the surface of Si QDs, whose presence greatly contributed toward the excellent water dispersibility of the Si QDs. The high PL quantum yield and water solubility makes as synthesized Si QDs a suitable candidate for biological applications such as imaging and sensing.

5.2.2.2. Structural characterization of Si QDs

To get insights into the morphology and the structure of the as synthesized Si QDs TEM imaging was done. TEM images of Si QDs shown in figure 5.2a confirm the formation of spherical Si QDs with an average size of 2.7 ± 0.4 nm. Inset of figure 5.2a shows the particle

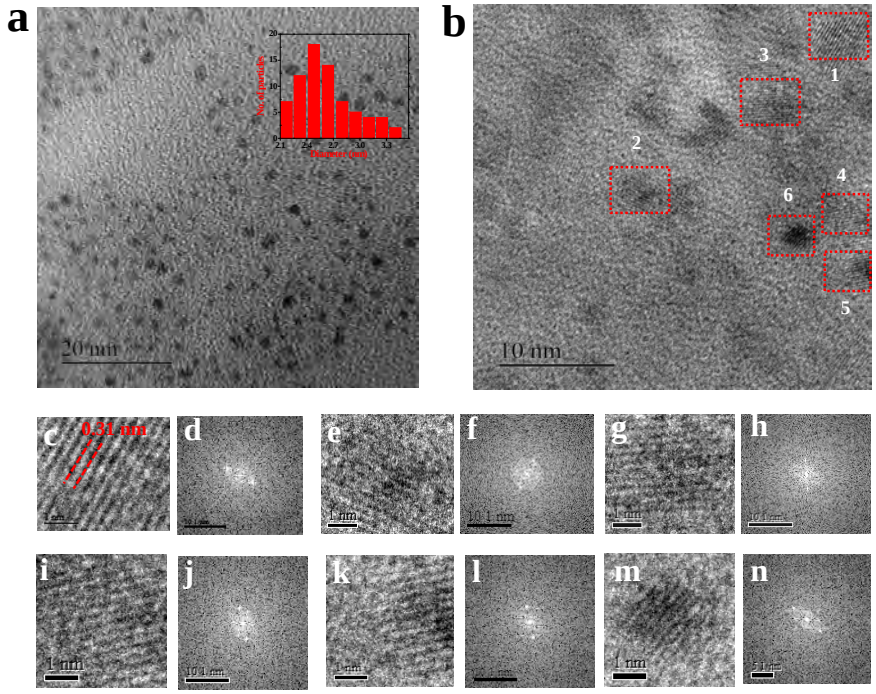

Figure 5.2. (a) TEM images (inset shows the particle size distribution) and (b) HRTEM images of the Si QDs. HRTEM images and the corresponding fast Fourier transform (FFT) images of the Si QDs: (c and d) particle 1; (e and f) particle 2; (g and h) particle 3; (i and j) particle 4; (k and l) particle 5, and (m and n) particle 6.

size distribution histogram plotted using recorded TEM images. The size obtained from TEM images was pretty close to the diameter obtained using DLS. The slight variation in the size

from the two measurements might have resulted because of the contribution coming from the hydration layer surrounding the Si QDs in the DLS study.[17] Si is prone to oxidation in an oxygenated environment and readily forms amorphous SiO_2. High resolution TEM images of the Si QDs (Figure 5.2b and 5.2c) show a clear lattice spacing of 0.31 nm, corresponding to the (111) plane of Si. The fast Fourier transformation (FFT) in figure 5.2d shows the symmetries corresponding to the (111) plane of the particle under analysis, confirming the crystallinity of the sample. The FFT images of the whole region in figure 5.2b (including many particles) were further analyzed. The fringe widths obtained from different particles (shown in Figure 5.2c-5.2n) were found to be 0.31 nm (Particle 1 and 5), 0.19 nm (Particle 2, 3, and 4), and 0.16 nm (Particle 6). The lattice fringe widths of 0.31 nm, 0.19 nm, and 0.16 nm corresponded to (111), (220), and (311) lattice planes of crystalline Si NPs. The crystallinity of the sample was further supported by the selected area electron diffraction (SAED) pattern (Figure 5.3a). Energy dispersive X-ray (EDX) studies (Figure 5.3b) confirm the presence of Si in the nanoparticles. The XRD pattern of as synthesized Si QDs exhibits three diffraction peaks at 2 Θ values of 28.4°, 47.3°, and 56.1° (shown in Figure 5.3c) which are indexable as the (111), (220), and (311) lattice planes of cubic Si, respectively. The XRD results were in accordance with previous reports.[21] The surface composition of as synthesized Si QDs was further determined by X-ray photoelectron spectroscopy (XPS). The full range XPS spectrum of Si QDs (Figure 5.4a) presents five major peaks at binding energy values of 101.5, 151.2, 283.9, 397.5, and 530.2 eV which correspond to Si 2p, Si 2s, C 1s, N 1s, and O 1s respectively.

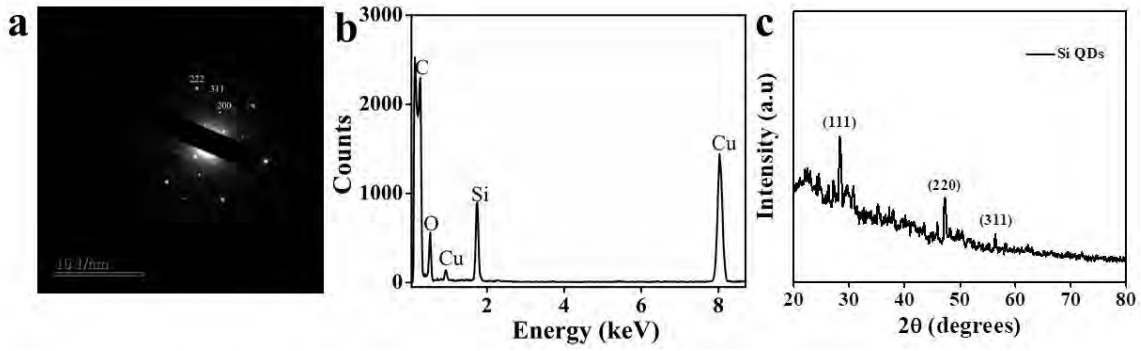

Figure 5.3. (a) SAED pattern, (b) EDX spectrum, and (c) powder X-ray diffraction pattern of the as prepared Si QDs.

In the high resolution Si 2p XPS spectrum of Si QDs (Figure 5.4b), peaks at binding energy values of 99.8, 100.6, 101.3, and 102.2 eV confirm the presence of Si −Si, Si −C, Si−N, and Si–O respectively.[23, 81] However, apart from the Si(0) oxidation state, Si(I) and Si(IV) were also

present, due to attachment of nitrogen and oxygen containing species on the surface of Si QDs.[23] The O 1s spectrum (Figure 5.4c) exhibits two peaks at binding energy values of 530.4 and 531.0 eV which can be attributed to Si−O.[80] The N 1s signal (Figure 5.4d) can be described by three fitted peaks at 397.9, 399.1, and 400 eV originating from N−Si, C−N−C, and N−$(C)_3$.[80] The C 1s spectrum (Figure 5.4e) exhibited five peaks centered at binding energy values of 282.2, 283.2, 284.2, 285.2, and 285.8 eV. Two peaks at 282.3 and 283.2 eV can be ascribed to C−Si.[82] Peaks at 284.2, 285.2, and 285.8 eV are associated with C−C/C=C, C−N, and C−OH/ C−O−C.[80] The XPS results are in accordance with FTIR results.

The electron-hole recombination process which gives rise to emission in Si QDs has contributions from both the radiative (quantum confinement) as well as non-radiative (surface traps) recombinations.[83] Recently, it has been reported that for Si QDs which have a size smaller than the Bohr excitonic radius of Si (≈ 4.2 nm), the nonradiative recombination process largely dominates over the radiative recombination process.[15, 83, 84] The area density of the dangling bonds at the surface of the Si QDs, responsible for the nonradiative recombination increase with a decrease in the size of the QDs, leading to an increase in the nonradiative recombination.

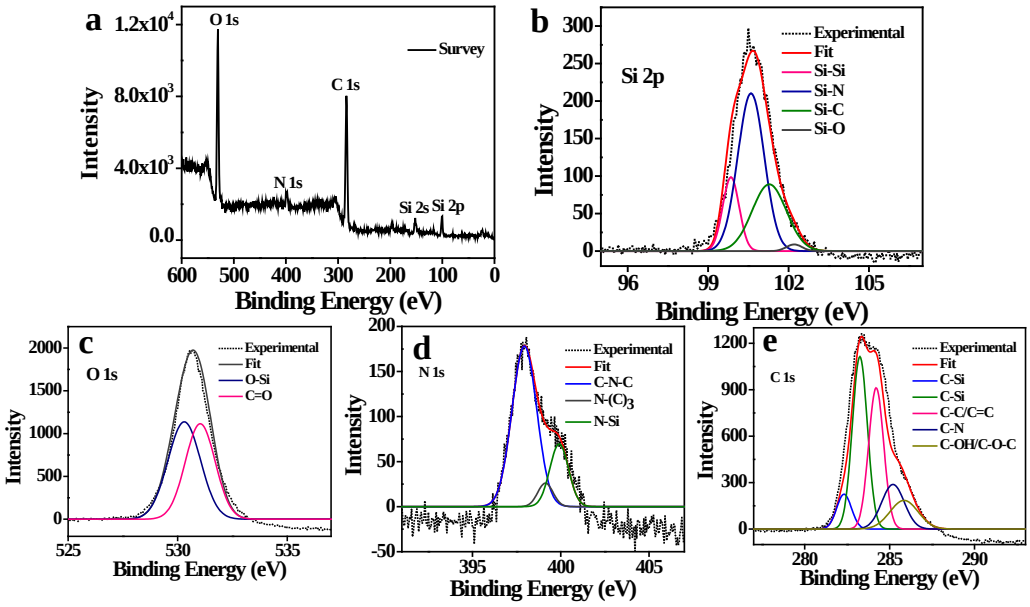

Figure 5.4. High resolution XPS spectra of Si QDs (a) full range, (b) Si(0), (c) O 1s, (d) N 1s , and (e) C 1s, respectively.

In our present case, the average size of the Si QDs is ≈ 2.7 nm, which is very small, when compared to the Bohr exciton radius of Si. This indicates that there is a large area density of

dangling bonds at the QD surface and hence the emission observed in the present case originates from the defect states. Furthermore, we observed that the emission maxima of the Si QDs shift towards red region upon increasing the excitation wavelength. It was observed that the emission maxima shifted from 450 nm to 468 nm when the excitation wavelength was changed from 340 to 380 nm (Figure 5.5). This red shift is consistent with earlier report[85] and suggests that the blue emission originates from the oxidation induced defects at the surface of Si QDs.

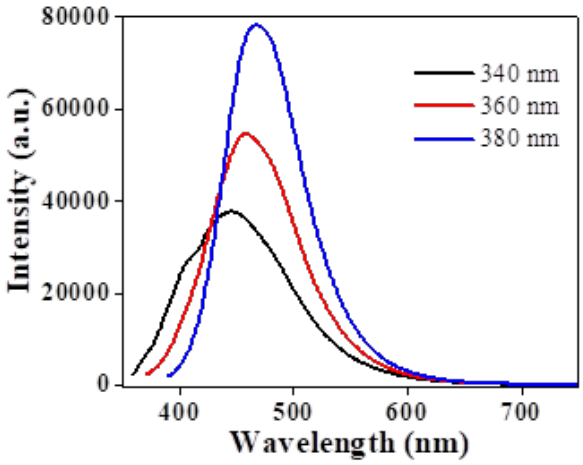

Figure 5.5. Fluorescence spectra of Si QDs at different excitation wavelengths showing a red shift in emission maxima with increasing excitation wavelength.

5.2.2.3. Stability studies of Si QDs

To ensure that the as synthesized QDs have practical applicability it was required to check their photothermal and chemical stability. The as prepared Si QDs stability was tested by subjecting them to different ionic strength, temperature, and pH conditions. The stability of QDs in solutions containing high salt is still challenging as the QDs are highly prone to agglomerate in cellular conditions.[86]. It was observed that the emission wavelength, as well as the emission intensity, was little affected by a change in the ionic strength of the medium. The QDs maintained their fluorescence intensity (Figure 5.6) even at a NaCl concentration of 200 mM, suggesting excellent salt tolerance. The stability of Si QDs at high salt concentration enables their easy conjugation with biomolecules such as oligonucleotides and can significantly enhance their stability in a wide range of biological conditions such as a cellular matrix. After determining the ionic stability of QDs, the fluorescence stability was examined for a wide range of heating temperature (20 to 80 °C). We found that the emission intensity of Si QDs was

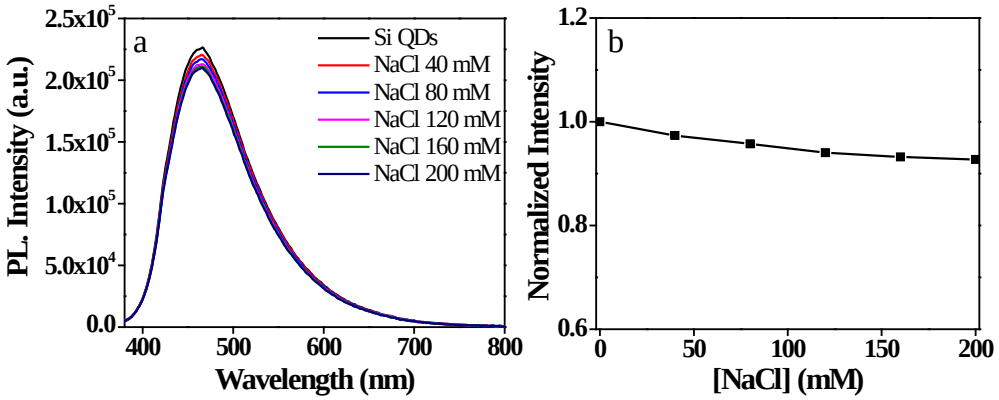

Figure 5.6. (a) Fluorescence spectra of Si QDs at different ionic strengths and (b) plot of variation of fluorescence intensity, with ionic strength.

largely dependent on temperature and quenching of fluorescence was observed with increasing temperature. When the temperature was increased from 20 to 80 °C, a 51% decrease in emission intensity was observed (Figure 5.7). This could be attributed to the nonradiative relaxation originated from the thermal activation of nonradiative trappings.[87] Interestingly, the

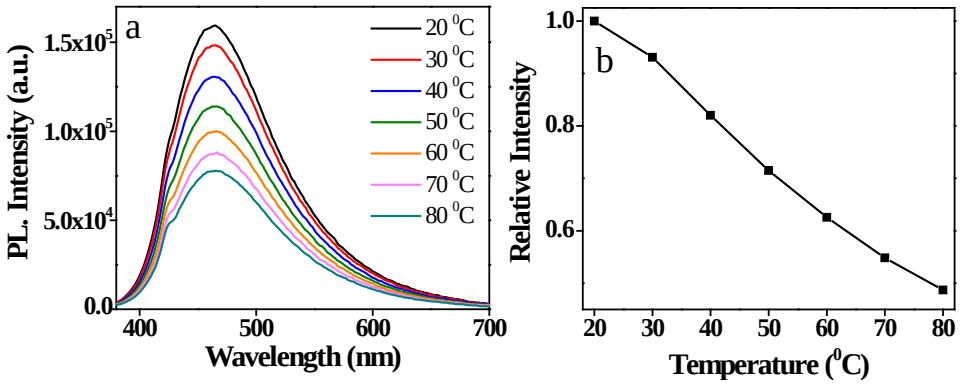

Figure 5.7. (a) Fluorescence spectra of Si QDs with varying temperature and (b) plot of relative emission intensity, with varying temperature.

fluorescence could be fully recovered upon cooling the solution (Figure 5.8a) and the reversible heating-cooling cycle could be repeated several times (Figure 5.8b). The reversible fluorescence response of Si QDs with temperature can be attributed to the synergistic effect of abundant oxygen-containing functional groups and hydrogen bonding with water, similar to those for carbon dots.[88] This reversible fluorescence property of Si QDs will be helpful while conjugating them with biomolecules such as DNA for sensing applications where recycling between certain temperature ranges is required for efficient binding. Thus, the Si QDs

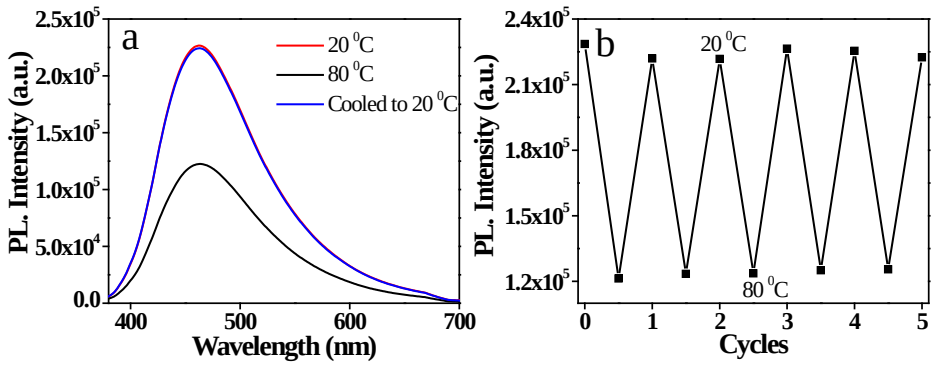

Figure 5.8. (a) Fluorescence spectra of Si QDs at 20 °C, at 80 °C, and after cooling back to 20 °C, and (b) temperature reversibility of Si QDs, during five consecutive heating−cooling cycles.

synthesized by the present method hold promise for applications in optical thermometry. We have also recorded the lifetime of Si QDs in the temperature range of −10 to 40 °C. We found the increment in the lifetime of Si QDs upon decreasing the temperature (Figure 5.9). A similar

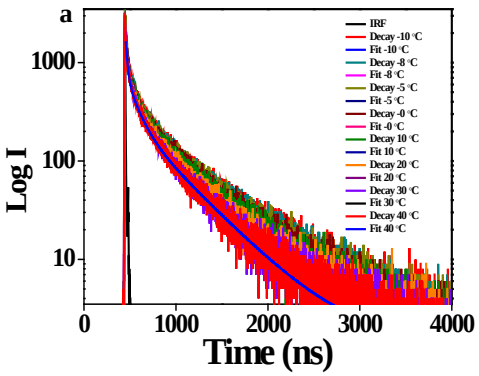

b

Temperature	b_1	τ_1	b_2	τ_2	b_3	τ_3	$\langle\tau\rangle = b_1\tau_1 + b_2\tau_2 + b_3\tau_3$
-10 °C	0.28	4.5	0.59	17.3	0.12	0.80	11.56
-8 °C	0.27	4.35	0.60	16.78	0.13	0.82	11.34
-5 °C	0.25	3.44	0.63	15.4	0.11	0.57	10.62
0 °C	0.25	3.79	0.60	15.6	0.14	0.74	10.41
10 °C	0.26	3.97	0.6	15.3	0.13	0.72	10.30
20 °C	0.26	3.46	0.62	13.7	0.12	0.68	9.47
30 °C	0.29	3.7	0.58	13.11	0.13	0.71	8.76
40 °C	0.28	3.11	0.59	12.68	0.12	0.54	8.43

Figure 5.9. (a) Temperature dependent decay curve of as synthesized Si QDs and (b) corresponding decay time components.

trend in lifetime with lowering of temperature has been reported for carbon dots.[87] This could be due to lowering of photoluminescence relaxation dynamics due to a decrease in the non-radiative decay processes with a decrease in temperature.[87] Further, we studied the stability of

Si QDs in a pH range of 2 to 10. As indicated by figure 5.10, the emission intensity of the Si QDs was maximum at pH 7.0. Upon increasing or decreasing the pH, a decrease in the fluorescence intensity of the Si QDs was observed, although there was no shift in the emission maximum. This pH-dependent fluorescence property of the Si QDs may be due to the difference in surface charge of Si QDs from protonated to deprotonated states with changing pH. [89]

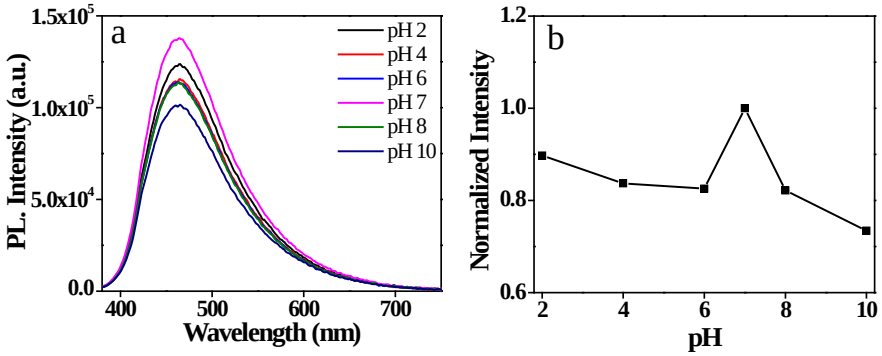

Figure 5.10. (a) Fluorescence spectra of Si QDs at pH 2, 4, 6, 7, 8 and 10 and (b) plot of normalized emission intensity against different pH.

5.2.2.4. Mechanism of formation of Si QDs

The mechanism of formation of Si QDs is schematically illustrated in scheme 5.1. In brief, APTES molecules are readily reduced by glucose molecules through oxidation reduction

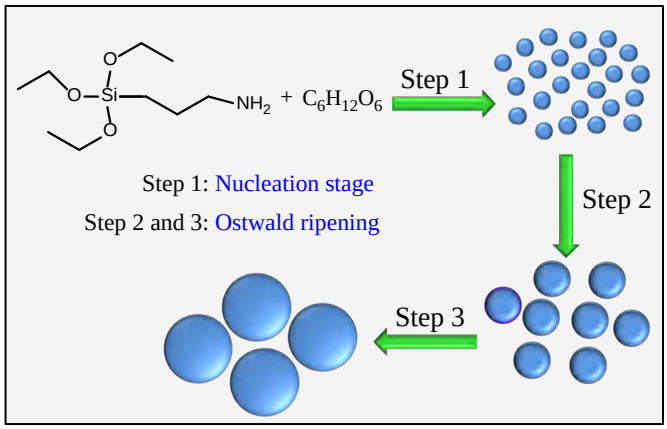

Scheme 5.1. Schematic depiction of the formation mechanism of Si QDs using APTES and glucose.

reaction leading to at first formation of crystal nuclei. With the progress of the reaction, the concentration of APTES reaches a minimum and the growth of crystal nuclei finally stops. Then

Ostwald ripening takes place and small sized nanocrystals are first formed. Further, the initially grown small nanocrystals dissolve in solution and deposit onto the larger growing nanocrystals due to their instability because of surface-to-volume ratio, finally forming larger, stable nanocrystals. Similar growth of Si nanocrystals has been reported using APTES as the Si precursor and trisodium citrate as the reductant. [17]

5.2.2.5. Synthesis and characterization of Au NP-Si QD hybrid NPs

In our present system, glucose was used as a reducing and stabilizing agent, which resulted in the presence of several oxygenated functionalities on the surface of the Si QDs as revealed from FTIR studies. So, it was speculated that the oxygenated groups on the surface of the Si QDs might be involved to reduce Au^{3+} ions to Au NPs, in a similar way to the reduction of metal salts by carbon dots and graphene oxide.[90-92] So we tried synthesizing Au NPs using our Si QDs as reducing agent without any external surfactant. The formation of Au NPs was accomplished by simple incubation of $HAuCl_4$ (final concentration of 0.6 mM) solution with the as synthesized Si QDs solution (0.1 mL of the dialyzed Si QDs) at room temperature. Within 30 min, the color of the solution converted into red from light yellow without any heating or photoexcitation, colorimetrically revealing the generation of Au NPs (Figure 5.11a).

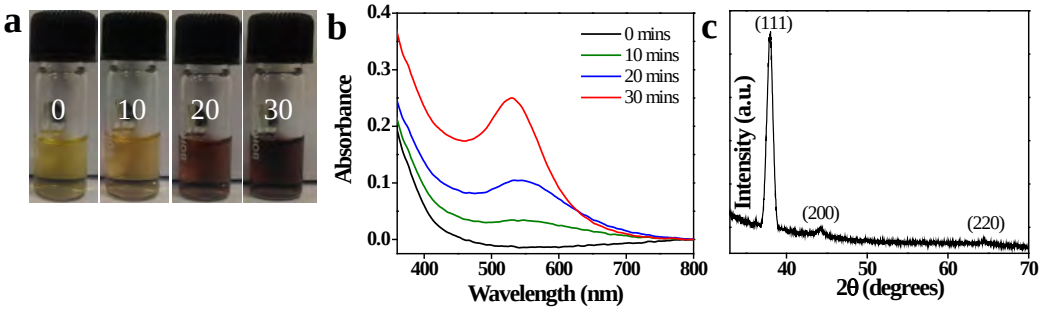

Figure 5.11. (a) Digital images, showing the progress of formation of Au NPs using Si QDs as reducing agent at 0, 10, 20, and 30 min after addition of $HAuCl_4$, (b) UV−visible spectra of the as prepared Au NPs showing the LSPR band at 527 nm at different times, and (c) powder X-ray diffraction pattern of the Au NPs synthesized using Si QDs.

The as prepared Au NPs showed their characteristic LSPR band centered at 527 nm (Figure 5.11b) confirming the presence of Au NPs. The peaks present in the XRD pattern of the NPs (Figure 5.11c) revealed the formation of face centered cubic gold nanostructures. To further get insights into the morphology and size of Au NPs formed we recorded the TEM images. The lower magnification TEM images shown in Figure 5.12a showed the presence of a mixture of

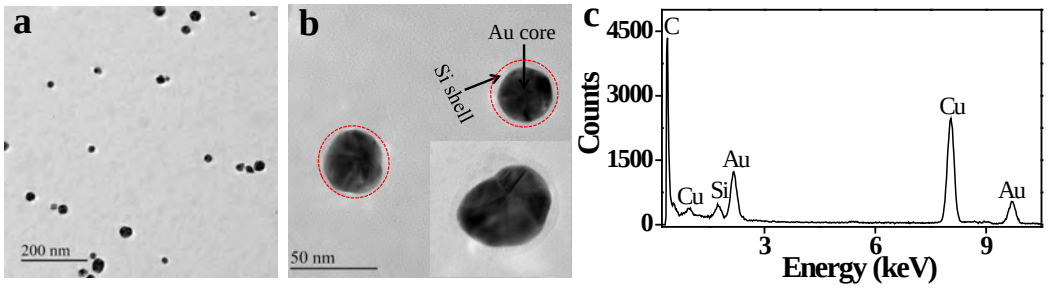

Figure 5.12. (a) TEM images of the Au NP-SiQD nanocomposite synthesized using Si QDs,(b) HRTEM images of the Au NP-Si QD composite showing the Si QD shell over the Au NP core, and (c) EDX spectrum of Au NP-Si QD hybrid NPs.

spherical and hexagonal shaped Au nanoparticles. The HRTEM images showed presence of a thin shell of Si QDs over the Au NPs (Figure 5.12b), resulting in a core–shell like morphology. The structures were termed as Si QD-Au NP hybrid nanostructures. The average diameter of the core–shell structure with spherical Au NPs in the core was calculated to be 30.8 ± 3.4 nm, with

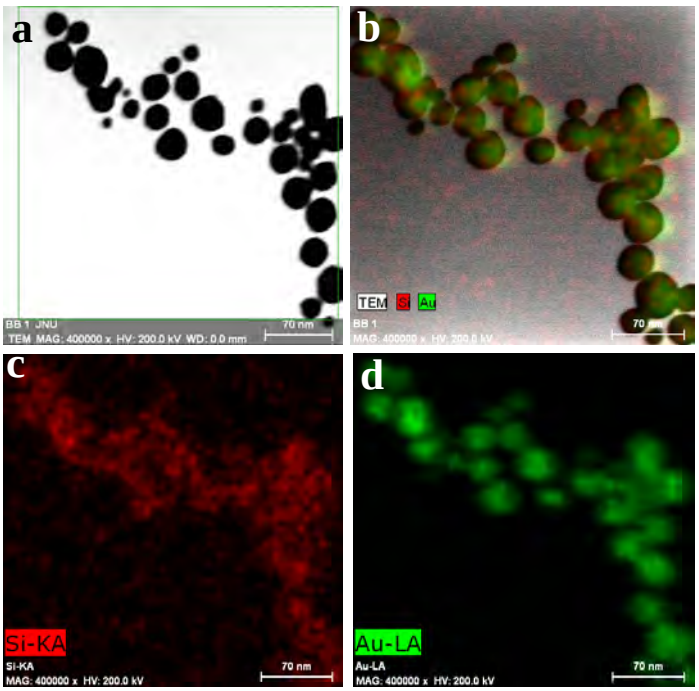

Figure 5.13. (a) Bright field STEM images of hybrid NP system and (b,c,d) the corresponding elemental mapping.

the thickness of the shell being about 5.9 nm. Further, the composition of the hybrid nanostructures was studied by EDX analysis. The EDX performed on the sample confirmed the

presence of both Au and Si (Figure 5.12c) in the hybrid NP system. To determine the elemental composition of the Si QD-Au NP hybrid NPs scanning TEM energy-dispersive X-ray spectroscopy (STEM-EDS) elemental mapping (shown in Figure 5.13) was done. The elemental mapping of hybrid NP system revealed that Si QDs are homogeneously distributed over Au NPs forming a hybrid core−shell like morphology with Au NP core and Si QD shell. To further confirm whether the coating over the Au core is of crystalline or amorphous Si, the lattice fringes in the HRTEM images of the Au NP −Si QD nanocomposite were analyzed. The top view of the Au NP–Si QD nanocomposite (shown in Figure 5.14a and 5.14b) shows lattice fringes of two different d spacings. The lines marked in the inverse FFT image (Figure 5.14d) of the same area as shown in figure 5.14b show the d-spacing of 0.31 nm, corresponding to the (111) plane of crystalline Si and a d-spacing of 0.23 nm that corresponds to the (111) plane of

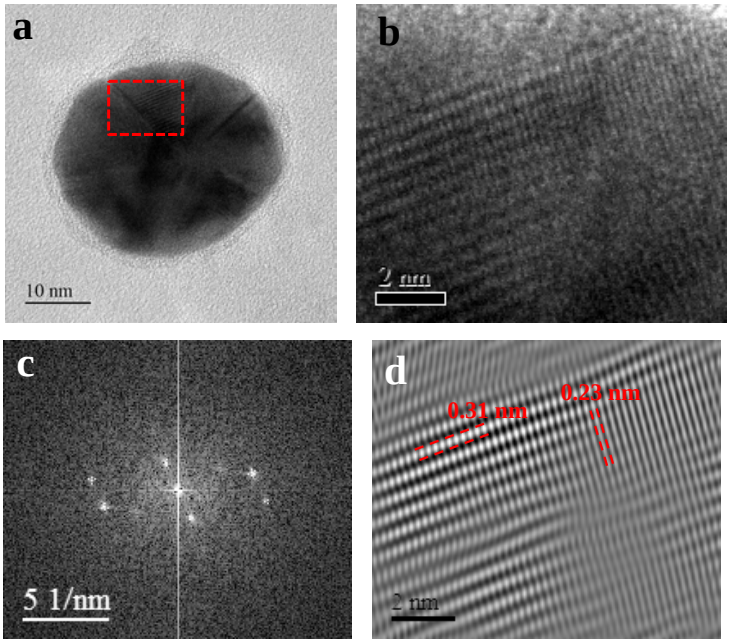

Figure 5.14. (a) TEM image of Au NP- Si QD nanocomposite, (b) selected area HRTEM, (c) FFT, and (d) inverse FFT images of selected area.

Au. To rule out the possibility that 0.31 nm d-spacing is coming because of Au, we analyzed the XRD of Au NPs synthesized using Si QDs. The powder XRD pattern (Figure 5.11c) suggested formation of fcc gold. None of the crystal planes in fcc gold corresponds to a fringe width of 0.31 nm, which further confirms the HRTEM pattern corresponding to the 0.31 nm d-spacing is because of the crystalline Si shell over Au NP. In the present system, the Si QDs act as reductant and also stabilized the nanocomposites because of the presence of glucose on the

surface of Si QDs. The concentration of reducing agents plays an important role to control the size and morphology of the nanoparticles.[93] So the effect of Si QDs concentration on the structure of the Au NP−Si QDs nanocomposites was investigated keeping the concentration of $HAuCl_4$ fixed. The nanocomposites were synthesized with two times (0.2 mL of Si QDs) and

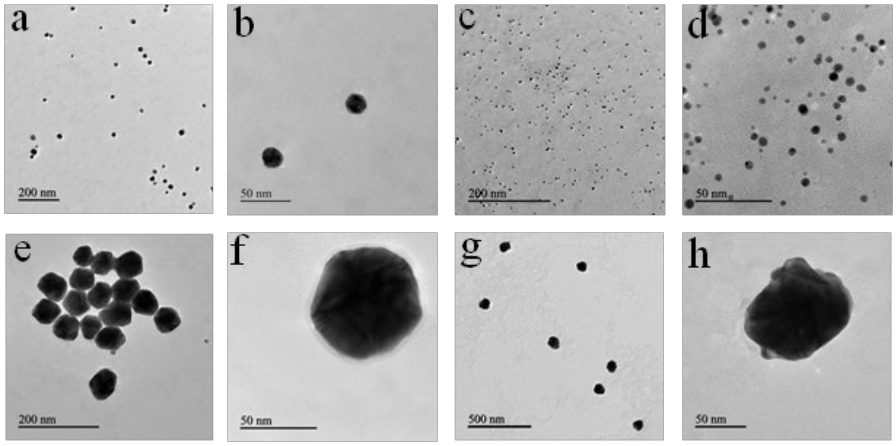

Figure 5.15. TEM images of Au NP- Si QD nanocomposite synthesized using (a and b) two times and (c and d) five times more concentration of Si QDs and TEM images of Au NP- Si QD nanocomposite synthesized using (e and f) two times and (g and h) five time less concentration of Si QDs.

five times (0.5 mL of Si QDs) higher concentrations of Si QDs than that of the initial Si QDs concentration (0.1 mL of the dialyzed Si QDs) and with two times and five times less concentration of Si QDs to the initial concentration. To determine the size and morphology of the nanocomposites synthesized using different concentration of Si QDs TEM images were recorded. We found a reduction in the overall size of the nanocomposite on increasing the concentration of Si QDs and an increase in the average composite size on decreasing the concentration of Si QDs. The TEM images (Figure 5.15(a,b,c,d) showed when the concentrations of Si QDs were increased to two times and five times, the average sizes of the nanocomposites were obtained to be ~24 nm and ~6 nm respectively. And when the concentrations of Si QDs were lowered to two times and five times, the average sizes of the composites increased to ~70 nm and ~93 nm, respectively (Figure 5.15(e,f,g,h)). The UV−visible spectra of Au NP−Si QDs nanocomposite synthesized using lower and higher concentration of Si QDs are shown in figure 5.16. When the concentration of Si QDs was increased, more Si QDs were available to reduce and stabilize the nanocomposite structures, which resulted in reduction of the overall size of the composites. Similarly, an increase in

composite size could be attributed to less number of Si QDs available on decreasing the concentration of Si QDs.

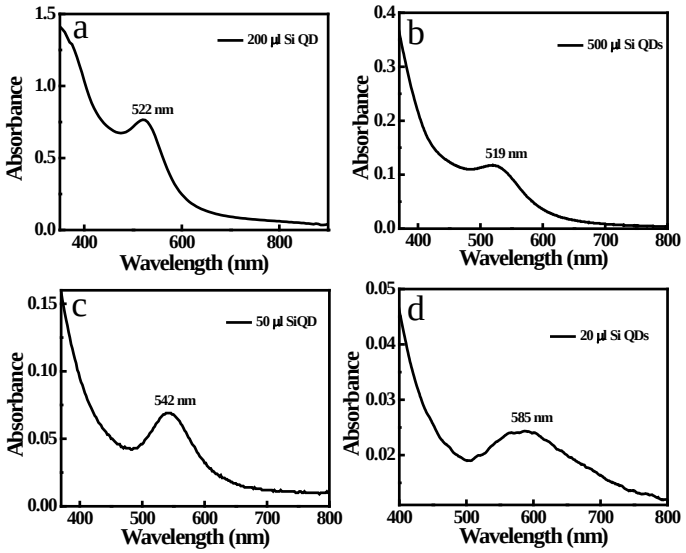

Figure 5.16. UV-Vis spectra of Au NP- Si QD nanocomposite synthesized using (a and b) two times and five times more concentration of Si QDs; and (c and d) two times and five time less concentration of Si QDs.

5.2.2.6. Steady state and time-resolved fluorescence study

The formation of Au NPs by Si QDs was accompanied by a partial quenching of emission of Si QDs (Figure 5.17a). It is well-known that in the vicinity of Au nanoparticles, the emission intensity of QDs undergoes quenching.[94] Further, time-resolved spectroscopic study was done

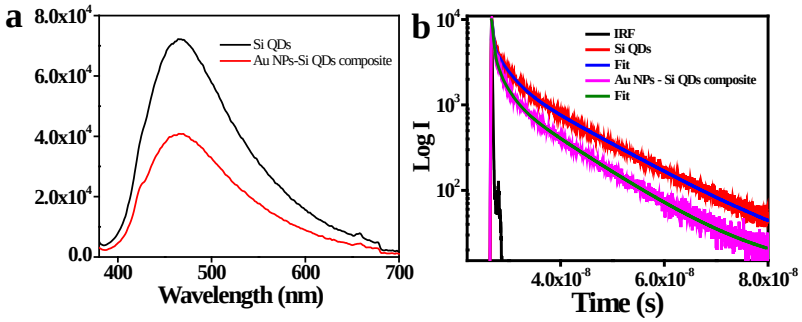

Figure 5.17. (a) Fluorescence emission spectra, and (b) decay curves of as synthesized Si QDs and Si QDs after the synthesis of Au nanoparticles.

for understanding the mechanism of quenching. It was found that the average decay time of Si QDs decreased from 9.82 to 6.8 ns after hybridization with Au nanoparticles (Figure 5.17b). The decrease in the average lifetime of the QDs is mainly attributed to the increase in nonradiative decay rates in the presence of Au NPs.[94] The decay time components of the pure Si QDs and Au NP−Si QD nanocomposites are listed in table 5.1. The decay times of Si QDs and Au NP−Si QD nanocomposites were found to exhibiting triexponential decay.

Table 5.1. Decay time components of the pure Si QD and Au NP-Si QD hybrid NPs

System	b_1	τ_1	b_2	τ_2	b_3	τ_3	$<\tau> = b_1\tau_1 + b_2\tau_2 + b_3\tau_3$	χ^2
Si QD	**0.22**	**2.65**	**0.71**	**13**	**0.08**	**0.25**	**9.82**	**1.37**
Au NPs – Si QDs composite	**0.22**	**2.05**	**0.59**	**10.8**	**0.17**	**0.33**	**6.8**	**1.15**

5.2.2.7. Catalytic activity of Au NP-Si QD hybrid NPs

Metallic NPs have shown tremendous applicability as heterogeneous catalysts for various organic transformations. [95-97] Colloidal hybrid NPs consisting of more than one NP system offers advanced properties compared to the single nanoparticle system due to a synergistic effect between two or more systems.[31] Therefore, we intended to study the catalytic ability of the Au NP −Si QD hybrid NP system. The catalytic potential of the Au NP−Si QD system was

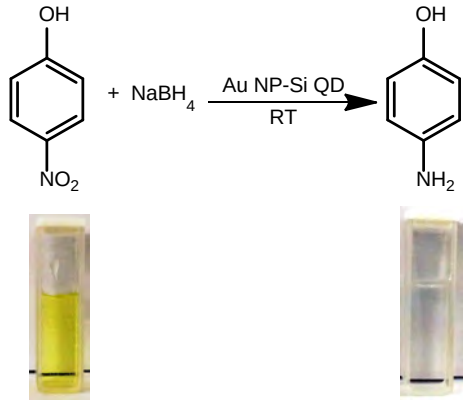

p-nitrophenol *p*-aminophenol

Scheme 5.2. Schematic representation for the reduction of p-nitrophenol to p-aminophenol by $NaBH_4$, using Au NP-Si QD hybrid NPs as a catalyst.

studied by carrying out the conversion of *p*-nitrophenol to *p*-aminophenol in the presence of $NaBH_4$ as reducing agent. The reaction is a surface catalyzed reaction and takes place on the surface of the nanoparticles, following a Langmuir-Hinshelwood mechanism.[98-100] First, the borohydride ions adsorb on the surface of Au nanoparticles and transfer a surface hydrogen species to the surface of the nanoparticles. Concomitantly, *p*-nitrophenol molecules are adsorbed on the surface of the nanoparticles. Both these steps are reversible and can be modeled in terms of Langmuir isotherm. Moreover, the adsorption/desorption equilibriums and diffusion of reactants to the nanoparticles are considered to be fast. The reduction of *p*-nitrophenol, which is the rate-determining step, occurs due to the reaction of adsorbed *p*-nitrophenol with the nanoparticles surface-bound hydrogen atoms. Finally, the product *p*-aminophenol desorbs, leaving free metal surface such that catalytic cycle can begin again. When $NaBH_4$ was added to *p*-nitrophenol, the solution undergoes an immediate color change from faint yellow to dark yellow. This can be attributed to *p*-nitrophenolate ions, which absorb at 400 nm. [101-103] Upon addition of Au NP −Si QD hybrid NPs to the *p*-nitrophenolate solution, the yellow color of the solution gradually turned colorless (Scheme 5.2). From the time dependent UV−visible studies (Figure 5.18a), it was found that the peak intensity at 400 nm was decreased with the appearance of a new peak at 300 nm due to the conversion of *p*-nitrophenolate ion to *p*-aminophenol. The Au NP-Si QD nanocomposite showed good catalytic efficacy, as evidenced

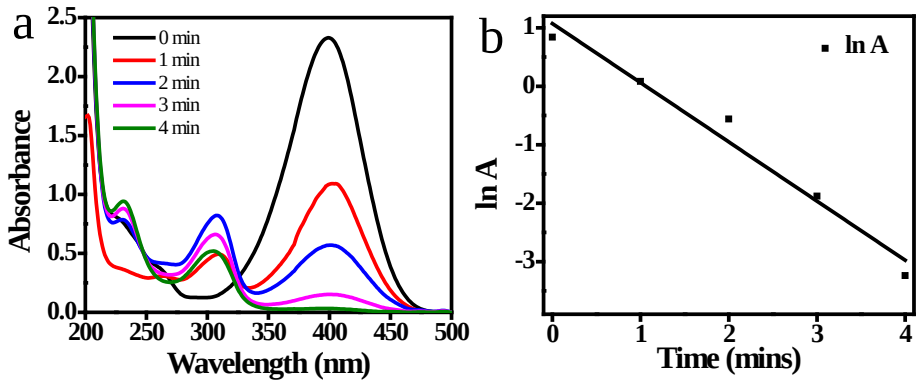

Figure 5.18. (a) Time dependent absorption spectra for the conversion of p-nitrophenol to p-aminophenol using $NaBH_4$ as the reducing agent and Au NP-Si QD as catalyst, and (b) natural log of absorbance at 400 nm versus time plot.

by the completion of the reaction in just 4 min. It is important to mention that a clear isosbestic point was not observed in the UV−visible spectra shown in figure 5.18a. This might be due to the scattering coming from H_2 gas which was produced during the reduction by $NaBH_4$.[103] Since

in the reduction, excess of $NaBH_4$ was taken, it was assumed that the concentration of $NaBH_4$ remains constant during the entire reaction. Therefore, the kinetics of the reaction can be calculated based on the consumption rate of *p*-nitrophenol. A linear graph was obtained when ln(absorbance) was plotted against time (Figure 5.18b), which indicated a pseudo-first-order kinetics. From the ln(absorbance) versus time plot, the apparent rate constant, k, was determined to be 1.7×10^{-2} s^{-1}, which is higher than previously reported rate constants of different types of Au nanostructures synthesized using biomolecules and carbon dots as reducing agents.[102-105] To get better insights into which part of the nanocomposite is responsible, control experiments were carried out with similar reaction conditions taking the same concentration of $NaBH_4$ but using either Si QDs or Au NPs (of the same concentration as in

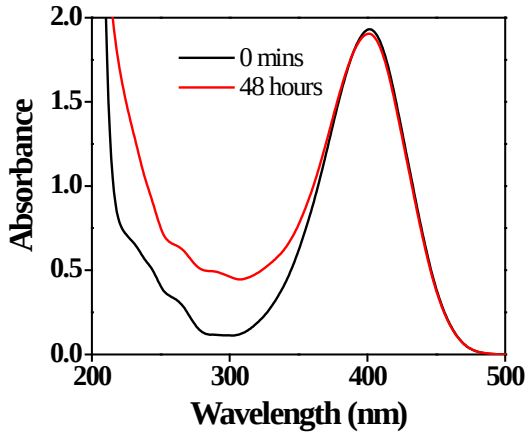

Figure 5.19. Control experiment showing the inability of Si QDs alone in catalyzing the reduction of p-nitrophenol to p-aminophenol even after 48 hours.

nanocomposite) alone. Controlled experiments using Si QDs indicated that Si QDs alone with the same concentration of $NaBH_4$ were incapable of catalyzing the reaction as there was no change in the color of the solution or intensity of the peak at 400 nm even after 2 days (Figure 5.19). The control catalytic reaction was performed in the presence of Au nanoparticles only with the same concentration of $NaBH_4$ by using spherical Au nanoparticles of the same size and same particle concentration (average size of 32 ± 2 nm with 0.66 nM Au nanoparticle concentration) as was used for nanocomposite structures. The Au NPs were prepared following a reported protocol after slight modifications.[106] The UV−visible absorption spectrum and corresponding TEM images of the Au NPs used in the catalytic reaction are shown in figure 5.20a and 5.20b, respectively. It was observed that with Au NPs only as catalyst the reaction is much slower and completed in 30 min (Figure 5.20c). The rate constant of the reaction was 1.8×10^{-3} s^{-1}, which is 10 times lower than the nanocomposite (Figure 5.20d). In our study, we

have found higher catalytic efficiency of the Au NP-Si QD hybrid nanocomposite compared to pure Au nanoparticles. This may be due to enhanced adsorption and electron transfer ability of the composite structure due to the modification of the electronic structure in the core −shell type nanocomposite structure because of plasmon−exciton interaction between semiconductor and metal.[85, 107] Since, the reduction of *p*-nitrophenol by $NaBH_4$ catalyzed by Au nanoparticles is a

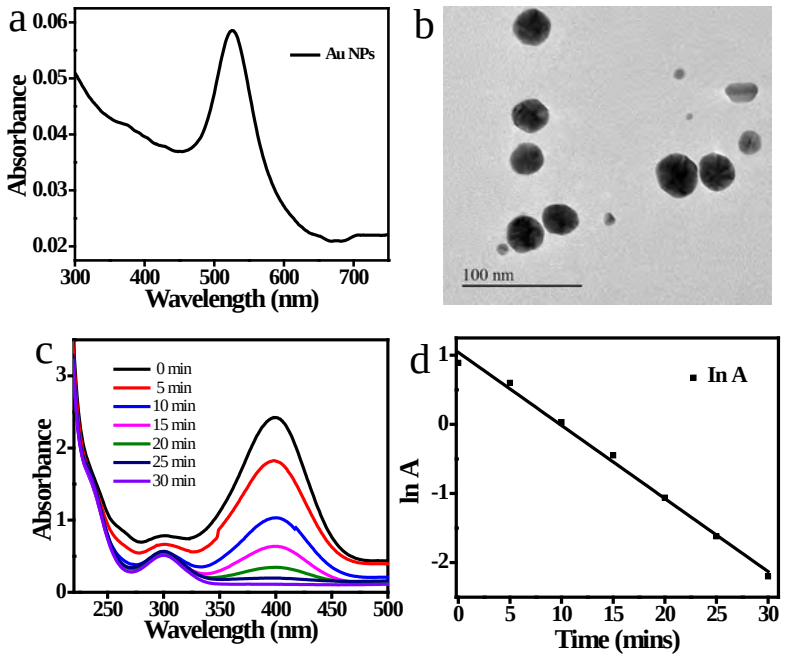

Figure 5.20. (a) UV-Vis spectrum of Au NPs alone showing SPR band at 527 nm, (b) TEM images of Au NPs used for carrying out catalysis reaction using only Au NPs, (c) time dependent UV-Vis spectra for the reduction of p-nitrophenol to p-aminophenol using $NaBH_4$ as the reducing agent and Au NP alone as a catalyst, and (d) plot of natural log of absorbance at 400 nm versus time.

surface catalyzed reaction, so the influence of the size on the catalytic performance of Au NP-Si QD hybrid nanocomposite would clearly be reflected by the changes in the reaction rate. We studied the catalytic properties of the different sized nanocomposites that were obtained after varying the concentration of Si QDs keeping the concentration of $HAuCl_4$ fixed. It was observed that the catalytic reaction became slower taking longer time for completion when the size of the nanocomposites is large (average sizes of ~70 nm and ~93 nm), and the catalytic reaction rate was faster for small sized nanocomposites (average sizes of ~24 nm and ~6 nm). For Au NP −Si QD nanocomposites of size 70 and 93 nm, the reaction times were found to be 8 and 12 min, respectively (as presented in Figure 5.21c and 5.21d). The corresponding rate constants

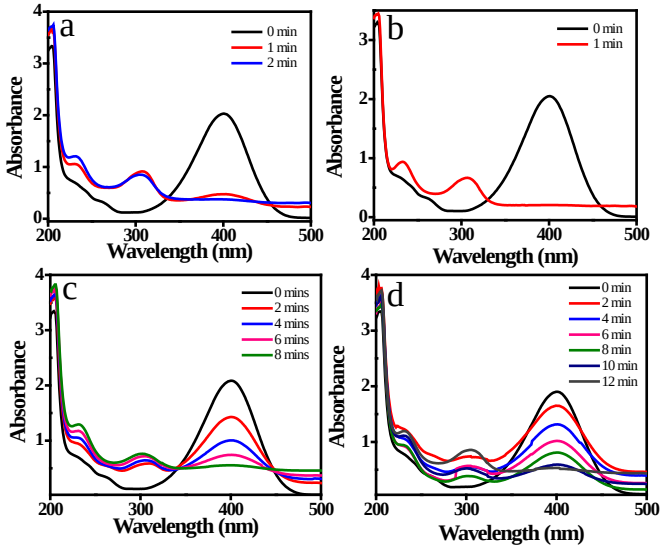

Figure 5.21. Time dependent UV-visible spectra for the reduction of p-nitrophenol to p-aminophenol using $NaBH_4$ as the reducing agent and Au NP- Si QD nanocomposite as a catalyst for (a and b) two and five times more (c and d) two and five times less concentration of Si QDs.

were found to be 2.7×10^{-3} s^{-1} and 1.8×10^{-3} s^{-1} (Figure 5.22c and 5.22d). For Au NP−Si QD nanocomposite of size 24 nm the catalysis time reduced to 2 min (Figure 5.21a). With further reduction of size to 6 nm, the catalysis reaction became very fast and finished in less than one

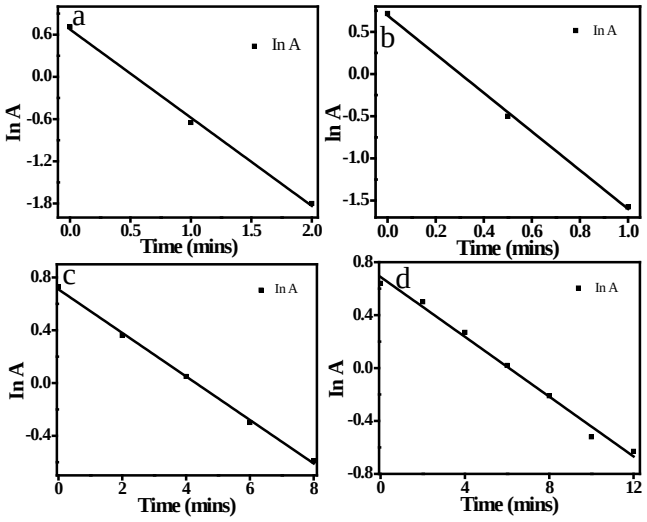

Figure 5.22. Plot of natural log of absorbance at 400 nm versus time for Au NP- Si QD nanocomposite synthesized using (a) two and (b) five times higher and (c) two and (d) five times lower concentration of Si QDs.

min (Figure 5.21b). The rate constants for catalysis reactions carried out using 24 and 6 nm Au NP- Si QD nanocomposite structures were obtained to be 2.1×10^{-2} s^{-1} and 3.8×10^{-2} s^{-1}, respectively (Figure 5.22a and 5.22b). The increase in the reaction rate constant with decreasing size of the nanocomposite may be attributed to the enhancement of the total surface area of the catalyst, as the particle concentration is higher for smaller sized nanocomposites.

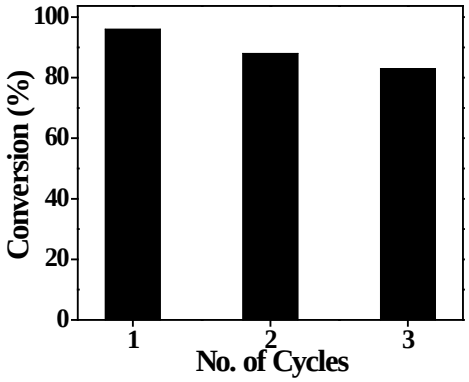

Figure 5.23. Reusability of the Au NP-Si QD hybrid NPs as catalyst for the reduction of p-nitrophenol.

The Au NP-Si QD hybrid NP system showed good reusability up to the third cycle tested (Figure 5.23). However, it was observed that a slightly longer time was needed to complete the reaction with the recycled catalyst, which might be due to the poisoning of the surface by adsorbed reactant molecules on the NPs. [108]

5.2.3. Conclusion

In the present study, we have developed a simple, one-pot, and environmentally benign synthetic route for the formation of Si quantum dots using glucose as a reducing agent. The fluorescence emission of the Si quantum dots showed excellent stability against ionic strength and showed a reversible quenching of fluorescence with an increase and decrease of temperature. The stability of Si QDs at high salt concentration and reversible fluorescence property enables their easy conjugation with biomolecules and significantly enhances its potentiality in bioimaging applications. The prepared Si quantum dots had abundant oxygenated functionalities which rendered them excellent water dispersibility. The oxygen rich functional groups were exploited to reduce Au^{3+} ions to Au nanoparticles to form a hybrid Au NP −Si QD nanocomposite. Such a hybrid nanoparticle system has prospects for being used as a multifunctional system in applications such as biology and energy harvesting. The synthesized Au NP−Si QD hybrid nanoparticles were employed as catalysts for the conversion of *p*-

nitrophenol to *p*-aminophenol. We found that the synthesized hybrid nanoparticles could be used as effective catalysts for the reduction of nitroarenes. Further, the results showed the usual trend of catalytic activity of surface catalyzed reactions, where nanoparticles with higher surface area to volume ratio demonstrated better efficiency. The simple room temperature synthesis of Si quantum dots and Au NP-Si QD hybrid nanoparticle using biomolecules such as glucose will add a newer dimension to the synthesis of hybrid nanoparticles using biomolecules.

Note:

- The permission has been granted by authors and corresponding author of the published paper prior to adopting in the present thesis. The associated relevant publication is:

Bhagwati Sharma[†], **Swati Tanwar**[†], and Tapasi Sen "One pot green synthesis of Si quantum dots and catalytic Au nanoparticle-Si quantum dot nanocomposite"***ACS Sustainable Chemistry and Engineering***, 2019, *7* (3), 3309–3318. ***(†Equal contribution)***

5.3. Si QDs for generation of white light emitting mixture

5.3.1. Experimental section

5.3.1.1. Materials

Gold chloride trihydrate ($HAuCl_4.3H_2O$), glutathione (GSH), L-alanine, L-aspartic acid, L-histidine, L-phenylalanine, L-arginine, L-glutamic acid, L-cysteine, polyvinylpyrrolidone (PVP), D-glucose and 3-aminopropyltriethoxysilane (APTES) were purchased from Sigma-Aldrich. Agarose was purchased from Himedia. Carbon coated transmission electron microscopy (TEM) grids used for TEM imaging were purchased from Ted Pella. Dialysis membrane with a molecular weight cut off of 0.5–1 kDa was purchased from Spectrum labs. Dialysis membrane with a molecular weight cut off of 7–10 kDa was purchased from Himedia. Salts used for sensing namely calcium carbonate, ferric nitrate nonahydrate, calcium chloride dihydrate, sodium chloride, zinc nitrate hexahydrate, magnesium chloride hexahydrate, sodium chlorate, cadmium nitrate tetrahydrate, nickel chloride hexahydrate, copper nitrate trihydrate, lead chloride, mercuric chloride, quinine sulphate dihydrate and sulphuric acid were purchased from Merck, India. All the chemicals were of analytical grade and were used without any further purification. Milli-Q water was used throughout the experiments.

5.3.1.2. Experimental procedures

5.3.1.2.1. Synthesis of blue emitting Si QDs

Si QDs were synthesized as described in section 5.2.1.2 of this chapter.

5.3.1.2.2. Synthesis of orange red emitting glutathione (GSH) capped Au NCs

The synthesis of GSH capped Au NCs was performed following a reported procedure.[91] Briefly, freshly prepared aqueous solutions of $HAuCl_4.3H_2O$ (20 mM, 0.5 mL) and GSH (100 mM, 0.15 mL) were mixed with 4.35 mL of ultrapure water at 25 ºC. The reaction mixture was heated to 70 ºC under gentle stirring (500 rpm) for 24 h and resulted in a pale yellow colored solution which indicated the formation of Au NCs. The as obtained solution was dialyzed against water using a 7 kDa dialysis membrane and was stored at 4 ºC for further use.

5.3.1.2.3. Synthesis of white light emitting mixture (WLEM)

As synthesized solutions of Si QDs and Au NCs were diluted first so that the emission intensity of both the components become almost identical. To generate white light emitting mixture, we have mixed the diluted solutions of Si QDs and Au NCs in different ratio. It was found that

white light emission was coming from a mixture of 200 mL of Au NCs to 2 mL solution of Si QDs.

5.3.1.2.4. Metal ions sensing

For metal ions sensing, 2 mL of as obtained WLEM was titrated with 4 mL (1 mM) solution of different metal salts. PL spectra of WLEM in presence of different metal ions were recorded after 5 minutes of incubation at room temperature.

As synthesized Si QDs, Au NCs, and WLEM were characterized by TEM, dynamic light scattering (DLS) study, UV-Vis spectrophotometer, photoluminescence (PL) spectrophotometer, and TCSPC measurements as described in chapter 2 of this thesis.

5.3.2. Results and discussion

5.3.2.1. Optical and structural characterizations of Si QDs and Au NCs

Optical and structural characterization of the as synthesized Si QDs was done in a similar manner as described in section 5.2.2.1 and 5.2.2.2 of this chapter. The size determined using DLS and TEM measurements (Figure 5.24a and 5.24b) were 3.6 nm and 2.7±0.3 nm respectively. The Si QDs were highly fluorescent and showed a blue emission with a maximum

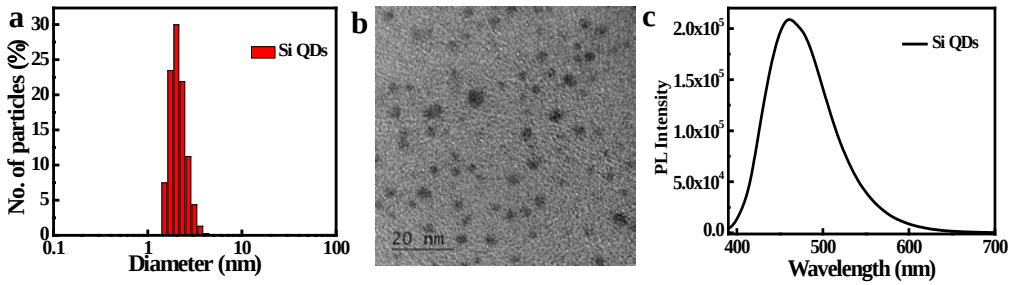

Figure 5.24. (a) DLS size distribution, (b) TEM images, and (c) PL spectrum of the as synthesized Si QDs.

at 464 nm upon excitation at a wavelength of 365 nm (Figure 5.24c). The UV-visible absorption spectrum of the as prepared Au NCs showed a broad absorption in the region of 200 to 400 nm without appearance of any prominent peak (Figure 5.25a). The absence of localized surface plasmon resonance band (SPR) in the absorption spectrum revealed the formation of very small sized Au nanoparticles. The as synthesized Au NCs showed orange red emission with a maximum centered at 620 nm upon excitation with 365 nm wavelength (Figure 5.25b), indicating the formation of Au nanoclusters. DLS study indicated the formation of particles with

an average size of 2.4 nm (Figure 5.25c). The size and morphology of the Au NCs were further ascertained from the TEM studies, which confirmed the formation of spherical Au NCs with an average dimension of 1.9 ± 0.8 nm (Figure 5.25d).

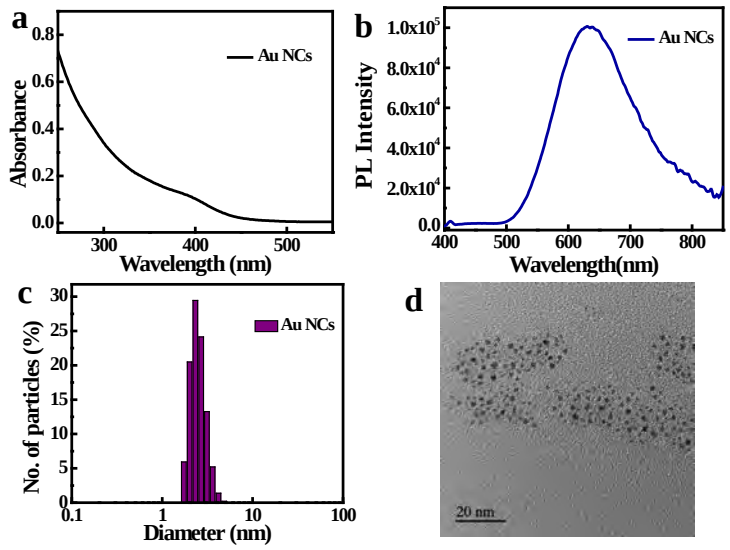

Figure 5.25. (a) UV- visible absorption spectrum of Au NCs, (b) PL spectrum of Au NCs (λ_{ex} = 365 nm), (c) DLS size distribution of the Au NCs, and (d) TEM images of Au NCs.

5.3.2.2. Generation and photoluminescence properties of WLEM

A general strategy for generating white light emission is mixing of two complementary colored luminescent materials. Since the bluish green emission of our Si QDs and reddish orange emission of the synthesized Au NCs are complementary to each other we tried generating WLEM by mixing their solutions. As demonstrated earlier, for getting white light emission in a range of states, including in solids, solutions, and gels it is important to equalize the emission intensities of both the complementary colored components.[109] At first, diluted solutions of Si QDs and Au NCs having equal PL intensities were prepared. Further, the diluted solutions of Si QDs and Au NCs we mixed in different ratios to generate WLEM. The PL spectra of the mixture solution after every step of addition of Au NCs solution to Si QDs solution was recorded and is shown in figure 5.26a. The chromaticity color co-ordinate helps us in identifying the quality of color regardless of its luminance. It is well reported that a perfect white light emitting source has CIE chromaticity coordinate of (0.33, 0.33). The chromaticity color co-ordinate of the as synthesized WLEM was determined using CIE (Commission Internationale del'Eclairage) diagram. The obtained Commission Internationale d'Eclairage (CIE) chromaticity co-ordinates of pure Si QDs, Au NCs, and their mixtures were compared with that of the perfect white light emitting

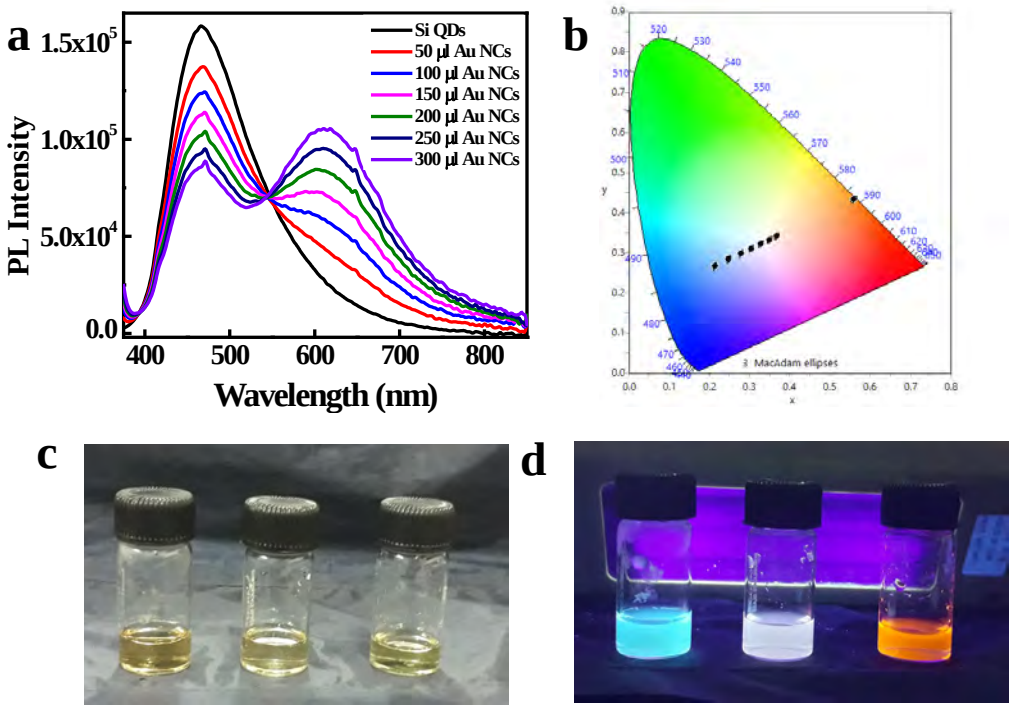

Figure 5.26. (a) PL spectra of Si QDs after addition of different volumes of Au NCs, (b) corresponding chromaticity plot for color co-ordinates, (c) digital images of Si QDs, WLEM and Au NCs in day light, and (d) digital images of Si QDs, WLEM and Au NCs under UV light (λ_{exc} =365 nm).

source. The CIE co-ordinate of as synthesized Si QDs was found to be (0.21, 0.26) in the blue region as represented in figure 5.26b. On the other hand, the CIE co-ordinate for the Au NCs was found to be in the red region with value of (0.56, 0.43) (Figure 5.26b). A careful investigation of the CIE co-ordinates of both Si QDs and Au NCs suggested that the mixing of both components in a particular ratio could cover the entire visible region, thus leading to the

Table 5.2. CIE co-ordinates of Si QDs with different volumes of Au NCs

Systems	X	Y
Si QDs	0.21	0.26
Si QDs + 50 µl Au NCs	0.25	0.28
Si QDs + 100 µl Au NCs	0.29	0.30
Si QDs + 150 µl Au NCs	0.30	0.31
Si QDs + 200 µl Au NCs	0.33	0.32
Si QDs + 250 µl Au NCs	0.35	0.33
Si QDs + 300 µl Au NCs	0.37	0.34
Au NCs	0.56	0.43

generation of white light. It is clearly visible from the emission spectra (shown in Figure 5.26a) that the pattern of the spectrum of Si QDs was changing gradually after addition of Au NCs to the Si QDs solution. The appearance of a new band at 620 nm was observed upon addition of Au NCs in addition to the initial peak present at 464 nm. It was found that with increasing concentration of Au NCs the intensity of the Si QDs peak centred at 464 nm was gradually decreasing along with an increase in the emission intensity of the Au NCs band at 620 nm. A clear iso-emissive point could be observed at 543 nm indicating the presence of only two emissive species in the system. It was observed that upon addition of Au NCs component, the CIE co-ordinates of the mixture system started moving from blue region toward that of perfect white source i.e. (0.33, 0.33) as shown in figure 5.26b and table 5.2. The analysis of CIE co-ordinates (Figure 5.26b) revealed the formation of WLEM with co-ordinate of (0.33, 0.32) when 200 mL of Au NCs solution was added to 2 mL solution of Si QDs. This value is pretty

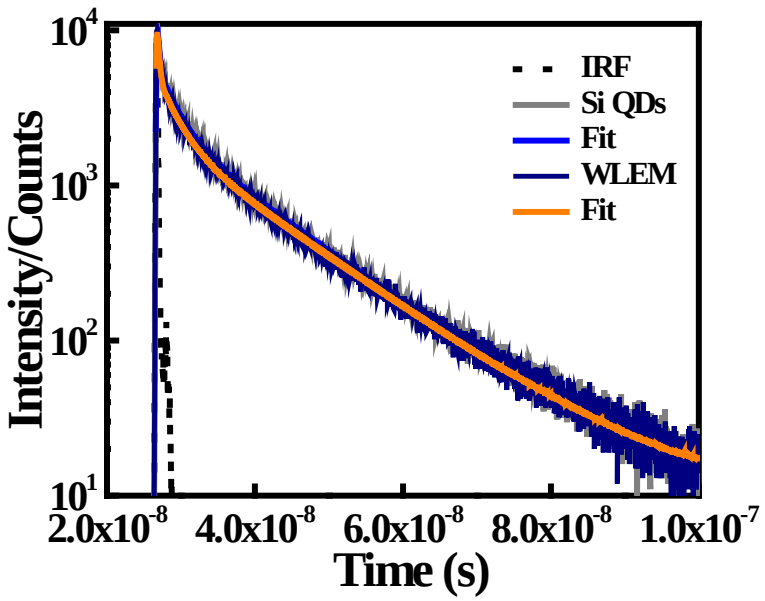

Figure 5.27. Lifetime decay curves of only Si QDs (Grey) and Si QDs in WLEM (Navy) excited at 402 nm. Black plot denotes the instrument response function.

close to that of perfect white light emitting source (0.33, 0.33). The digital images under daylight and under UV light for blue emitting Si QDs, orange emitting Au NCs, and white light emitting mixture are shown in figure 5.26c and 5.26d. It was evident from figure 5.26a that addition of increasing volume of Au NCs to the Si QDs solution led to quenching in the emission of Si QDs at 464 nm. In order to get insights into the nature of quenching, lifetime

Table 5.3. Decay time components of only Si QDs and Si QDs in WLEM

System	b_1	τ_1	b_2	τ_2	b_3	τ_3	$<\tau> = b_1\tau_1 + b_2\tau_2 + b_3\tau_3$	χ^2
Si QDs	0.23	2.7	0.71	12.7	0.07	0.26	9.5	1.3
WLEM	0.22	2.65	0.71	13	0.08	0.25	9.82	1.3

measurements of Si QDs and WLEM were performed. The lifetime of Si QDs and WLEM were collected at 464 nm with an excitation wavelength of 402 nm (Figure 5.27). It was found that lifetime of Si QDs remained almost unaltered in Si QDs solution (9.5 ns) and WLEM (9.8 ns) which further confirmed the involvement of static quenching mechanism behind the PL quenching of Si QDs (Table 5.3).

5.3.2.3. Structural characterizations of WLEM

In order to have an insight into the morphology of the WLEM, the as synthesized WLEM was characterized using TEM. Figure 5.28a and 5.28b show the low and high resolution TEM images of WLEM which indicate the formation of agglomerated structures of different shapes.

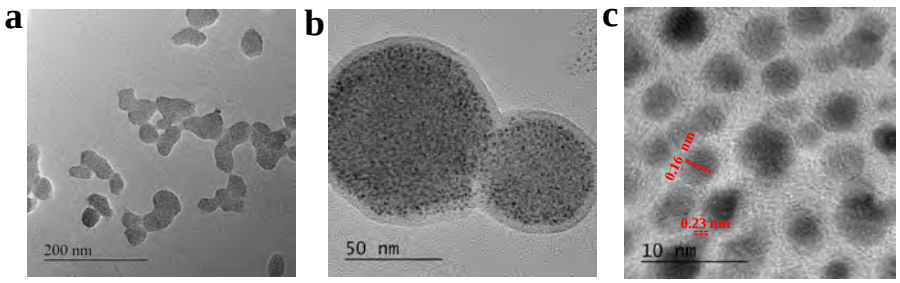

Figure 5.28. (a) and (b) TEM, and (c) HRTEM images of WLEM.

The HRTEM images of the agglomerated structures (Figure 5.28c) show lattice fringes of d-spacing of 0.23 nm corresponding to (111) plane of Au and 0.16 nm corresponding to (311) plane of Si. The structure formed is similar to that of a core–shell type morphology where the aggregated Au NCs form the core and the Si QDs form a continuous thin shell of thickness around 5 nm. To confirm the nature of the core and the shell, we performed a scanning transmission electron microscopy-energy dispersive X-ray spectroscopy (STEM-EDS) elemental mapping for the WLEM (Figure 5.29). STEM-EDS elemental mapping images showed that the Si QDs are homogeneously distributed over Au NCs in the agglomerated structures and the Au NCs aggregates form the core. The binding of the Si QDs with Au NCs can be attributed to the presence of various functional moieties in GSH that is present on the

surface of Au NCs. The formation of aggregates further supports the strong interaction between Si QDs and Au NCs which can result in static quenching of PL intensity of Si QDs.

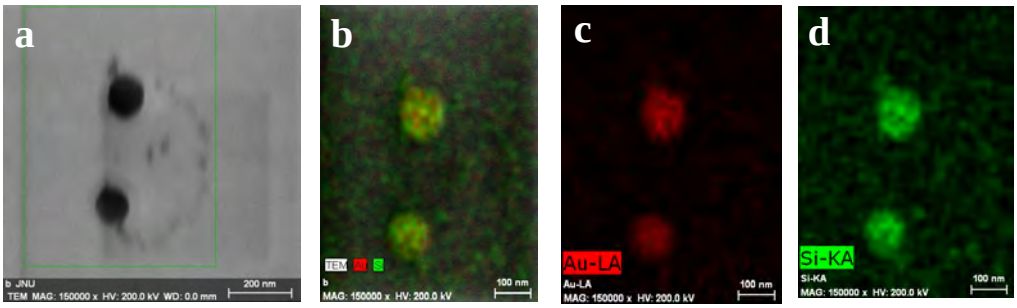

Figure 5.29. (a) Bright field STEM images of WLEM, and (b,c,d) the corresponding elemental mapping.

5.3.2.4. Stability studies of WLEM

For a fluorescent material to be used for applications such as in sensing, it is important for the material to be stable towards light and temperature. Therefore, it was imperative for us to study the stability of the WLEM under these conditions. It was observed that the as synthesized WLEM showed photostability over a longer period of time (more than 3 months) at room temperature, hence, making it a suitable candidate as phosphor material in LED applications. Optical response of the WLEM toward temperature was studied by recording its temperature

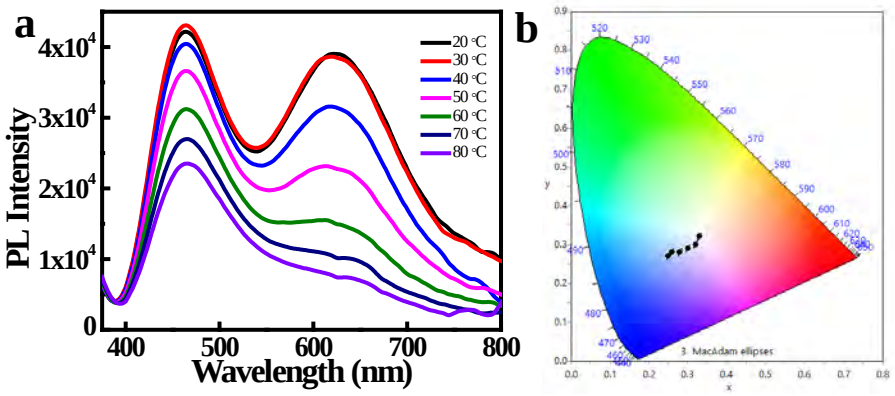

Figure 5.30. (a) PL spectra of WLEM in the temperature range of 20 ºC to 80 ºC, and (b) corresponding CIE plot.

dependent PL spectra in the range of 20 ºC to 80 ºC (Figure 5.30a). It was observed that the PL intensity of the WLEM decreased significantly with increasing temperature from 20 ºC to 80 ºC.

The emission intensity of Si QDs component present in the WLEM decreased by approximately half of its intensity at 80 ºC, whereas the temperature induced PL quenching was more than 90% in case of Au NCs component in the WLEM. The higher rate of temperature induced PL quenching for Au NCs compared to Si QDs resulted in shifting of CIE co-ordinates of WLEM towards bluish region (as shown in Figure 5.30b). Interestingly, it was found that upon cooling the WLEM from 80 ºC to 20 ºC, its white light emission properties regained (as shown in Figure 5.31a). The percentage of quenching was found to be more in case of Au NCs ~ 90% with that of Si QDs ~ 51%. Quenching of PL intensity can be attributed to enhanced nonradiative relaxations due to activation of nonradiative defect/surface trappings states with increasing temperature.[110, 111] The reversible thermo responsive behavior can be ascribed to synergistic effects between oxygen rich functional groups present on the surface of QDs and hydrogen bonding with water.[110] This reversible thermo-response of WLEM was repeated several times and was found to be stable for several heating and cooling cycles (Figure 5.31b and 5.31c). The

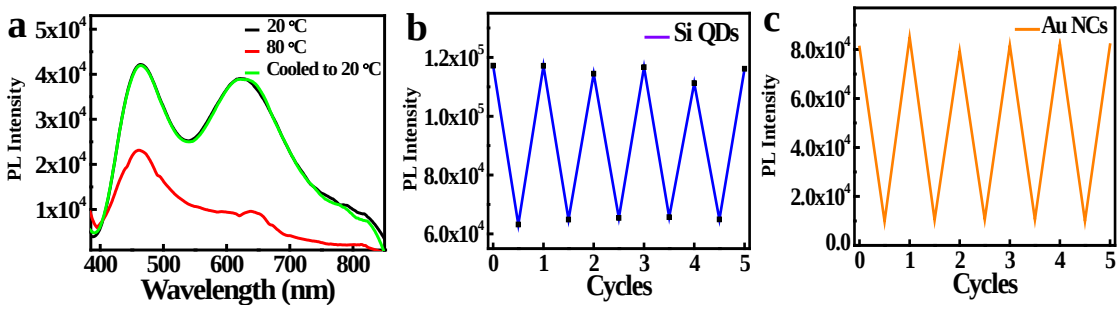

Figure 5.31. (a) PL spectra of WLEM at 20 ºC and 80 ºC, (b) and (c) change in PL intensity of Si QDs, and Au NCs in WLEM during consecutive heating–cooling cycles.

reversible thermo-response and water soluble luminescent properties of as synthesized WLEM make it suitable for optical thermometry and thermography applications. [112, 113]

5.3.2.5. Optical properties of WLEM

For practical application of white light emitting materials, it is essential that the white light be generated in solid or in gel state. Therefore, to justify the candidature of the as synthesized WLEM as a potential phosphor material for utilities in WLEDs, white light emission was studied in both gel form and solid state condition. In order to check the emission in gel form, both the components of WLEM were mixed together with melted agarose in the same concentration as those were used for preparing WLEM. After gelification, it was found that gel is also giving white light emission upon UV light illumination (as shown in Figure 5.32a). PL

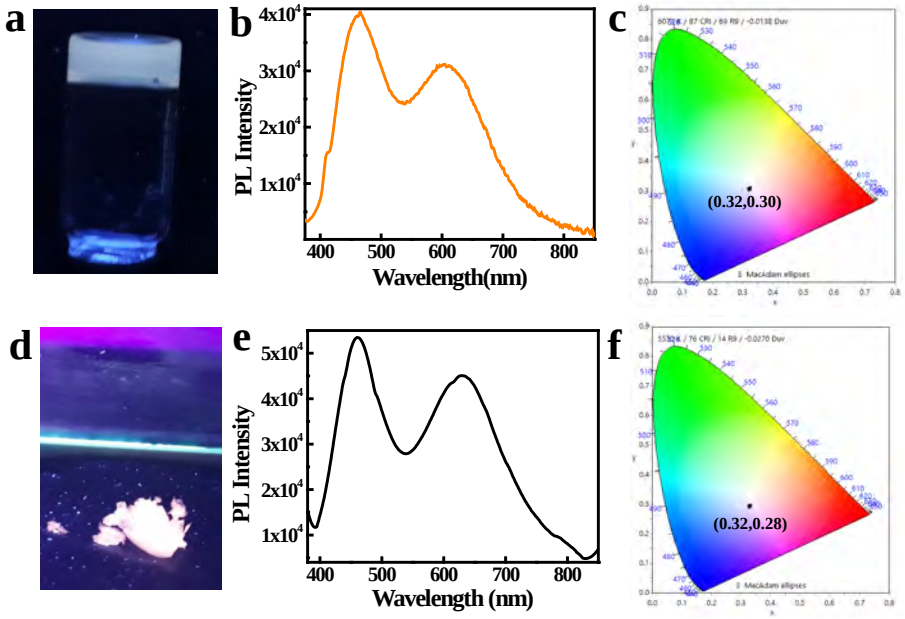

Figure 5.32. (a) Digital image of WLEM incorporated in agarose gel under UV light (λ_{exc}=365 nm), (b) PL spectrum of WLEM incorporated in agarose gel, (c) corresponding chromaticity plot for color co-ordinate, (d) digital image of WLEM incorporated in powder form under UV light (λ_{exc}=365 nm), (e) PL spectrum of WLEM incorporated in powder form, and (f) corresponding chromaticity plot for color co-ordinate.

spectrum of gel was similar to that of liquid WLEM with CIE co-ordinate of (0.32, 0.30) (shown in Figure 5.32b and 5.32c). The solid state emission coming from the WLEM in powder form also showed high quality white light emission with very good CIE co-ordinate (0.32, 0.28) (Figure 5.32d–f). Further, we also studied white light emission from thin film. A thin film was

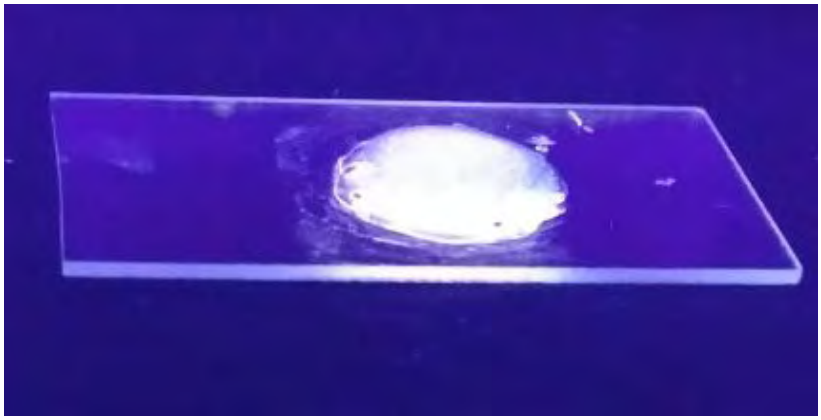

Figure 5.33. (a) Digital image of WLEM incorporated in PVP film under UV light (λ_{exc} = 365 nm).

generated by mixing aqueous solutions of PVP, Au NCs and Si QDs in appropriate ratio, which showed white light emission upon illumination by a UV lamp (λ_{exc}=365 nm) (Figure 5.33).Thus, the as-synthesized WLEM, apart from liquid and solid forms, can also be changed to gel and film states without losing its white light emission property.

5.3.2.6. WLEM for Hg^{2+} ions and reversible thiol sensing

White light emitting mixtures can be used for sensing applications as they can easily undergo a change in color upon interaction with a particular analyte of interest because of the presence of two or three components in WLEMs. It is well established that the interaction of Hg^{2+} ions

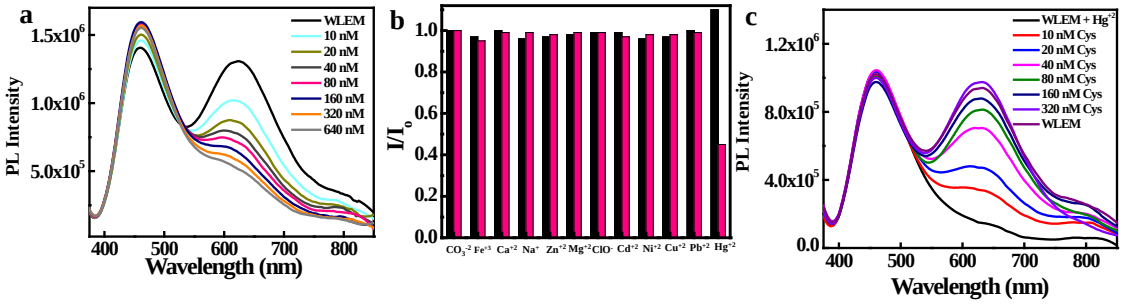

Figure 5.34. (a) PL spectra of WLEM upon addition of different concentration of Hg^{2+} ions, and (b) change in PL intensity of Si QDs (black) and Au NCs (pink) in the WLEM upon addition of different ions, and (c) PL spectra of WLEM having Hg^{2+} ions with different concentration of Cys.

with Au NCs leads to quenching of emission of Au NCs due to d^{10}–d^{10} interaction. [114] Therefore, it was reasonable to speculate that the interaction of Hg^{2+} ions with WLEM would lead to quenching of emission of Au NCs, in turn changing the color of emission of the mixture. Also, it is known that heavy metal ions like Hg^{2+} ions are highly toxic to both human and aquatic animals and is known as notorious environmental pollutant. Therefore, we were interested in sensing Hg^{2+} ions using our WLEM. When different concentrations of Hg^{2+} ions were added to the WLEM, a gradual decrease in peak centred at 620 nm due to Au NCs (Figure 5.34a) was obtained with increasing concentration of Hg^{2+} ions. On the other hand, the emission due to Si QDs at 464 nm remained unaltered. Upon illumination of the mixture under UV lamp, it was observed that the color of the mixture changed from white to blue after addition of 640 nM Hg^{2+} ions. The sensing mechanism of Hg^{+2} ions by the WLEM is based on high-affinity Hg^{+2}-Au^{+} interactions. The surface of the as synthesized Au NCs is stabilized by a high content of Au (I)- thiolate complexes [91] and Hg^{+2} ions are known for having a strong affinity for Au^{+}

Table 5.4. Comparison of molecular sensors for mercury detection[a]

Material	Chemical probe	LOD	Reference
Quantum dots	CdS quantum dots	25.2 ng mL^{-1}	Anal. Methods, 2016,8, 6512-6519
	Nitrogen doped carbon dots	0.65 µM	New J. Chem., 2018,42, 6824-6830
Organic molecules	Squaraine dye	1.3×10^{-7} M	Sens. Actuator B- Chem, 2012, 173, 874-881
	Azobenzene	20 µM	Chem.: Eur. J, 2011, 17, 7276-7281
	Phenoxazinone	100 nM	J. Am. Chem. Soc., 2003, 125, 3418-3419
Biomolecules	DNA oligonucleotides	40 nM	Angew. Chem., Int. Ed., 2004, 43, 4300-4302
	DNA- Au nanoparticles conjugate	10 µM	J. Am. Chem. Soc., 2008, 130, 3244-3245
Nanoparticles	Gold nanoparticles	10 µM	J Anal Methods Chem., 2012, 2012
	Gold nanoparticles	100 nM	Angew. Chem., Int. Ed., 2007, 46, 4093-4096
Polymers	Polythiophene with thymine moiety	30 µM	Macromol. Rapid Commun., 2006, 27, 389-392
	Poly(3-(3'-N,N,N-triethylamino-1'-propyloxy)-4-methyl-2,5-thiophene hydrochloride)	42 nM	Adv. Mater., 2007, 19, 1471-1474

[a]LOD = limit of detection

ions.[114] Upon addition of Hg^{+2} ions to Au NCs solution, strong bonding interactions between the d^{10} centers [(Hg^{2+} ($4f^{14}5d^{10}$) and Au^{+} ($4f^{14}5d^{10}$)] take place which results in quenching of orange emission of Au NCs, which resulted in the emission of Si QDs only to observe. The designed method was found to be fast and sensitive toward sensing of Hg^{2+} ions and the limit of detection was found to be 10 nM (Figure 5.34a). Comparison of previously developed small molecular sensors for detection of Hg^{2+} ions shown in table 5.4 indicates that our system is showing better sensitivity than the previously reported ones. Further, the selectivity of the present system was also studied by recording the PL spectra of the WLEM in the presence of different metal cations and anions with a concentration of 1 mM. It was observed that the addition of metal anions and cations such as CO_3^{2-}, Fe^{3+}, Ca^{2+}, Na^{+}, Zn^{2+}, Mg^{2+}, ClO_3^{-}, Cd^{2+}, Ni^{2+},Cu^{2+}, and Pb^{2+} showed no significant change in the PL intensity of WLEM (Figure 5.34b), indicating high selectivity of the system for Hg^{2+} ions. Thus the present system could be employed for the fast, selective, sensitive and visual sensing of Hg^{2+} ions. Interestingly, the white light emission can fully be recovered again by the subsequent addition of a thiol containing amino acid Cys with a limit of detection of 10 nM (Figure 5.34c). Comparative analysis of other known molecular sensors for Cys detection (Table 5.5) indicates higher sensitivity of our system than the previously reported

Table 5.5. Comparison of molecular sensors for Cys detection

Material	Chemical probe	LOD	Reference
Organic molecules	Cinamaldehyde and Pyrimidine	0.10 µM	Sens. Actuator B- Chem., 2018, 255, 2756-2763
	Curcumin	1 µM	Anal. Methods, 2013,5, 3965-3969
	Spiropyran	40 nM	Angew. Chem., Int. Ed., 2006, 45, 4944-4948
Nanoparticles	Gold nanorods	Micromolar range	J. Am. Chem. Soc., 2005, 127 , 6516–6517
	Nickel oxide nanoflowers	1.1 µM	J. Mater. Chem. B, 2014, 2, 6097
	Gold nanoparticles	10-100 µM	Anal. Chim. Acta, 2010, 671, 80-84
Polymer	Polythiophene	12.6 µM	Sens. Actuator B- Chem., 2016, 232, 448-453
	Poly[3-(3-*N*,*N*-diacetateaminopropoxy)-4-methyl thiophene disodium salts	0.33 µM	Talanta, 2019, 198, 128-136
Quantum dots	Methyl viologen coated CdS QDs	0.1 µM	Small, 2011, 7, 1624-1628
	CdTe QDs	0.87 µM	Talanta, 2009,77, 1654-1659
Biomolecules	DNA- gold nanoparticles conjugate	100 nM	Nano Lett. 2008, 8, 2, 529-533

LOD = limit of detection

ones. Digital images of WLEM, WLEM with Hg^{2+} and WLEM with Hg^{2+} ions and Cys under UV light are shown in figure 5.35. Thiols have a very strong binding affinity toward Hg^{2+} ions. Thus, the rapid recovery of white light emission can be attributed to the binding of Cys with Hg^{2+} ions. Since, Hg^{2+} ions are now bound to the thiol group in Cys, the d^{10}–d^{10} interaction of Hg^{2+} ions with the Au^{+} ion on the surface of the Au NCs is obviously weakened, thus leading to regain of the emission of Au NCs, which in turn leads to recovery of the white emission of the

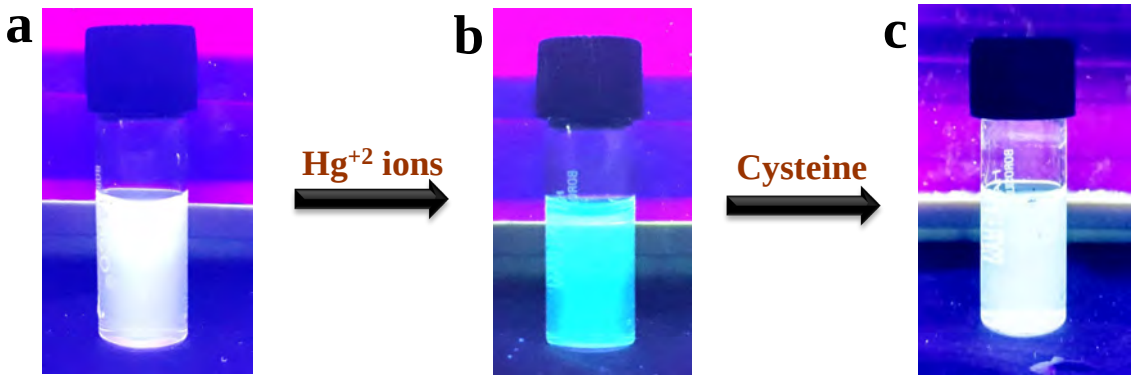

Figure 5.35. Digital images of (a) WLEM, (b) WLEM with Hg^{2+}, and (c) WLEM with Hg^{2+} ions and Cys under UV light (λ_{ex}=365 nm).

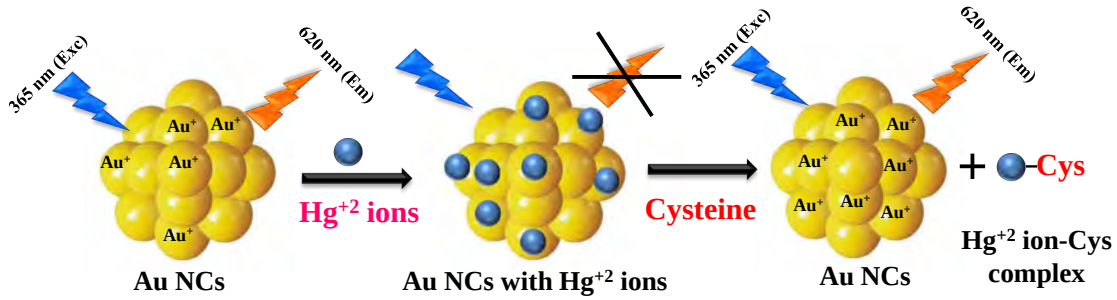

Scheme 5.3. Schematic depiction of reversible "ON–OFF" PL quenching of Au NCs in WLEM mixture.

WLEM.[115] This reversible "ON–OFF" of white light emission was found to be very specific to Cys residue only. Scheme 5.3 illustrates the mechanism of reversible "ON–OFF" PL quenching of Au NCs in WLEM in the presence of Hg^{2+} ions and Cys. The control experiments were

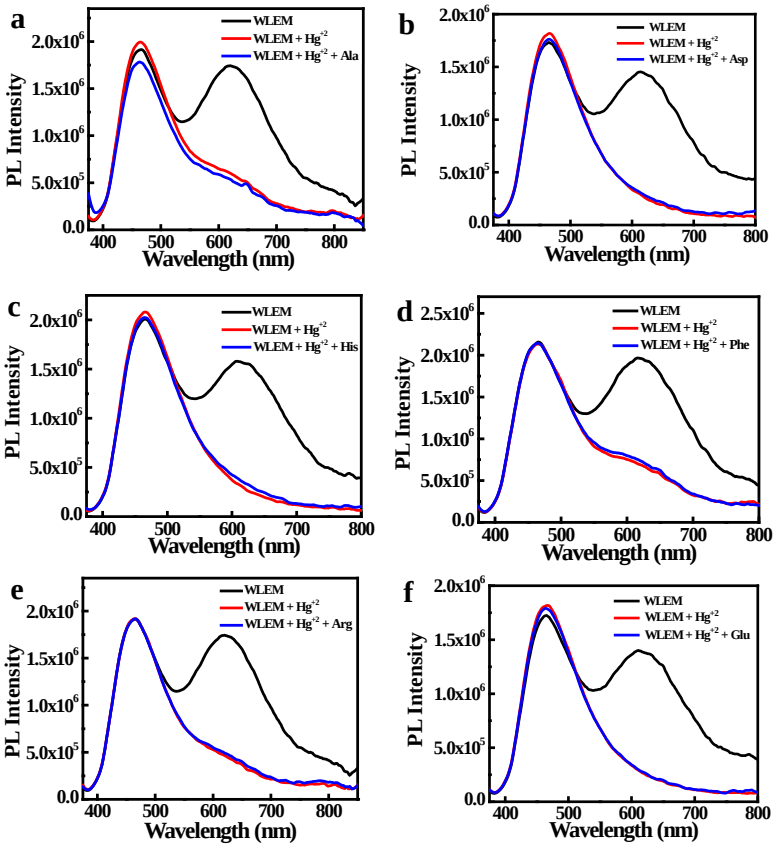

Figure 5.36. Fluorescence intensity change of WLEM with Hg^{2+} ions in presence of different amino acids (a) alanine, (b) aspartic acid, (c) histidine, (d) phenylalanine, (e) arginine, and (f) glutamic acid.

performed by taking different non-thiol amino acids such as alanine, aspartic acid, histidine, phenylalanine, arginine, and glutamic acid, however, no change in PL intensity was observed as shown in figure 5.36. To get better insights into ion-induced structural changes, TEM imaging of WLEMs after addition of Hg^{2+} ions followed by Cys addition was done. TEM images represented in figure 5.37 revealed the distortion of agglomerated structures of WLEM upon addition of Hg^{2+} ions, this further validates our hypothesis of dissolution of Au NCs structures due to binding of Hg^{2+} ions with GSH (Figure 5.37a and 5.37b). Furthermore, upon introduction of Cys to this WLEM with Hg^{2+} ions, reformation of agglomerated structures take place exactly like pure WLEM (TEM images shown in Figure 5.37c and 5.37d), which results in recovery of white light emission from the mixture.

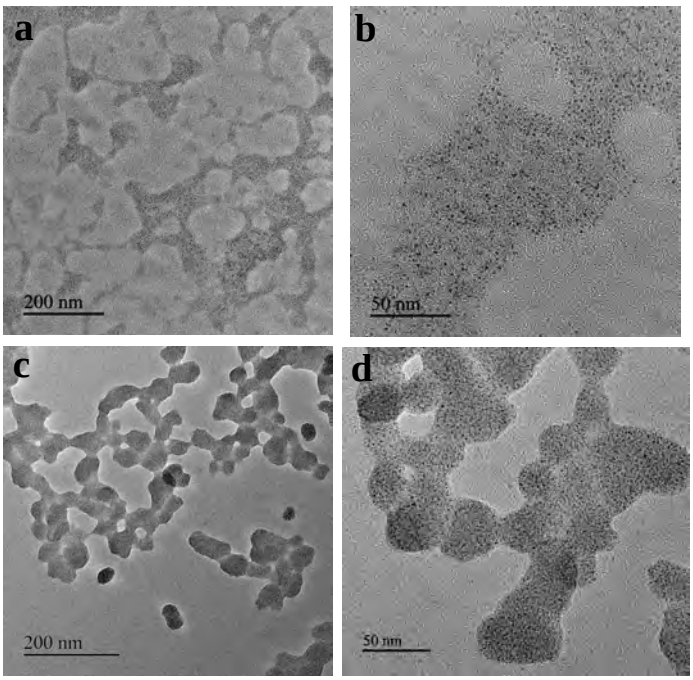

Figure 5.37. TEM images of WLEM (a and b) with Hg^{+2} ions, and (c and d) with Hg^{+2} ions and Cys.

5.3.3. Conclusion

In the present study, we have designed a simple solution based approach for generation of WLEM. It is noteworthy that the as generated WLEM can be converted to solid, gel or in the form of film, making it a suitable candidate for solid state devices. The reversible thermo-response property of WLEM could be utilized in optical thermometry and thermography applications. Furthermore, this system was found to be showing fast, sensitive, and selective

sensing of Hg^{2+} ions and thiol containing amino acid Cys. Such biofriendly white light emitting material holds promise for being used in selective sensing of a wide range of chemical or biological species based on their specific chemical interaction with the individual components present in the WLEM and also in bioimaging.

Note:

- The permission has been granted by authors and corresponding author of the published paper prior to adopting in the present thesis. The associated relevant publication is:

Swati Tanwar, Bhagwati Sharma, Vishaldeep Kaur, and Tapasi Sen "White light emission from a mixture of silicon quantum dots and gold nanoclusters and its utilities in sensing of mercury (II) ions and thiol containing amino acid" ***RSC Advances*** 2019,**9**, 15997-16006. ***(Selected for editor's collection focusing on fluorescent sensors)***

5.4. Immobilization of single Si QD on DNA origami

5.4.1. Experimental section

5.4.1.1. Materials

N-(3-Dimethylaminopropyl)-N′-ethylcarbodiimide hydrochloride (EDC), trisodium citrate, N-Hydroxysulfosuccinimide sodium salt (NHS), 3 kDa and 100 kDa amicon filters, 3-aminopropyltriethoxysilane (APTES), tris(hydroxymethyl)aminomethane (Tris base), phosphate buffer saline (PBS) tablets, and ethylenediaminetetraacetic acid disodium salt (EDTA) were purchased from Sigma-Aldrich. Sodium hydroxide, sodium chloride, tween 20, acetic acid and hydrochloric acid (HCl) were procured from Merck, India, and magnesium chloride hexahydrate ($MgCl_2.6H_2O$) from SRL. M13mp18 single stranded DNA was procured from New England Biolabs and was used without further treatment. All unmodified staple strands were purchased from Integrated DNA Technologies, Inc. (IDT) with standard desalting purification. 5′-amine modified single stranded DNA was purchased from IDT with HPLC purification. Dialysis membrane with a molecular weight cut off of 0.5–1 kDa was purchased from Spectrum labs. Sephacryl S-300 high resolution resin was bought from GE Healthcare. Micro bio spin chromatography columns were purchased from Bio-Rad. Carbon coated Cu TEM grids and AFM mica discs (V1 quality) were procured from Ted Pella and Agar Scientific. All the experiments were performed using Milli-Q water**.**

5.4.1.2. Experimental procedures

5.4.1.2.1. Synthesis of Si QDs

Si QDs were synthesized by a slight modification of the previously reported method.[116] Briefly, 1 gram of trisodium citrate and 1 mL of APTES was dissolved in 30 mL of water. The mixture was transferred to a 50 mL Teflon hydrothermal autoclave reactor and saturated by N_2 gas. The mixture was then heated at 200 ºC for about 12 hours. After the successful completion of the reaction, the reaction mixture was purified using 1 kDa dialysis membrane for 12 hours. The purified mixture was used for conjugating with DNA.

5.4.1.2.2. Conjugation of Si QDs with amine labeled DNA

For conjugating with DNA oligonucleotides, the as-synthesized Si QDs solution was diluted in PBS buffer with final OD of 0.3. After dilution, the pH of the Si QDs solution was adjusted to 5 using 1 N HCl solution. Subsequently, 20 µL of 50 mM EDC and 12 µL of 50 mM NHS aqueous solutions were mixed with the above Si QD solution, respectively. The mixture was kept at mild stirring for 2 hours in dark. Further, 25 µL of 100 µM amine labeled DNA

oligonucleotide solution was added to the mixture and was kept for overnight stirring. During the conjugation, the salt concentration was increased with 4 times addition of 3.8 μL of PBS, 2M NaCl, 0.1% Vol Tween 20 buffer solution in a time interval of 20 min. After the reaction, the excess DNA was then removed from the Si QD-DNA conjugates using 3 kDa amicon filter and washing 3 times with PBS buffer having 100 mM NaCl. The purified Si QD-DNA conjugates were then stored at 4 ºC. The sequence of amine labeled DNA is given in table 11 of appendix A.

5.4.1.2.3. Synthesis of rectangular DNA origami

The rectangular DNA origami was synthesized as described in chapter 3 of this thesis. Briefly, the rectangular DNA origami was self-assembled by folding a long single-stranded M13mp18 viral genomic DNA by a set of ~214 short staple strands using a 1.5 h annealing program. Annealing was performed in 1× TAE buffer with scaffold concentration of 2 nM, 10-fold excess of regular staples, and 20-fold excess of modified staples. Sequence of all the short staple sequences and edge staples are given in table 1, 2 and table 3 of the appendix A respectively. The annealed rectangular DNA origami was then purified using Sephacryl S-300 HR resin.

5.4.1.2.4. Immobilization of single Si QD on DNA origami

The purified rectangular DNA origami was then mixed with Si QD-DNA conjugates with 0.3 M NaCl. The mixture was heated repeatedly between 40 and 20°C for 12 h, being kept in a PCR thermocycler. The final product was used for AFM and TEM imaging.

As synthesized Si QDs and DNA origami were characterized by AFM, UV-Vis spectrophotometer, photoluminescence spectrophotometer, and FTIR as described in chapter 2 of this thesis.

5.4.2. Results and discussion

5.4.2.1. Optical and structural characterizations of as synthesized Si QDs

Si QDs were synthesized hydrothermally using an aqueous solution of APTES and trisodium citrate. Where, APTES was used as source of Si and trisodium citrate as reducing and stabilizing agent. The appearance of a pale yellow color from the colorless reaction mixture indicated the formation of Si QDs. Photoluminiscence (PL) spectra of the resultant Si QDs (Figure 5.38a) showed emission centered at 460 nm upon excitation at 355 nm with symmetrical excitation and emission peaks. The PL spectra indicated that the synthesized Si QDs possess good photoluminescence properties. To get insights into the nature of surface

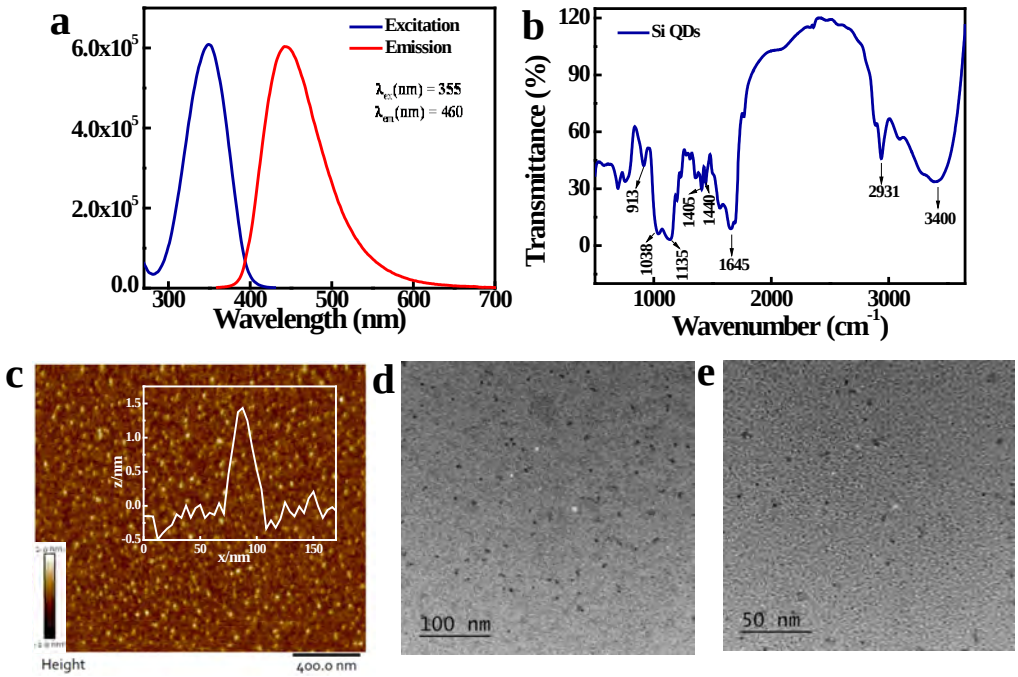

Figure 5.38. (a) Excitation and emission spectra of the Si QDs, (b) FTIR spectrum of the Si QDs, (c) AFM images of Si QDs (inset shows the height profile), and (d and e) TEM images of the Si QDs.

functionalities surrounding the Si QDs, FTIR measurement was performed. The FTIR spectrum of the Si QDs is shown in figure 5.38b in the range of 4000−500 cm^{-1}. The FTIR spectrum showed a broad peak at 3410 cm^{-1} for Si QDs which may be attributed to O−H stretching vibration. The peaks at 2933 and 1445 cm^{-1} were assigned to the C−H stretching and bending vibrations, respectively. While the strong intensity peak at 1645 cm^{-1} could be assigned to the C=O stretching of the carboxylic group, the band at 1405 cm^{-1} was originated from C−O–H bending vibrations. The peak at 1120 cm^{-1} was due to Si–C asymmetric deformation, and the peak at 1043 cm^{-1} was attributed to Si−O−Si stretching vibrations. Additionally, a peak due to Si−O stretching of the Si−O−H group at 911 cm^{-1} was observed. These results confirm the presence of plenty of hydrophilic oxygenated functional groups on the surface of Si QDs, whose presence greatly contributed toward the excellent water dispersibility of the Si QDs. Further, the carboxyl groups present on the surface of Si QDs can be used for conjugation with amine labeled DNA oligonucleotides. To get insights into the morphology and the structure of the as synthesized Si QDs AFM (Figure 5.38c) and TEM (Figure 5.38d and 5.38e) imaging was done. AFM and TEM images confirmed the formation of Si QDs with an average size of 1.5 ± 0.4 nm.

5.4.2.2. DNA functionalization of Si QDs

The FTIR measurements revealed that the synthesized Si QDs are having many carboxyl groups on their surface (Figure 5.38b) and are water soluble. We used well established protocol of EDC-NHS coupling for their conjugation with amine labeled DNA (shown in Scheme 5.4). [117] EDC was used to activate the carboxyl groups present on the surface of Si QDs. EDC activated Si QDs were further reacted with sulfo-NHS to prevent the hydrolysis of EDC-ester and increase the yield of DNA functionalized Si QDs.[86]

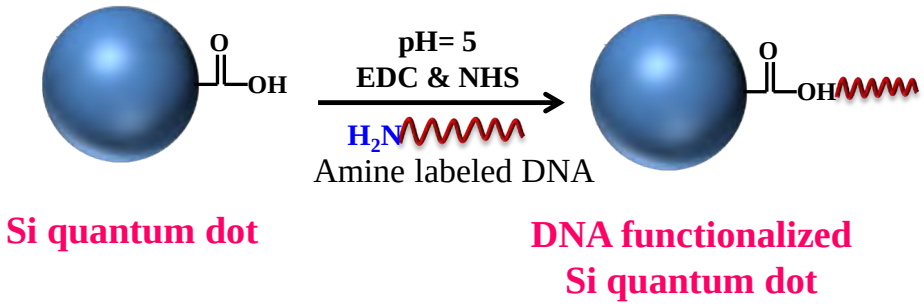

Scheme 5.4. Schematic depiction of the DNA functionalization of Si QDs.

In order to achieve an efficient covalent coupling, the conjugation reaction was carried at a pH of 5. Under a high pH value, the carboxylic acid group of Si QDs becomes deprotonated, thus, lowering the reactivity of EDC.

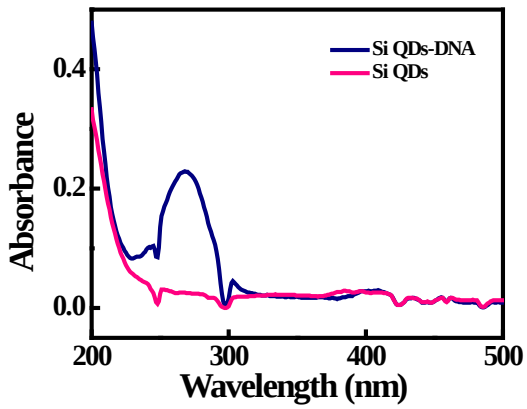

Figure 5.39. UV-Vis absorption spectra of Si QDs and DNA conjugated Si QDs.

The UV-Vis spectrum of DNA conjugated Si QDs recorded using a nanodrop instrument showed a peak at 260 nm corresponding to nucleic acids. The UV-Vis absorption data

confirmed successful conjugation of the as-synthesized Si QDs with amine labeled DNA oligonucleotides.

5.4.2.3. Design of DNA origami-Si QD hybrid structure

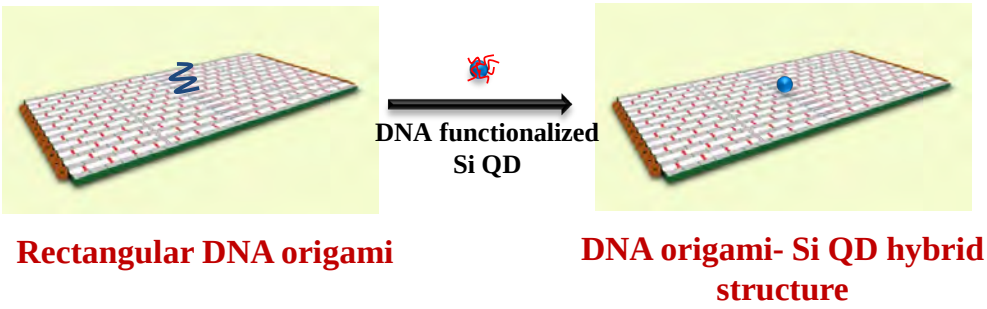

Scheme 5.5. Schematic depiction of the immobilization of single Si QD on DNA origami.

For capturing a DNA functionalized Si QD on the origami template, a staple with sequence number 111 (Table 1 of appendix A) was extended at 3' position with DNA sequence complementary to that of amine labeled DNA (as shown in Scheme 5.5). The purified origami solution was then mixed with DNA conjugated Si

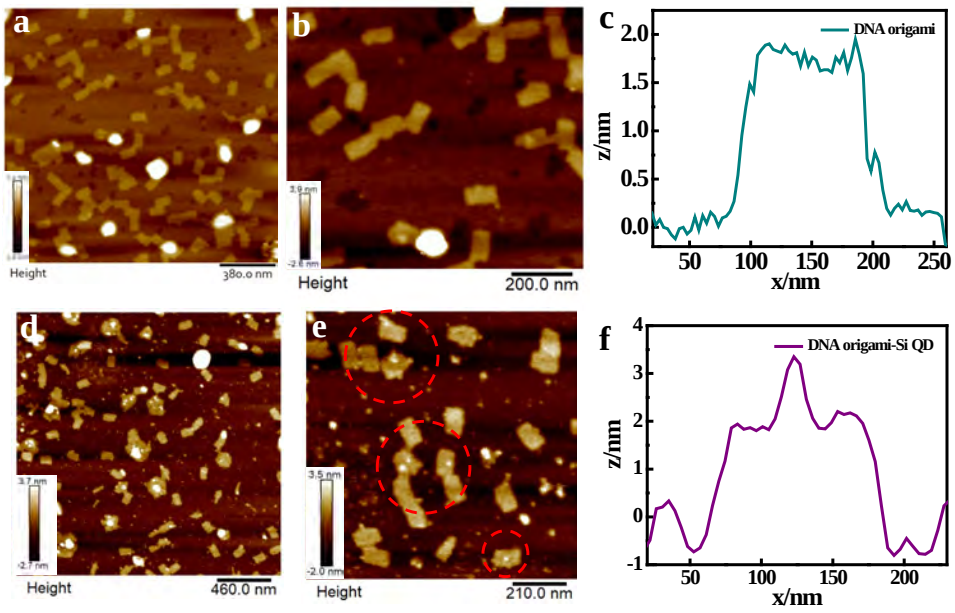

Figure 5.40. (a and b) AFM images of rectangular DNA origami, and (c) corresponding height profile. (d and e) AFM images of rectangular DNA origami-Si QD hybrid structure, and (f) corresponding height profile.

QDs and was recycled between 40ºC to 30ºC for 12 hours in a PCR thermocycler. The DNA origami-Si QDs conjugates were then imaged using AFM. AFM images of rectangular DNA origami with and without Si QD are shown in figure 5.40. The position of the staple sequence used for capturing the Si QD on DNA origami resides exactly in the middle of the origami template. A difference in height profile of ~ 1.5 nm from the height of the origami template (~ 2 nm) in the middle of the structure matched well with the size of Si QD (~ 1.5 nm) confirming successful immobilization of single Si QD on DNA origami (Figure 5.40f).

5.4.3. Conclusion

In summary, the results included in the thesis confirm successful immobilization of single Si QD on DNA origami which is a positive step towards merging a single QD with a single plasmonic nanoantenna. The judicial choice of placing single QD in the plasmonic hotspot instead of organic fluorophores will help in creating functional single QD-based nanosensors that will have extremely high sensitivity and stability. The programmable nature of the DNA origami template allows site-specific localization of optical species and metal nanoparticles for building novel plasmonic nanostructures. Future studies will focus on the immobilization of single Si QD in the plasmonic hotspot of the synthesized Au@Ag NS dimer plasmonic nanoantennas for single molecule spectroscopic, sensing, and imaging applications.

References

1. G. H. Carey, A. L. Abdelhady, Z. Ning, S. M. Thon, O. M. Bakr and E. H. Sargent, *Chemical reviews*, 2015, **115**, 12732-12763.
2. Q. D. S. Cells, *Journal of Physical Chemistry C*, 2008, **112**, 18737-18753.
3. I. L. Medintz, H. T. Uyeda, E. R. Goldman and H. Mattoussi, *Nature materials*, 2005, **4**, 435.
4. W. C. W. Chan, D. J. Maxwell, X. Gao, R. E. Bailey, M. Han and S. Nie, *Current Opinion in Biotechnology*, 2002, **13**, 40-46.
5. J. P. Wolfgang, G. Daniele, P. Teresa, Z. Daniela, M. Christine, C. W. Shara, B. Rosanne, A. L. G. Mark, A. L. Carolyn and A. P. Alivisatos, *Nanotechnology*, 2003, **14**, R15.
6. T. Rajh, O. I. Micic and A. J. Nozik, *The Journal of Physical Chemistry*, 1993, **97**, 11999-12003.
7. B. A. Kairdolf, A. M. Smith and S. Nie, *Journal of the American Chemical Society*, 2008, **130**, 12866-12867.
8. J. O. Winter, T. Y. Liu, B. A. Korgel and C. E. Schmidt, *Advanced Materials*, 2001, **13**, 1673-1677.
9. M. Bottrill and M. Green, *Chemical communications*, 2011, **47**, 7039-7050.
10. K. Li, J. Chen, S. Bai, X. Wen, S. Song, Q. Yu, J. Li and Y. Wang, *Toxicology in Vitro*, 2009, **23**, 1007-1013.
11. L. Pavesi, L. Dal Negro, C. Mazzoleni, G. Franzo and F. Priolo, *Nature*, 2000, **408**, 440.
12. Y. He, S. Su, T. Xu, Y. Zhong, J. A. Zapien, J. Li, C. Fan and S.-T. Lee, *Nano Today*, 2011, **6**, 122-130.
13. Y. Zhong, F. Peng, X. Wei, Y. Zhou, J. Wang, X. Jiang, Y. Su, S. Su, S. T. Lee and Y. He, *Angewandte Chemie International Edition*, 2012, **51**, 8485-8489.
14. Z. Kang, Y. Liu and S.-T. Lee, *Nanoscale*, 2011, **3**, 777-791.
15. X. Cheng, S. B. Lowe, P. J. Reece and J. J. Gooding, *Chemical Society Reviews*, 2014, **43**, 2680-2700.
16. Y. Su, X. Wei, F. Peng, Y. Zhong, Y. Lu, S. Su, T. Xu, S.-T. Lee and Y. He, *Nano letters*, 2012, **12**, 1845-1850.
17. Y. Zhong, F. Peng, F. Bao, S. Wang, X. Ji, L. Yang, Y. Su, S.-T. Lee and Y. He, *Journal of the American Chemical Society*, 2013, **135**, 8350-8356.
18. J. Wang, D.-X. Ye, G.-H. Liang, J. Chang, J.-L. Kong and J.-Y. Chen, *Journal of Materials Chemistry B*, 2014, **2**, 4338-4345.
19. N. O'Farrell, A. Houlton and B. R. Horrocks, *International Journal of Nanomedicine*, 2006, **1**, 451-472.
20. S. Pramanik, S. K. E. Hill, B. Zhi, N. V. Hudson-Smith, J. J. Wu, J. N. White, E. A. McIntire, V. S. S. K. Kondeti, A. L. Lee, P. J. Bruggeman, U. R. Kortshagen and C. L. Haynes, *Environmental Science: Nano*, 2018, **5**, 1890-1901.
21. Y. Zhong, X. Sun, S. Wang, F. Peng, F. Bao, Y. Su, Y. Li, S.-T. Lee and Y. He, *ACS Nano*, 2015, **9**, 5958-5967.
22. J. Zhang and S.-H. Yu, *Nanoscale*, 2014, **6**, 4096-4101.
23. S. Bose, M. A. Ganayee, B. Mondal, A. Baidya, S. Chennu, J. S. Mohanty and T. Pradeep, *ACS Sustainable Chemistry & Engineering*, 2018, **6**, 6203-6210.
24. B. Liao, W. Wang, X. Deng, B. He, W. Zeng, Z. Tang and Q. Liu, *RSC Advances*, 2016, **6**, 14465-14467.
25. B. Liao, H. Lv, X. Deng, B. He and Q. Liu, *Journal of Nanoparticle Research*, 2017, **19**, 265.
26. F. Erogbogbo, K.-T. Yong, I. Roy, R. Hu, W.-C. Law, W. Zhao, H. Ding, F. Wu, R. Kumar and M. T. Swihart, *ACS nano*, 2010, **5**, 413-423.
27. F. Erogbogbo, K.-T. Yong, I. Roy, G. Xu, P. N. Prasad and M. T. Swihart, *ACS nano*, 2008, **2**, 873-878.
28. A. Shiohara, S. Hanada, S. Prabakar, K. Fujioka, T. H. Lim, K. Yamamoto, P. T. Northcote and R. D. Tilley, *Journal of the American Chemical Society*, 2009, **132**, 248-253.
29. M. L. Mastronardi, F. Maier-Flaig, D. Faulkner, E. J. Henderson, C. Kübel, U. Lemmer and G. A. Ozin, *Nano letters*, 2011, **12**, 337-342.
30. X. Pi, T. Yu and D. Yang, *Particle & Particle Systems Characterization*, 2014, **31**, 751-756.

31. R. Costi, A. E. Saunders and U. Banin, *Angewandte Chemie International Edition*, 2010, **49**, 4878-4897.
32. K. K. Haldar, N. Pradhan and A. Patra, *Small*, 2013, **9**, 3424-3432.
33. J. Zeng, J. Huang, C. Liu, C. H. Wu, Y. Lin, X. Wang, S. Zhang, J. Hou and Y. Xia, *Advanced Materials*, 2010, **22**, 1936-1940.
34. T. Mokari, E. Rothenberg, I. Popov, R. Costi and U. Banin, *Science*, 2004, **304**, 1787-1790.
35. W. Shi, H. Zeng, Y. Sahoo, T. Y. Ohulchanskyy, Y. Ding, Z. L. Wang, M. Swihart and P. N. Prasad, *Nano letters*, 2006, **6**, 875-881.
36. H. Gu, R. Zheng, X. Zhang and B. Xu, *Journal of the American Chemical Society*, 2004, **126**, 5664-5665.
37. J. Li, S. K. Cushing, F. Meng, T. R. Senty, A. D. Bristow and N. Wu, *Nature Photonics*, 2015, **9**, 601-607.
38. J.-S. Lee, E. V. Shevchenko and D. V. Talapin, *Journal of the American Chemical Society*, 2008, **130**, 9673-9675.
39. U. Banin, Y. Ben-Shahar and K. Vinokurov, *Chemistry of Materials*, 2013, **26**, 97-110.
40. S. K. Dutta, S. K. Mehetor and N. Pradhan, *The journal of physical chemistry letters*, 2015, **6**, 936-944.
41. S. Selvan, P. K. Patra, C. Y. Ang and J. Y. Ying, *Angewandte Chemie*, 2007, **119**, 2500-2504.
42. H. Sugimoto, M. Fujii and K. Imakita, *Nanoscale*, 2016, **8**, 10956-10962.
43. A. Inoue, M. Fujii, H. Sugimoto and K. Imakita, *The Journal of Physical Chemistry C*, 2015, **119**, 25108-25113.
44. N. A. Harun, M. J. Benning, B. R. Horrocks and D. A. Fulton, *Nanoscale*, 2013, **5**, 3817-3827.
45. M. Ray, T. S. Basu, N. R. Bandyopadhyay, R. F. Klie, S. Ghosh, S. O. Raja and A. K. Dasgupta, *Nanoscale*, 2014, **6**, 2201-2210.
46. J. Karpiuk, E. Karolak and J. Nowacki, *Physical Chemistry Chemical Physics*, 2010, **12**, 8804-8809.
47. N. Guo, Y. Huang, M. Yang, Y. Song, Y. Zheng and H. You, *Physical Chemistry Chemical Physics*, 2011, **13**, 15077-15082.
48. S. Pimputkar, J. S. Speck, S. P. DenBaars and S. Nakamura, *Nature Photonics*, 2009, **3**, 180.
49. E. F. Schubert and J. K. Kim, *Science*, 2005, **308**, 1274-1278.
50. N. C. George, K. A. Denault and R. Seshadri, *Annual Review of Materials Research*, 2013, **43**, 481-501.
51. K. L. Wustholz, C. L. Brosseau, F. Casadio and R. P. Van Duyne, *Physical Chemistry Chemical Physics*, 2009, **11**, 7350-7359.
52. W. Xie, S.-R. Zhang, D.-Y. Du, J.-S. Qin, S.-J. Bao, J. Li, Z.-M. Su, W.-W. He, Q. Fu and Y.-Q. Lan, *Inorganic Chemistry*, 2015, **54**, 3290-3296.
53. Q.-Y. Yang, K. Wu, J.-J. Jiang, C.-W. Hsu, M. Pan, J.-M. Lehn and C.-Y. Su, *Chemical Communications*, 2014, **50**, 7702-7704.
54. S. K. Panda, S. G. Hickey, H. V. Demir and A. Eychmüller, *Angewandte Chemie International Edition*, 2011, **50**, 4432-4436.
55. M. J. Bowers, J. R. McBride and S. J. Rosenthal, *Journal of the American Chemical Society*, 2005, **127**, 15378-15379.
56. Y. Ledemi, A.-A. Trudel, V. A. G. Rivera, S. Chenu, E. Veron, L. A. Nunes, M. Allix and Y. Messaddeq, *Journal of Materials Chemistry C*, 2014, **2**, 5046-5056.
57. S. Dang, J.-H. Zhang and Z.-M. Sun, *Journal of Materials Chemistry*, 2012, **22**, 8868-8873.
58. P. Malakar, D. Modak and E. Prasad, *Chemical Communications*, 2016, **52**, 4309-4312.
59. Q.-Y. Yang and J.-M. Lehn, *Angewandte Chemie International Edition*, 2014, **53**, 4572-4577.
60. M. Lismont and L. Dreesen, *Materials Science and Engineering: C*, 2012, **32**, 1437-1442.
61. J. Joseph and A. A. Anappara, *Journal of Luminescence*, 2016, **178**, 128-133.
62. J. Joseph and A. A. Anappara, *ChemPhysChem*, 2017, **18**, 292-298.
63. R. Nishiyabu, Y. Sugino and Y. Kubo, *Chemical Communications*, 2013, **49**, 9869-9871.
64. F. d. J. Trindade, E. R. Triboni, B. Castanheira and S. Brochsztain, *The Journal of Physical Chemistry C*, 2015, **119**, 26989-26998.
65. M. K. Barman, B. Paramanik, D. Bain and A. Patra, *Chemistry – A European Journal*, 2016, **22**, 11699-11705.

66. U. Goswami, S. Basu, A. Paul, S. S. Ghosh and A. Chattopadhyay, *Journal of Materials Chemistry C*, 2017, **5**, 12360-12364.
67. S. Mandani, B. Sharma, D. Dey and T. K. Sarma, *RSC Advances*, 2016, **6**, 84599-84603.
68. C.-C. Tu, J. H. Hoo, K. F. Böhringer, L. Y. Lin and G. Cao, *Opt. Express*, 2014, **22**, A276-A281.
69. B. Ghosh, Y. Masuda, Y. Wakayama, Y. Imanaka, J.-i. Inoue, K. Hashi, K. Deguchi, H. Yamada, Y. Sakka, S. Ohki, T. Shimizu and N. Shirahata, *Advanced Functional Materials*, 2014, **24**, 7151-7160.
70. P. Holzmeister, G. P. Acuna, D. Grohmann and P. Tinnefeld, *Chemical Society Reviews*, 2014, **43**, 1014-1028.
71. M. Bauch, K. Toma, M. Toma, Q. Zhang and J. Dostalek, *Plasmonics*, 2014, **9**, 781-799.
72. Y. Liu, J. Zhou, B. Wang, T. Jiang, H.-P. Ho, L. Petti and P. Mormile, *Physical Chemistry Chemical Physics*, 2015, **17**, 6819-6826.
73. A. B. Taylor and P. Zijlstra, *ACS Sensors*, 2017, **2**, 1103-1122.
74. Y. Zhang, V. Pan, X. Li, X. Yang, H. Li, P. Wang and Y. Ke, *Small*, 2019, **15**, 1900228.
75. A. Puchkova, C. Vietz, E. Pibiri, B. Wünsch, M. Sanz Paz, G. P. Acuna and P. Tinnefeld, *Nano Letters*, 2015, **15**, 8354-8359.
76. T. Zhang, N. Gao, S. Li, M. J. Lang and Q.-H. Xu, *The Journal of Physical Chemistry Letters*, 2015, **6**, 2043-2049.
77. G. P. Acuna, F. M. Möller, P. Holzmeister, S. Beater, B. Lalkens and P. Tinnefeld, *Science*, 2012, **338**, 506-510.
78. F. Nicoli, T. Zhang, K. Hübner, B. Jin, F. Selbach, G. Acuna, C. Argyropoulos, T. Liedl and M. Pilo-Pais, *Small*, 2019, **15**, 1804418.
79. A. Kinkhabwala, Z. Yu, S. Fan, Y. Avlasevich, K. Müllen and W. E. Moerner, *Nature Photonics*, 2009, **3**, 654-657.
80. Y. Han, Y. Chen, J. Feng, J. Liu, S. Ma and X. Chen, *Analytical Chemistry*, 2017, **89**, 3001-3008.
81. J. Wu, J. Dai, Y. Shao and Y. Sun, *RSC Advances*, 2015, **5**, 83581-83587.
82. G. Wen, X. Zeng, X. Wen and W. Liao, *Journal of Applied Physics*, 2014, **115**, 164303.
83. X. Liu, Y. Zhang, T. Yu, X. Qiao, R. Gresback, X. Pi and D. Yang, *Particle & Particle Systems Characterization*, 2016, **33**, 44-52.
84. S. Zhou, Z. Ni, Y. Ding, M. Sugaya, X. Pi and T. Nozaki, *ACS Photonics*, 2016, **3**, 415-422.
85. E. V. Shevchenko, M. I. Bodnarchuk, M. V. Kovalenko, D. V. Talapin, R. K. Smith, S. Aloni, W. Heiss and A. P. Alivisatos, *Advanced Materials*, 2008, **20**, 4323-4329.
86. A. Samanta, Z. Deng, Y. Liu and H. Yan, *Nano Research*, 2013, **6**, 853-870.
87. P. Yu, X. Wen, Y.-R. Toh and J. Tang, *The Journal of Physical Chemistry C*, 2012, **116**, 25552-25557.
88. Y. Yang, W. Kong, H. Li, J. Liu, M. Yang, H. Huang, Y. Liu, Z. Wang, Z. Wang and T.-K. Sham, *ACS applied materials & interfaces*, 2015, **7**, 27324-27330.
89. Y. Han, Y. Chen, J. Feng, J. Liu, S. Ma and X. Chen, *Analytical Chemistry*, 2017, **89**, 3001-3008.
90. S. Mandani, B. Sharma, D. Dey and T. K. Sarma, *Nanoscale*, 2015, **7**, 1802-1808.
91. Z. Luo, X. Yuan, Y. Yu, Q. Zhang, D. T. Leong, J. Y. Lee and J. Xie, *Journal of the American Chemical Society*, 2012, **134**, 16662-16670.
92. N. Zhang, H. Qiu, Y. Liu, W. Wang, Y. Li, X. Wang and J. Gao, *Journal of Materials Chemistry*, 2011, **21**, 11080-11083.
93. H.-s. Kim, Y. S. Seo, K. Kim, J. W. Han, Y. Park and S. Cho, *Nanoscale Research Letters*, 2016, **11**, 230.
94. K. K. Haldar, T. Sen and A. Patra, *The Journal of Physical Chemistry C*, 2010, **114**, 4869-4874.
95. D. Astruc, *Nanoparticles and catalysis*, Wiley-VCH-Verl., Weinheim, 2008.
96. A. Corma and H. Garcia, *Chemical Society Reviews*, 2008, **37**, 2096-2126.
97. Y. Mikami, A. Dhakshinamoorthy, M. Alvaro and H. García, *Catalysis Science & Technology*, 2013, **3**, 58-69.
98. S. Wunder, F. Polzer, Y. Lu, Y. Mei and M. Ballauff, *The Journal of Physical Chemistry C*, 2010, **114**, 8814-8820.
99. B. Baruah, G. J. Gabriel, M. J. Akbashev and M. E. Booher, *Langmuir*, 2013, **29**, 4225-4234.

100. R. Ciganda, N. Li, C. Deraedt, S. Gatard, P. Zhao, L. Salmon, R. Hernández, J. Ruiz and D. Astruc, *Chemical Communications*, 2014, **50**, 10126-10129.
101. T. Aditya, A. Pal and T. Pal, *Chemical communications*, 2015, **51**, 9410-9431.
102. B. Sharma, S. Mandani and T. K. Sarma, *Journal of Materials Chemistry B*, 2014, **2**, 4072-4079.
103. B. Sharma, S. Mandani and T. K. Sarma, *Journal of Nanoparticle Research*, 2015, **17**, 4.
104. M. Rashid and T. K. Mandal, *Advanced Functional Materials*, 2008, **18**, 2261-2271.
105. J. B. Essner, C. H. Laber and G. A. Baker, *Journal of Materials Chemistry A*, 2015, **3**, 16354-16360.
106. I. V. Safenkova, A. V. Zherdev and B. B. Dzantiev, *Journal of Immunological Methods*, 2010, **357**, 17-25.
107. H.-L. Jiang, T. Akita, T. Ishida, M. Haruta and Q. Xu, *Journal of the American Chemical Society*, 2011, **133**, 1304-1306.
108. T. Yu, J. Zeng, B. Lim and Y. Xia, *Advanced Materials*, 2010, **22**, 5188-5192.
109. Y. Yang, T. Wang, P. Yin, W. Yin, S. Zhang, Z. Lei, M. Yang, Y. Ma, W. Duan and H. Ma, *Materials Chemistry Frontiers*, 2019, **3**, 505-512.
110. B. Sharma, S. Tanwar and T. Sen, *ACS Sustainable Chemistry & Engineering*, 2019, **7**, 3309-3318.
111. X. Wen, P. Yu, Y.-R. Toh and J. Tang, *The Journal of Physical Chemistry C*, 2012, **116**, 11830-11836.
112. E. J. McLaurin, L. R. Bradshaw and D. R. Gamelin, *Chemistry of Materials*, 2013, **25**, 1283-1292.
113. C. D. S. Brites, P. P. Lima, N. J. O. Silva, A. Millan, V. S. Amaral, F. Palacio and L. D. Carlos, *Nanoscale*, 2012, **4**, 4799-4829.
114. J. Xie, Y. Zheng and J. Y. Ying, *Chemical Communications*, 2010, **46**, 961-963.
115. J. Wu, R. Sheng, W. Liu, P. Wang, J. Ma, H. Zhang and X. Zhuang, *Inorganic Chemistry*, 2011, **50**, 6543-6551.
116. Y. Guo, L. Zhang, F. Cao, L. Mang, X. Lei, S. Cheng and J. Song, *Analytical Methods*, 2016, **8**, 2723-2728.
117. D. Zhou, L. Ying, X. Hong, E. A. Hall, C. Abell and D. Klenerman, *Langmuir*, 2008, **24**, 1659-1664.

Chapter 6

Plasmonic nanoantennas for label free sensing of single protein molecule

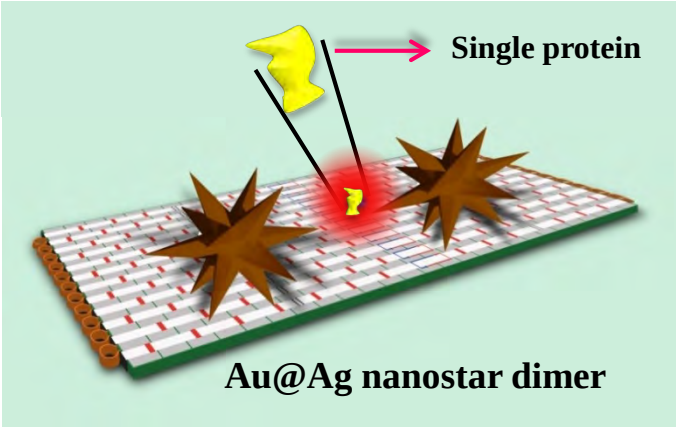

6.1. Introduction

Highly sensitive single-molecule label-free sensing methods have applications in both the fundamental research and healthcare diagnostics.[1] Single molecule sensors enable measuring analytes with sensitivity levels that allow detection and analysis of single molecules. This is important for the diagnosis of diseases where a single molecule or microorganism has a tremendous impact on the fate of the clinical condition.[2] Scanning each and every molecule further helps in identifying rare aberrant molecules among the healthy ones.[3] In the optical domain, fluorescence spectroscopy has emerged as a method of choice for developing single molecule sensors owing to several associated advantages such as parallel and multiplexed detection, high sensitivity, site-specific labeling, and high signal to noise ratio.[4-7] Although widely employed, requirement of sophisticated instruments and labeling of molecules has severely limited its applicability for commercial applications. Labeling is not feasible for sensing applications where the analysis has to be done directly in the samples without prior washing. The other disadvantages of labeling are increased cost and time per detection, change in structure and activity of molecules, and induced variability.[8, 9] This has sparked interest in both the scientific community and the relevant industries to develop so-called "label-free" sensors.

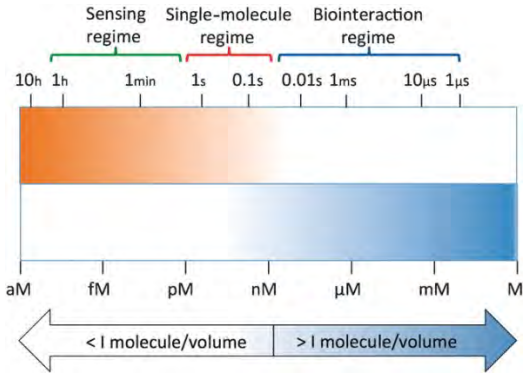

Figure 6.1. Concentration range required for single molecule sensing and studying biological interactions. (Reprinted with permission from ref. [1],2016 WILEY-VCH Verlag GmbH & Co. KGaA, Weinheim)

Due to diffraction limited optics, single molecule measurements are done at ultralow concentrations (1 pM to 1 nM),[10] however, many biomolecular interactions such as enzyme-ligand and protein-DNA interactions take place at higher concentrations with dissociation constants in µM range (Figure 6.1).[10, 11] Thus an optical single molecule sensor should be compatible with these high concentrations such that only a single biomolecule occupies the

probe volume at one time. This discrepancies in the concentration limit can be efficiently addressed using plasmonics and nanophotonics.

Over the past few decades, plasmonic sensors have demonstrated their capacity for achieving single molecule sensitivity at concentrations as high as tens of micromolars, [12, 13] without the need of chemical labeling.[14, 15] The generated electric field around plasmonic nanoparticles decays rapidly into the medium surrounding thereby enhancing the interactions between the excited plasmons and the molecule. These plasmon-molecular interactions result in a significant enhancement in fluorescence emission, [16-18] Raman scattering intensities,[19-21] and detectable shifts in resonance band. [22] Till now numerous elegant strategies have been developed to detect single molecules by analyzing shifts in the longitudinal surface plasmon resonance (SPR) band induced due to plasmon molecule interactions. For example, Zijlstra et al. reported plasmon mediated label free sensing of single Streptavidin protein molecules by monitoring the change in the SPR band of gold nanorods using photothermal microscopy.[14] Ament et al. utilized plasmon spectroscopy technique for real-time monitoring of single fibronectin protein binding dynamics and desorption and adsorption processes.[23]

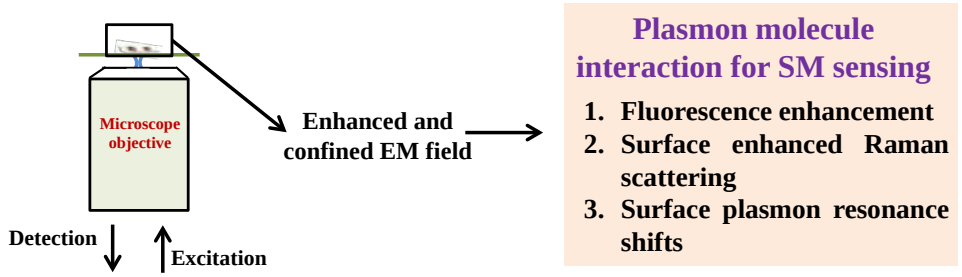

Scheme 6.1. Scheme depicting different modes of plasmon mediated single molecule sensing.

Later, Dantham et al. reported detection of single thyroid cancer marker and bovine serum albumin using nanoplasmonic hybrid microcavity.[24] Very recently, Verschueren et al. developed an inverted-bowtie plasmonic nanopore biosensor for the optical trapping and SPR based sensing of single beta-amylase protein.[25] Although, change in the SPR wavelength of plasmonic nanoparticle due to plasmon-molecule interactions within the hotspot of plasmonic sensors offers a simple means to detect analytes. These single-wavelength measurements fail to provide any molecule specific information which is required for the identification of the molecule of interest from a mixture. Structural specific information helps in ruling out the possibility of getting similar shifts in the SPR from impurity or any other molecule showing similar SPR shifts. This challenge can be very easily overcome using Surface-enhanced Raman spectroscopy

(SERS). SERS is a molecule specific technique that has the ability to detect a molecule from a group of molecules. [26, 27] And it has already proven its ability to provide sensitivity down to single molecule level. [28-32] For example, Freedman et al. showed SERS based label-free sensing using plasmonic nanopipettes designed by a dielectrophoretic assembly of gold nanoparticles to form a rough gold sphere at the tip of a nanopipette.[33] Chen et al. designed a novel plasmonic nanoslit device by combining SERS with nanopore fluidics for single nucleobase sensing. [34] Brule et al. for the first time studied changes in the conformations of single BSA protein using dynamic SERS experiments.[35] In simple words, SERS based plasmonic sensors provide ultimate sensitivity along with detailed information of molecules which helps in analyzing complex samples containing diverse analytes.

Among all the fabrication techniques,[36-39] electron beam lithography is the most prevalent technique widely employed to synthesize nanoantennas such as bow-tie,[16, 40] gold nanoparticle[41, 42] and nanorod dimers,[43] Yagi-Uda,[44] and plasmonic nanopores.[45] Due to its inability to fabricate nanoantennas with interparticle gaps of < 10 nm its applicability is limited.[46] DNA origami is a powerful method of nanofabrication as it provide tight control over the self-assembly of nanoparticles into complex antenna designs and localizing the desired target molecule in the antenna hot spot.[47-52] Tanwar et al. used DNA origami as a template for assembling Au nanostar dimer structures with different interparticle gaps and stoichiometry. The dimer structures were found to be giving enhancement factor in the order of 10^{10}, strong enough for single molecule sensing.[53] Heck et al. [54] self-assembled silver nanolenses on DNA origami scaffolds and further employed them for SERS based sensing of single streptavidin protein selectively placed in the plasmonic hotspot. Further, Kaminska et al. [18] have shown that DNA origami based optical antennas can be used for the detection of single peridinin−chlorophyll a−protein complex in the plasmonic hotspot. Proteins are the structural elements and machinery of every single cell of the body and play critical role in functioning and maintaining biological architecture and homeostasis of human body. In case of onset of disease such as cancer, the concentration level of several proteins in the body gets misregulated therefore are considered to be potent biomarkers for detection of early-onset of diseases.[55, 56] Development of label free single protein detection methods is important for getting molecular information critical for fundamental biochemical research and for clinical laboratory diagnosis.[57, 58]

This chapter demonstrates label-free SERS based plasmonic sensing of a single thrombin protein molecule. Single thrombin protein was captured in the plasmonic hotspot of Au@Ag nanostar dimer structure using two thrombin binding aptamer DNA sequences. Further, it has

been shown that the designed plasmonic nanoantennas have the potential to be used as a label-free sensor for the detection of a single protein molecule.

6.2. Experimental section

6.2.1. Materials

Tween 20, ammonium hydroxide (NH_4OH, 25%), hydrochloric acid (HCl), and acetic acid (CH_3COOH) were purchased from Merck. Gold chloride trihydrate ($HAuCl_4.3H_2O$, purity ≥ 99.9%), trisodium citrate dihydrate ($Na_3C_6H_5O_7$), Magnesium chloride hexahydrate ($MgCl_2.6H_2O$), HEPES buffer solution (pH=5), ethylenediaminetetraacetic acid disodium (EDTA), L-Ascorbic acid, sodium dodecyl sulfate (SDS), silver nitrate ($AgNO_3$), tris(hydroxymethyl)aminomethane (Tris base), tris-(carboxyethyl) phosphine hydrochloride (TCEP.HCl), 1 M Potassium phosphate monobasic solution (KH_2PO_4), phosphate buffer saline (PBS) tablets, 1 M potassium phosphate dibasic solution (K_2HPO_4), and sodium chloride (NaCl) were purchased from Sigma-Aldrich and used without further purification. M13mp18 single stranded DNA was purchased from New England Biolabs. All modified, unmodified, and aptamer modified staple DNA sequences were purchased from Integrated DNA Technologies (IDT) with standard desalting. Thiol labeled DNA oligonucleotides were purchased from IDT with HPLC purification. Human alpha-thrombin native protein and BSA were purchased from Thermo Fischer and Sigma Aldrich respectively. Sephacryl S-300 high resolution resin was procured from GE Healthcare. Carbon coated Cu TEM grids were purchased from Ted Pella. AFM mica discs of V1 quality were bought from Agar Scientific. Si wafer (double side polished with resistivity 1-10 ohm.cm) was purchased from Ekta Marketing corporation. Micro bio spin chromatography columns for packing of resin were purchased from Bio-Rad. All the experiments were carried out in ultrapure water.

6.2.2. Experimental procedures

6.2.2.1. Synthesis and DNA functionalization of Au@Ag nanostars (Au@Ag NSs)

Au@Ag NSs were synthesized by coating a thin layer of Ag on premade Au NSs. Au nanostars (Au NSs) were prepared by seed-mediated method as described in chapter 3 of this thesis.[53] To 1 mL solution of Au NSs, 1 µL each of 0.1 M $AgNO_3$ and 0.1M ascorbic acid were added respectively while the solution was on stirring. This was followed by the addition of 2 µL solution of NH_4OH. The color of the solution immediately changed from blue to purple indicating the coating of Ag on Au NSs. A 40 µL aliquot of 0.1 M SDS solution was then added to the solution and further stirred for 5 minutes. Excess unreacted reactants were then removed

by centrifuging at 4000 rcf for 10 min. Finally, the synthesized Au@Ag NSs were resuspended in 5 mM HEPES buffer (pH-3) and were used for DNA functionalization.

The synthesized Au@Ag NSs were functionalized with a mixed DNA sequence having thiol modification at 5′ end (Table 7 of appendix A). The protocol followed was modified from Zhang et al.[59] To 1 mL solution of Au@Ag NSs suspended in HEPES buffer, 25 µL of 200 µM thiol modified ssDNA oligonucleotides were added with mild stirring. After 30 minutes, 20 µL of 10% Tween 20 and 4:5 mixture of KH_2PO_4 and K_2HPO_4 buffers with a time gap of 15 minutes were added. The mixture was kept for overnight mild stirring. Afterward, 2M NaCl, 0.1% Vol Tween 20 buffer solution was added stepwise over 2 hours to the stirred solution until a final concentration of 750 mM was reached. The mixture was further kept for overnight stirring. The Au@Ag NSs DNA conjugates were purified by 3 times centrifugation at a rate of 5,000 × g, 15 min for each time. The supernatant was carefully removed and the nanoparticles were finally resuspended in 0.5×TAE buffer and stored at 4 ºC for further use.

6.2.2.2. Incorporation of thrombin binding aptamers on DNA origami

The rectangular DNA origami of dimension ~ 90 × 60 nm was synthesized using the design proposed by Paul Rothemund.[48] Genomic DNA of M13mp18 bacteriophage was used as a scaffold that was folded into a rectangular shape using 213 short staple DNA sequences.[53] For folding 2 nM of the scaffold, modified and unmodified staple strands were added in 10 and 20 fold excess in 1× TAE-12.5 mM $MgCl_2$ buffer respectively. The mixture was heated to 90 ºC and slowly cooled down to 20 ºC in ~ 1.5 hours. Dimerization of rectangular DNA origami (dimension ~180 × 60 nm) was done using aptamer modified branching staples. To an equimolar mixture of unpurified origami A and origami B solutions, 22 branching[53] and 2 aptamer modified branching staples were added in 40-fold excess and the mixture was incubated at room temperature for 24 h in 50× TAE-12.5 mM $MgCl_2$ buffer. The dimerized rectangular DNA origami having thrombin binding aptamers was then purified using Sephacryl S-300 resin. Details of aptamer modified branching staples are given table 12 of appendix A.

6.2.2.3. Immobilization of single thrombin protein in the plasmonic hotspot of Au@Ag NS dimer nanoantennas

Strategy I. Purified dimerized rectangular DNA origami was mixed with thrombin in a molar ratio of 1:2 and was kept at room temperature for 2 hours. After the binding of thrombin, the thrombin-DNA origami conjugates were mixed with DNA functionalized Au@Ag NSs and kept at room temperature for 24 hours. Further, the hybrid structures were immobilized on Si wafer

for AFM correlated Raman measurements. The Au@Ag NSs-DNA origami-thrombin hybrid nanostructures were diluted in 10 × TAE-200 mM $MgCl_2$ buffer and incubated on plasma cleaned Si wafer for 2 hours being kept in a moist chamber. The unbound sample was washed using MQ water.

Strategy II. Purified dimerized rectangular DNA origami was mixed with DNA functionalized Au@Ag NSs in a molar ratio of 1:2 in 0.5 × TAE buffer having 6.25 mM $MgCl_2$ and 300 mM NaCl. The mixture was kept in PCR thermocycler and repeatedly heated from 40°C to 20°C for 12 hours with a ramp rate of - 0.1°C/s. The synthesized Au@Ag NSs dimer nanostructures were then immobilized on oxygen plasma cleaned Si wafer (1 × 1 cm^2). The Au@Ag NSs DNA origami hybrid nanostructures were then diluted in 10× TAE buffer having 200 mM $MgCl_2$ and incubated on Si wafer for 2 hours being kept in a moist chamber. The unbound sample was washed using MQ water. The immobilized Au@Ag NS dimer nanoantennas were then incubated with 20 nM of thrombin solution for 4 hours followed by washing with MQ water to remove unbound protein.

6.2.2.4. Detection of single thrombin protein using AFM correlated Raman measurements

Different areas of Si wafer were scanned using AFM for getting the desired area having sparsely distributed Au@Ag dimer structures. The same area was scanned under the confocal Raman microscope for recording Raman scattering signals. For the Raman measurements included in this study laser excitation of 532 nm with laser power of 1 mW was used. All the other parameters such as integration time, number of accumulations were kept same throughout the study for a fair comparison.

As synthesized Au@Ag NSs, DNA origami, DNA origami-thrombin conjugates, and Au@Ag NSs-DNA origami hybrid nanostructures were characterized by TEM, AFM, UV-Vis spectrophotometer, and confocal Raman microscopy as described in chapter 2 of this thesis.

6.3. Results and discussion

Thrombin is a serine proteinase that plays a fundamental role in the coagulation cascade. Development of a label free detection system for its sensing will help in early diagnosis of clinical conditions like tumor growth, metastasis, and angiogenesis.

6.3.1. Aptamer assisted capturing of single thrombin protein on DNA origami

The term “aptamer” is derived from the combination of a Latin word '*aptus*' (to fit) with a Greek word '*méros*' (part). Basically, they are short oligonucleotides that selectively target and bind

with high affinity to a wide variety of target molecules including antibiotics,[60] amino acids,[61] proteins,[62] viruses,[63] and even whole cell.[64] Nucleic-acid aptamers have attracted intense interest and found wide applications in a range of areas due to their high specificity, sensitivity, and low production cost.[65] Another important aspect of aptamers is that they can be easily incorporated into DNA origami structures by simply modifying one of the staple strands with the aptamer

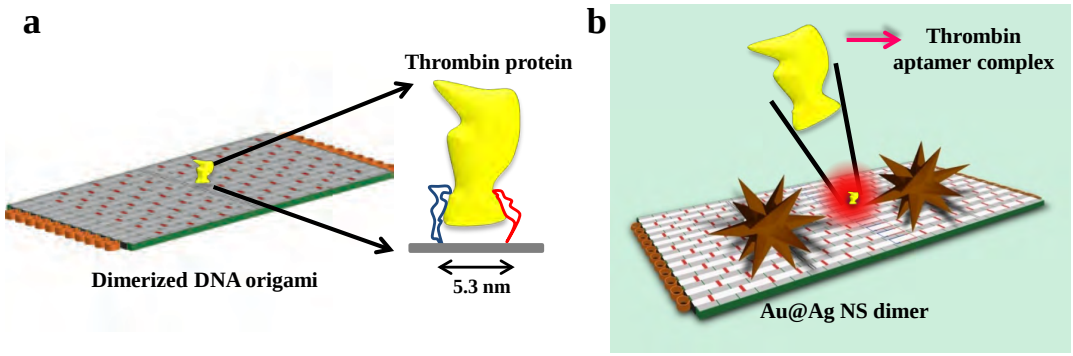

Scheme 6.2. Schematic depiction of (a) aptamer assisted capturing of single thrombin on DNA origami, and (b) Au@Ag NS dimer-DNA origami-thrombin complex.

sequence. The design of our DNA origami-based single protein nanosensor is schematically illustrated in scheme 6.2. For capturing single thrombin protein molecule on rectangular DNA origami, two branching staples were modified with closed-loop thrombin binding aptamer sequences. The position of the aptamer modified branching staples resides exactly in the middle of the DNA origami template where the plasmonic hotspot is expected to form. Scheme 6.3 illustrates the dimerization of rectangular DNA origami using 22 branching and 2 aptamer modified branching staples. The aptamer sequences used for capturing thrombin protein are well characterized previously and are known to bind specifically and cooperatively to thrombin protein. [6669] The binding sites of the two aptamers are at opposite sides of the thrombin protein molecule (as shown in scheme 6.2a). The 15 mer aptamer sequence GGTTGGTGTGGTTGG in its folded form consists of two G-tetrads that form a chair-like conformation via the Hoogsten-type guanine-guanine base pairing.[67, 68] It is known for having a high affinity for fibrinogen-recognition exosite of thrombin.[66] The second selected 29 mer aptamer sequence AGTCCGTGGTAGGGCAGGTTGGGGTGACT forms a combined quadruplex duplex structure and has a binding affinity for heparin-binding exosite of the thrombin protein.[69] While incorporating the aptamers in between the branching staple sequence, a poly T sequence was added to both the stems so that both the aptamers have 3D flexibility for rotation. Another deciding factor for achieving strong and high yield binding of thrombin was inter-aptamer

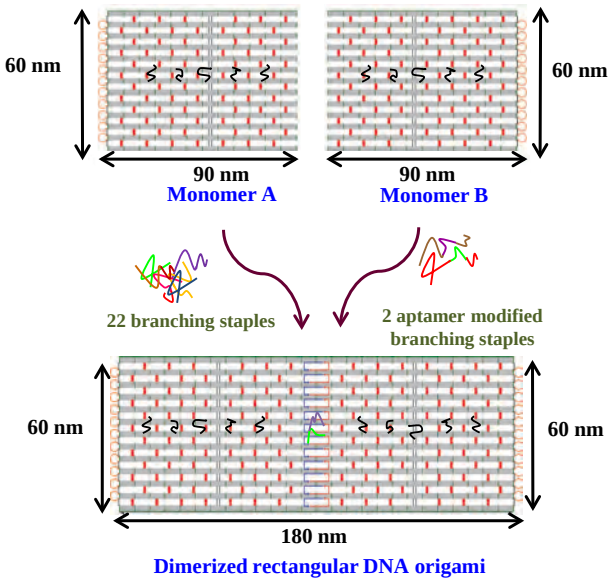

Scheme 6.3. Schematic depiction of incorporation of thrombin binding aptamers on DNA origami.

distance. The two aptamer sequences were expected to act as a bivalent single molecular species that will create a docking site on the DNA origami template for capturing single thrombin

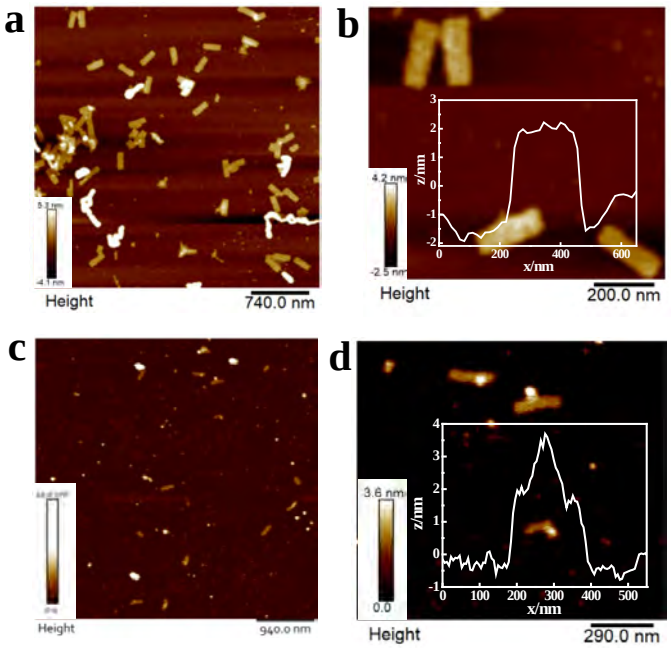

Figure 6.2. AFM images of dimerized DNA origami (a and b) without, and (c and d) with single thrombin protein. The inset shows the corresponding height profile.

protein. Size of a single thrombin protein is ~ 4.1 × 4.1 nm, any inter-aptamer distances greater than 5 nm would have resulted in less binding or binding of two thrombin molecules separately to each aptamer sequence. So, the branching staples used for modification were selected such that after modification the centre-to-centre distances between the two aptamers will be ~ 5 nm. Further, the presence of poly T sequences at the stems of both the aptamer will allow free movement of the aptamers that will compensate for small changes in the size of thrombin and inter-aptamer distance. Folded rectangular DNA origami monomer A and monomer B were allowed to dimerize with 22 usual and 2 aptamer modified branching staples. AFM images of

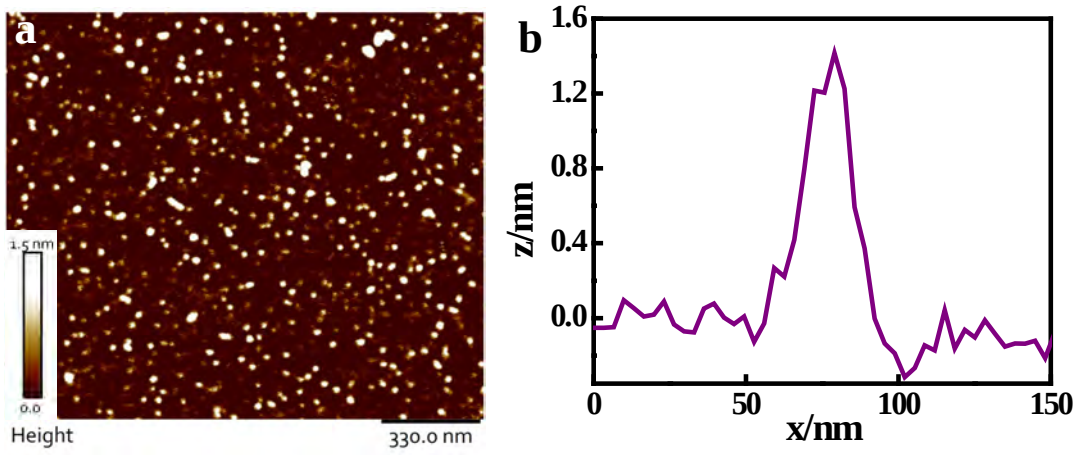

Figure 6.3. (a) AFM images, and (b) corresponding height profile of thrombin protein.

dimerized DNA origami without (Figure 6.2a and 6.2b) and with (Figure 6.2c and 6.2d) thrombin confirmed successful immobilization of thrombin at the predefined site. To further confirm that the pronounced feature in the middle of the DNA origami template is thrombin, AFM images of thrombin protein were recorded (Figure 6.3). The height profile of thrombin protein matched well with the thrombin on DNA origami.

6.3.2. Design of Au@Ag NS dimer-DNA origami-thrombin hybrid nanostructures

The Au@Ag NSs were synthesized using the protocol described in the experimental section. Optical and structural characterizations of the synthesized nanostars were done using UV-Vis spectrophotometer and TEM imaging respectively. The UV-Vis spectrum of the synthesized nanostars showed an SPR band around 555 nm (Figure 6.4a). Further, TEM images confirmed the formation of Au@Ag NSs with an average size of 70 ± 6 nm. After successful synthesis of the Au@Ag NSs, the Au@Ag NSs were conjugated with thiol labeled ssDNA oligonucleotides

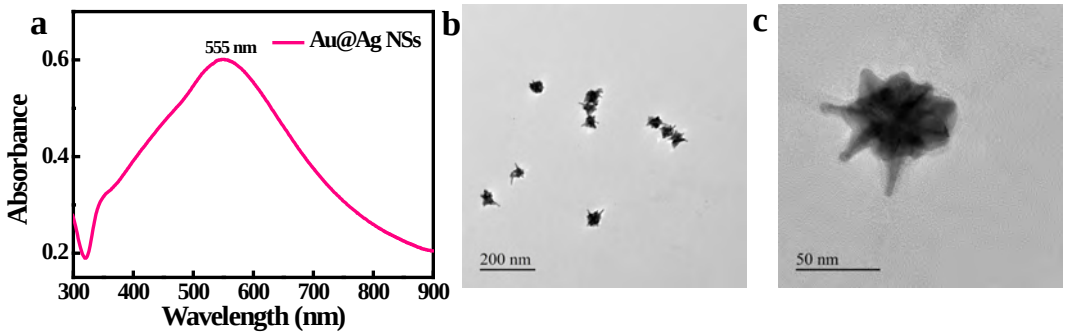

Figure 6.4. (a) UV-Vis spectrum, and (b and c) TEM images of Au@Ag NSs.

using pH assisted protocol reported by Zhang et al. with modifications.[59] The DNA conjugated Au@Ag NS dimers were then assembled on dimerized DNA origami template using two different sets of capture staple sequences. Figure 6.5 shows the position of staple sequences

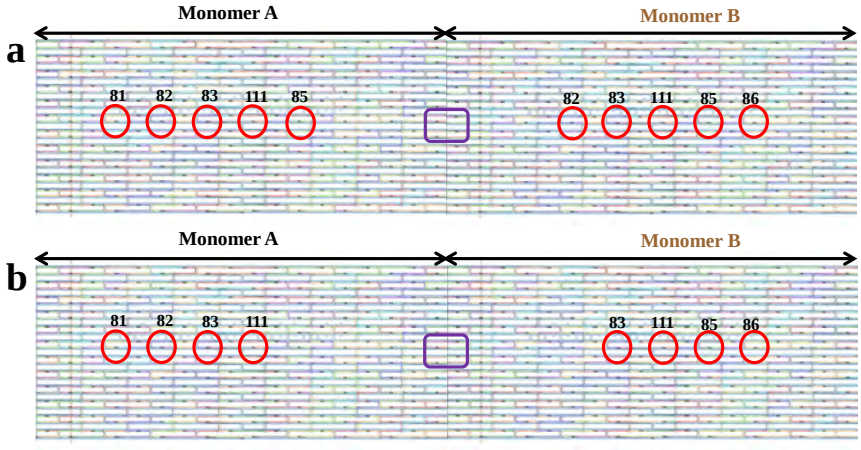

Figure 6.5. Dimerized rectangular DNA origami design showing position of capture staple sequences used for synthesis of Au@Ag NS dimers of gap (a) 10 and (b) 15 nm. Position of thrombin binding aptamers is represented by purple colored box.

used for capturing Au@Ag NSs on the DNA origami template. To confirm successful immobilization of the Au@Ag NS dimers on DNA origami and to determine the interparticle gap, TEM imaging of the assembled Au@Ag NS dimer structures was done. TEM images (Figure 6.6) confirmed successful immobilization of the Au@Ag NS dimer structures on DNA origami. Further, we found that the average interparticle gap of dimer structures assembled

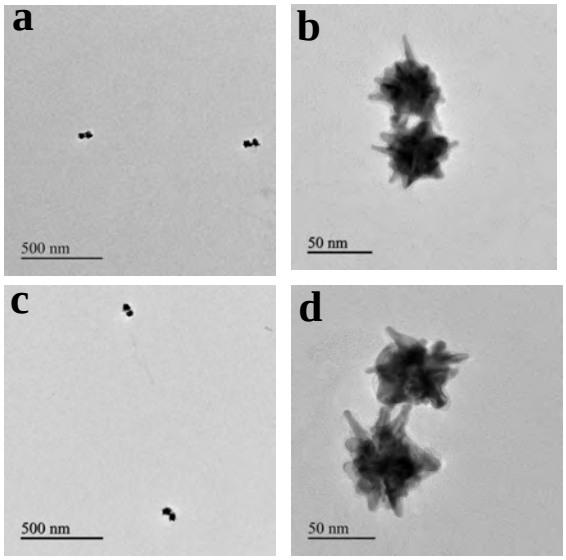

Figure 6.6. TEM images of Au@Ag NS dimers of average interparticle gap sizes of (a and b) 10 nm, and (c and d) 15 nm.

using capture staples shown in figure 6.5a is 10 nm (Figure 6.6a and 6.6b) and that of shown in figure 6.5b is 15 nm (Figure 6.6c and 6.6d). For immobilization of single thrombin protein in the plasmonic hotspot of Au@Ag NS dimer structures, two different strategies were followed. In strategy I, at first thrombin protein was immobilized on the DNA origami template and then DNA origami-thrombin structures were incubated with DNA functionalized Au@Ag NSs for immobilization of Au@Ag NSs. Strategy II involved incubation of premade Au@Ag NS dimer structures with thrombin protein solution. Strategy II was followed to check the efficiency of the designed nanosensor to directly capture the target molecule into the plasmonic hotspot from the analyte solution.

6.3.3. SERS based label free detection of single thrombin protein

After successful synthesis of the Au@Ag NS dimer-thrombin hybrid nanostructures, AFM correlated Raman measurements[53] were done to record Raman signatures of thrombin protein. The self-assembled hybrid nanoantennas were identified using AFM imaging followed by scanning the same area for Raman signals. For all the SERS measurements a laser excitation of 532 nm was used. At first, the Au@Ag NS dimer-thrombin hybrid structures assembled using strategy I were used for recording Raman signatures of thrombin protein. The hybrid structures immobilized on Si wafer were identified using AFM imaging and then scanned under a confocal Raman microscope for Raman signals. Figure 6.7 shows AFM correlated Raman measurements

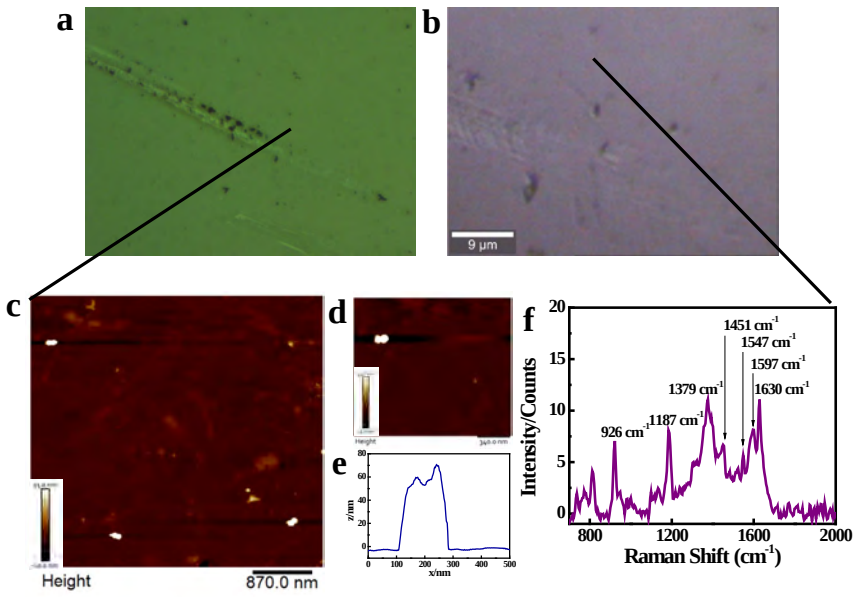

Figure 6.7. Single molecule SERS measurements of thrombin protein in the Au@Ag NS dimer nanoantennas of 10 nm interparticle gap. (a and b) Optical images recorded using AFM and confocal Raman microscopes respectively (black line indicates the scanned area). (c) AFM images of the nanoantenna structures. (d and e) High resolution AFM image of single nanoantenna structure with its height profile. (f) Corresponding single molecule SERS spectrum.

of Au@Ag NSs dimer structures with an average interparticle gap size of 10 nm. In the single molecule SERS spectrum of thrombin protein (Figure 6.7f), the peaks corresponding to C–N stretching (1187 cm^{-1}), amide II (1597 cm^{-1}), and amide I (1630 cm^{-1}) bond of proteins were very clearly visible.[70, 71] Apart from these typical protein peaks, the peak at 926 cm^{-1} due to N–C_α–C stretching of α-helix and the peak at 1379 cm^{-1} due to Tryptophan were also present in the SERS spectrum.[71] Human alpha thrombin is an alpha rich protein,[72] the range of wavenumbers

Table 6.1. Raman peaks of proteins obtained from literature. [70, 71]

Peak (cm^{-1})	**Assignment**
924–943	N–C_α–C for α-helix
1190	C–N stretching of protein
1327-1370	Tryptophan
1440-1450	C-H deformations
1586	Amide II of protein
1625-1680	Amide I of protein

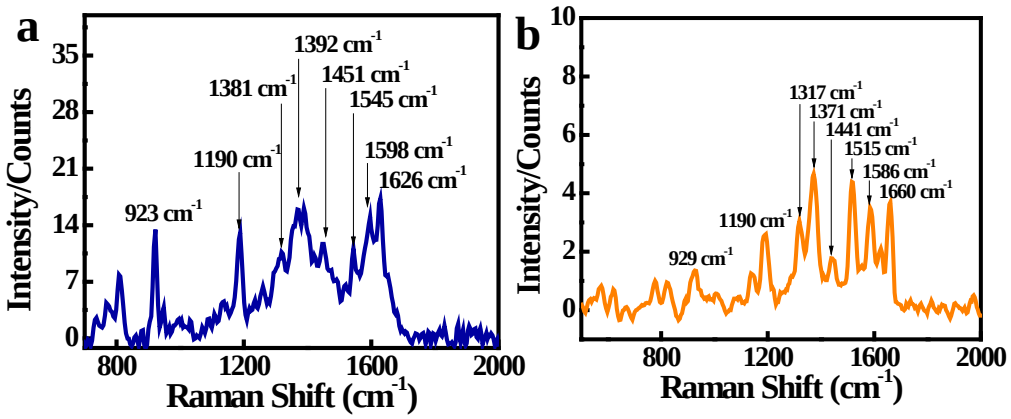

Figure 6.8. Single molecule SERS spectra of thrombin protein placed in the plasmonic hotspot of Au@Ag NS dimer nanoantenna of an average interparticle gap size of (a) 10 nm and (b) 15 nm.

of Raman peaks of an alpha rich protein are given in table 6.1. The obtained peaks were matching with the literature. It was found that among average interparticle gap sizes of 10 and 15 nm, the SERS intensities were higher for 10 nm gap (Figure 6.8a) then 15 nm (Figure 6.8b). The higher SERS intensity for 10 nm gap can be attributed to the high intensity of electromagnetic field generated in between the Au@Ag NS dimer nanoantenna.[73] To check whether the designed nanosensor can directly capture thrombin protein from the solution, SERS measurements were carried out using Au@Ag NS dimer-thrombin hybrid structures assembled

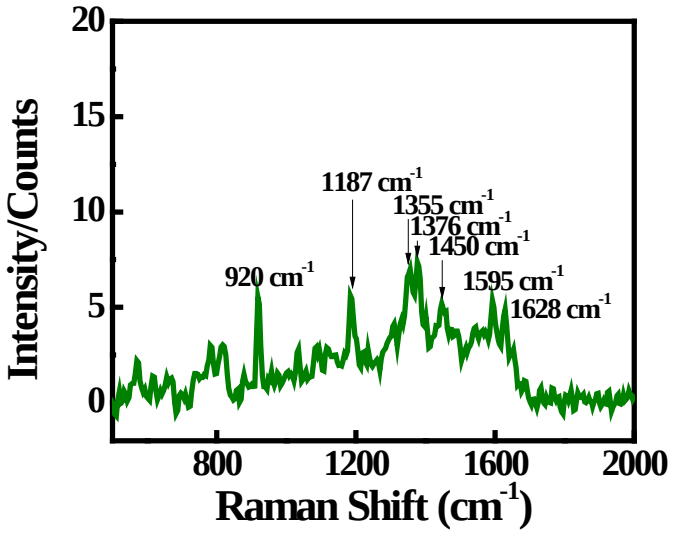

Figure 6.9. Single molecule SERS spectrum of thrombin protein captured in the hotspot of Au@Ag NS dimer nanoantenna from thrombin solution.

using strategy II as described in the experimental section. The SERS signals were recorded using Au@ Ag NS dimer nanoantennas with an average interparticle gap size of 15 nm. Larger gap size was tried so that thrombin protein gets ample space to go into the hotspot and bind with the aptamers. Interestingly, we were able to record Raman signature peaks of thrombin protein. The results demonstrate that the designed nanoantenna has the potential to be used as a label free nanosensor for sensing molecules whose capturing probes are immobilized in the hotspot of the dimer nanoantenna.

Specificity test. Molecular recognition selectivity is very important for any sensing system. To check whether the designed system is specific for thrombin, SERS measurements using interfering protein BSA were carried out. BSA is analogous to thrombin and is usually used for carrying out cross-reactivity studies for thrombin specific sensors.[74] Further, to check if the docking site created in the hotspot region is specific to thrombin or any other protein molecule of similar size can show binding affinity, specificity tests were done using myoglobin. The size of a myoglobin protein is ~ 3.5 nm close to that of thrombin protein.[75] Cross-reactivity studies were carried out using strategy I: at first protein molecules were allowed to bind to aptamer sequences incorporated on the dimerized DNA origami template followed by Au@Ag NSs binding. Interestingly, no peaks corresponding to BSA (Figure 6.10a) and myoglobin (Figure 6.10b) proteins were observed in the SERS spectrum. The results show that the designed nanosensor is specific to thrombin protein.

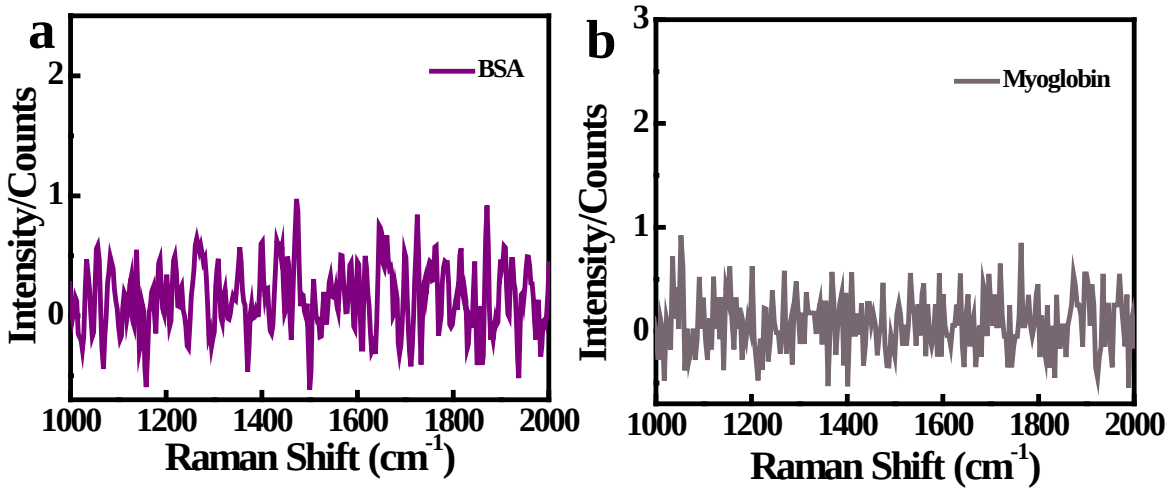

Figure 6.10. SERS spectra of Au@Ag NS dimer with (a) BSA and (b) myoglobin protein.

6.4. Conclusion

This chapter provides a glimpse of the utility of DNA origami assembled plasmonic nanoantennas for label free sensing of single protein molecule. Single thrombin protein was precisely localized in the plasmonic hotspot of Au@Ag NS dimer nanoantennas using aptamer protein interactions. The modular structure of DNA origami allowed introduction of two different thrombin binding aptamers on the DNA origami template at a position where the plasmonic hotspot was expected to form. The two aptamers created a docking site of ~ 5 nm which can hold only a single thrombin protein of size ~ 4 nm. After binding of thrombin protein molecule in the plasmonic hotspot we were able to record Raman vibrational bands at 1140, 1540, and 1635 cm^{-1} which are characteristic bands of the protein. The intensity of Raman peaks was higher when the interparticle gap size was 10 nm than 15 nm due to difference in intensity of the electromagnetic field generated. Further, it was found that the sensing is specific for thrombin protein as no peaks were obtained when similar experiments were repeated with BSA and myoglobin protein. The designed plasmonic nanosensor hold promise for being used as a label free sensor for detection of single protein molecules.

References

1. J. J. Gooding and K. Gaus, *Angewandte Chemie International Edition*, 2016, **55**, 11354-11366.
2. J. J. Gooding, *ACS Sensors*, 2016, **1**, 1163-1164.
3. A. Ishijima and T. Yanagida, *Trends in Biochemical Sciences*, 2001, **26**, 438-444.
4. S. Shashkova and M. C. Leake, *Biosci Rep*, 2017, **37**, BSR20170031.
5. R. P. Haugland, M. T. Z. Spence, I. D. Johnson and A. Basey, *The handbook : a guide to fluorescent probes and labeling technologies*, Eugene (Or.) : Molecular probes, 10th ed. edn., 2005.
6. S. Nie, D. Chiu and R. Zare, *Science*, 1994, **266**, 1018-1021.
7. S. Weiss, *Science*, 1999, **283**, 1676-1683.
8. L. Yin, W. Wang, S. Wang, F. Zhang, S. Zhang and N. Tao, *Biosens Bioelectron*, 2015, **66**, 412-416.
9. S. Subramanian, H.-Y. Wu, T. Constant, J. Xavier and F. Vollmer, *Advanced Materials*, 2018, **30**, 1801246.
10. P. Holzmeister, G. P. Acuna, D. Grohmann and P. Tinnefeld, *Chemical Society Reviews*, 2014, **43**, 1014-1028.
11. M. J. Levene, J. Korlach, S. W. Turner, M. Foquet, H. G. Craighead and W. W. Webb, *Science*, 2003, **299**, 682-686.
12. A. Puchkova, C. Vietz, E. Pibiri, B. Wünsch, M. Sanz Paz, G. P. Acuna and P. Tinnefeld, *Nano Letters*, 2015, **15**, 8354-8359.
13. S. Khatua, H. Yuan and M. Orrit, *Physical Chemistry Chemical Physics*, 2015, **17**, 21127-21132.
14. P. Zijlstra, P. M. R. Paulo and M. Orrit, *Nature Nanotechnology*, 2012, **7**, 379-382.
15. K. M. Mayer, F. Hao, S. Lee, P. Nordlander and J. H. Hafner, *Nanotechnology*, 2010, **21**, 255503.
16. A. Kinkhabwala, Z. Yu, S. Fan, Y. Avlasevich, K. Müllen and W. E. Moerner, *Nature Photonics*, 2009, **3**, 654-657.
17. M. Bauch, K. Toma, M. Toma, Q. Zhang and J. Dostalek, *Plasmonics*, 2014, **9**, 781-799.
18. I. Kaminska, J. Bohlen, S. Mackowski, P. Tinnefeld and G. P. Acuna, *ACS Nano*, 2018, **12**, 1650-1655.
19. F. Mathieu, S. Liao, J. Kopatsch, T. Wang, C. Mao and N. C. Seeman, *Nano Letters*, 2005, **5**, 661-665.
20. R. Zhang, Y. Hong, B. M. Reinhard, P. Liu, R. Wang and L. Dal Negro, *ACS Applied Materials & Interfaces*, 2018, **10**, 27928-27935.
21. K. Kneipp, H. Kneipp, V. B. Kartha, R. Manoharan, G. Deinum, I. Itzkan, R. R. Dasari and M. S. Feld, *Physical Review E*, 1998, **57**, R6281-R6284.
22. E. M. Larsson, C. Langhammer, I. Zorić and B. Kasemo, *Science*, 2009, **326**, 1091-1094.
23. I. Ament, J. Prasad, A. Henkel, S. Schmachtel and C. Sönnichsen, *Nano Letters*, 2012, **12**, 1092-1095.
24. V. R. Dantham, S. Holler, C. Barbre, D. Keng, V. Kolchenko and S. Arnold, *Nano Letters*, 2013, **13**, 3347-3351.
25. D. Verschueren, X. Shi and C. Dekker, *Small Methods*, 2019, **3**, 1800465.
26. L. Rodríguez-Lorenzo, R. A. Álvarez-Puebla, I. Pastoriza-Santos, S. Mazzucco, O. Stéphan, M. Kociak, L. M. Liz-Marzán and F. J. García de Abajo, *Journal of the American Chemical Society*, 2009, **131**, 4616-4618.
27. S. E. J. Bell and N. M. S. Sirimuthu, *Journal of the American Chemical Society*, 2006, **128**, 15580-15581.
28. D.-K. Lim, K.-S. Jeon, H. M. Kim, J.-M. Nam and Y. D. Suh, *Nature Materials*, 2010, **9**, 60-67.
29. Y. Wang and J. Irudayaraj, *Philos Trans R Soc Lond B Biol Sci*, 2012, **368**, 20120026-20120026.
30. K. Kneipp, Y. Wang, H. Kneipp, L. T. Perelman, I. Itzkan, R. R. Dasari and M. S. Feld, *Physical Review Letters*, 1997, **78**, 1667-1670.

31. S. Nie and S. R. Emory, *Science*, 1997, **275**, 1102-1106.
32. J. Prinz, C. Heck, L. Ellerik, V. Merk and I. Bald, *Nanoscale*, 2016, **8**, 5612-5620.
33. K. J. Freedman, C. R. Crick, P. Albella, A. Barik, A. P. Ivanov, S. A. Maier, S.-H. Oh and J. B. Edel, *ACS Photonics*, 2016, **3**, 1036-1044.
34. C. Chen, Y. Li, S. Kerman, P. Neutens, K. Willems, S. Cornelissen, L. Lagae, T. Stakenborg and P. Van Dorpe, *Nature Communications*, 2018, **9**, 1733.
35. T. Brulé, A. Bouhelier, A. Dereux and E. Finot, *ACS Sensors*, 2016, **1**, 676-680.
36. G. Yang, J. Nanda, B. Wang, G. Chen and D. T. Hallinan, *ACS Applied Materials & Interfaces*, 2017, **9**, 13457-13470.
37. Y.-W. Wang, K.-C. Kao, J.-K. Wang and C.-Y. Mou, *The Journal of Physical Chemistry C*, 2016, **120**, 24382-24388.
38. A. Kinkhabwala, Z. Yu, S. Fan, Y. Avlasevich, K. Müllen and W. E. Moerner, *Nature Photonics*, 2009, **3**, 654.
39. A. Biswas, I. S. Bayer, A. S. Biris, T. Wang, E. Dervishi and F. Faupel, *Advances in Colloid and Interface Science*, 2012, **170**, 2-27.
40. J.-S. Huang, V. Callegari, P. Geisler, C. Brüning, J. Kern, J. C. Prangsma, X. Wu, T. Feichtner, J. Ziegler, P. Weinmann, M. Kamp, A. Forchel, P. Biagioni, U. Sennhauser and B. Hecht, *Nature Communications*, 2010, **1**, 150.
41. S. S. Aćimović, M. P. Kreuzer, M. U. González and R. Quidant, *ACS Nano*, 2009, **3**, 1231-1237.
42. W. Rechberger, A. Hohenau, A. Leitner, J. R. Krenn, B. Lamprecht and F. R. Aussenegg, *Optics Communications*, 2003, **220**, 137-141.
43. Y. Yao, M. A. Kats, P. Genevet, N. Yu, Y. Song, J. Kong and F. Capasso, *Nano Letters*, 2013, **13**, 1257-1264.
44. A. G. Curto, G. Volpe, T. H. Taminiau, M. P. Kreuzer, R. Quidant and N. F. van Hulst, *Science*, 2010, **329**, 930-933.
45. O. N. Assad, T. Gilboa, J. Spitzberg, M. Juhasz, E. Weinhold and A. Meller, *Advanced Materials*, 2017, **29**, 1605442.
46. B. D. Gates, Q. Xu, M. Stewart, D. Ryan, C. G. Willson and G. M. Whitesides, *Chemical Reviews*, 2005, **105**, 1171-1196.
47. G. P. Acuna, F. M. Möller, P. Holzmeister, S. Beater, B. Lalkens and P. Tinnefeld, *Science*, 2012, **338**, 506-510.
48. P. W. K. Rothemund, *Nature*, 2006, **440**, 297-302.
49. P. Zhan, P. K. Dutta, P. Wang, G. Song, M. Dai, S.-X. Zhao, Z.-G. Wang, P. Yin, W. Zhang, B. Ding and Y. Ke, *ACS Nano*, 2017, **11**, 1172-1179.
50. F. N. Gür, F. W. Schwarz, J. Ye, S. Diez and T. L. Schmidt, *ACS Nano*, 2016, **10**, 5374-5382.
51. W. P. Klein, C. N. Schmidt, B. Rapp, S. Takabayashi, W. B. Knowlton, J. Lee, B. Yurke, W. L. Hughes, E. Graugnard and W. Kuang, *Nano Letters*, 2013, **13**, 3850-3856.
52. R. Schreiber, N. Luong, Z. Fan, A. Kuzyk, P. C. Nickels, T. Zhang, D. M. Smith, B. Yurke, W. Kuang, A. O. Govorov and T. Liedl, *Nature Communications*, 2013, **4**, 2948.
53. S. Tanwar, K. K. Haldar and T. Sen, *Journal of the American Chemical Society*, 2017, **139**, 17639-17648.
54. C. Heck, Y. Kanehira, J. Kneipp and I. Bald, *Angewandte Chemie International Edition*, 2018, **57**, 7444-7447.
55. A. Srivastava and D. J. Creek, *Proteomics*, 2019, **19**, 1700448.
56. G. Zheng, F. Patolsky, Y. Cui, W. U. Wang and C. M. Lieber, *Nature Biotechnology*, 2005, **23**, 1294-1301.
57. S. H. Leuba and J. Zlatanova, *Biology at the Single Molecule Level*, Elsevier Science, 2001.
58. P. Zhang, J. Jiang, R. Yuan, Y. Zhuo and Y. Chai, *Journal of the American Chemical Society*, 2018, **140**, 9361-9364.
59. X. Zhang, M. R. Servos and J. Liu, *Chemical Communications*, 2012, **48**, 10114-10116.
60. H. Schürer, K. Stembera, D. Knoll, G. Mayer, M. Blind, H.-H. Förster, M. Famulok, P. Welzel and U. Hahn, *Bioorganic & Medicinal Chemistry*, 2001, **9**, 2557-2563.
61. A. Geiger, P. Burgstaller, H. von der Eltz, A. Roeder and M. Famulok, *Nucleic Acids Research*, 1996, **24**, 1029-1036.
62. L. C. Bock, L. C. Griffin, J. A. Latham, E. H. Vermaas and J. J. Toole, *Nature*, 1992, **355**, 564-566.

63. M. Dobbelstein and T. Shenk, *Journal of Virology*, 1995, **69**, 8027-8034.
64. K. Sefah, D. Shangguan, X. Xiong, M. B. O'Donoghue and W. Tan, *Nature Protocols*, 2010, **5**, 1169-1185.
65. G. Marrazza, *Biosensors (Basel)*, 2017, **7**, 5.
66. L. R. Paborsky, S. N. McCurdy, L. C. Griffin, J. J. Toole and L. L. Leung, *Journal of Biological Chemistry*, 1993, **268**, 20808-20811.
67. K. Y. Wang, S. H. Krawczyk, N. Bischofberger, S. Swaminathan and P. H. Bolton, *Biochemistry*, 1993, **32**, 11285-11292.
68. R. F. Macaya, P. Schultze, F. W. Smith, J. A. Roe and J. Feigon, *Proceedings of the National Academy of Sciences*, 1993, **90**, 3745-3749.
69. D. M. Tasset, M. F. Kubik and W. Steiner, *Journal of Molecular Biology*, 1997, **272**, 688-698.
70. C. V. Pagba, S. M. Lane, H. Cho and S. Wachsmann-Hogiu, *Journal of Biomedical Optics*, 2010, **15**, 1-8, 8.
71. A. Rygula, K. Majzner, K. M. Marzec, A. Kaczor, M. Pilarczyk and M. Baranska, *Journal of Raman Spectroscopy*, 2013, **44**, 1061-1076.
72. V. d. A. Silva, M. T. Cargnelutti, G. M. Giesel, L. C. Palmieri, R. Q. Monteiro, H. Verli and L. M. T. R. Lima, *PLOS ONE*, 2011, **6**, e24735.
73. B. J. Kennedy, S. Spaeth, M. Dickey and K. T. Carron, *The Journal of Physical Chemistry B*, 1999, **103**, 3640-3646.
74. Y. Liu, N. Liu, X. Ma, X. Li, J. Ma, Y. Li, Z. Zhou and Z. Gao, *Analyst*, 2015, **140**, 2762-2770.
75. S. Papadopoulos, K. D. Jürgens and G. Gros, *Biophys J*, 2000, **79**, 2084-2094.

Chapter 7

Conclusion

"Arriving at one goal is the starting point to another"

- John Dewey

7.1. Summary of this thesis

This thesis presents a set of contributions to the field of nanophotonics which are based on the potential of plasmonic nanoantennas to enhance and localize electromagnetic fields for single-molecule spectroscopic and sensing applications. Optical spectroscopy at the ultimate limit of a single molecule has been a research area with tremendous focus because it yields full distribution and dynamics of the system instead of an average value, thus exposing normally hidden heterogeneities in a complex system. Plasmonic nanoantennas spatially confine light on the nanometre scale concentrating electromagnetic field in a volume of only a few hundred nm^3 or less. This nanoscale field confinement by metallic nanostructures leads to strong enhancement of usually weak single molecule signals. This thesis consists of six chapters including chapter 7.

The introductory chapter gives an overview of the importance and limitations of single molecule measurements, a historical overview of optical properties of metal nanoparticles, fundamentals of plasmonic nanoantennas and their applicability for enhancing single molecule spectroscopic signals. Salient features of the DNA origami technique and its utility for the fabrication of plasmonic nanoantennas with tunable interparticle gaps and stoichiometry are also discussed. In the second chapter, the synthetic protocols and characterization techniques used for the work presented in this thesis have been described. Solution based synthesis of Au structures such as Au nanostars, Au@Ag nanostars, and Au nanoclusters. This chapter also discusses the synthesis of quantum dots, DNA origami and self-assembly of plasmonic nanoantennas (with tunable interparticle gaps and stoichiometry) on DNA origami. In the rest four chapters, the design of novel plasmonic nanoantennas and their utility for single molecule spectroscopic and sensing applications have been discussed separately.

The important achievements of the work can be summarized as given below:

1) The programmable nature of the DNA origami technique allowed fabrication of Au nanostar dimer structures with tunable interparticle gaps and stoichiometry. It also enabled precise positioning of the single Texas red (TR) dye molecule in the conjunction region of the nanostars which is difficult to achieve using sophisticated techniques like electron beam lithography. The designed monomer and dimer structures were found to be significantly enhancing Raman signals of single TR dye molecules located in the plasmonic hotspot. The obtained enhancement factors (EFs) were in the range of 10^9-10^{10}, which are high enough for single analyte detection. The interparticle gaps strongly

influence the EFs. The EFs of TR dye slightly decreased upon increasing the interparticle gap from 7 to 13 nm due to changes in the intensity of the generated electromagnetic field. It was also found that the EFs decreased by a factor of ~ 13 for nanostar dimer structures with higher negative curvature. SERS-active wide conjunction region of 13 nm can provide enough space for the accommodation of large biomolecule of interest.

2) Bimetallic Au@Ag nanoparticles have superior optical properties than their monometallic counterparts because they combine the best of both metals i.e. enhanced plasmonic properties (high extinction coefficient) of Ag and chemical stability of Au in one structure. Au@Ag nanostars were prepared by epitaxial growth of Ag over premade Au nanostars. They were assembled on the rectangular DNA origami template with different interparticle gap sizes and stoichiometry. The Au@Ag nanostar dimer and monomer structures were found to be showing broadband field enhancement effects. The designed nanoantennas significantly enhanced SERS signals of single FAM, Cy3, and Texas red (TR) dye molecules, which correspond to different regions of the visible spectrum. Among all the three dyes, the EFs were found to be highest for Cy3 dye due to close resonance between the SPR of Au@Ag nanostars and molecular absorption of Cy3 dye. The EFs for TR and FAM dye molecules were also in the order of 10^9-10^{10}, sufficient for single molecule detection. The Au@Ag NS dimer nanoantennas with an interparticle gap size of 5 nm were found to be showing 10-fold enhancement in the fluorescence signals of single Cy3 dye molecule positioned in the hotspot. The designed Au@Ag NS dimers showed ultrasensitive detection of bacterial biomarker pyocyanin with a LOD of 500 pM. The obtained results suggest that the designed nanoantennas have the potential to be transformed into a label-free SERS based plasmonic sensor for clinically important molecules.

3) A one-pot, green, cost effective, and energy-efficient synthetic strategy for the synthesis of Si QDs has been reported. Blue emitting Si QDs were synthesized at room temperature using 3-aminopropyltriethoxysilane (APTES) as the silicon source and a commonly available sugar, glucose, as a reducing and stabilizing agent. These Si QDs showed a reversible thermo-responsive emission in the temperature range of 20-80 ^{0}C and high ionic stability required for conjugation with biomolecules such as DNA. The oxygen rich functional groups on the surface of Si QDs were exploited to reduce Au^{3+} ions to Au nanoparticles to form a hybrid Au NP−Si QD nanocomposite, possessing catalytic activity for reduction of nitroarenes. The blue emitting Si QDs upon mixing with orange red emitting Au nanoclusters (Au NCs) led to the generation of white light emitting mixture

(WLEM) with (0.33,0.32) chromaticity color co-ordinate. The generated WLEM further showed fast, sensitive, and selective reversible sensing of Hg^{+2} ions and thiol containing amino acid Cysteine with a LOD of 10 nM. The synthesized Si QDs were then conjugated with DNA oligonucleotides and immobilized on the DNA origami template at predefined position. The AFM results confirmed immobilization of single Si QD on the DNA origami.

4) Plasmon assisted label-free sensing of single thrombin protein on Au@Ag NS dimer nanoantennas has been reported. Single thrombin protein was captured in the plasmonic hotspot using thrombin binding aptamers as a biomolecular receptor. After binding of thrombin protein molecule in the plasmonic hotspot, vibrational bands at 1140, 1540, and 1635 cm^{-1} which are characteristic of proteins were enhanced significantly. The designed nanosensor was specific for thrombin protein. The DNA origami assembled plasmonic nanoantennas hold promise for being used as a label-free sensor for the detection of single protein molecules.

Thus, DNA origami is a versatile platform for self-assembling plasmonic nanoantennas with different modifications allowing them to be used for single molecule spectroscopic and sensing applications.

7.2. Scope for the future work

The work presented in this thesis provides comprehensive information about how DNA origami can be used for designing novel plasmonic nanoantennas which can further be utilized for nanoplasmonic sensing. However, joint multidisciplinary efforts are required to demonstrate the practical usability of these results in the field of nanoplasmonics.

For example,

1) The designed plasmonic nanoantennas can be used for single molecule fluorescence enhancement studies using fluorescence-lifetime imaging microscopy. These studies will be helpful in understanding the effect of interparticle gaps, stoichiometry, and the size and shape of different types of nanoparticles on the fluorescence enhancement factors. Further, the results will help in developing cost-effective and sensitive fluorescence based imaging and sensing platforms.
2) Single quantum dot-metal hybrid nanostructures will open the window to a new class of photostable probes for single-molecule spectroscopic applications. Despite several advanced capabilities to produce the nanoantennas and the quantum dots separately,

merging a single quantum dot with a single plasmonic nanoantenna is an ongoing challenge.

3) Designing an implantable SERS and fluorescence based sensor is the future of diagnostics. DNA origami assembled plasmonic nanoantennas has set the foundation for designing implantable high-performance single-molecule sensors for *in vivo* spectroscopic sensing and imaging of important analytes.
4) The dynamic behavior of single biomacromolecules is different from an ensemble system. Plasmonic nanoantennas will not only help in understanding the basic molecular dynamics and kinetics but will also help in the innovation of new clinical diagnostics and pharmaceutical drug evaluation methods.

Appendix A

Table 1: Sequences of staple strands: DNA origami

Colored DNA sequences at the 3′ end of staple sequences at the positions of 80,81,82,83,85,86,87,111 are the modified sequences used for immobilization of Au nanostars on DNA origami.

Name	**Sequence 5' to 3'**
2	ACGTTAGTAAATGAATTTTCTGTAAGCGGAGT
3	CGTAACGATCTAAAGTTTTGTCGTGAATTGCG
4	TGTAGCATTCCACAGACAGCCCTCATCTCCAA
5	TGAGTTTCGTCACCAGTACAAACTTAATTGTA
6	CAAGCCCAATAGGAACCCATGTACCGTAACAC
7	CTCAGAGCCACCACCCTCATTTTCCTATTATT
8	CCCTCAGAACCGCCACCCTCAGAACTGAGACT
9	TATCACCGTACTCAGGAGGTTTAGCGGGGTTT
10	TATAAGTATAGCCCGGCCGTCGAG
11	GAGAATAGCTTTTGCGGGATCGTCGGGTAGCA
12	AATAATAAGGTCGCTGAGGCTTGCAAAGACTT
13	AAAAAAGGACAACCATCGCCCACGCGGGTAAA
14	TCGGTTTAGCTTGATACCGATAGTCCAACCTA
15	AATGCCCCGTAACAGTGCCCGTATGTGAATTT
16	CTGAAACAGGTAATAAGTTTTAACCCCTCAGA
17	CCTCAAGAATACATGGCTTTTGATAGAACCAC
18	AGGGTTGAATAAATCCTCATTAAATGATATTC

19	CAGCGAAAAACTTTCAACAGTTTCTGGGATTTTGCTAAAC
20	AAAGGCCGAAAGGAACAACTAAAGCTTTCCAG
21	ATATATTCTTTTTTCACGTTGAAAATAGTTAG
22	CAATGACACTCCAAAAGGAGCCTTACAACGCC
23	CTTAAACATCAGCTTGCTTTCGAGAAACAGTT
24	TGCCTTGACTGCCTATTTCGGAACAGGGATAG
25	AGTGTACTTGAAAGTATTAAGAGGCCGCCACC
26	TAAGCGTCGAAGGATTAGGATTAGTACCGCCA
27	GGAAAGCGACCAGGCGGATAAGTGAATAGGTG
28	ACGGCTACTTACTTAGCCGGAACGCTGACCAA
29	TTTCATGAAAATTGTGTCGAAATCTGTACAGA
30	ATACGTAAAAGTACAACGGAGATTTCATCAAG
31	AAACGAAATGACCCCCAGCGATTATTCATTAC
32	GAGCCGCCCCACCACCGGAACCGCCTAAAACA
33	GCCACCACTCTTTTCATAATCAAACCGTCACC
34	CACCAGAGTTCGGTCATAGCCCCCGCCAGCAA
35	TGAGGCAGGCGTCAGACTGTAGCGTAGCAAGG
36	ACAAACAAAATCAGTAGCGACAGATCGATAGC
37	ACGGTCAAGACAGCATCGGAACGAACCCTCAG
38	CGCCTGATGGAAGTTTCCATTAAACATAACCG
39	GCGAAACATGCCACTACGAAGGCATGCGCCGA
40	CTCATCTTGAGGCAAAAGAATACACTCCCTCA

41	AACCAGAGACCCTCAGAACCGCCAGGGGTCAG
42	GTTTGCCACCTCAGAGCCGCCACCGATACAGG
43	TCGGCATTCCGCCGCCAGCATTGACGTTCCAG
44	TGCCTTTAGTCAGACGATTGGCCTGCCAGAAT
45	CTTTGAAAAGAACTGGCTCATTATTTAATAAA
46	CCAGGCGCTTAATCATTGTGAATTACAGGTAG
47	AGTAATCTTAAATTGGGCTTGAGAGAATACCA
48	CCAAATCACTTGCCCTGACGAGAACGCCAAAA
49	TTATTCATAGGGAAGGTAAATATTCATTCAGT
50	GACTTGAGAGACAAAAGGGCGACAAGTTACCA
51	AATCACCAAATAGAAAATTCATATATAACGGA
52	CCGGAAACACACCACGGAATAAGTAAGACTCC
53	AGCACCGTTAAAGGTGGCAACATAGTAGAAAA
54	GGACGTTGTCATAAGGGAACCGAAAGGCGCAG
55	CGATTTTAGAGGACAGATGAACGGCGCGACCT
56	TTTCAACTATAGGCTGGCTGACCTTGTATCAT
57	GAATAAGGACGTAACAAAGCTGCTGACGGAAA
58	ATTGAGGGTAAAGGTGAATTATCAATCACCGG
59	AGCGCCAACCATTTGGGAATTAGATTATTAGC
60	TCACAATCGTAGCACCATTACCATCGTTTTCA
61	ACGCAAAGGTCACCAATGAAACCAATCAAGTT

62	ACGAACTAGCGTCCAATACTGCGGAATGCTTT
63	AAAGATTCAGGGGGTAATAGTAAACCATAAAT
64	CATTCAACGCGAGAGGCTTTTGCATATTATAG
65	GGAATTACTCGTTTACCAGACGACAAAAGATT
66	AAAAGTAATATCTTACCGAAGCCCAACACTAT
67	GAAGGAAAATAAGAGCAAGAAACAACAGCCAT
68	ATACCCAAGATAACCCACAAGAATAAACGATT
69	TTATTACGGTCAGAGGGTAATTGAATAGCAGC
70	TACATACAGACGGGAGAATTAACTACAGGGAA
71	TAAATATTGGAAGAAAAATCTACGACCAGTCA
72	ACTGGATAACGGAACAACATTATTACCTTATG
73	TTTGCCAGATCAGTTGAGATTTAGTGGTTTAA
74	CCAAAATATAATGCAGATACATAAACACCAGA
75	CATAACCCGAGGCATAGTAAGAGCTTTTTAAG
76	GCAATAGCGCAGATAGCCGAACAATTCAACCG
77	GCCCAATACCGAGGAAACGCAATAGGTTTACC
78	ATCAGAGAAAGAACTGGCATGATTTTATTTTG
79	TGAACAAACAGTATGTTAGCAAACTAAAAGAA
80	AAACAGTTGATGGCTTAGAGCTTATTTAAATACTAAGCTATCGA
81	CAAAAATCATTGCTCCTTTTGATAAGTTTCATCTAAGCTATCGA
82	TCAGAAGCCTCCAACAGGTCAGGATCTGCGAACTAAGCTATCGA
83	AAGAGGAACGAGCTTCAAAGCGAAGATACATTCTAAGCTATCGA

84	CCTAATTTACGCTAACGAGCGTCTATATCGCG
85	ATTATTTAACCCAGCTACAATTTTCAAGAACGCTAAGCTATCGA
86	TTTTGTTTAAGCCTTAAATCAAGAATCGAGAACTAAGCTATCGA
87	CTTTACAGTTAGCGAACCTCCCGACGTAGGAACTAAGCTATCGA
88	GCGCATTAGCTTATCCGGTATTCTAAATCAGA
89	ATATAATGCATTGAATCCCCCTCAAATCGTCA
90	TTTTTGCGCAGAAAACGAGAATGAATGTTTAG
91	TACCTTTAAGGTCTTTACCCTGACAAAGAAGT
92	GAAGCAAAAAAGCGGATTGCATCAGATAAAAA
93	TTTTAATTGCCCGAAAGACTTCAATTCCAGAG
94	TCTTACCAGCCAGTTACAAAATAAATGAAATA
95	TATTTTGCTCCCAATCCAAATAAGTGAGTTAA
96	AGGTTTTGAACGTCAAAAATGAAAGCGCTAAT
97	GAGGCGTTAGAGAATAACATAAAAGAACACCC
98	TGCAACTAAGCAATAAAGCCTCAGTTATGACC
99	TCCATATACATACAGGCAAGGCAACTTTATTT
100	CGAGTAGAACTAATAGTAGTAGCAAACCCTCA
101	TCGCAAATGGGGCGCGAGCTGAAATAATGTGT
102	ATCGGCTGCGAGCATGTAGAAACCAGCTATAT
103	GGTATTAAGAACAAGAAAAATAATTAAAGCCA
104	CAAGCAAGACGCGCCTGTTTATCAAGAATCGC
105	TCATTACCCGACAATAAACAACATATTTAGGC

106	TATAGAAGCGACAAAAGGTAAAGTAGAGAATA
107	GCTAAATCCTGTAGCTCAACATGTATTGCTGA
108	CAAAATTAAAGTACGGTGTCTGGAAGAGGTCA
109	CAATAAATACAGTTGATTCCCAATTTAGAGAG
110	TCAATTCTTTTAGTTTGACCATTACCAGACCG
111	TTTCATTTGGTCAATAACCTGTTTAATCAATACTAAGCTATCGA
112	CTAATTTATCTTTCCTTATCATTCATCCTGAA
113	TAAGTCCTACCAAGTACCGCACTCTTAGTTGC
114	AATGCAGACCGTTTTTATTTTCATCTTGCGGG
115	CCAGACGAGCGCCCAATAGCAAGCAAGAACGC
116	CTGTAATATTGCCTGAGAGTCTGGAAAACTAG
117	CAACGCAATTTTTGAGAGATCTACTGATAATC
118	TATATTTTAGCTGATAAATTAATGTTGTATAA
119	AGGTAAAGAAATCACCATCAATATAATATTTT
120	GCGTTATAGAAAAAGCCTGTTTAGAAGGCCGG
121	ACGCTCAAAATAAGAATAAACACCGTGAATTT
122	CATATTTAGAAATACCGACCGTGTTACCTTTT
123	AGAGGCATAATTTCATCTTCTGACTATAACTA
124	TAAAGTACCGCGAGAAAACTTTTTATCGCAAG
125	AGAGAATCGGTTGTACCAAAAACAAGCATAAA
126	TCAGGTCACTTTTGCGGGAGAAGCAGAATTAG
127	GGTAGCTAGGATAAAAATTTTTAGTTAACATC

128	ACCGTTCTAAATGCAATGCCTGAGAGGTGGCA
129	AGACAGTCATTCAAAAGGGTGAGATATCATAT
130	AATTACTACAAATTCTTACCAGTAATCCCATC
131	AGGCGTTACAGTAGGGCTTAATTGACAATAGA
132	AATGGTTTACAACGCCAACATGTAGTTCAGCT
133	TTTTAGTTTTTCGAGCCAGTAATAAATTCTGT
134	CATGTCAAGATTCTCCGTGGGAACCGTTGGTG
135	AGAAAAGCAACATTAAATGTGAGCATCTGCCA
136	GCAAATATCGCGTCTGGCCTTCCTGGCCTCAG
137	GTTAAAATTTTAACCAATAGGAACCCGGCACC
138	TTAAGACGTTGAAAACATAGCGATTTAAATCA
139	ATCAAAATCGTCGCTATTAATTAACGGATTCG
140	TAACCTCCATATGTGAGTGAATAAACAAAATC
141	TATGTAAACCTTTTTTAATGGAAAAATTACCT
142	ACAAAGAAATTAATTACATTTAACACATCAAG
143	GATTGACCGATGAACGGTAATCGTAGCAAACA
144	ACCCGTCGTCATATGTACCCCGGTAAAGGCTA
145	CTTTCATCCCCAAAAACAGGAAGACCGGAGAG
146	AAATAATTTTAAATTGTAAACGTTGATATTCA
147	GCTCATTTTCGCATTAAATTTTTGAGCTTAGA
148	TAGAATCCCTGAGAAGAGTCAATAGGAATCAT

149	CTGTAAATCATAGGTCTGAGAGACGATAAATA
150	AAATCAATGGCTTAGGTTGGGTTACTAAATTT
151	TTGAATTATGCTGATGCAAATCCACAAATATA
152	TAGATGGGGGGTAACGCCAGGGTTGTGCCAAG
153	GTTTGAGGGAAAGGGGGATGTGCTAGAGGATC
154	GAAGATCGGTGCGGGCCTCTTCGCAATCATGG
155	GCTTCTGGTCAGGCTGCGCAACTGTGTTATCC
156	CTTTTACACAGATGAATATACAGTAAGCGCCA
157	CCTGATTGAAAGAAATTGCGTAGACCCGAACG
158	GCGCAGAGATATCAAAATTATTTGACATTATC
159	GAGCAAAAACTTCTGAATAATGGAAGAAGGAG
160	AAAACAAATTCATCAATATAATCCTATCAGAT
161	CACGACGTGTAATGGGATAGGTCAAAACGGCG
162	ATTAAGTTCGCATCGTAACCGTGCGAGTAACA
163	CAGCTGGCGGACGACGACAGTATCGTAGCCAG
164	GGCGATCGCACTCCAGCCAGCTTTGCCATCAA
165	TTCGCCATTGCCGGAAACCAGGCAAACAGTAC
166	TTTAACGTTCGGGAGAAACAATAATTTTCCCT
167	ACAGAAATCTTTGAATACCAAGTTCCTTGCTT
168	AACCTACCGCGAATTATTCATTTCCAGTACAT
169	TGGATTATGAAGATGATGAAACAAAATTTCAT
170	CTTGCATGCATTAATGAATCGGCCCGCCAGGG

171	CCCGGGTACTTTCCAGTCGGGAAACGGGCAAC
172	TCATAGCTACTCACATTAATTGCGCCCTGAGA
173	GCTCACAATGTAAAGCCTGGGGTGGGTTTGCC
174	CGACAACTAAGTATTAGACTTTACAGCCGGAA
175	TTATTAATGCCGTCAATAGATAATCAGAGGTG
176	ATTTTGCGTCTTTAGGAGCACTAAGCAACAGT
177	CGGAATTATTGAAAGGAATTGAGGTGAAAAAT
178	GATGGCAAAATCAATATCTGGTCACAAATATC
179	GGGAGAGGTGTAAAACGACGGCCATTCCCAGT
180	GCCAGCTGCCTGCAGGTCGACTCTGCAAGGCG
181	ACTGCCCGCCGAGCTCGAATTCGTTATTACGC
182	GTGAGCTAGTTTCCTGTGTGAAATTTGGGAAG
183	GCATAAAGTTCCACACAACATACGAAACAATT
184	GGATTTAGCGTATTAAATCCTTTGTTTTCAGG
185	AGATTAGATTTAAAAGTTTGAGTACACGTAAA
186	CTAAAATAGAACAAAGAAACCACCAGGGTTAG
187	ATCAACAGTCATCATATTCCTGATTGATTGTT
188	TGGTTTTTAACGTCAAAGGGCGAAGAACCATC
189	AGCTGATTACAAGAGTCCACTATTGAGGTGCC
190	GAGTTGCACGAGATAGGGTTGAGTAAGGGAGC
191	CCAGCAGGGGCAAAATCCCTTATAAAGCCGGC
192	ACGAACCAAAACATCGCCATTAAATGGTGGTT

193	AGGCGGTCATTAGTCTTTAATGCGCAATATTA
194	GCCACGCTATACGTGGCACAGACAACGCTCAT
195	CTAAAGCAAGATAGAACCCTTCTGAATCGTCT
196	AAACCCTCACCAGTAATAAAAGGGATTCACCAGTCACACG
197	TATCAGGGCGGTTTGCGTATTGGGAACGCGCG
198	TGGACTCCCTTTTCACCAGTGAGACCTGTCGT
199	AGTTTGGAGCCCTTCACCGCCTGGTTGCGCTC
200	GAATAGCCGCAAGCGGTCCACGCTCCTAATGA
201	CCGAAATCCGAAAATCCTGTTTGAAATACCGA
202	TAGCCCTACCAGCAGAAGATAAAAACATTTGA
203	GAATGGCTAGTATTAACACCGCCTCAACTAAT
204	GCGTAAGAGAGAGCCAGCAGCAAAAAGGTTAT
205	GCCAACAGTCACCTTGCTGAACCTGTTGGCAA
206	CGATGGCCCACTACGTAAACCGTC
207	ACCCAAATCAAGTTTTTTGGGGTCAAAGAACG
208	GTAAAGCACTAAATCGGAACCCTAGTTGTTCC
209	CCCCGATTTAGAGCTTGACGGGGAAATCAAAA
210	GAACGTGGCGAGAAAGGAAGGGAACAAACTAT
211	CGGCCTTGCTGGTAATATCCAGAACGAACTGA
212	CCGCCAGCCATTGCAACAGGAAAAATATTTTT
213	GGAAATACCTACATTTTGACGCTCACCTGAAA
214	GAAATGGATTATTTACATTGGCAGACATTCTG

Table 2: Sequences of edge staples for monomer origami A

Poly T sequences (Red) are added in edge staples to avoid aggregation due to stacking interactions.

Name	Sequence 5' to 3'
Edge19	CAGCGAAATTTTTTTTAACTTTCAACAGTTTCTGGGATTTTGCTAAACTTTTT
Edge37	ACGGTCAATTTTTTTTTTGACAGCATCGGAACGAACCCTCAG
Edge54	GGACGTTGTTTTTTTTTTTCATAAGGGAACCGAAAGGCGCAG
Edge71	TAAATATTTTTTTTGGAAGAAAAATCTACGACCAGTCA
Edge89	ATATAATGTTTTTTTTCATTGAATCCCCCTCAAATCGTCA
Edge107	GCTAAATCTTTTTTTTTTTTTCTGTAGCTCAACATGTATTGCTGA
Edge125	AGAGAATCTTTTTTGGTTGTACCAAAAACAAGCATAAA
Edge143	GATTGACCTTTTTTTTTTGATGAACGGTAATCGTAGCAAACA
Edge161	CACGACGTTTTTTTTTTTGTAATGGGATAGGTCAAAACGGCG
Edge179	GGGAGAGGTTTTTTTTTTTGTAAAACGACGGCCATTCCCAGT
Edge197	TATCAGGGTTTTTTCGGTTTGCGTATTGGGAACGCGCG
Edge206	TTTTTTTCGATGGCCCACTACGTAAACCGTC

Table 3: Sequences of edge staples for monomer origami B

Name	Sequence 5' to 3'
Edge10	TTTTTTTTTTATAAGTATAGCCCGGCCGTCGAG
Edge18	AGGGTTGATTTTTTATAAATCCTCATTAAATGATATTC
Edge36	ACAAACAATTTTTTTTTTTAATCAGTAGCGACAGATCGATAGC

Edge53	AGCACCGTTTTTTTTTTAAAGGTGGCAACATAGTAGAAAA
Edge70	TACATACATTTTTTTTTTTGACGGGAGAATTAACTACAGGGAA
Edge88	GCGCATTATTTTTTTTTTTGCTTATCCGGTATTCTAAATCAGA
Edge106	TATAGAAGTTTTTTTTTTTCGACAAAAGGTAAAGTAGAGAATA
Edge124	TAAAGTACTTTTTTCGCGAGAAAACTTTTTATCGCAAG
Edge142	ACAAAGAATTTTTTTTTATTAATTACATTTAACACATCAAG
Edge160	AAAACAAATTTTTTTTTTTTTCATCAATATAATCCTATCAGAT
Edge178	GATGGCAATTTTTTTTTTTTTTAATCAATATCTGGTCACAAATATC
Edge196	AAACCCTCTTTTTTTTTTTACCAGTAATAAAAGGGATTCACCAGTCACACG TTTTT

Table 4: Sequences of branching staples for monomer origami A

Name	**Sequence 5' to 3'**
Branc19	AGGGTTGAAACTTTCAACAGTTTCTGGGATTT
Branc37	ACAAACAAGACAGCATCGGAACGAACCCTCAG
Branc54	AGCACCGTTCATAAGGGAACCGAAAGGCGCAG
Branc71	TACATACAGGAAGAAAAATCTACGACCAGTCA
Branc89	GCGCATTACATTGAATCCCCCTCAAATCGTCA
Branc107	TATAGAAGCTGTAGCTCAACATGTATTGCTGA
Branc125	TAAAGTACGGTTGTACCAAAAACAAGCATAAA
Branc143	ACAAAGAAGATGAACGGTAATCGTAGCAAACA
Branc161	AAAACAAAGTAATGGGATAGGTCAAAACGGCG
Branc179	GATGGCAATGTAAAACGACGGCCATTCCCAGT

Branc197	AAACCCTCCGGTTTGCGTATTGGGAACGCGCG
Branc206	GTCACACGCGATGGCCCACTACGTAAACCGTC

Table 5: Sequences of branching staples for monomer origami B

Name	Sequence 5' to 3'
Branc10	TGCTAAACTATAAGTATAGCCCGGCCGTCGAG
Branc18	CAGCGAAAATAAATCCTCATTAAATGATATTC
Branc36	ACGGTCAAAATCAGTAGCGACAGATCGATAGC
Branc53	GGACGTTGTAAAGGTGGCAACATAGTAGAAAA
Branc70	TAAATATTGACGGGAGAATTAACTACAGGGAA
Branc88	ATATAATGGCTTATCCGGTATTCTAAATCAGA
Branc106	GCTAAATCCGACAAAAGGTAAAGTAGAGAATA
Branc124	AGAGAATCCGCGAGAAAACTTTTTATCGCAAG
Branc142	GATTGACCATTAATTACATTTAACACATCAAG
Branc160	CACGACGTTTCATCAATATAATCCTATCAGAT
Branc178	GGGAGAGGAATCAATATCTGGTCACAAATATC
Branc196	TATCAGGGACCAGTAATAAAAGGGATTCACCA

Table 6: Dye labeled sequence

Name	Sequence 5' to 3'
Branc106-DYE	GCTAAATCCGACAAAAGGTAAAGTAGAGAATATTTT**(Texas red)**

Table 7: Thiol labeled sequence

Name	Sequence 5' to 3'
Thiol labeled sequence	**5′Thiol-**CGTCGTATTCGATAGCTTAG

Table 8: Dye labeled sequences

Name	Sequence 5' to 3'
Bran 106-FAM	GCTAAATCCGACAAAAGGTAAAGTAGAGAATATTTT**(FAM)**
Bran 106-Cy3	GCTAAATCCGACAAAAGGTAAAGTAGAGAATATTTT**(Cy3)**
Bran 106- TR	GCTAAATCCGACAAAAGGTAAAGTAGAGAATATTTT**(TR)**

Table 9: Biotin labeled sequences

Name	Sequence 5' to 3'
Bio-120	**Biotin**- TTGCGTTATAGAAAAAGCCTGTTTAGAAGGCCGG
Bio-27	**Biotin**-TTGGAAAGCGACCAGGCGGATAAGTGAATAGGTG
Bio-11	**Biotin**- TTGAGAATAGCTTTTGCGGGATCGTCGGGTAGCA
Bio-188	**Biotin**- TTTGGTTTTTAACGTCAAAGGGCGAAGAACCATC

Table 10: Branching and dye labeled staple used for single molecule fluorescence studies

Name	Sequence 5' to 3'
Bran_L_106	GCTAAATCCGACAAAAGGTAAAGTAGAGAATAATTGTATGAGTAG AGATTTGTAAGAGCTGTTAGTTAGCTCGCTCAGCTAATAGTTGCCC ACACAACGTCAAAATTAGAGAACGGTCGTAACATTATCG

Bran_L_106_ Cy3	**Cy3**TTCGATAATGTTACGACCGTTCTCTAATTTTGACGTTGTGTGGG CAACTATTAGCTGAGCGAGCTAACTAACAGCTCTTACAAATCTCT ACTCATACAAT

Table 11: Amine labeled sequence

Name	Sequence 5' to 3'
Amine labeled sequence	**5′Amine**-TTTTTCGATAGCTTAG

Table 12: Aptamer labeled branching staple sequences

Red colored DNA sequences are the thrombin binding aptamers.

Name	Sequence 5' to 3'
Apt_106	GCTAAATCCGACAAAATTTTAGTCCGTGGTAGGGCAGGTTGGGGTGAC TTTTTGGTAAAGTAGAGAATA
Apt_107	TATAGAAGCTGTAGCTTTTTGGTTGGTGTGGTTGGTTTT CAACATGTATTGCTGA

List of publications

*(1) **Swati Tanwar**, Krishna Kanta Haldar, and Tapasi Sen "DNA origami directed Au nanostar dimers for single-molecule surface-enhanced Raman scattering" ***Journal of the American Chemical Society***, 2017, 139 (48), 17639-17648.

*(2) Bhagwati Sharma†, **Swati Tanwar**†, and Tapasi Sen "One pot green synthesis of Si quantum dots and catalytic Au nanoparticle-Si quantum dot nanocomposite"***ACS Sustainable Chemistry and Engineering***, 2019, *7* (3), 3309–3318. ***(†Equal contribution)***

*(3) **Swati Tanwar**, Bhagwati Sharma, Vishaldeep Kaur, and Tapasi Sen "White light emission from a mixture of silicon quantum dots and gold nanoclusters and its utilities in sensing of mercury (II) ions and thiol containing amino acid" ***RSC Advances*** 2019,**9**, 15997-16006. ***(Selected for editor's collection focusing on fluorescent sensors)***

(4) Krishna Kanta Haldar, Rathindranath Biswas, **Swati Tanwar**, Tapasi Sen, and Jouko Lahtinen "One-Pot Synthesis of Au Embedded ZnO Nanorods Composite Heterostructures with Excellent Photocatalytic Properties"***ChemistrySelect*** 2018, 3, 7882 – 7890.

(5) Krishna Kanta Haldar, **Swati Tanwar**, Rathindranath Biswas, Tapasi Sen and Jouko Lahtinen "Noble copper-silver-gold trimetallic nanobowls: an efficient catalyst". Manuscript accepted in the ***Journal of Colloid and Interface Science*** 2019, 556, 140-146.

*(6) **Swati Tanwar**, Vishaldeep Kaur, Gagandeep Kaur, and Tapasi Sen "Broadband enhancement of single molecule Raman signals using Au@Ag NS dimer nanoantennas". ***(Manuscript communicated)***

*(7) **Swati Tanwar**, Vishaldeep Kaur, Gagandeep Kaur, and Tapasi Sen "SERS based Label free sensing of single protein molecule in the plasmonic hotspot". ***(Manuscript under preparation)***

(8) **Swati Tanwar**, Vishaldeep Kaur, Gagandeep Kaur, and Tapasi Sen "DNA origami assembled Au@Ag nanostar dimer nanoantennas for label-free sensing of pyocyanin". ***(Manuscript to be communicated)***

(9) Gagandeep Kaur, **Swati Tanwar**, Vishaldeep Kaur, Tapasi Sen "Interfacial design of gold/silver core-shell nanostars for plasmon enhanced photocatalytic coupling of 4-aminothiophenol". ***(Manuscript under revision)***

(10) Vishaldeep Kaur, **Swati Tanwar**, Gagandeep Kaur, and Tapasi Sen "Immobilization of single Si QD on DNA origami for photophysical studies".

[N.B. *articles included in this thesis]

Conference presentations

1. ***Best poster presentation prize,*** **"**DNA origami directed self assembled hybrid nanoantennas for single molecule spectroscopic and sensing applications" **Swati Tanwar,** Vishaldeep Kaur, Gagandeep Kaur, and Tapasi Sen, poster presentation delivered at "**1st CRIKC Chemistry Symposium 2019**" (9th -10th November 2019), organized by IISER Mohali, India.
2. ***Best oral presentation prize,*** "DNA origami nanoantennas for enhancing single molecule spectroscopic applications" **Swati Tanwar,** Bhagwati Sharma**,** Vishaldeep Kaur and Tapasi Sen, oral and poster presentation delivered at **" 3rd INST In-house symposium 2018 "** (22nd November 2018) organized by Institute of Nano Science and Technology, Mohali, India.
3. "DNA origami directed self-assembled hybrid nanoantennas for single molecule spectroscopy applications" **Swati Tanwar,** Bhagwati Sharma, Vishaldeep Kaur and Tapasi Sen, poster presentation delivered at **"2nd INST In-house symposium"** (11th -12th December 2017) organized by Institute of Nano Science and Technology, Mohali, India.
4. ***Best oral presentation prize,*** "DNA origami directed self-assembled hybrid nanoantennas for single molecule spectroscopy applications" **Swati Tanwar,** Bhagwati Sharma, Vishaldeep Kaur and Tapasi Sen, oral and poster presentation delivered at **"CeNS – INST symposium"** (16th – 18th November 2017) organized by CeNS, India.
5. "DNA origami directed self-assembled hybrid nanoantennas for single molecule spectroscopy applications" **Swati Tanwar,** Bhagwati Sharma, Vishaldeep Kaur, and Tapasi Sen poster presentation delivered at **" Third CRIKC Nanoscience day"** (29th August 2017), organized by CSIR-CSIO, India.
6. "DNA origami directed self-assembly of Au nanostar dimer nanoantenna material for single molecule fluorescence enhancement" **Swati Tanwar**, Ashok Kumar Ganguli, and Tapasi Sen poster presentation delivered at 1st **" One day in house symposium"** (18th November 2016), organized by Institute of Nano Science and Technology, Mohali, India.

7. Attended one day symposium on "Optics and photonics based technologies and instruments for civil society" (21st October 2016) organized by CSIR-CSIO, India.
8. "DNA origami directed Au nanostar dimer for single molecule fluorescence enhancement" **Swati Tanwar**, Ashok Kumar Ganguli, and Tapasi Sen, poster presentation delivered at **" Second CRIKC Nanoscience day"** (8th August 2016),

organized by Institute of Nano Science and Technology, Mohali, India.

9. "Plasmonic nanoantenna for single molecule fluorescence enhancement" **Swati Tanwar**, Ashok Kumar Ganguli and Tapasi Sen poster presentation delivered at **"18th National Symposium in Chemistry (NSC-18)"** (5th -7th February 2016), organized by Institute of Nano Science and Technology and Panjab University, India.
10. Attended **10th CRSI-RSC Symposium** (4th February 2016) organized by Institute of Nano Science and Technology and Panjab University, India.
11. ***Best poster prize*** in **Har Gobind Khorana exhibition pavilion** organized by Punjab State Council for Science & Technology, India (January 2016).
12. Attended Renishaw Inside for Raman conference (December 2015), organized by Indian Institute of Science Education and Research Mohali, India.
13. ***Best poster presentation prize*** "DNA directed assembly of anisotropic plasmonic nanostructures for single molecule fluorescence enhancement" **Swati Tanwar**, Ashok Kumar Ganguli ,and Tapasi Sen poster presentation delivered at **"2nd AISRF Meeting on "Advanced Nanomaterials for Energy, Optoelectronics and Biological Applications"** (25th – 27th November 2015), organized by Institute of Nano Science and Technology, Mohali, India.
14. "Plasmonic metal nanoparticles based assemblies for single molecule fluorescence enhancement" **Swati Tanwar**, Ashok Kumar Ganguli, and Tapasi Sen, poster presentation delivered at **"6th MRS Trilateral Symposium"** (23rd -25th November 2015), organized by Institute of Nano Science and Technology, Mohali, India.
15. "Design of DNA-directed self-assembled plasmonic nanoantennas for fluorescence enhancement" **Swati Tanwar**, Ashok Kumar Ganguli, and Tapasi Sen, poster presentation delivered at **"Chemical Frontiers 2015, 6th Edition"** (August 2015), organized by Indian Institute of Technology, Mumbai and JNCASR Bangalore at Goa, India.
16. ***Best scientific poster award***, "Design of DNA-directed self-assembled plasmonic nanoantennas for fluorescence enhancement" **Swati Tanwar**, Ashok Kumar Ganguli, and Tapasi Sen, poster presentation delivered at **"First CRIKC Nanoscience day"** (22nd July 2015), organized by Institute of Nano Science and Technology, Mohali, India.
17. Attended Advance microscopy and Imaging Technique workshop (16th -17th January 2015) organized by Olympus and Institute of Nano Science and Technology, Mohali, India.

18. "Design of DNA-directed self-assembled plasmonic nanoantennas for fluorescence enhancement" **Swati Tanwar**, Ashok Kumar Ganguli, and Tapasi Sen, poster presentation delivered at **One day conclave on Nano Biotechnology** (22nd December 2014), organized by Institute of Nano Science and Technology, Mohali, India.
19. Attended **one day workshop on Electron microscopy and NMR** (15th December 2014) organized by JEOL and Institute of Nano Science and Technology, Mohali, India.
20. ***Best scientific poster presentation prize,*** (2014) "Metal nanoparticles based assemblies for energy applications" **Swati Tanwar**, Tapasi Sen, and Ashok Kumar Ganguli, poster presentation delivered at a **scientific poster presentation** in Hindi competition organized by Town official language implementation committee, Government of India.

Vita

Swati Tanwar

Ph.D. Research Scholar
Institute of Nano Science and Technology
&
Indian Institute of Science Education and Research Mohali

Swati Tanwar completed her bachelor's degree in Applied Life Sciences and Master's degree in Chemistry from Delhi University in 2010 and 2012 respectively. From August 2012 to November 2013 she worked as a project assistant at CSIR-Institute of Genomics and Integrative Biology, India with Dr. Pradip Nahar. In August 2014 she joined the Institute of Nano Science and Technology, Mohali as a Ph.D. student under the guidance of Dr.Tapasi Sen. She authored several research articles and have presented her research work in several National and International conferences in some of which she was awarded. Her research interests include fabrication of plasmonic nanoantennas for single molecule spectroscopic and sensing applications.